Magazine of Civil Engineering

Online peer-reviewed open-access scientific journal in the field of Civil and Construction Engineering

Founder and Publisher: Peter the Great St. Petersburg Polytechnic University

This journal is registered by the Federal Service for Supervision of Communications, Information Technology, and Mass Media (ROSKOMNADZOR) in 2020. Certificate El No. FS77-77906 issued February 19, 2020.

Periodicity: 8 issues per year

Publication in the journal is open and free for all authors and readers.

Indexing: Scopus, Web of Sceince (ESCI, RSCI), DOAJ, Compendex, EBSCO, Google Academia, Index Copernicus, ProQuest, Ulrich's Serials Analysis System, CNKI

Corresponding address: 29 Polytechnicheskaya st., Saint Petersburg, 195251, Russia

Chief science editor: associate member of RAS, Sc.D. in Engineering, Vitaly V. Sergeev

Deputy chief science editors:
Sc.D. in Engineering, Galina L. Kozinetc

Sc.D. in Engineering, Sergey V. Korniyenko

Executive editor: Ekaterina A. Linnik

Translator, editor: Darya Yu. Alekseeva

DT publishing specialist:
Anastasiya A. Kononova

Contacts:
E-mail: mce@spbstu.ru
Web: http://www.engstroy.spbstu.ru

Date of issue: 14.11.2022

Contents

Contents

Magazine of Civil Engineering

Research article

Model of pile-frozen soil interaction in a closed form

O. V. Tretiakova ✉

Perm National Research Polytechnic University, Perm, Russia

Perm State Agro-Technological University named after Academician D.N. Pryanishnikov, Perm, Russia

✉ *olga_wsw@mail.ru*

Abstract. The object of the research is pile-soil interaction under freezing and frost heaving. Modeling of pile-soil interaction on the basis of joint solution of static equilibrium equations, physical equations for stresses and equation of thermal conductivity is considered. No such solutions have been found in existing publications. In this study, a model of pile-soil interaction in the form of a closed analytical solution with respect to the pile geometry was developed. Methods of continuum mechanics and elasticity theory were used. The model was a mathematical record of the equilibrium of forces acting on the pile. It was reduced to second-order algebraic equations with respect to its geometric parameters. The static equations of force equilibrium written in quadratic form related the geometric parameters of the pile to the stress-strain state and the thermal characteristics of the soil. Physical equations for heaving stresses and the thermal conductivity equation closed the problem. The model was developed as applied to a pile with an upper reverse taper. It reflected the performance of the pile during freezing and frost heaving and allowed determining its required geometric parameters under the given soil and climatic conditions.

Citation: Tretiakova, O.V. Model of pile-frozen soil interaction in a closed form. Magazine of Civil Engineering. 2022. 115(7). Article No. 11501. DOI: 10.34910/MCE.115.1

1. Introduction

The geometric parameters of foundations, especially of piles under freezing and soil frost heaving, are governed by the equilibrium condition of acting forces. They include the external load and the stress-strain components of soil. The external load is specified in each design case. The components of the stress-strain state of soil are the stresses and forces arising at the boundary of the soil-pile system, including frost heaving stresses and forces. Such a stress-strain state can be described by Hooke's law in the framework of elasticity theory. The stress-strain state is conditioned by thermal-physical characteristics of soil and the position of frost boundary.

It can be seen that to determine geometric parameters of piles in freezing and frost heaving conditions, it is necessary to jointly solve static equations of force equilibrium with physical equations in the form of Hooke's law and thermal conductivity equation.

The thermal conductivity equation makes it possible to determine the position of the frost boundary. Bonacina and Comini [1] gave an analytical solution to the problem of phase transitions in time in a range of temperatures. The thermal effect of the phase transition was approximated by the heat capacity of the soil. This method can be applied to determining the position of the frost boundary in time. The thermal conductivity equation, which takes into account the heat capacity, as a function of the temperature field in three dimensions, was studied by Dauzhenko and Gishkelyuk [2]. The method can be successfully applied to solve Stefan problem for the phase transition and to determine the position of the frost boundary. Vlasov and Volkov [3] considered the thermal state of a two-phase system and presented a mathematical model of the quasi-stationary temperature field of the system. The system was represented as an isotropic half-

space with a moving phase boundary. Such a model reflects the state of freezing soil with moving frost boundary, but requires a special solution for this case. Alekseyev in his paper [4] analyzed the methods for numerical simulation of heat transfer in freezing soil based on Stefan problem solution. The thermal impact of structures located in the soil was taken into account. He presented the results of determining the position of the frost boundary in different software packages. However, the above studies did not relate the thermal-physical characteristics of soil and the position of the frost boundary to the stress-strain state of soil and the parameters of foundations.

The physical equations, in the form of Hooke's law, make it possible to calculate frost heaving stresses around foundations. Yin, X. and others [5] developed a system of equations describing the state of soil during freezing and frost heaving. Their system included equations for modeling the migration of water, steam, and heat transfer in freezing soil. They also gave the equations for stresses in soil in the framework of elasticity theory. The author of the current research believes that it would be promising to extend this system of equations to the case of a rigid inclusion in soil, i.e. a pile. The next important research was carried out by Korshunov, Doroshenko and Nevzorov [6]. They used a numerical model of frozen soil to obtain the coefficients of elastic and elastic-plastic compressibility of soil, and also the rate of change in the Young's modulus with temperature. However, they did not introduce a rigid inclusion in the form of a pile into the model. If they had done that, it would make it possible to obtain static equilibrium equations within the framework of elasticity theory, which would connect the law of motion of the frost boundary, frost heave stresses, and geometric parameters of the piles. Volokhov in his paper [7] predicted values of the tangential frost heaving forces on the side surface of the foundation in a range of temperatures. He also showed the dependence of these forces on the properties of the contact zone of the frozen soil and the foundation, i.e., the foundation material and the roughness of its surface. It would also be interesting to consider the geometric parameters of the foundation, as well as its configuration. Ladanyi and Foriero [8] proposed a closed solution for calculating the tangential frost heaving forces acting on a pile. They combined the effects of frost freezing and frost heaving rate, pile size and soil temperature at any depth along the pile in time. Domashchuk [9] calculated the tangential frost heaving forces on the basis of the rate and value of soil surface frost heaving, and also the temperature of the frozen soil. He also investigated frost heaving forces acting on vertical, horizontal, and inclined elements embedded in frozen soil. Kim and his colleagues [10] established the dependence of tangential frost stresses on the foundation material, soil type and temperature, and the position of the frost boundary. The data they obtained could be used to make static equations of force equilibrium with respect to geometric parameters of foundations under these conditions. Nazarov and Istomin [11] analyzed the stress-strain state of a pile foundation under the influence of the stress state and the thermal expansion coefficient of the material in a range of temperatures. Nazarov and Poselsky [12] assessed the stress-strain state of the pile foundation under the influence of the moisture content and the temperature of the soil for different materials of the pile. But they did not take into account the geometric parameters of the foundation and therefore did not make up the static equations of force equilibrium with respect to these parameters. Alekseyev [13] presented the cases of the stress-strain state of the freezing soil around foundations of different types and made up the equilibrium equations. These cases were described using generalized Hooke's law and the theory of thermoelasticity without considering geometric parameters of the foundation. Normal stresses of frost heaving were considered in [14] as a function of soil deformation and stiffness of structures experiencing frost heaving pressure. However, the stiffness of concrete foundations is relatively constant in many cases. Therefore, models of normal frost heaving stresses relative to the geometric parameters of foundations are of greater interest. Liu, Wang [15] obtained a model of the interaction of frozen soil with a single pile on the basis of experimental data. The model took into account the effects of the changing normal pressure of frozen soil, negative temperature and soil moisture over time. Unfortunately, we did not see the development of the model in the form of an equilibrium force equation with respect to the geometric parameters of the pile. Alekseev [16] conducted extensive studies of normal horizontal frost heaving forces. A more complete use of the results would give the dependence of these forces on the geometric parameters of the foundation and its configuration. It is known that normal frost heaving forces reach significant values. If the direction of normal heaving forces was changed, positive factors for the performance of the foundation could be obtained.

Such factors were found by Huang and Sheng [17]. They illustrated the effect of belled pile geometry on the stress-strain state of freezing soil. It was shown that around the pile with an extension in the lower part, the restraining forces were formed. Those forces counteracted the tangential frost heaving forces causing the pile to rise. This fact complied with the results obtained by the author [18-19] of the current research. However, Huang and Sheng did not show the dependence of forces acting on the pile on their geometry although the results of their research allowed them to obtain such a dependence and on its basis to make static equations of equilibrium forces with respect to the geometric parameters of the piles. Chae, Cho and others [20] used the numerical simulation results in order to find out the influence of the shape and size of the pile bell on the belled piles displacement behaviors under pullout load in thawed soil conditions. Dickin and Leung [21] reported on the effect of the angle of the enlarged pile base on its uplift capacity. However, their studies were not related to the frost heaving forces of the soil. Li and Xu [22]

considered a set of force factors around a composite pile with carved grooves in seasonally frozen and permafrost soil layers. The force factors included frost heaving forces, forces from negative friction during soil thawing, which arise in the course of several autumn-winter seasons. Li and Xu showed the influence of the pile geometry on the permafrost layer and its importance for keeping the layer frozen. The obtained components of the stress-strain state of the soil, together with the results of thermophysical studies, could be used to make the static equilibrium equations of forces with respect to the pile geometric characteristics. Abbasov [23] developed recommendations for the use of flat profiled piles in freezing soil. The self-anchoring effect of the pile due to its geometry was shown in his work. However, static equations of force equilibrium with respect to the geometric parameters of the pile were not given.

Yushkov and Repetsky [24] determined the stresses and heaving forces acting on the double-tapered pile and the displacements of the pile. The anchoring effect of normal heaving forces acting on the top cone of the pile during its lifting by tangential frost heaving forces was noted. The equation for pile bearing capacity, based on the static equilibrium of acting forces, was derived. However, the solution of this equation with respect to the geometric parameters of the pile was not given. Oswell and Nixon [25] analyzed the problem of reducing the bearing capacity of foundations under changing thermal characteristics of permafrost. The adaptation of foundations to such conditions can be achieved through their geometry. Alekseev [26] studied the pile-frozen soil system. The system was represented as a cylindrical element, which was shifted under the effect of soil frost heaving. The problem of determining the dimensions and components of the stress-strain state of this element was solved. But the results were not written down in the form of static equilibrium equations of forces in the considered system with respect to geometry of the pile. Kurbatsky's method [27] provided a non-standard solution of the static problem with respect to these parameters. Linell and Lobacz in their report [28] presented technical recommendations on the design and construction of foundations in the areas of deep seasonal frost and permafrost. The report took into account the geological and climatic conditions of the construction site. It would be useful to combine these data into a general scheme of finding the geometric parameters of foundations. Ladanyi and Foriero [29] considered the calculation of a vertically and horizontally loaded pile in permafrost based on the balance between axial and bending stresses. They defined a general procedure for calculating these parameters with respect to the pile geometry. Their calculation could be used for ground frost heaving conditions when supplemented with appropriate heaving forces.

Thus, there has not been found a model of pile-soil interaction obtained by a simultaneous solution of three kinds of equations with respect to the pile geometry under frost heaving. These three equations are the static equilibrium equations, thermal conductivity ones and physical equations for stresses. Therefore, the purpose of the research is to develop such a generalized model of the freezing soil-pile system as a closed analytical solution with respect to the pile geometry.

To achieve the purpose, the three kinds of equations were considered, i.e. static equations of force equilibrium with respect to the pile geometry; physical equations in the form of Hooke's law for soil frost heaving stresses; thermal conductivity equation to determine the position of the frost boundary.

2. Methods

The model was built in the framework of continuum mechanics, i.e. the static equilibrium equations of forces, the thermal conductivity equation and physical equations in the form of Hooke's law were used, which provided closed form of the model.

The static equilibrium equations of force at the soil-pile boundary related the foundation geometry with the stress-strain state and the thermal characteristics of the frozen soil. The normal frost heaving stresses were derived from the physical equations in the form of Hooke's law. The thermal conductivity equation allowed to obtain the frost boundary position.

The model was a generalized way of obtaining pile geometry. It was a mathematical expression of equilibrium condition of a pile. This model was reduced to second-order algebraic equations with respect to the geometry of the reverse taper pile. The model was considered by the author in [18], [30], [31].

2.1. Static equations with respect to the pile geometry

Static equilibrium equations with respect to the pile geometry were given for two design schemes: the frost boundary position (1) within the pile variable cross-section and (2) within the pile constant cross-section, as shown in Fig. 1.

In Figure 1 σ_f, τ_{fi}, f_i are the frost heaving normal and tangential stresses, the design value of soil resistance along the pile in the thawed soil, respectively; P- the sum of the external load and the pile's own weight; α is angle of the pile taper surface.

Magazine of Civil Engineering, 115(7), 2022

(a) | (b)
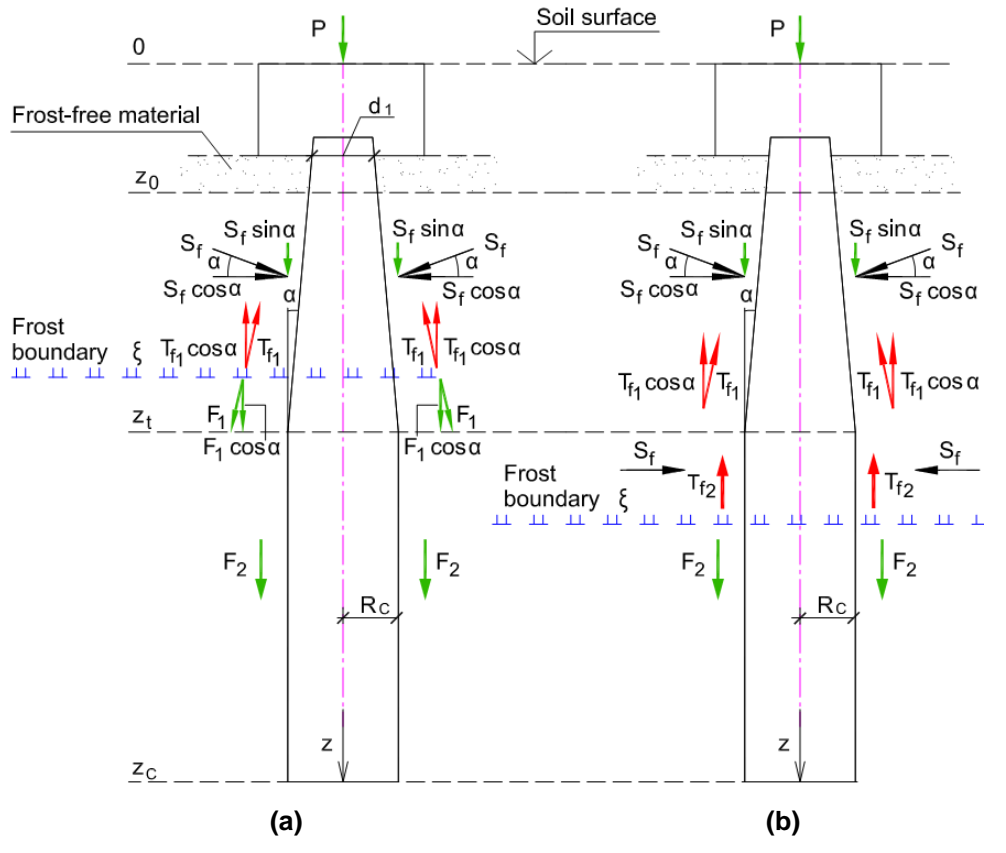
the frost boundary position within the pile variable cross-section | the frost boundary position within the pile constant cross-section

Figure 1. Design schemes of the pile

A pile with an upper reverse taper was considered. Static equilibrium equations of pile forces, acting on the pile under freezing and frost heaving of the soil were as follows (Fig. 1, a, b):

if $z_0 < \xi < z_t$ (Figure 1, a): $-P - S_f \sin\alpha + (T_{f1} - F_1)\cos\alpha - F_2 = 0$, (1)

if $z_0 < z_t < \xi$ (Figure 1, b): $-P - S_f \sin\alpha + T_{f1}\cos\alpha + T_{f2} - F_2 = 0$. (2)

Integral forces on lateral area of the pile (see Figure 1):

if $\xi < z_\kappa$: $\quad S_f = \int_0^\xi \sigma_f 2\pi R_t(z)dz$, $\qquad$ if $\xi > z_t$: $\quad S_f = \int_0^{z_t} \sigma_f 2\pi R_t(z)dz$,

$$T_{f_1} = \int_0^\xi \tau_{f1} 2\pi R_t(z)dz, \qquad\qquad T_{f_1} = \int_0^{z_t} \tau_{f1} 2\pi R_t(z)dz,$$

$$F_1 = \int_\xi^{z_t} f_1 2\pi R_t(z)dz, \qquad\qquad T_{f_2} = \int_{z_t}^\xi \tau_{f2} 2\pi R_c dz,$$

$$F_2 = \int_{z_t}^{z_c} f_2 2\pi R_c dz. \qquad\qquad F_2 = \int_\xi^{z_c} f_2 2\pi R_c dz.$$

The area of a unit annular strip along the taper perimeter (dF_t):

$$dF_t = 2\pi R_t(z)dz. \tag{3}$$

Taking into account the variable radius of the taper, expression (3) will be written:

$$dFt = 2\pi[R_c - \sin\alpha(z_t - z)]dz. \tag{4}$$

The area of a unit annular strip along the perimeter of cylindrical part of the pile is as follows:

$$dF_c = 2\pi R_c dz .$$
(5)

Taking into account the above expressions for the integral forces and (3), (4), (5), if cos α ≈ 1, equations (1), (2) take the form:

if $z_0 < \xi < z_t$ (Figure 1, a):

$$-P - (\int_{z_0}^{\xi} \sigma_f dF_t) \sin \alpha + \int_{z_0}^{\xi} \tau_{f1} dF_t - \int_{\xi}^{z_t} f_1 dF_t - \int_{z_t}^{z_c} f_2 dF_c = 0 ,$$
(6)

if $z_0 < z_t < \xi$ (Figure 1,б):

$$-P - (\int_{z_0}^{z_t} \sigma_f dF_t) \sin \alpha + \int_{z_0}^{z_t} \tau_{f_1} dF_t + \int_{z_t}^{\xi} \tau_{f2} dF_c - \int_{\xi}^{z_c} f_2 dF_c = 0.$$
(7)

Based on expressions (6), (7) and taking into account the area of the strip of the taper (4), the static equilibrium equations of forces are written as the second-order algebraic equations with respect to the angle of the pile taper.

If frost boundary position is $z_0 < \xi < z_t$:

$$\sigma_f (z_t \xi - z_t z_0 - 0.5\xi^2 + 0.5z_0^2)(\sin \alpha)^2 +$$

$$+ [-R_c \sigma_f (\xi - z_0) - \tau_{f_1}(z_t \xi - z_t z_0 - 0.5\xi^2 + 0.5z_0^2) + 0.5f_1(z_t - \xi)^2](\sin \alpha) +$$
(8)

$$+ R_c [\tau_{f1}(\xi - z_0) - f_1(z_t - \xi) - f_2(z_c - z_t)] - 0.5\pi^{-1}P = 0.$$

If frost boundary position is $z_0 < z_t < \xi$:

$$0.5\sigma_f (z_t - z_0)^2 (\sin \alpha)^2 +$$

$$+ [-R_c \sigma_f (z_t - z_0) - 0.5\tau_{f1}(z_t - z_0)^2](\sin \alpha) +$$
(9)

$$+ R_c [\tau_{f1}(z_t - z_0) + \tau_{f2}(\xi - z_t) - f_2(z_c - \xi)] - 0.5\pi^{-1}P = 0.$$

The solution of equations (8) and (9) with respect to the value of sin α, allows to obtain the pile geometric parameters, that is the angle of the pile taper α as shown in Figure 1.

The equations take into account the stress-strain state of the soil and the thermal characteristics of the frozen soil.

2.2. Physical equation in the form of Hooke's law for normal frost heaving stresses

In this model, the static equations of equilibrium of acting forces were supplemented by physical equations in the form of Hooke's law for normal frost heaving stress.

Based on the linear elastic deformability of soils, the author used the theory of elasticity to find the stresses of frost heaving. The equation for normal heaving stresses was written in the form of Hooke's law and took into account the thermal characteristics of the soil. The Young's modulus of elasticity in the equation was replaced by the deformation modulus.

Normal heaving stresses were found in the open system. In paper [32] the author showed that frost heaving occurs when the total volume of frozen and unfrozen water exceeds the volume of pores in the soil. This causes an increase in the soil volume and the development of normal frost heaving stress σ_f. The normal frost heaving stress is developed at the contact of the expanding soil with the foundation surfaces. Thus frost heaving stress is, on the one hand, the function of the soil porosity; on the other hand, it is caused by "excess moisture" resulting in the formation of "excess ice", that exceeds the pore volume.

The expression for normal frost heaving stress at z depth is as follows [32]:

$$\sigma_f = E_f \frac{h_{heave}}{z} \cdot \left[1 - e \left(1 - w_w \frac{\rho_d}{\rho_w} - 1.09w \frac{\rho_d}{\rho_w} \right) \right] k_{ан},$$
(10)

where E_f is the deformation modulus of frozen soil (кN/cm²), z is a coordinate from the day surface (cm); w is the natural moisture of soil and w_w is the water content due to unfrozen water, e is a porosity ratio; ρ_d is the dry density; ρ_w is the free water density: ρ_d / ρ_w is the coefficient of mass moisture to volumetric moisture; k_{an} is the anisotropy factor taking into account the direction of the heaving forces; h_{heave} is the displacement of soil under frost heaving resulting from water sucking up. According to Konrad's formula [33], [34], the displacement of soil under frost heaving resulting from water sucking up, h_{heave}, is as follows

$$h_{heave} = 1.09 \cdot SP \cdot \tau \cdot grad \ t \ , \tag{11}$$

where SP is the segregation potential of soil, t is the frost heaving time and $grad \ t$ is the temperature gradient.

After substituting equation (11) into equation (10), the formula of normal frost heaving stress as the function of moisture, leading to "excess ice", was obtained.

$$\sigma_f = E_f \frac{1.09 \cdot SP \cdot \theta \cdot grad \ t}{z} \cdot \left[1 - e \left(1 - w_w \frac{\rho_d}{\rho_w} - 1{,}09 w \frac{\rho_d}{\rho_w} \right) \right] k_{ан}, \tag{12}$$

The formula of the tangential frost heaving stresses was given in [18].

$$\tau_f = \left[c_{soil} - 1.09(w + (SP \cdot \theta \cdot grad \ t \cdot k_{an}/z)(c_{soil} - c_{ice}) \right] +$$
$$+ \eta_{soil} \gamma_{soil} z(tg \varphi_{soil}) \left(1 - 1.09(w + (SP \cdot \theta \cdot grad \ t \cdot k_{an}/z)) \right) + \tag{13}$$
$$+ \eta_{ice} \gamma_{ice} z(tg \varphi_{ice}) 1.09(w + (SP \cdot \theta \cdot grad \ t \cdot k_{an}/z)),$$

where c_{soil} is the soil specific cohesion; c_{ice} is the ice shear resistance; η_{soil} and η_{ice} are the coefficients of the lateral pressure of soil and ice; γ_{soil} and γ_{ice} are the volume density of soil and ice; φ_{soil} and φ_{ice} are the angles of internal friction of soil and ice, respectively.

The tangential frost heaving stress can also be found on the base research by Labuz and Zang [35].

2.3. Thermal conductivity Equation and determining the position of the frost boundary

The frost boundary position was determined on the basis of the thermal conductivity equation. It was assumed that the soil within the pile length was homogeneous; the deformation modulus of frozen soil within the pile length was constant; the temperature along the depth of the freezing layer changed linearly. It was also assumed that the temperature did not change along the x- and y- coordinates, but did so along the z-coordinate.

Phase transitions of water into ice were taken into account in theoretical modeling of heat and mass transfer processes in the soil and the Stefan problem was used. As a freezing soil region has a movable phase boundary the freezing boundary movement condition was written as:

$$q_f - q_{thawed} = Q_{phase} \xi^{/} \tag{14}$$

After substituting expressions for heat fluxes ($q = \lambda \ grad \ t$), the equation (14) took the form of the law of motion of the freezing boundary:

$$\lambda_f \frac{\partial t_f(z, \theta)}{\partial z} - \lambda_{thawed} \frac{\partial t_{thawed}(z, \theta)}{\partial z} = Q_{phase} \frac{\partial \xi(\theta)}{\partial \theta} \ , \tag{15}$$

where ξ is the frost boundary position; θ is freezing period; t_f, t_{thawed} are temperature of frozen and thawed zones; λ_f, λ_{thawed} are coefficients of thermal conductivity of frozen and thawed soil; Q_f is specific heat of phase transitions (heat of freezing); q_f, q_{thawed} are heat fluxes in thawed and frozen zones:

$q_f = \lambda_f \ grad \ t_f, \quad q_{thawed} = \lambda_{thawed} \ grad \ t_{thawed}.$

Provided that at the transit point temperature t is zero, $(z, \theta) = const = 0$, and, the temperature along the depth of the freezing layer changes linearly, the Stefan condition (15) was written in the form of a differential equation:

$$Q_{phase}\frac{d\xi}{d\theta} = \frac{-\lambda_f t_{surf}}{\xi}, \tag{16}$$

The solution of the equation was a function that allowed to find the frost boundary position i.e. the depth of freezing at constant temperature on the soil surface:

$$\xi(\theta) = \sqrt{\frac{2\lambda_f |t_{surf}|\theta}{Q_{phase}}}, \tag{17}$$

where $|t_{surf.}|$ is the absolute value of negative soil surface temperature.

An expression for the case of variable surface temperature was obtained by averaging it over some intervals (decades or months). A graph of the variation of the soil temperature along the depth of the layer is shown in Figure 2. In the Figure 2: t_f is the soil temperature at the design level along freezing layer; t_{thawed} is the temperature of thawed soil; θ is freezing period.
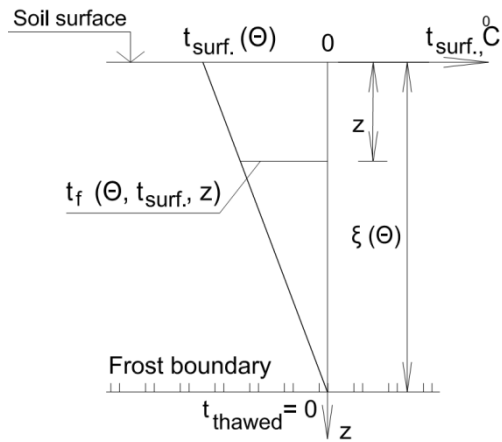
Figure 2 - Graph of the soil temperature variation by the depth of the freezing layer.

From the similarity of the triangles in Figure 2 it followed:

$$\frac{t_f(\theta,z)}{t_{surf}(\theta)} = \frac{\xi(\theta)-z}{\xi(\theta)} = 1 - \frac{z}{\xi(\theta)}, \tag{18}$$

Then the soil temperature in the freezing layer was determined from the expression:

$$t_f(\theta,z) = t_{surf}(\theta)\left[1 - \frac{z}{\xi(\theta)}\right]. \tag{19}$$

The derivative of this function on the coordinate was then as follows:

$$\frac{\partial t_f(\theta,z)}{\partial z} = -\frac{t_{surf}(\theta)}{\xi(\theta)}. \tag{20}$$

Just as in the case of constant surface temperature, it was assumed that Stefan's condition was valid for the movable phase boundary during soil freezing (15).

Since at the phase boundary $t_f < 0$, and $t_{thawed} = 0$, we wrote down the expression for heat flux in thawed zone as follows: $\lambda_{thawed}\,(\partial t_{thawed}(z,\theta)/\partial z) = 0$

Then Stefan's condition (15) took the form:

$$\lambda_f \frac{\partial t_f(\theta,z)}{\partial z} = Q_{phase}\frac{\partial \xi(\theta)}{\partial \theta}. \tag{21}$$

Then Stefan's condition (15) became:

$$\lambda_f\left(-\frac{t_{surf}(\theta)}{\xi(\theta)}\right) = Q_{phase}\frac{\partial\xi(\theta)}{\partial\theta} \quad\Rightarrow\quad \frac{\partial\xi(\theta)}{\partial\theta} = -\frac{\lambda_f}{Q_{phase}}\frac{t_{surf}(\theta)}{\xi(\theta)}. \tag{22}$$

After separating the variables, it became:

$$\xi d\xi = -\frac{\lambda_f}{Q_{phase}}t_{surf}(\theta)d\theta. \tag{23}$$

Then it was assumed that the law of temperature change in time was known (see Figure 2) and in the time interval from 0 to θ the surface temperature was constant ($t_{surf\,(i+1)}$ = const = θ). Integrating expression (23) in the time interval from 0 to θ and in coordinates from 0 to ξ resulted in:

$$\int_0^\xi \xi d\xi = -\frac{\lambda_f}{Q_{phase}}\int_0^\theta t_{surf}\,d\theta = -\frac{\lambda_f t_{surf}}{Q_{phase}}\int_\theta^\theta d\theta \quad\Rightarrow\quad \frac{\xi^2}{2} = -\frac{\lambda_f t_{surf}}{Q_{phase}}\theta \tag{24}$$

Then the equation for determining the frost boundary position at a constant step in time from θ_1 to θ_{i+1} with the corresponding temperature interval took the form:

$$\xi = \left[-\frac{2\lambda_f t_{surf}}{Q_{phase}}\theta\right]^{0.5}. \tag{25}$$

Assuming that within a step from θ_1 to θ_{i+1} the surface temperature was constant and equal to the average value ($t_{surf\,(i+1)}$ = const), expression (25) was integrated

$$\int_{\xi_i}^{\xi_{i+1}} \xi d\xi = -\frac{\lambda_f}{Q_{phase}}\int_{\theta_i}^{\theta_{i+1}}t_{surf}(\theta)d\theta, \tag{26}$$

where i is step numbers, i = 1,2,3 ..., into which the considered time period was divided.

Replacing $t_{surf}(\theta)$ with a step function with values of t_{surf} averaged over months, it was obtained:

$$\int_{\xi_i}^{\xi_{i+1}} \xi d\xi = -\frac{\lambda_f}{Q_{phase}}\int_{\theta_i}^{\theta_{i+1}}t_{surf\,(i+1)}d\theta = -\frac{\lambda_f t_{surf\,(i+1)}}{Q_{phase}}\int_{\theta_i}^{\theta_{i+1}}d\theta, \tag{27}$$

Equation (27) was transformed:

$$\frac{\xi_{i+1}^2 - \xi_i^2}{2} = -\frac{\lambda_f t_{surf\,(i+1)}}{Q_{phase}}(\theta_{i+1} - \theta_i), \tag{28}$$

Hence, the equation for step-by-step determination of the frost boundary position at each new step in time θ_{i+1} became as follows:

$$\xi_{i+1} = \left[\xi_i^2 - \frac{2\lambda_f t_{surf\,(i+1)}}{Q_{phase}}(\theta_{i+1} - \theta_i)\right]^{0.5}, \tag{29}$$

θ_i is the value of the frost boundary position at the previous step.

The position of the frost boundary under buried structures could also be determined by two parameters: the internal temperature in the structure and the radius of thermal influence of the structure on the soil. This radius was considered to be the distance from the structure at which the natural temperature of the soil was preserved. The position of the frost boundary was determined from the condition of linear temperature distribution at that distance. The internal temperature in the tunnel was found from the heat balance equation. The radius of thermal influence of the structure on the soil was obtained from the equation:

$$R = \sqrt{\frac{2\lambda_{red}(t_{\mathrm{int}} - t_z)}{Q}} \, , \qquad (30)$$

where Q is the average annual vertical heat flux in the soil around the structure; λ_{red} is the reduced coefficient of thermal conductivity; "t_{int}" is the internal temperature in the structure; t_z is the temperature of free soil at the considered depth.

The numerical complex developed by Ulitsky, Kudryavtsev, Paramonov, and Sakharov [36], [37] could also be used to determine the position of the frost boundary. Models of the thermal conductivity of frozen soils to find the position of the frost boundary were given in [38].

3. Results and Discussion

The model developed by the author had the following assumptions:

- The frost boundary, which was horizontal, was movable. As it advanced, the thawed soil transitioned to the frozen state.

- In frozen and thawed soil, elastic physical relationships were true.

- The temperature at the soil surface was variable.

- The delay in soil cooling and freezing described in the second Fourier law was not taken into account in this paper, and the temperature of frozen soil at a certain depth was considered at the same time as that at the surface.

The limitations of the model for the case of a reverse taper pile were as follows:

- A vertical friction pile was considered.

-The length of the cylindrical part of the pile was assumed to be not less than the length that provided the bearing capacity of the pile in thawed soil.

-The length and angle of the taper were limited by the diameter of the pile at the place of its embedding in the grillage (d_1), as shown in the figure 1.

The model was a system of equations:

Static equilibrium equations of forces if $z_0 < \xi < z_t$:

$$-P - (\int_{z_0}^{\xi} \sigma_f \, dF_t)\sin\alpha + \int_{z_0}^{\xi} \tau_{f1} \, dF_t - \int_{\xi}^{z_t} f_1 \, dF_t - \int_{z_t}^{z_c} f_2 \, dF_c = 0 \, .$$

Static equilibrium equations of forces if $z_0 < z_t < \xi$:

$$-P - (\int_{z_0}^{z_t} \sigma_f \, dF_t)\sin\alpha + \int_{z_0}^{z_t} \tau_{f_1} \, dF_t + \int_{z_t}^{\xi} \tau_{f2} \, dF_c - \int_{\xi}^{z_c} f_2 \, dF_c = 0.$$

The area of a unit annular strip along the taper perimeter

$$dF_t = 2\pi[R_c - \sin\alpha(z_t - z)]dz \, ,$$

The area of a unit annular strip along the perimeter of cylindrical part of the pile

$$dF_c = 2\pi R_c dz,$$

Static equilibrium equations of forces with respect to the angle of the pile taper if frost boundary position $z_0 < \xi < z_t$:

$$\sigma_f(z_t\xi - z_t z_0 - 0.5\xi^2 + 0.5z_0^2)(\sin\alpha)^2 +$$
$$+[-R_c\sigma_f(\xi - z_0) - \tau_{f_1}(z_t\xi - z_t z_0 - 0.5\xi^2 + 0.5z_0^2) +$$
$$+0.5f_1(z_t - \xi)^2](\sin\alpha) + R_c[\tau_{f1}(\xi - z_0) -$$
$$-f_1(z_t - \xi) - f_2(z_c - z_t)] - 0.5\pi^{-1}P = 0 \, ,$$

if frost boundary position $z_0 < z_t < \xi$:

$$0.5\sigma_f(z_t - z_0)^2(\sin\alpha)^2 +$$
$$+[-R_c\sigma_f(z_t - z_0) - 0.5\tau_{f1}(z_t - z_0)^2](\sin\alpha) +$$
$$+R_c[\tau_{f1}(z_t - z_0) + \tau_{f2}(\xi - z_t) - f_2(z_c - \xi)] - 0.5\pi^{-1}P = 0.$$

Frost heave normal stresses:

$$\sigma_f = E_f \frac{1.09 \cdot SP \cdot \theta \cdot grad\ t}{z} \cdot \left[1 - e\left(1 - w_w\frac{\rho_d}{\rho_w} - 1.09w\frac{\rho_d}{\rho_w}\right)\right]k_{an}.$$

Frost heave tangential stresses:

$$\tau_f = [c_{soil} - 1.09(w + (SP \cdot \theta \cdot grad\ t \cdot k_{an}/z)(c_{soil} - c_{ice})] +$$
$$+ \eta_{soil}\gamma_{soil}z(tg\varphi_{soil})(1 - 1.09(w + (SP \cdot \theta \cdot grad\ t \cdot k_{an}/z)) +$$
$$+ \eta_{ice}\gamma_{ice}z(tg\varphi_{ice})1.09(w + (SP \cdot \theta \cdot grad\ t \cdot k_{an}/z)),$$

Frost boundary position:

$$\xi_{i+1} = \left[\xi_i^2 - \frac{2\lambda_f t_{surf\ (i+1)}}{Q_{phase}}(\theta_{i+1} - \theta_i)\right]^{0.5}$$

The frost boundary position under embedded structures can also be found by two parameters: the internal temperature in the structure and the radius of thermal influence of the structure on the soil.

Design schemes for the model are shown in Figure 1.

The interpretation of the resulting model was done as in the example. A shallow tunnel partly located in seasonally freezing layer was considered. Based on the data of standard engineering-geological surveys and loads from the tunnel, geometric parameters of piles with upper reverse taper under the tunnel columns were determined. The position of frost boundary was found from the tunnel floor level. Length of piles was 3.2 m., diameter of cylindrical part of pile was 0.5 m. Tangential frost heaving stresses were taken according to geotechnical survey data. Normal horizontal frost heaving stresses were calculated at the level of the center line of the taper. The angles of the pile tapers were calculated from the static equations of equilibrium of acting forces. The static equations were solved taking into account the variability of the pile cross section and were written in the form of second-order algebraic equations with respect to the sine of the pile taper angle. The results of the calculations are shown in Table 1.

Table 1. Calculation results for the author's model.

Pile model	Frost boundary position, m	Frost heaving normal stress, кN/m²	Pile geometric characteristics		Pile volume, m³
			Taper angle, degrees	Taper length, m	
№1	2.1	57	7.5	1.1	0.543
№2	2.1	52	5.5	1.28	0.528
№3	2.1	48	4.2	1.46	0.516
№4	2.1	45	3.4	1.6	0.519

Thus, the example above showed that the author's model allowed to determine the required geometric parameters of piles from the condition of equilibrium of acting forces. This ensured the absence of vertical displacements of piles and the stability of the overlying structures in the given climatic and soil conditions.

The equations developed in the previous works by Repetsky, Yushkov [24], and other researchers made it possible to check the specified geometric parameters of the piles in the conditions under consideration. If the parameters did not satisfy, it would be necessary to set new parameters of the piles. The criterion was the vertical displacement of the piles, which required comparison with the limit values. Note that such values were also found from the joint calculation of the pile and the overlying structure. That increased the labor intensity of the solution process. In the author's model, the required parameters of the pile were determined in one step – when solving equilibrium equations.

The dimensions and working conditions of the piles in the author's model corresponded to the experimental models of the piles in Repetsky's thesis research. The results of the author's calculation coincided with the experimental data with deviations of 3.2–17.66%, as shown in Table 2. The upward deviations of calculated pile taper angles from the experimental data from 3.2 to 17.7 % proved Repetsky's

resulting data. The downward deviations of calculated angles from 8.2 to 13.6 % characterized the equilibrium of the experimental piles in the soil, which also coincided with the data in his research.

Table 2. Comparison of the author's analytical model with experimental data.

Pile model	Taper angle, degrees		Deviations of calculated angles from experimental, %	Vertical displacement of experimental pile, mm,
	Experiment	Calculation		
№ 1	6.0	7.5	+17.66	1.2
№ 2	5.0	5.5	+3.21	0.85
№ 3	4.5	4.2	−8.15	0.55
№ 4	4.0	3.4	−13.6	0.4

The author's model was implemented in an automated calculation module [39]. The module made it possible to reduce the labor intensity of calculations; provided a systematic approach to solving the problem, taking into account the multifactor calculations, and gave opportunities to add new modules in the development of calculation capabilities.

4. Conclusions

Thus, the author proposed a model of the freezing soil-pile system as a closed analytical solution with respect to geometric parameters of the pile.

The model included the solution of static equilibrium equations of forces with respect to geometric parameters of the pile; physical equations in the form of Hooke's law for soil frost heaving stresses; thermal conductivity equations for determining the position of frost boundary.

The obtained solutions made it possible to get geometric parameters of the pile required for pile equilibrium in the soil. That means that its vertical displacements during freezing and frost heaving were eliminated which ensured the integrity of the overlying structures.

Besides, the author's model made it possible to get a number of variants for geometric parameters of the pile, satisfying the condition of equilibrium. Among them, solutions with minimum material capacity were selected as the most economically efficient ones..

Further research directions could be the adaptation of the model to piles of other configurations, application of the model to bridge structure supports in cold regions, and development of an automated calculation module.

References

1. Bonacina, C., Comini, G., Fasano, A., Primicerio, M. Numerical solution of phase-change problems. International Journal of Heat and Mass Transfer. 1973. 16(10). Pp. 1825–1832. DOI:10.1016/0017-9310(73)90202-0.
2. Dauzhenka, T.A., Gishkeluk, I.A. Quasilinear heat equation in three dimensions and stefan problem in permafrost soils in the frame of alternating directions finite difference scheme. Lecture Notes in Engineering and Computer Science. 2013. 1. Pp. 1–6.
3. Vlasov, P., Volkov, I. Quasi-Stationary Temperature Field of Two-Layer Half-Space With Moving Boundary. Science and Education of the Bauman MSTU. 2015. 15(05). Pp. 126–136. DOI:10.7463/0515.0775760.
4. Alekseev, A., Gribovskii, G., Vinogradova, S. Comparison of analytical solution of the semi-infinite problem of soil freezing with numerical solutions in various simulation software. IOP Conference Series: Materials Science and Engineering. 2018. 365(4). Pp. 2020. DOI:10.1088/1757-899X/365/4/042059.
5. Yin, X., Liu, E., Song, B., Zhang, D. Numerical analysis of coupled liquid water, vapor, stress and heat transport in unsaturated freezing soil. Cold Regions Science and Technology. 2018. 155. Pp. 20–28. DOI:10.1016/j.coldregions.2018.07.008. URL: https://doi.org/10.1016/j.coldregions.2018.07.008.
6. Korshunov, A.A., Churkin, S. V., Nevzorov, A.L. Calibration of PLAXIS frozen/unfrozen soil model according to results of laboratory tests and in-situ monitoring. Lecture Notes in Civil Engineering. 2020. 50. Pp. 105–120. DOI:10.1007/978-981-15-0454-9_12.
7. Volokhov, S.S. Influence of adfreezing conditions on the strength of soil freezing with materials in shear. Osnovaniya, Fundamenty i Mekhanika Gruntov. 2003. No. 6. Pp. 28–32.
8. Ladanyi, B., Foriero, A. Evolution of frost heaving stresses acting on a pile. Proceedings of Permafrost - Seventh International Conference. 1998. (No. 55). Pp. 623–633.
9. Domaschuk, L. Frost Heave Forces on Embedded Structural Units. Proceedings of the 4th Canadian Permafrost Conference. 1982. Pp. 487–496.
10. Kim, M., Seo, H., Lawson, W., Jayawickrama, P.W. Tangential Heave Stress for the Design of Deep Foundations Revisited. Proceedings of the International Conference on Cold Regions Engineering. 2015. (January). Pp. 404–415. DOI:10.1061/9780784479315.036.
11. Istomin, A.D., Nazarov, T.A. Numerical studies of reinforced concrete pile foundations on permafrost soils at low climatic temperatures. Journal of Physics: Conference Series. 2020. 1425(1). Pp. 012082. DOI:10.1088/1742-6596/1425/1/012082.

12. Poselskiy, F.F., Nazarov, T.A., Budilov, D. V. Evaluation of Temperature and Humidity Effects on High Pile Foundation Platforms in Yakutia. IOP Conference Series: Materials Science and Engineering. 2018. 463(3). Pp. 032078. DOI:10.1088/1757-899X/463/3/032078.

13. Alekseev, A. Stress-Strain State of the Heaving Soil During Freezing. Structural Mechanics and Analysis of Constructions. 2020. 4(291). Pp. 72–77. DOI:10.37538/0039-2383.2020.4.72.77

14. Ji, Y., Zhou, G., Zhou, Y., Hall, M.R., Zhao, X., Mo, P.Q. A separate-ice based solution for frost heaving-induced pressure during coupled thermal-hydro-mechanical processes in freezing soils. Cold Regions Science and Technology. 2018. 147(August 2017). Pp. 22–33. DOI:10.1016/j.coldregions.2017.12.011. URL: https://doi.org/10.1016/j.coldregions.2017.12.011.

15. Liu, J., Wang, T., Tai, B., Lv, P. A method for frost jacking prediction of single pile in permafrost. Acta Geotechnica. 2020. 15(2). Pp. 455–470. DOI:10.1007/s11440-018-0711-0.

16. Alekseev, A.G. Procedure for investigation of the pressure acting on walls retaining soil subject to freezing-thawing. Soil Mechanics and Foundation Engineering. 2007. 44(3). Pp. 94–98. DOI:10.1007/s11204-007-0017-y.

17. Huang, X., Sheng, Y. Experimental study on anti-frost jacking of belled pile in seasonally frozen ground regions. Springer Series in Geomechanics and Geoengineering. 2018. (216849). Pp. 1368–1371. DOI:10.1007/978-3-319-97115-5. URL: http://link.springer.com/10.1007/978-3-319-97115-5.

18. Tretyakova, O. V., Yushkov, B.S. Inverted-Cone Piles for Transport Constructions in Seasonally Freezing Soils. Soil Mechanics and Foundation Engineering. 2017. 54(3). Pp. 173–176. DOI:10.1007/s11204-017-9453-5.

19. Tretiakova, O. Reduction in Tangential Frost Heaving Forces By the Pile Geometry Change. Architecture and Engineering. 2017. 2(1). Pp. 61–68. DOI:10.23968/2500-0055-2017-2-1-61-68.

20. Chae, D., Cho, W., Na, H.Y. Uplift capacity of belled pile in weathered sandstones. International Journal of Offshore and Polar Engineering. 2012. 22(4). Pp. 297–305.

21. Dickin, E.A., Leung, C.F. The influence of foundation geometry on the uplift behaviour of piles with enlarged bases. Canadian Geotechnical Journal. 1992. 29(3). Pp. 498–505. DOI:10.1139/t92-054.

22. Li, N., Xu, B. A new type of pile used in frozen soil foundation. Cold Regions Science and Technology. 2008. 53(3). Pp. 355–368. DOI:10.1016/j.coldregions.2007.10.005.

23. Abbasov, P.A., Kovalevskii, A.A. Behavior of piles with ribbed surfaces in sand soils. Soil Mechanics and Foundation Engineering. 1984. 21(2). Pp. 69–75. DOI:10.1007/BF01710704.

24. Yushkov, V., Repetsky, D. Construction of foundations in oil industry. Environmental protection in oil and gas complex. 2008. (12). Pp. 12–17.

25. Oswell, J.M., Nixon, J.F. Thermal Design Considerations for Raised Structures on Permafrost. Journal of Cold Regions Engineering. 2015. 29(1). Pp. 04014010. DOI:10.1061/(asce)cr.1943-5495.0000075.

26. Alekseev, A. Interaction of a Single Pile with Freezing Heaving Soil. Earthquake engineering. Constructions safety. 2020. (1). Pp. 48–52.

27. Kupchikova, N. V., Kurbatskiy, E.N. Analytical Method Used to Calculate Pile Foundations with the Widening Up on a Horizontal Static Impact. IOP Conference Series: Materials Science and Engineering. 2017. 262(1). Pp. 012102. DOI:10.1088/1757-899X/262/1/012102.

28. Linell, K.A., Lobacz, E.F. Design and Construction of Foundations in Areas of Deep Seasonal Frost and Permafrost. CRREL Special Report (US Army Cold Regions Research and Engineering Laboratory). 1980. (80–34). Pp. 2021.

29. Foriero, A., Ladanyi, B. Design of Piles in Permafrost under Combined Lateral and Axial Load. Journal of Cold Regions Engineering. 1991. 5(3). Pp. 89–105. DOI:10.1061/(asce)0887-381x(1991)5:3(89).

30. Tret'iakova, O. V. Simulation transport tunnels' piles behavior in heaving soils. Transport. Transport Faciilities. Ecology. 2019. (3). Pp. 72–82. DOI:10.15593/24111678/2019.03.09.

31. Tretiakova, O.V. Buronabivnaya svaya [Bored pile]. Patent Russia. 2016131617. 2017.

32. Tretiakova, O. V. Normal stresses of frost heaving as function of excess moisture. Magazine of Civil Engineering. 2017. 76(8). Pp. 130–139. DOI:10.18720/MCE.76.12.

33. Konrad, J.M., Morgenstern, N.R. Segregation Potential of a Freezing Soil. Canadian geotechnical journal. 1981. 18(4). Pp. 482–491. DOI:10.1139/t81-059.

34. Konrad, J.M. Procedure for Determining He Segregation Potential of Freezing Soils. Geotechnical Testing Journal. 1987. 10(2). Pp. 51–58. DOI:10.1520/gtj10933j.

35. Labuz, J.F., Zang, A. Mohr-Coulomb failure criterion. Rock Mechanics and Rock Engineering. 2012. 45(6). Pp. 975–979. DOI:10.1007/s00603-012-0281-7.

36. Ulitskii, V.M., Sakharov, I.I., Paramonov, V.N., Kudryavtsev, S.A. Bed – Structure System Analysis for Soil Freezing and Thawing Using the Termoground Program. Soil Mechanics and Foundation Engineering. 2015. 52(5). Pp. 240–246. DOI:10.1007/s11204-015-9335-7.

37. Kudryavtsev, S., Valtseva, T., Bugunov, S., Kotenko, Z., Paramonov, V., Saharov, I., Sokolova, N. Numerical simulation of the work of a low-settlement embankment on a pile foundation in the process of permafrost soil thawing. Lecture Notes in Civil Engineering. 2020. No. 50. Pp. 73–82. DOI:10.1007/978-981-15-0454-9_9.

38. He, H., Flerchinger, G.N., Kojima, Y., Dyck, M. A review and evaluation of 39 thermal conductivity models for frozen soils. Geoderma. 2021. 382(15). Pp. 114694. DOI:10.1016/j.geoderma.2020.114694.

39. Tretiakova, O.V. Tretiakov, A.V. Raschet i konstruirovanie svai s verkhnim obratnym konusom [Calculation and design the reverse taper pile]. Perm, Perm National Research Polytechnic University, 2017.

Contacts:

Olga Tretiakova*, PhD in Technical Science*
E-mail: olga_wsw@mail.ru

Comparative feasibility analysis of fly ash bricks, clay bricks and fly ash incorporated clay bricks

S. Dash[1] ✉ iD **, L. Panda[2]** iD **, I. Mohanty[1]** iD **, P. Gupta[3]** iD

[1] Synergy Institute of Engineering and Technology, Dhenkanal, Odisha, India

[2] KIIT Deemed to be University, Bhubaneswar, Odisha, India

[3] SRM Institute of Science and Technology, Delhi-NCR Campus, Modinagar, Ghaziabad, UP, India

✉ subhakantadash9@gmail.com

Abstract. Recycling of industrial wastes like fly ash into construction materials is attaining more momentum nowadays towards enhancing the characteristics and performance of materials in terms of strength and durability. This article attempts to present the effect of fly ash inclusion on the properties of bricks through a comparative feasibility analysis of fly ash bricks (FB), clay bricks (CB), and fly ash incorporated clay bricks (FC). For experimentation, twelve brick specimens were made using fly ash, clay, lime, gypsum, sand, and water in different proportions followed by sun-drying and firing methods. Sieve analysis, X-ray diffraction (XRD), Scanning electron microscope (SEM), Energy Dispersive X-ray Fluorescence (EDXRF), Fourier-transform infrared spectroscopy (FTIR), compressive strength, and efflorescence tests were performed to study the properties of brick specimens. Various factors such as the effect of drying, heating temperature, and percentage of ash addition on the bricks were also observed. The laboratory results indicated that out of the above-mentioned three bricks, FB showed better performance than CB and FC. The compressive strength and water absorption values for FB were found in the range of 8.50–12.18 MPa and 10.84–13.11 %, respectively. Thus, based on the experimental observations and results, the mix design FB-3 (25 % fly ash, 20 % lime, 2 % gypsum, 53 % sand) exhibited the optimum compressive strength of 10.25 MPa with a water absorption value of 11.16 %. This mix design can be recommended as a substitute for conventional bricks against aggressive environment contributing immensely towards solid waste management and sustainable development.

Citation: Dash, S., Panda, L., Mohanty, I., Gupta, P. Comparative feasibility analysis of fly ash bricks, clay bricks and fly ash incorporated clay bricks. Magazine of Civil Engineering. 2022. 115(7). Article No. 11502. DOI: 10.34910/MCE.115.2

1. Introduction

The history of brick manufacturing is dating back to 8000 BC. Brick is considered one of the most important raw materials for construction purpose [1]. The use of fly ash during brick manufacturing is a significant step towards waste management, resource conservation, and sustainable development, as brick manufacturing requires a substantial amount of natural resources, mostly clay, leading to resource depletion as well as negative effects on the surrounding ecosystem [2]. On the other hand, fly ash is a waste material disposed of in and around the Thermal Power Plants (TPPs). Therefore, the use of coal fly ash (CFA) during brick making can be a feasible alternative and will reduce environmental burden [3]; but the use of CFA during brick manufacturing needs to be explored in every dimension so that its use can be

environmentally friendly and sustainable. Approximately 30 % of the world population use clay bricks for constructing their accommodations and other buildings [4, 5]. Bricks are generally prepared by moulding clay mixture in block forms, followed by sun drying and firing. Burnt clay bricks can achieve better strength than sun-dried bricks. The different factors such as the nature of material and manufacturing process affect the properties of the bricks [6, 7]. Temperature is also another key parameter that controls the development of bricks [8–10]. It helps in melting of oxides and silica present in the clay. After cooling, a bond forms between the clay particles [5, 6]. Nearly 300 million tonnes of fertile soil is consumed per day in India for brick manufacturing [11–13]. Similarly, 700 million tonnes of clay bricks are manufactured every year in Ontario, Canada [8]. As a consequence, clay deposits are depleting fast in various parts of the world due to rapid urbanization, commercialization, and industrialization. To put a brake on the decreasing levels of soil deposits, countries like China and India restricted the use of clay in brick manufacturing [14, 15]. It has also been reported that these bricks are low in strength and durability. To overcome these shortcomings, some pozzolanic material may be added to bricks to increase the strength of the material [16–18]. In the past decade various waste materials have been incorporated in clay bricks to improve compressive strength and water absorption values [19–21].

The purpose of this paper is to throw some light on the effect of fabrication process, variation of constituent materials, ash content on different physicochemical and mechanical properties of three types of brick specimens. The key factors taken into consideration are fly ash to binder ratio, drying and heating temperatures, and incorporation of fly ash content in clay brick.

2. Methods

2.1. Raw materials

The materials used in making of brick specimens were Class-F fly ash (as per ASTM C618 standard), clay, lime, gypsum, and water. Fly ash and clay were procured from NALCO, Anugul and Brahmani river bed, and Odisha, respectively. Lime was used as a binding agent and gypsum was used as a long-term strength gainer in bricks. The 2 mm passing and 1 mm retained sand size was used in the brick mix design. The water to cement ratio of 0.45 was used uniformly in all the mixtures.

2.2. Fabrication of brick specimens

In this method, three varieties of bricks, viz. fly ash bricks (FB), clay bricks (CB), and fly ash incorporated clay bricks (FC), were prepared. Brick techniques such as hand mixing followed by sun drying and heating were adopted for brick manufacturing. The schematic representation of FB, CB and FC preparation is given in Fig. 1.
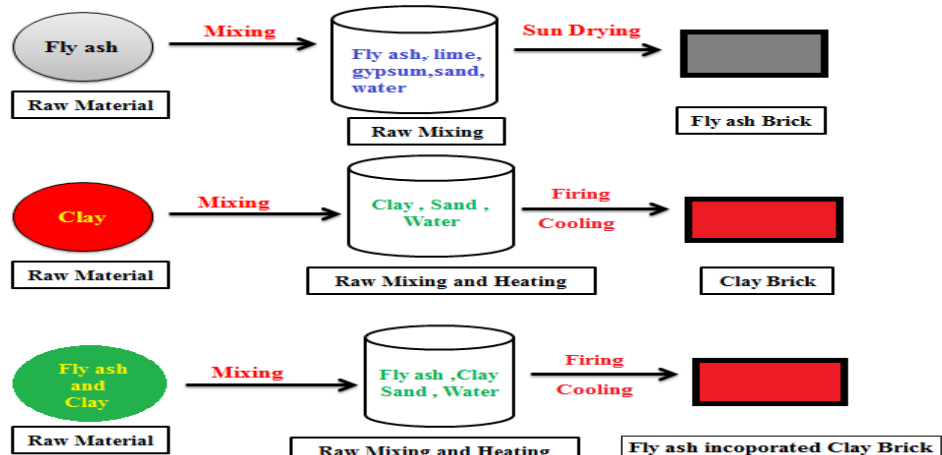
Figure 1. Schematic representation of preparation of brick specimens.

The methodology of FC making was quite similar to that of clay brick. In FC, fly ash was added to clay in different ratios. The ingredients required for the fabrication of bricks were fly ash, clay, lime, gypsum, and water. These materials were taken in different proportions and mixed in a disc and a calculated amount of water was added to get a homogeneous mixture. The mixed proportions of brick specimens are given in Table 1. An automated brick production unit was used to prepare the bricks of standard $190\times90\times90$ mm^3 size as per Indian standard IS 12894 (Bureau of Indian Standards, 2011). A flat pan mixer and two rollers attached to the brick production unit effectively mixed and grinded the raw materials. Such type of arrangement is more beneficial for mixing of the raw material; however, it limits the mixing capability.

Table 1. Mix proportions of FB, CB, and FC.

	FB				
Mix ID	Fly ash (%)	Clay (%)	Lime (%)	Gypsum (%)	Sand (%)
FB-1	15	------	30	2	53
FB-2	20	------	25	2	53
FB-3	25	------	20	2	53
FB-4	30	------	15	2	53
FB-5	35	------	10	2	53
FB-6	40	------	5	2	53
	CB				
CB-7	------	100	------	------	------
	FC				
FC-8	5	95	------	------	------
FC-9	10	90	------	------	------
FC-10	15	85	------	------	------
FC-11	20	50	------	------	------
FC-12	25	75	------	------	------

2.3. Testing Methods

The physicochemical and mechanical properties of raw materials and bricks were examined as per Indian Standards by performing sieve analysis, XRD, SEM, FTIR, EDXRF, compressive strength (IS 3495, 2002), water absorption (IS 3495, 2002), and efflorescence tests (IS 3495, 2002). Some factors like sun drying, firing temperature, and constituent materials ratio which affect the properties of the brick production were also studied.

3. Results and Discussion

3.1. Characterization of Raw materials

3.1.1. Sieve analysis

The particle size distribution of fly ash and clay was analysed by using Malvern particle size analyser (Model Micro-P, range 0.05–550 micron). The particle size distribution of raw materials is shown in Fig. 2. Fly ash particles are much finer than the particles of clay. It is evident by the average particle size of 10 μm for fly ash and 86 μm for clay.
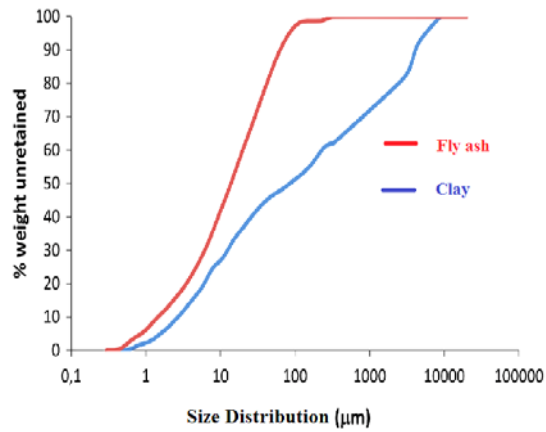
Figure 2. Particle size distribution of fly ash and clay.

3.1.2. Chemical analysis

The chemical compositions of fly ash and clay were analysed by using EDXRF (Model no. EDX7000) and the results are tabulated in Table 2. Fly ash is mainly composed of silica, alumina, iron oxides calcium, manganese. The major Si content in fly ash is 59.512 %, while in clay it is 63.450 %. Similarly, Al and Fe contents are 26.078 % and 7.509 % in fly ash, whereas in clay they are 14.116 % and 13.409 %, respectively.

Table 2. EDXRF analysis of fly ash and clay.

				Fly ash					
Analyte	Si	Al	Fe	K	Ca	Mn	Cr	Pb	Zn
Result	59.512	26.078	7.509	1.888	1.492	0.075	0.048	0.024	0.039
				Clay					
Analyte	Si	Al	Fe	K	Ca	Mn	Cr	Ir	Zn
Result	63.450	14.116	13.409	4.201	2.115	0.202	0.130	0.026	0.022

3.1.3. XRD and SEM analysis

The XRD pattern of fly ash and clay is shown in Fig. 3 (a, b). XRD pattern of coal fly ash shows small peaks which can be attributed to the presence of a small amount of quartz and mullite. But in clay, the major mineral phases are Quartz, Illite, Muscovite, Rutile, Kaolinite, and Hematite. The morphological study of fly ash shows that the samples mainly comprised small, spherical particles. SEM analysis of clay indicates the presence of particles of distinct angular sizes and to a lesser extent of spherical sizes. SEM micrographs of fly ash and clay are shown in Fig. 3 (c, d).

(a) XRD of fly ash

(b) XRD of clay

(c) SEM of fly ash

(d) SEM of clay
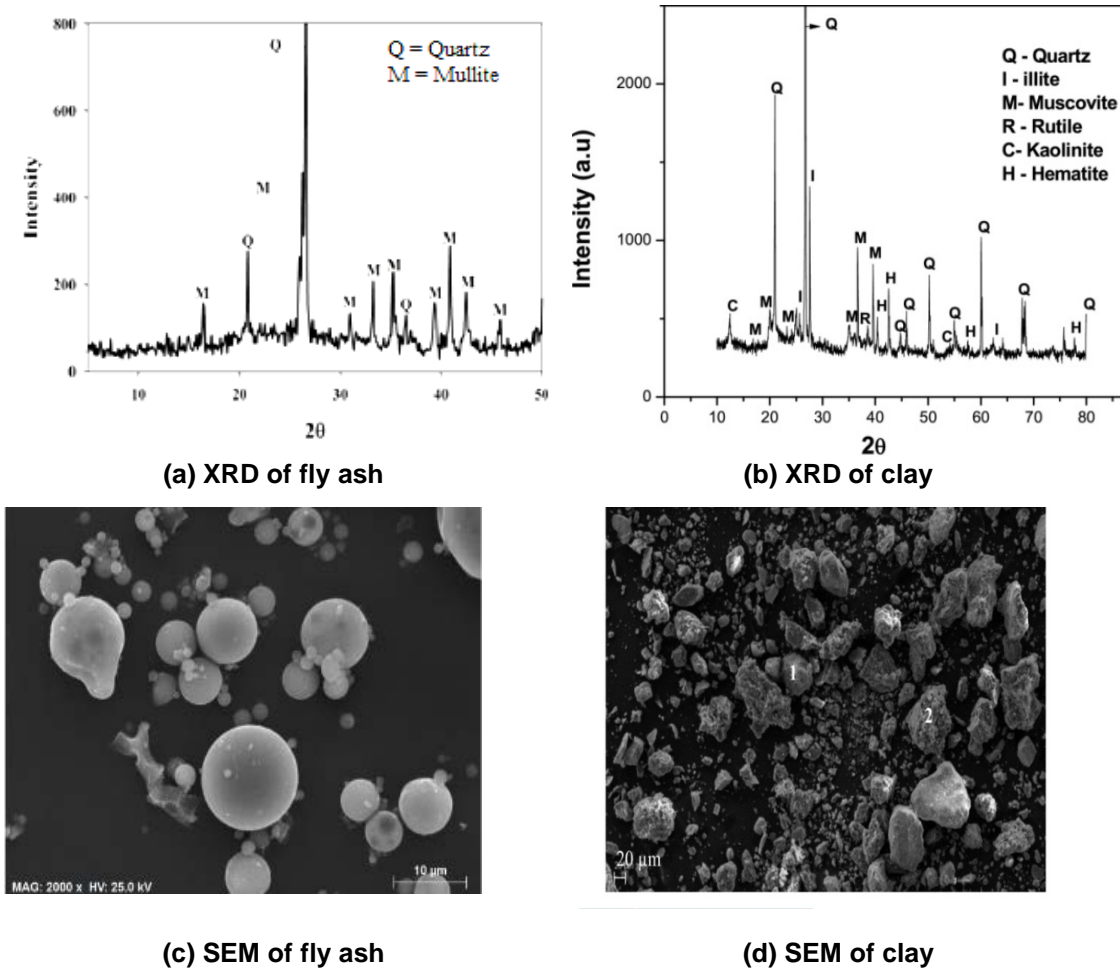
Figure 3. XRD and SEM analysis of fly ash and clay.

3.1.4. FTIR analysis of fly ash and clay

FTIR analysis of fly ash and clay is given in Fig. 4. The IR spectrum of fly ash shows bands at 3441, 3072, 3044, 2985, 2870, 2826, 1621, 1504, 1463, 1027, 694,541 cm^{-1}. In fly ash, broadband at 3441.21cm^{-1} is due to O–H stretching vibrations. The peak around 3100–3000 cm^{-1} may be due to some aromatic C–H stretching. Peaks at 2870.37 cm^{-1}, 2826.54 cm^{-1}, and 2985.76 cm^{-1} are due to the presence of organic carbon. A peak at 1621.09 cm^{-1} in the spectra indicates the adsorbed or associated water molecules (O–H bending frequency). The peaks at 1504.83 cm^{-1} and 1463.14 cm^{-1} may be assigned to carbonates present in the sample. The IR spectrum of clay shows bands at 3695, 3619, 3431, 3010, 2870, 2830, 1875, 1630, 1462, 1025, 778,694 cm^{-1}. The peak at 3695.83 cm^{-1} is due to the Si–O–H vibration of clays, kaolinite, and Fe oxides. The peak at 3431.02 cm^{-1} may be attributed to O–H stretching of H-bonded water. The peak at 3010.01 cm^{-1} is due to aromatic C–H stretching. The peaks

at 2870.56 cm^{-1} and 2830.09 cm^{-1} are assigned to the presence of organic carbon. The peak at 1875.90 cm^{-1} is due to calcite (overtone/combination band). The peak observed at 1630.53 cm^{-1} corresponds to O–H bending vibration of water.
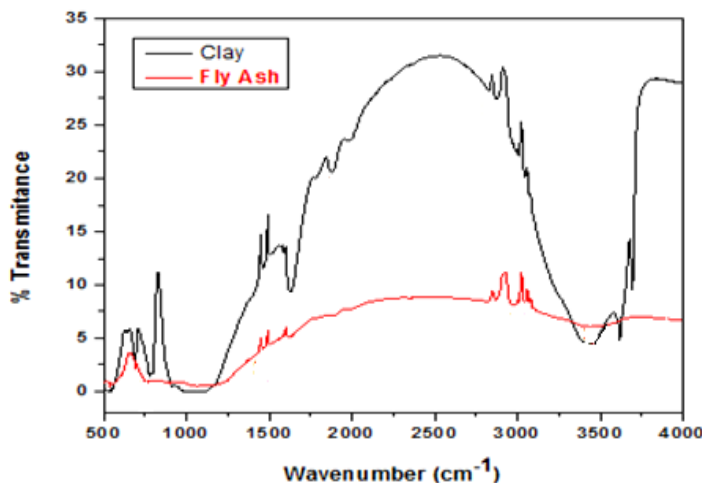

Figure 4. FTIR analysis of fly ash and clay.

3.2. Mechanical properties

3.2.1. Compressive strength and water absorption

The moisture content and mixing sequence plays an important role in the mechanical performance of bricks. Water absorption test on a brick is conducted to find out the amount of moisture content absorbed by the brick under excessive conditions. It also determines the durability of the brick specimens. Low water absorption represents high compressive strength, durability and good quality of brick. The strength of the bricks was tested using a compressive strength machine as shown in Fig. 5. Mechanical tests of the brick specimens were performed at KIIT Deemed to be University, Bhubaneswar. Around twelve brick specimens were used to study the effect on mechanical properties. Table 3 presents the compressive strength and water absorption values of different brick mixes. From the experimental results, it is clear that FB-1 showed the maximum compressive strength of 12.18 MPa with water absorption of 10.84 %. CB-7 received compressive strength of 7.88 MPa with a water absorption of 13.78 %. Similarly, FC-12 observed a low value of compressive strength (6.47 MPa) with a high value of water absorption (16.10 %). Overall, the mix design FB-3 showed the compressive strength of 10.25 MPa with water absorption of 11.16 %, which is the optimum and satisfied the basic requirement of the bricks. The optimal mix percentage of FB-3 was 25 % fly ash, 20 % lime, 2 % gypsum, and 53 % sand. As the compressive strength of the material increases, the water absorption value decreases. During the fabrication process of bricks, it was found that CB has some pores in its body structure in comparison to FB, which were responsible for a higher value of water absorption and lower value of compressive strength than those for FB. In case of FC, compressive strength decreased with the gradual increase in the percentage of fly ash. The compressive strength reduction increased by more than 50 %, with 20 % and 25 % fly ash add-ons. Therefore, it is concluded that FB showed better mechanical properties than CB and FC.

(a) Compressive strength of FB (b) Compressive strength of CB

Figure 5. Compressive strength analysis of FB and CB.

Table 3. Mechanical properties of different brick specimens.

Mix ID	Compressive strength (28 days)	Water absorption (%)
FB-1	12.18	10.84
FB-2	11.07	11.21
FB-3	10.25	11.66
FB-4	9.46	12.16
FB-5	9.10	12.74
FB-6	8.50	13.11
CB-7	7.88	13.78
FC-8	7.66	14.10
FC-9	7.48	14.58
FC-10	7.15	15.26
FC-11	6.78	15.85
FC-12	6.47	16.10

3.3. Effect of various parameters on brick specimens

3.3.1. Effect of constituent material and sun drying on FB strength properties

Fly ash, in presence of moisture, reacts with lime and gypsum to form compounds having cementitious properties. This property was used for FB production. Higher-strength bricks can be obtained by increasing lime content in the mixture. The lime reacts with oxide components like silica, alumina, and iron oxide of fly ash to develop different types of lime bearing phases like calcium silicate, calcium aluminate, calcium aluminosilicate, etc., and these phases are subsequently hydrated in the presence of water to form different hydrates. The moisture content of the brick decreased with an increase in the time of sun drying. The reason was that the moisture evaporation increased with the increase in time when the brick was dried in the environment under the sun. When the brick was dried, its moisture content was between 10–12 %, which is the atmospheric moisture content of the brick.

3.3.2. Effect of firing temperature on CB strength properties

Temperature is also another key parameter that controls the development of bricks. It helps to melt the oxides and silica present in the clay. After cooling, bond formation takes place within the clay particles. The fusibility of clay causes it to become hard and solid with a relatively low absorption when properly fired. This process improves the strength of the specimens. There is a relationship between the firing temperature and compressive strength. Compressive strength of bricks is remarkably improved by firing at higher temperatures. With increase in firing temperature (700–1000 °C), compressive strength was found to be increased.

3.3.3. Effect of ash content on FC strength properties

The compressive strength of FC decreased with a gradual increase in the percentage of fly ash. This is because, during the mixing process, when fly ash was incorporated, it didn't mix properly with clay, and simultaneously when it was allowed for heat treatment, the mass of the fly ash didn't fuse and remained as such in the bricks. It seems that the fly ash doesn't react properly with clay to form bonding in FC.

3.4. Efflorescence test of FB, CB and FC

Generally, this test is carried out to know, if some soluble salts like magnesium sulfate, sodium sulfate, sodium carbonate, and potassium sulfate are present in the brick. A white deposition is seen in the brick specimen when immersed in water for 7 to 45 days. Then the bricks are allowed to dry for 60 days and observations are recorded for efflorescence. In case of CB and FC, a slight efflorescence of 8.5 % of the CB surface area was observed and its percentage decreased with the addition of fly ash in CB. But in FB, percentage of efflorescence was found to be negligible. The reason is that fly ash can bind salts and free lime, which causes a low percentage of efflorescence. Therefore, FB showed better performance in the efflorescence test. The efflorescence results on brick specimens are shown in Fig. 6.

(a) FB   **(b) CB**   **(c) FC**
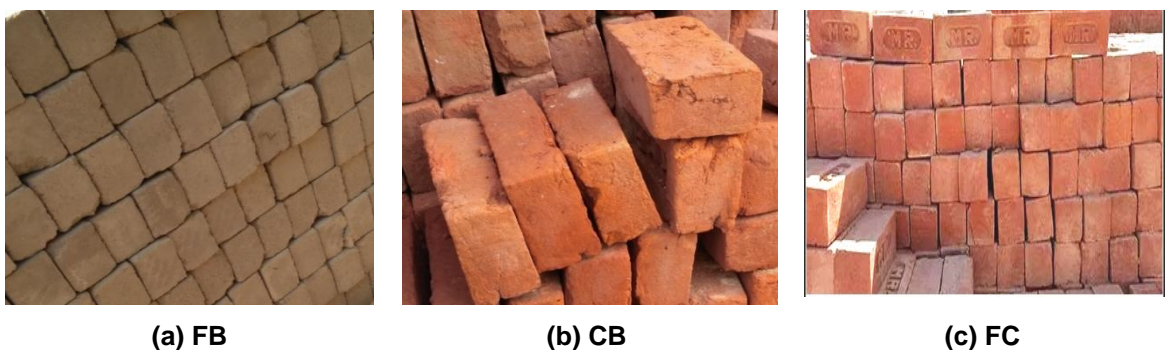
**Figure 6. Visual appearance of the different sets of bricks
after the exposure period for efflorescence.**

3.5. Effect of firing process on colour of CB

After the firing process there is a change in colour, mass and dimensions of bricks. The colour of bricks before the firing process was greyish-brown and grey. After firing process, due to the content of iron oxides, CB presented a red-orange colour, independent of the amount of incorporated residue, whereas in case of FB the colour was black and in FC the colour remained red.

3.6. Works by other authors

Pimraksa and Chindaprasirt [22] reported that the bricks made with untreated diatomite (with 15 % lime and 5 % gypsum) showed reasonably high strength of 14.5 MPa and low density of 0.88 g/cm^3 [22]. Miqueleiz et al. [23] studied the lightweight brick samples made with lime and coal ash (CA) waste, which tended to achieve higher strength values of 5 MPa. The compressive strength resistance reduced as the clay replacement level increased [23]. Muntohar and Rahman [24] developed lightweight masonry block made from oil palm kernelshell, which achieved the maximum strength of 22 MPa [24]. Eliche-Quesada et al. [25] manufactured CB using commercial clay and different waste ratios: fired at 1000 °C for 4 h, they showed the compressive strength value of 10 MPa [25]. Gourav and Venkatarama Reddy [26] reported that it is possible to produce fly ash-lime-gypsum bricks having 8–10 MPa wet compressive strength and reasonably low values of water absorption [26].

Table 4. Works by other authors.

Reference	Year	Observations
Pimraksa and Chindaprasirt [22]	2009	Brick showed compressive strength value of 14.5 MPa
Miqueleiz et al. [23]	2013	Brick made with fly ash showed compressive strength value of 5 MPa
Gourav and Venkatarama Reddy [26]	2014	Fly ash lime gypsum bricks showed compressive strength value of 8–10 MPa
Eliche-Quesada et al. [25]	2018	Fired CB showed compressive strength value of 10 MPa

4. Conclusions

In the present study, a comparative feasibility analysis was done for fly ash bricks (FB), clay bricks (CB), and fly ash incorporated clay bricks (FC). The following conclusions are drawn on the basis of experimental outcomes:

1. Fly ash rich in SiO_2 and Al_2O_3 has a chemical composition similar to that of clays used in the manufacturing of fired CB. Therefore, the use of fly ash may reduce the consumption of clay as a raw material for bricks.

2. A comparison in the bond strength in three types of bricks shows that FB has a better bond strength than standard CB and FC.

3. With the increase in firing temperature, the comprehensive strength of CB gradually increases. It is concluded that the compressive strength of the FC decreases with an increasing percentage of fly ash. Because when FC is exposed to firing at a certain temperature, the fly ash present in clay is not fused and doesn't mix with clay. It remains the same, so the bond between fly ash and clay does not form.

4. From the experimental results, mix design FB-1 showed the maximum compressive strength value of 12.18 MPa with the lowest water absorption of 10.84 %. Mix design FC-12 showed the lowest value of compressive strength 6.47 MPa with the highest value of water absorption, 16.10 %.

5. Mix design FB-3 (25 % fly ash, 20 % lime, 2 % gypsum, 53 % sand) exhibited the optimum compressive strength of 10.25 MPa with water absorption value of 11.16 % and is recommendable on the basis of experimental results.

6. FB showed better performance than CB and FC with respect to efflorescence. The efflorescence of 8.5 % was seen on the surface area of CB. It was observed that the efflorescence percentage decreases with the incorporation of fly ash in CB. For incorporation of 20 % and 25 % of fly ash in CB, the efflorescence percentage was found to be 3.8 % and 3.6 %, respectively.

7. Fly ash bricks are hi-tech bricks of improved quality used for construction and masonry structures. They are the best replacement for normal CB and have better mechanical properties. The fabrication of FB is cost-effective in terms of saving firing time, heating temperature, which are necessary steps in the case of CB. Overall, FB showed satisfactory performance as compared to CB and FC.

References

1. Houben, H., Guillaud, H. Earth construction: A Comprehensive Guide, CRA-Terre EAG, Intermediate Technology Publications, London, UK, 1994. 1–9 pp.

2. Koroneos, C., Dompros, A. Environmental assessment of brick production in Greece. Building and Environment. 2007. 42 (5). Pp. 2114–2123. DOI: http://dx.doi.org/10.1016/j.buildenv.2006.03.006

3. Abbas, S., Saleem, M.A., Kazmi, S.M.S., Munir, M.J. Production of sustainable clay bricks using waste fly ash: mechanical and durability properties. Journal of Building Engineering. 2017. 14. Pp. 7–14. DOI: http://dx.doi.org/10.1016/j.jobe.2017.09.008

4. Niroumand, H., Zain, M.F.M., Alhosseini, S.N. The influence of nano-clays on compressive strength of earth bricks as sustainable materials. Procedia- Social and Behavioral Sciences. 2013. 89 (9). Pp. 862–865. DOI: https://doi.org/10.1016/j.sbspro.2013.08.945

5. Kazmi, S.M.S., Abbas, S., Saleem, M.A., Munir, M.J., Khitab, A. Manufacturing of sustainable clay bricks: utilization of waste sugarcane bagasse and rice husk ashes. Construction and Building Materials. 2016. 120 (9). Pp. 29–41. DOI: https://doi.org/10.1016/j.conbuildmat.2016.05.084

6. Muñoz, V.P., Morales, O.M.P., Mendívil, G.M.A., Muñoz, V.L. Fired clay bricks manufactured by adding wastes as a sustainable construction material- A Review. Construction and Building Materials. 2014. 63 (7). Pp. 97–107. DOI: 10.1016/j.conbuildmat.2014.03.045

7. More, A., Tarade, A., Anant, A. Assessment of suitability of fly ash and rice husk ash burnt clay bricks. International Journal of Scientific and Research Publications. 2014. 4 (7). Pp. 1–6.

8. Pawar, A., Garud, D. Engineering properties of clay bricks with the use of fly ash. International Journal of Research in Engineering and Technology. 2014. 3 (9). Pp. 75–80. DOI: https://doi.org/10.15623/ijret.2014.0321016

9. Kumar, R., Hooda, N. An experimental study on properties of fly ash bricks. International Journal of Mechanical Engineering and Robotics Research. 2014. 2 (9). Pp. 56–67.

10. Chidiac, S.E., Federico, L.M. Effects of waste glass additions on the properties and durability of fired clay brick. Canadian Journal of Civil Engineering. 2017. 34 (11). Pp. 1458–1466. DOI: https://doi.org/10.1139/L07-120

11. Chen, D., Li, O.Z., Xin, F. Five-year plans, China finance and their consequences. China Journal of Accounting Research. 2017. 10 (3). Pp. 189–230. DOI: https://doi.org/10.1016/j.cjar.2017.06.001

12. Chen, Y., Zhang, Y., Chen, T., Zhao, Y., Bao, S. Preparation of eco-friendly construction bricks from hematite tailings. Construction and Building Materials. 2011. 25 (4). Pp. 2107–2111. DOI: https://doi.org/10.1016/j.conbuildmat.2010.11.025

13. Görhan, G., Şimşek, O. Porous clay bricks manufactured with rice husks. Construction and Building Materials. 2013. 40 (3). Pp. 390–396. https://doi.org/10.1016/j.conbuildmat.2012.09.110

14. Djangang, C., Kamseu, E., Elimbi, A., Lecomte, G., Blanchart, P. Net-shape clay ceramics with glass waste additive. Materials Sciences and Applications. 2014. 5. Pp. 592–602. DOI: https://doi.org/10.4236/msa.2014.58061

15. Baykal, G., Doven, A.G. Utilization of fly ash by pelletization process, theory, application areas, and research result. Resource Conservation Recycling. 2000. 30 (1). Pp. 59–77. DOI: https://doi.org/10.1016/S0921-3449(00)00042-2

16. Bhattacharjee, M., Rahman, A., Ashrafuzzaman, M., Barua, S. Effect of aggregate properties on the crushing strength of concrete. International Journal of Materials Science and Applications. 2015. 4 (5). Pp. 343–349.

17. Bijen, J.M. Manufacturing processes of artificial lightweight aggregates from fly ash. The International Journal of Cement Composites and Lightweight Concrete. 1986. 8 (3). Pp. 191–199.

18. Chia, K.S., Zhang, M.H. Water permeability and chloride penetrability of high strength lightweight aggregate concrete. Cement and Concrete Research. 2002. 32 (4). Pp. 639–645. DOI: https://doi.org/10.1016/S0008-8846(01)00738-4

19. Dwivedi, A., Kumar, M.K. Fly ash – waste management and overview: A Review. Recent Research in Science and Technology. 2014. 6 (1). Pp. 30–35.

20. Kayali, O. Fly ash lightweight aggregates in high-performance concrete. Construction and Building Materials. 2008. 22 (12). Pp. 2393–2399. DOI: https://doi.org/10.1016/j.conbuildmat.2007.09.001

21. Mangialardi, T. Sintering of MSW fly ash for reuse as a concrete aggregate. Journal of Hazardous Materials. 2001. 87 (1-3). 225–239. DOI: https://doi.org/10.1016/S0304-3894(01)00286-2

22. Pimraksa, K., Chindaprasirt, P. Lightweight bricks made of diatomaceous earth, lime and gypsum. Ceramics International. 2009. 35. Pp. 471–478. DOI: https://doi.org/10.1016/j.ceramint.2008.01.013

23. Miqueleiz, L., Ramirez, F., Oti, J.E., Seco, A., Kinuthia, J.M., Oreja, I., Urmeneta, P. Alumina filler waste as clay replacement material for unfired brick production. Engineering Geology. 2013. 163. Pp. 68–74. DOI: https://doi.org/10.1016/j.enggeo.2013.05.006.

24. Muntohar, A.S., Rahman, M.E. Lightweight masonry block from oil palm kernelshell, Construction and Building Materials. 2014. 54. Pp. 477–484. DOI: https://doi.org/10.1016/j.conbuildmat.2013.12.087

25. Eliche-Quesada, D., Sandalio-Pérez, J.A., Martínez-Martínez, S.L., Pérez-Villarejo, S., Sánchez-Soto. P.J. Investigation of use of coal fly ash in eco-friendly construction materials: fired clay bricks and silica-calcareous non fired bricks. Ceramic International. 2018. 44. Pp. 4400–4412. DOI: https://doi.org/10.1016/j.ceramint.2017.12.039

26. Gourav, K., Venkatarama Reddy, B.V. Characteristics of compacted fly ash bricks and fly ash brick masonry. Journal of Structural Engineering. 2014. 41, Pp. 144–157.

Information about authors:

Subhakanta Dash, *PhD*
ORCID: https://orcid.org/0000-0002-4487-4530
E-mail: subhakantadash9@gmail.com

Laxmidhar Panda, *PhD*
ORCID: https://orcid.org/0000-0002-4678-0650
E-mail: ld.laxmi@gmail.com

Itishree Mohanty, *PhD*
ORCID: https://orcid.org/0000-0001-9610-0601
E-mail: imohanty09@gmail.com

Piyush Gupta, *PhD*
ORCID: https://orcid.org/0000-0002-7612-6916
E-mail: piyushg.1977@gmail.com

Water treatment residue and coal fly ash geopolymers

Q.M. Do[1] [iD] **, H.U.P. Nguyen[1]** [iD] **, V.Q. Le[2]** [iD] **, M.D. Hoang[3]** ✉ [iD]

[1] *Ho Chi Minh City University of Technology – Vietnam National University, Ho Chi Minh City, Vietnam*

[2] *Vietnam Institute for Building Materials, Hanoi, Vietnam*

[3] *Vietnam Institute for Building Science and Technology, Hanoi, Vietnam*

✉ *hmduc@yahoo.com*

Abstract. Water treatment residue (WTR) from water purification is a non-hazardous solid waste commonly discharged in landfills. WTR contains aluminosilicates and can participate in geopolymerization. Due to the low alkaline activity of WTR, we used coal fly ash with the WTR to coal fly ash ratio from 80 wt% to 50 wt% and activated it with the 8M NaOH solution. The specimens were cured in normal conditions for 28 days at room temperature, and in an autoclave for 7 days under a pressure of 2 MPa and temperature of 215 ℃. The test results showed that the compressive strength of geopolymers cured in an autoclave reached 28.8 MPa, which is much higher than for those cured in normal conditions with only 13.2 MPa. The microstructure (XRD, SEM) and chemical bonding (FTIR) analyses confirmed the analcime crystal formation in the geopolymers.

1. Introduction

Water treatment residue (WTR) is waste obtained from water purification plants. The solid waste is not hazardous, but discharging it into a landfill requires a large land area and is an environmental challenge. Over the years, there have been many studies on using WTR in the production of building materials. WTR is used to partially replace clay in the production of bricks and ceramics [1-5], lightweight aggregates [6–8], and cement [9–11]. WTR can also be used as a mineral admixture [12–16] in cement concrete. Another promising application is the use of WTR in the production of alkali-activation materials (AAM) or geopolymer [17–22].

AAM is a cement-like material obtained by the reaction between an aluminosilicate precursor and an alkaline activator. Initially, the aluminosilicate precursor dissolves in an alkaline solution to form free SiO_4 and AlO_4 units. Then, the reaction between them under alkaline conditions produces a hydrous alkaline-aluminosilicate and/or alkali-alkali earth-aluminosilicate phase [23]. The formation can be described as a polymer-like condensation process, where the loss of water between two hydroxyl groups occurs in inorganic materials, and the materials can be named "geopolymers" [24]. The geopolimerization starts with oligomer condensation into a small ribbon-like molecule.

Several industrial byproducts and wastes, including WTR, blast furnace slag, rice husk, CFA, mining waste, and steel slag, can be used as aluminosilicate precursors to produce AAM. Alkaline-activated

solutions are mainly composed of alkalis of sodium or potassium and water glass. The aluminosilicate or silica precursors are dissolved in the alkaline-activated solution to create alkaline solutions. The condensation process of this alkaline solution forms geopolymer materials. Of course, if the condensation process does not occur, a geo-material does not form. The problem resulting from this reaction is that the alkali cations (K^+ and Na^+) are outside the polymerization network's structure. These cations can freely migrate in contact with water generating leaches to increase pH and low long-term characteristics.

One of the important characteristics of geopolymers is the presence of zeolites. The presence of analcime crystals in various ancient cements confirms that this zeolite is a stable, final stage of the long thermal transition of zeolitic materials [26]. The proportion of oxides participating in the $M_n[-(SiO_2)_z - AlO_2]_n \cdot mH_2O$ bonding chain affects the bonding strength. MacKenzie et al. [27] reported that the optimal molar ratios are in the range of $SiO_2/Al_2O_3 < 3.3$, $H_2O/Na_2O < 10$, and $Na_2O/SiO_2 < 0.3$. During geopolymerization, when the zeolites crystallize, the formation of the zeolite with different structures depends on the Si/Al ratios used. The higher the silicate content, the more analcime crystals can be obtained [28].

Hydrothermal curing at high temperatures and pressure are better than atmospheric conditions for analcime to crystallize and develop. Yuan-yuan Ge et al. reported a simple method to fabricate large-size single analcime crystals using the geopolymer-gels-conversion method. The crystal's architecture is icositetrahedron with a diameter range from 50 μm to 1200 μm. It also shows that the analcime's synthesis of single crystals depends on the hydrothermal time [28]. Kupwade-Patil and Allouche investigated the alkali silica reaction between reactive aggregates and the geopolymer matrix. They used one class C and two class F fly ashes to produce the geopolymer matrix and found the analcime crystals [29]. A high molar ratio of Na_2O/SiO_2 in the activated solution or low Si/Al molar ratio in aluminosilicate precursors tend to produce loose particles (pseudo-zeolitic structure, mainly Q4) rather than continuously well-connected NASH gel [24, 26, 30]. The rational content of the silicates is essential to form a compact alkali-aluminosilicate geopolymer with continuous gels, especially for aluminosilicate precursors with a lower Si/Al ratio [31].

WTR contains silicone and aluminum oxides, which hardly dissolve in alkaline solutions. Thus, it is not possible to use WTR alone for geopolymer production. In this case, the additional aluminosilicate precursors like fly ash (FA), rice husk ash (RHA), ground granulated blast furnace slag (GGBFS), or metakaolin (MK) play an important role. Waijarean N. et al. reported that the WTR was activated by heating in an electric furnace at 800 °C for 1 hour and fine grinding. At the same heating temperature, the aluminosilicate in WRT can be transferred to MK. In addition, we can use rice husk to adjust the molar SiO_2/Al_2O_3 ratio of the mix from 1.78 to 2.00 [32]. In similar experiments, the WTR mixture with 10M NaOH was heated at 800 °C for 1 h to create a geopolymer. The molar ratios of the geopolymer were $Na_2O/SiO_2 = 0.28$, $SiO_2/Al_2O_3 = 1.78$, $H_2O/Na_2O = 11.11$ and $H_2O/Al_2O_3 = 9.67$ [22].

Geraldo et al. used sodium silicate solution ($Na_2O.nSiO_2.mH_2O$) and sodium hydroxide (NaOH) as the alkaline activator. The alkali source was an alternative sodium silicate solution made from a mixture of NaOH and RHA. MK was partially replaced by WTR in the proportions of 0 wt%, 15 wt%, 30 wt%, and 60 wt%. The additional RHA was used in the geopolymer mixtures to keep SiO_2/Al_2O_3 molar ratio constant. Geopolymer mortars were cured at room temperature and had a compressive strength of 25 MPa at 28 days corresponding to a replacement ratio of 15% [17].

Using sodium silicate solution (Na_2SiO_3) and NaOH solution in a Na_2SiO_3/NaOH 80:20 mass ratio is considered optimal for all tests of Suksiripattanapong C. et al. [33]. The WTR-CFA geopolymers were dried at 75 °C, 85 °C, and 95 °C for 72 hours. The strength of WTR-CFA geopolymers dried at 75 °C, 85 °C, and 95 °C for 72 hours was 20 MPa, 18 MPa, and 16 MPa, respectively, meeting the strength requirements for bearing masonry units according to the Thai Industrial Standard.

A recent study on AAM from red mud and fly ash [34] showed that curing at high temperatures and high pressure in an autoclave increased the solubility of oxides and accelerated the reaction. AAM mixture of 26.3 wt% fly ash and 73.7 wt% red mud, activated by a 1M NaOH solution, reaches a strength of up to 20 MPa and a softening coefficient of more than 0.90.

In this study, we propose a treatment option for WTR of water purification plants in Vietnam as unfired building materials. WTR was used with CFA to produce geopolymer by autoclave technology at high temperatures and pressure. Unlike most previous studies that use the oxides content of raw materials to calculate the $SiO_2/Al2O_3$ molar ratio, we used the dissolved fraction in NaOH solution with different concentrations. This study focused on the compressive strength and microstructure characteristics of geopolymer with different WTR ratios cured in normal and autoclaved conditions.

2. Materials and Methods

2.1. Materials

Raw materials for the geopolymer were the WTR disposal of the Thu Duc water purification plant (Ho Chi Minh City, Vietnam) and the CFA (class F) of the Vinh Tan thermal power plant (Binh Thuan, Vietnam). The chemical compositions were detected using X-ray fluorescence (XRF) analysis. The physical properties are given in Table 1 and Table 2, respectively.

***Table 1. Chemical compositions of raw materials.***

Material	Oxides content, wt.%									
	SiO_2	Al_2O_3	Fe_2O_3	P_2O_5	Na_2O	K_2O	CaO	TiO_2	Other	LOI
WTR	32.8	26.3	33.7	0.223	-	0.126	1.91	3.59	0.967	6.38
CFA	48.93	26.19	11.22	-	-	6.94	1.52	1.38	2.27	1.55

Table 2. Physical properties of raw materials.

Material	Moisture content, wt%	Bulk density, kg/m^3	Density, g/cm^3	Mean particle size, μm
WTR	5.11	565	2.61	29.9
CFA	0.1	595	2.20	45.5

2.2. The alkaline activity of oxides

We used the solubility in an alkaline solution to estimate the alkaline activity of oxides in raw materials. The active oxides dissolved and reacted with alkaline according to the following equations (1 and 2):

$$SiO_2.nH_2O + 2NaOH = Na_2SiO_3 + (n + 1) H_2O \tag{1}$$

$$Al_2O_3.nH_2O + 2NaOH = 2NaAlO_2 + (n + 1) H_2O \tag{2}$$
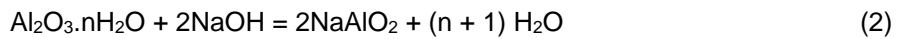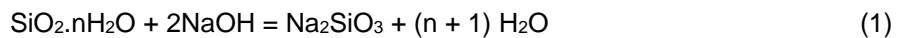
We dried the WTR or CFA at 120°C to constant mass. Then, we put 25 g of the dried WTR or CFA and 25 ml of xM (where x is a molar index) NaOH solution into a stainless-steel bomb. The bomb was tightly screwed and placed in the oven at (80 ± 2) °C for 24 hours. After that, we cooled it down to room temperature. We filtered the sample in the flask and collected the filtrate in the test tube. The solution was filtered to determine the content of dissolved silicon, iron, and aluminum oxides (Table 3).

Table 3. Dissolved oxides content in an alkaline solution of different concentration.

Items		Dissolved oxides content, wt% at a concentration of alkaline activators of								
		1M	2M	3M	4M	5M	6M	7M	8M	9M
WTR	SiO_2	0.46	0.71	0.90	1.10	1.35	1.67	1.89	2.06	2.24
	Al_2O_3	1.56	3.08	3.21	4.47	5.42	6.51	7.59	8.90	20.12
	Fe_2O_3	0.03	0.03	0.05	0.07	0.09	0.13	0.17	0.19	0.20
CFA	SiO_2	2.33	3.34	4.58	6.78	8.66	9.34	10.65	12.06	13.68
	Al_2O_3	4.56	4.66	4.66	4.69	4.70	4.72	4.76	4.76	4.76

Test results in Table 3 show the acceleration of the dissolution process of oxide in raw materials while increasing the alkaline activator concentration. An interesting phenomenon observed is the dissolved content of aluminum oxide of WTR increases from 1.56 % to 20.12 % while increasing the NaOH concentration from 1M to 9M. Meanwhile, it varies in a narrow range of (4.56–4.76) % in the case of CFA.

The dissolved content of silicon oxide in both WTR and CFA increases proportionally with the NaOH concentration from 1M to 9M. But the dissolved content of silicon oxide of WTR, even in 9M NaOH solution (2.24 %), is less than that of CFA in 1M NaOH solution (2.33 %). This result explains the essential role of CFA in geopolymer formation in the WTR-CFA system.

2.3. Specimen preparation

We mixed the dried WTR and CFA powder at a predetermined weight ratio (GP-1, GP-2, GP-3, and GP-4). After that, the NaOH 8M solutions were added to mixtures at the weight ratio of the NaOH solution to (WTR+CFA) equal to 0.15, as shown in Table 4.

Table 4. Mix proportion and curing condition.

Sample	WTR/CFA, wt%	NaOH/(WTR+CFA), wt%	Curing condition	
			Atmosphere	Autoclave
GP-1	80	0.15	28 days, room temperature	2 MPa, 7 h
GP-2	75	0.15	28 days, room temperature	2 MPa, 7 h
GP-3	65	0.15	28 days, room temperature	2 MPa, 7 h
GP-4	50	0.15	28 days, room temperature	2 MPa, 7 h

The mixtures had to be mixed for at least 30 minutes to ensure the powder dissolved into the NaOH solution. We poured the sludge into 80 mm long, 40 mm wide, and 20 mm high molds. Then, we compressed the sample with a pressing speed of 1 MPa/s and forming pressure of 3.5 MPa using Technotech experimental press. The sample's weight was about 70 gr (Fig.1). We divided these green samples into two groups. The first group was cured in an autoclave at a pressure of 2 MPa and temperature of about 215 ºC for 7 hours. The second group was cured at room temperature for 28 days. The series for the compressive strength test comprised three specimens.

Figure 1. Geopolymer samples.

2.4.   Methods of analysis

Inductively coupled plasma mass spectrometry (ICP-MS) was used to determine the activated silica and alumina. In this case, the 2.5 g of WTR and CFA were digested with 25 mL of the 8M NaOH solution in screw-top PTFE-lined stainless-steel bombs at (80 ± 2) °C for 24 hours following filtrate through a 25 mm filter.

We used Bruker/Siemens D5000 automated X-ray powder diffractometer to analyze the composition of raw materials and geopolymers. The XRD analysis used CuK radiation with a step size of 0.02°, a scan speed of 0.02° per 2 s, and a scan range of 10–55 2theta (diffraction angle). We also used FEI Quanta 200 Scanning Electron Microscope (SEM) at an accelerating voltage of 20 kV to examine the morphologies and microstructure of the materials.

The bonding interactions of raw materials and geopolymers were analyzes based on a Fourier Transform Infrared (FTIR) Spectrum using a spectrometer set Nicolet 6700 with scan frequencies range of 400–2000 cm^{-1}.

A compression testing machine (Tecnotest of Via DelleIndustrie, Inc., Italy) was used to determine the unconfined compressive strength of geopolymer specimens. The strain rate was 1.5% per minute. We polished two specimen's ends with sandpaper to meet the requirements on flatness and perpendicularity. Then, we applied a thin oil layer on the two specimen's ends to reduce the friction and the shear stress between the surfaces of the plates and the specimen.

3.   Results and Discussions

3.1. XRD analysis
The XRD patterns of WTR, CFA, and GP-1 (normal and autoclave curing) are shown in Fig 2.

a)

b)
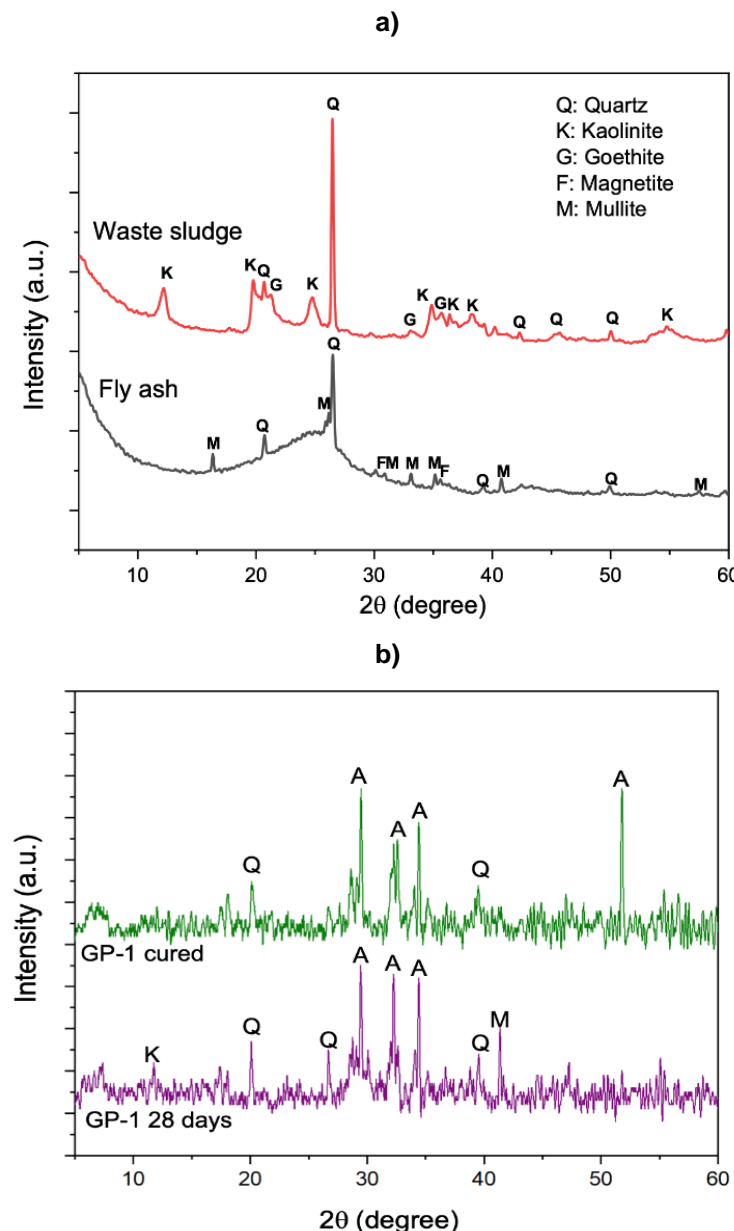
Figure 2. XRD patterns of CFA and WTR (a); GP-1 normally cured for 28 days, GP-1 autoclave cured for 7 hours (b).

The characteristic peaks of mullite (M), goethite (F), kaolinite (K), and quartz (Q) are visible on XRD patterns of WTR and CFA (Fig. 2a). These peaks disappeared on XRD patterns of GP-1 (normal and autoclave curing). The intensity of Q characteristic peaks is significantly reduced (Fig. 2b).

The results are evidence of the geopolymer formation based on WTR and CFA. In Fig. 2b, the analcime characteristic peaks (A) of zeolite are visible on XRD patterns of GP-1 specimens. The results also reveal that autoclave curing can improve the relative crystallinity of analcime zeolite. After 7 hours of curing in an autoclave under 2 MPa pressure, the relative crystallinity is better than after 28 days of curing in normal conditions.

3.1. FTIR analysis

The FTIR spectra of WTR, CFA, and GP-1 (normal and autoclave curing) are shown in Fig 3.
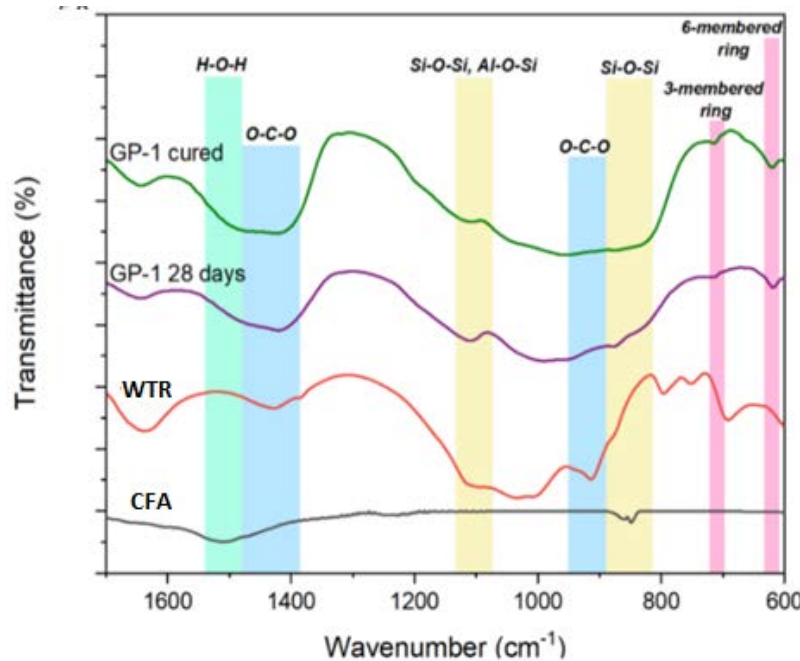
**Figure 3. FTIR spectra of CFA, WTR, and GP-1 (normal and autoclave curing).**

The vibrations in the 850–1200 cm^{-1} range on the FTIR spectra indicate the footprint of geopolymer bonds. The distribution of SiQ^n structural units has to be reflected by the broadness of this band. It is well known that the stretching vibrations of the –Si–O–Si– bonds of the SiQ^n structural units are FTIR active in the 850–1200 cm^{-1} range. The FTIR absorption band centered around 1200 cm^{-1}, 1100 cm^{-1}, 950 cm^{-1}, 900 cm^{-1}, and 850 cm^{-1} show the presence of the SiQ^4, SiQ^3, SiQ^2, SiQ^1, and SiQ^0 units, respectively. These values shift to lower wavenumbers when the degree of silicon substitution by aluminum in the second coordination sphere increases due to the weaker Al-O bonds [35].

In Fig. 3, the FTIR spectra showed a maximum absorption band in the range of 1050–1150 cm^{-1}, consistent with the predominance of SiQ^3 and SiQ^4 structural units over SiQ^0, SiQ^1, and SiQ^2 ones. The FTIR spectra also show the systematic shift of the maximum absorption band toward higher wavenumbers in the autoclave-cured geopolymer. It indicates the predominance of the SiQ^4 structural unit over the SiQ^3 in the produced gelatinous silicate phases. The silicon-oxygen ring vibrational bands occur in the wavenumbers region of 500–800 cm^{-1} [36].

In the FTIR spectra, we also can investigate the silicone-oxygen ring vibrational band in the geopolymer specimen. Three-membered and six-membered rings showed sharp peaks at 750–770 cm^{-1} and 600–620 cm^{-1}, respectively. The presence of six-membered rings is a conclusive proof that analcime is viable in geopolymer structures [37]. The sludge specimens are more sensitive to atmospheric carbonation than the geopolymer samples by the displays of carbonate species at 1450 cm^{-1} and 870 cm^{-1}.

3.2. SEM analysis

Fig. 4(a) and Fig. 4(b) show the microstructure of WTR and CFA. Fig. 4(c) and Fig. 4(d) show the microstructure of the geopolymer specimens.
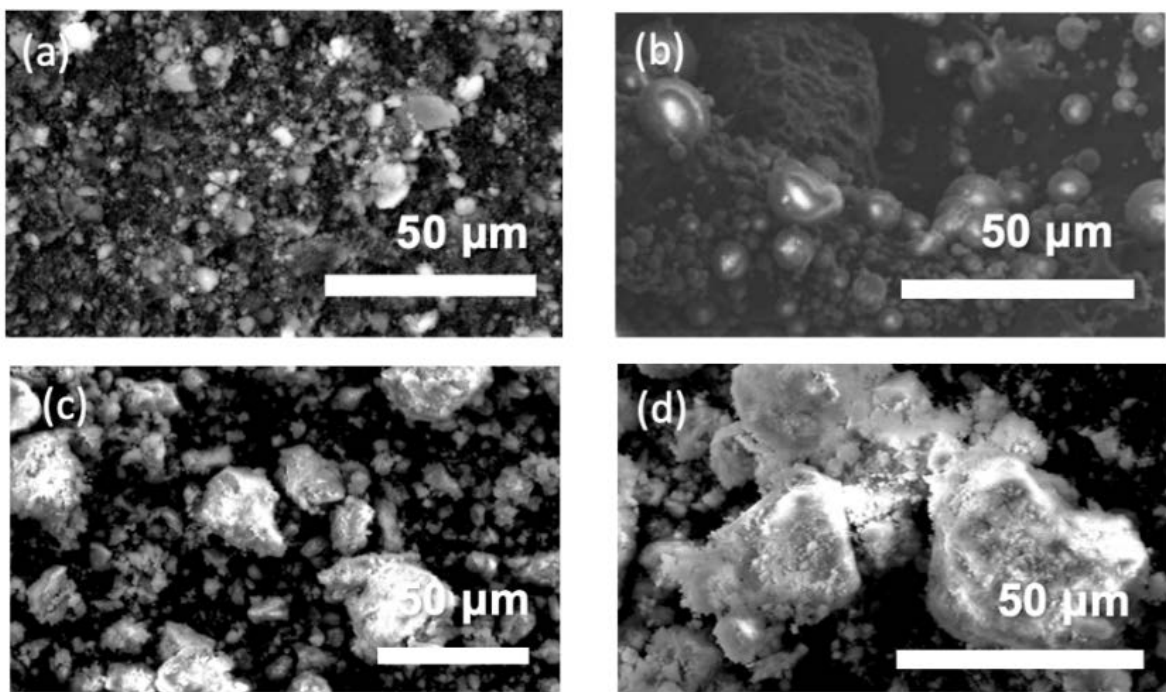
Figure 4. SEM images of WTR (a), CFA (b), normally cured GP-1 (c), and autoclave cured GP-1 (d).

In SEM images in Fig. 4, we can find the WTR particles in the form of irregularly shaped aggregates created by much smaller particles. They are likely hematite particles. The shape of the CFA particles is generally spherical. The regular geopolymer particles are variable in size and have a thin shell or plate-like shape. The WTR and CFA microstructures can help us to identify the originality of some phases (e.g., non-reactive or unreacted reactive phases) in the final products.

The microstructure in SEM images is porous and inhomogeneous with micro-voids and micro-cracks. The formation of voids and cracks may occur due to shrinkage caused by water evaporation, outside load (e.g., compressive testing load), or entrained air bubbles. The analcime zeolite crystals formed in autoclave conditions are coarser than in normal conditions. The crystallization rate depends on the saturation of the solution and the heterogeneous nucleation agents. These agents may be crystalline and amorphous aluminosilicate particles insoluble in the solution [10, 37]. In autoclave conditions, the analcime crystals grew significantly faster and coarser, and therefore the microstructure was more inhomogeneous. This phenomenon implied the critical role of autoclave curing in crystallizing analcime in geopolymer materials.

3.3. Compressive Strength

Fig. 5 shows the compressive strength test results and the calculated SiO_2/Al_2O_3 ratio (based on Table 3 with 8M NaOH solution) of GP-1, GP-2, GP-3, and GP-4 samples under different curing conditions. The results showed that the control specimens with a WTR/CFA ratio of 80 % cured in normal conditions did not harden and did not develop compressive strength. In this case, autoclave curing is essential to stimulate the reaction and increase compressive strength to 7.0 MPa.

Increasing the SiO_2/Al_2O_3 ratio and the content of CFA also improves the compressive strength of geopolymers in both curing conditions. Lowering the WTR/CFA ratio from 80% to 50% increased the SiO_2/Al_2O_3 ratio from 0.49 to 1.79 and the compressive strength from zero to 13.2 MPa (normally cured) and from 7.0 MPa to 28.8 MPa (autoclave cured). Excluding the control specimens, all geopolymers meet the strength requirements for unfired materials following the Vietnam national standard (> 3.5 MPa).

Geopolymers cured in autoclave conditions for 7 hours had higher compressive strength than those cured in normal conditions for 28 days (Fig. 5). These results are clear evidence of the superiority of autoclave technology in forming analcime crystals. The high pressure in the autoclave created a better condition for breaking the bonds in the precursors (WTR, CFA) and the formation of geopolymer structure $Mn[-(SiO_2)_z - AlO_2]_n \cdot mH_2O$.
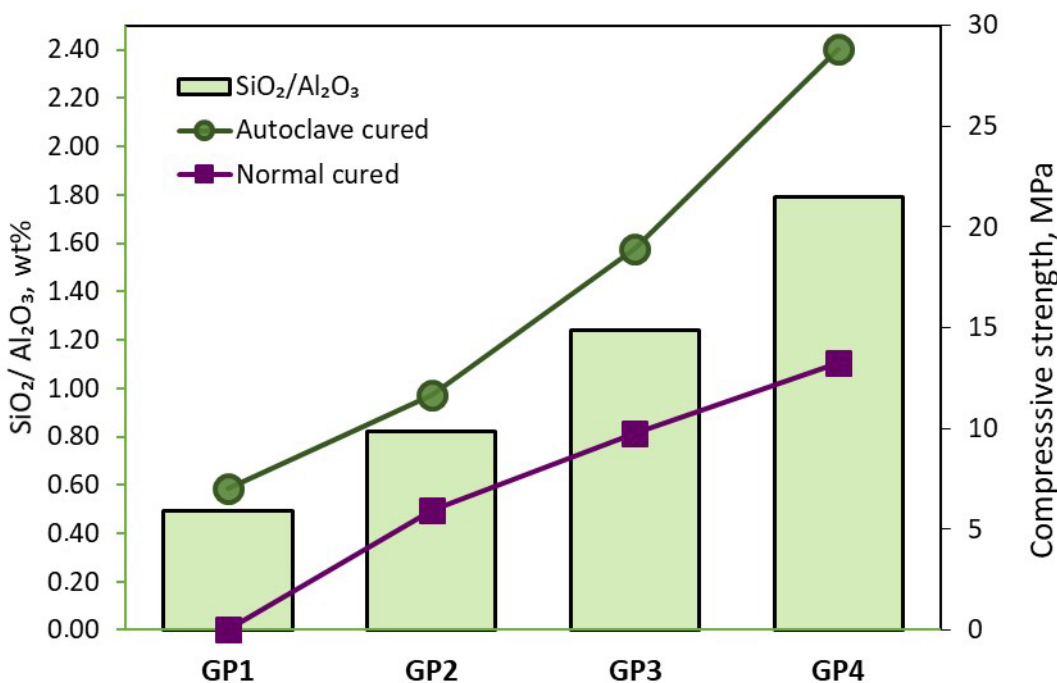
Figure 5. Compressive strength and the active SiO2/Al2O3 ratio under different curing conditions.

4. Conclusions

Geopolymers were successfully synthesized with WTR, CFA, and 8M NaOH solutions by autoclaving at 2 MPa pressure for 7 hours or normal curing in the atmosphere for 28 days. The results showed that the compressive strength of the autoclave cured geopolymer reached 28.8 MPa, which is significantly higher than in those cured in normal conditions (13.2 MPa). Increasing the SiO_2/Al_2O_3 ratio increased the compressive strength of geopolymers in both curing conditions.

The microstructure (XRD, SEM) and chemical bonding (FTIR) analysis confirmed the analcime crystal formation in the geopolymer. Autoclaving is an effective curing technology that improves the geopolymerization and the compressive strength of geopolymers using WTR.

References

1. Benlalla, A., Elmoussaouiti, M., Dahhou, M., Assafi, M. Utilization of water treatment plant sludge in structural ceramics bricks. Applied Clay Science. 2015. 118. Pp. 171–177. DOI:10.1016/j.clay.2015.09.012.

2. Cremades, L. V., Cusidó, J.A., Arteaga, F. Recycling of sludge from drinking water treatment as ceramic material for the manufacture of tiles. Journal of Cleaner Production. 2018. 201. Pp. 1071–1080. DOI:10.1016/j.jclepro.2018.08.094.

3. Ewais, E.M.M., Elsaadany, R.M., Ahmed, A.A., Shalaby, N.H., Al-Anadouli, B.E.H. Insulating Refractory Bricks from Water Treatment Sludge and Rice Husk Ash. Refractories and Industrial Ceramics. 2017. 58(2). Pp. 136–144. DOI:10.1007/S11148-017-0071-6.

4. Teixeira, S.R., Santos, G.T.A., Souza, A.E., Alessio, P., Souza, S.A., Souza, N.R. The effect of incorporation of a Brazilian water treatment plant sludge on the properties of ceramic materials. Applied Clay Science. 2011. 53(4). Pp. 561–565. DOI:10.1016/j.clay.2011.05.004.

5. Erdogmus, E., Harja, M., Gencel, O., Sutcu, M., Yaras, A. New construction materials synthesized from water treatment sludge and fired clay brick wastes. Journal of Building Engineering. 2021. 42. Pp. 102471. DOI:10.1016/J.JOBE.2021.102471.

6. Huang, C.H., Wang, S.Y. Application of water treatment sludge in the manufacturing of lightweight aggregate. Construction and Building Materials. 2013. 43. Pp. 174–183. DOI:10.1016/j.conbuildmat.2013.02.016.

7. Xu, G.R., Zou, J.L., Li, G.B. Effect of sintering temperature on the characteristics of sludge ceramsite. Journal of Hazardous Materials. 2008. 150(2). Pp. 394–400. DOI:10.1016/J.JHAZMAT.2007.04.121.

8. Huang, C.H., Wang, S.Y. Application of water treatment sludge in the manufacturing of lightweight aggregate. Construction and Building Materials. 2013. 43. Pp. 174–183. DOI:10.1016/J.CONBUILDMAT.2013.02.016.

9. Dahhou, M., El Moussaouiti, M., Arshad, M.A., Moustahsine, S., Assafi, M. Synthesis and characterization of drinking water treatment plant sludge-incorporated Portland cement. Journal of Material Cycles and Waste Management. 2018. 20(2). Pp. 891–901. DOI:10.1007/S10163-017-0650-0.

10. Chen, H.X., Ma, X., Dai, H.J. Reuse of water purification sludge as raw material in cement production. Cement and Concrete Composites. 2010. 32(6). Pp. 436–439. DOI:10.1016/j.cemconcomp.2010.02.009.

11. Pan, J.R., Huang, C., Lin, S. Reuse of fresh water sludge in cement making. Water Science and Technology. 2004. 50(9). Pp. 183–188. DOI:10.2166/WST.2004.0566.

12. Ahmad, T., Ahmad, K., Alam, M. Investigating calcined filter backwash solids as supplementary cementitious material for recycling in construction practices. Construction and Building Materials. 2018. 175. Pp. 664–671. DOI:10.1016/J.CONBUILDMAT.2018.04.227.

13. Gastaldini, A.L.G., Hengen, M.F., Gastaldini, M.C.C., Do Amaral, F.D., Antolini, M.B., Coletto, T. The use of water treatment plant sludge ash as a mineral addition. Construction and Building Materials. 2015. 94. Pp. 513–520. DOI:10.1016/j.conbuildmat.2015.07.038.

14. Liu, Y., Zhuge, Y., Chow, C.W.K., Keegan, A., Li, D., Pham, P.N., Huang, J., Siddique, R. Properties and microstructure of concrete blocks incorporating drinking water treatment sludge exposed to early-age carbonation curing. Journal of Cleaner Production. 2020. 261. Pp. 121257. DOI:10.1016/J.JCLEPRO.2020.121257.

15. Sales, A., De Souza, F.R., Almeida, F.D.C.R. Mechanical properties of concrete produced with a composite of water treatment sludge and sawdust. Construction and Building Materials. 2011. 25(6). Pp. 2793–2798. DOI:10.1016/j.conbuildmat.2010.12.057.

16. Godoy, L.G.G. de, Rohden, A.B., Garcez, M.R., Da Dalt, S., Bonan Gomes, L. Production of supplementary cementitious material as a sustainable management strategy for water treatment sludge waste. Case Studies in Construction Materials. 2020. 12. Pp. e00329. DOI:10.1016/J.CSCM.2020.E00329.

17. Geraldo, R.H., Fernandes, L.F.R., Camarini, G. Water treatment sludge and rice husk ash to sustainable geopolymer production. Journal of Cleaner Production. 2017. 149. Pp. 146–155. DOI:10.1016/J.JCLEPRO.2017.02.076.

18. Hwang, C.L., Chiang, C.H., Huynh, T.P., Vo, D.H., Jhang, B.J., Ngo, S.H. Properties of alkali-activated controlled low-strength material produced with waste water treatment sludge, fly ash, and slag. Construction and Building Materials. 2017. 135. Pp. 459–471. DOI:10.1016/J.CONBUILDMAT.2017.01.014.

19. Ji, Z., Pei, Y. Geopolymers produced from drinking water treatment residue and bottom ash for the immobilization of heavy metals. Chemosphere. 2019. 225. Pp. 579–587. DOI:10.1016/J.CHEMOSPHERE.2019.03.056.

20. Nimwinya, E., Arjharn, W., Horpibulsuk, S., Phoo-Ngernkham, T., Poowancum, A. A sustainable calcined water treatment sludge and rice husk ash geopolymer. Journal of Cleaner Production. 2016. 119. Pp. 128–134. DOI:10.1016/J.JCLEPRO.2016.01.060.

21. Suksiripattanapong, C., Horpibulsuk, S., Chanprasert, P., Sukmak, P., Arulrajah, A. Compressive strength development in fly ash geopolymer masonry units manufactured from water treatment sludge. Construction and Building Materials. 2015. 82. Pp. 20–30. DOI:10.1016/j.conbuildmat.2015.02.040.

22. Waijarean, N., MacKenzie, K.J.D., Asavapisit, S., Piyaphanuwat, R., Jameson, G.N.L. Synthesis and properties of geopolymers based on water treatment residue and their immobilization of some heavy metals. Journal of Materials Science. 2017. 52(12). Pp. 7345–7359. DOI:10.1007/S10853-017-0970-4.

23. Provis, J.L. Alkali-activated materials. 114. Elsevier Ltd, 01-12-2018.

24. Davidovits, J. Geopolymer - Chemistry and Application2015. ISBN:9782954453118.

25. Davidovits, J. Geopolymers: ceramic-like inorganic polymers. Journal of Ceramic Science and Technology. 2017. 8(3). Pp. 335–350. DOI:10.4416/JCST2017-00038.

26. He, Y., Cui, X. min, Liu, X. dong, Wang, Y. pin, Zhang, J., Liu, K. Preparation of self-supporting NaA zeolite membranes using geopolymers. Journal of Membrane Science. 2013. 447. Pp. 66–72. DOI:10.1016/J.MEMSCI.2013.07.027.

27. MacKenzie, K.J.D., Brew, D.R.M., Fletcher, R.A., Vagana, R. Formation of aluminosilicate geopolymers from 1:1 layer-lattice minerals pre-treated by various methods: a comparative study. Journal of materials science. 2007. 42(12). Pp. 4667–4674. DOI:doi.org/10.1007/s10853-006-0173-x.

28. Ge, Y.Y., Tang, Q., Cui, X.M., He, Y., Zhang, J. Preparation of large-sized analcime single crystals using the Geopolymer-Gels-Conversion (GGC) method. Materials Letters. 2014. 135. Pp. 15–18. DOI:10.1016/J.MATLET.2014.07.122.

29. Kupwade-Patil, K., Allouche, E.N. Impact of alkali silica reaction on fly ash-based geopolymer concrete. Journal of Materials in Civil Engineering. 2015. 25(1). Pp. 131–139. DOI:10.1061/(ASCE)MT.1943-5533.0000579.

30. Provis JL and Van Deventer JSJ. Geopolymers: Structure, Processing, Properties and Industrial Applications. CRC/Woodhead, 2009.

31. Duxson, P., Provis, J.L. Designing precursors for geopolymer cements. Journal of the American Ceramic Society. 2008. 91. Pp. 3864–3869. DOI:10.1111/j.1551-2916.2008.02787.x.

32. Waijarean, N., Asavapisit, S., Sombatsompop, K., MacKenzie, K.J.D. The Effect of the Si/Al Ratio on the Properties of Water Treatment Residue (WTR)-Based Geopolymers. Key Engineering Materials. 2014. 608. Pp. 289–294. DOI:10.4028/www.scientific.net/KEM.608.289.

33. Suksiripattanapong, C., Srijumpa, T., Horpibulsuk, S., Sukmak, P., Arulrajah, A., Du, Y.J. Compressive strengths of water treatment sludge-fly ash geopolymer at various compression energies. Lowland Technology International. 2017. 17(3). Pp. 147–156. DOI:10.14247/lti.17.3_147.

34. Hoang, M.D., Do, Q.M., Le, V.Q. Effect of curing regime on properties of red mud based alkali activated materials. Construction and Building Materials. 2020. 259. Pp. 119779. DOI:10.1016/j.conbuildmat.2020.119779.

35. Dimas, D., Giannopoulou, I., Panias, D. Polymerization in sodium silicate solutions: a fundamental process in geopolymerization technology. Journal of Materials Science. 2009. 44(14). Pp. 3719–3730. DOI:10.1007/s10853-009-3497-5.

36. Lecomte, I., Henrist, C., Liegeois, M., Maseri, F., Rulmont, A., Cloots, R. (Micro) structural comparison between geopolymers, alkali-activated slag cement and Portland cement. Journal of the European Ceramic Society. 2006. 26(16). Pp. 3789–3797. DOI:10.1016/j.jeurceramsoc.2005.12.021.

37. Sitarz, M., Handke, M., Mozgawa, W. Identification of silico oxygen rings in SiO2 based on IR spectra. SpectrochimicaActa Part A: Molecular and Biomolecular Spectroscopy. 2020. 56(9). Pp. 1819–1823. DOI:10.1016/S1386-1425(00)00241-9.

38. Itani, L., Liu, Y., Zhang, W., Bozhilov, K.N., Delmotte, L., Valtchev, V. Investigation of the physicochemical changes preceding zeolite nucleation in a sodium-rich aluminosilicate ge. Journal of the American Ceramic Society. 2009. 131(29). Pp. 10127–10139. DOI:10.1021/ja902088f.

Contacts:

Quang Minh Do, *PhD*
ORCID: https://orcid.org/0000-0001-5714-1259
E-mail: mnh_doquang@hcmut.edu.vn

Huynh Uyen Phuong Nguyen,
ORCID: *https://orcid.org/0000-0002-7256-4097*
E-mail: *phuongup@gmail.com*

Van Quang Le, *PhD*
ORCID: *https://orcid.org/0000-0003-0922-9891*
E-mail: *quanghuce83@gmail.com*

Minh Duc Hoang, *PhD*
ORCID: *https://orcid.org/0000-0001-8413-8741*
E-mail: *hmduc@yahoo.com*

Contact interaction of multilayer slabs with an inhomogeneous base

M.M. Mirsaidov[1] ✉ iD **, K. Mamasoliev[2]** iD

[1] *Tashkent Institute of Irrigation and Agricultural Mechanization Engineers, Tashkent, Uzbekistan*

[2] *Samarkand State Institute of Architecture and Civil Engineering, Lolazor Samarkand, Uzbekistan*

✉ *theormir@mail.ru*

Abstract. The article is devoted to the development of mathematical models and new methods for solving contact problems of multilayer elements of structures with an inhomogeneous base, considering their mechanical, structural features, and to the assessment of their internal force factors. A mathematical model was developed and an analytical method was proposed for assessing the internal force factors in multilayer strip slabs on an inhomogeneous base under various loads. The solution of the problems under consideration is based on a series expansion of the reactive pressure of an inhomogeneous base in terms of orthogonal ultra-spherical Gegenbauer polynomials; the solution is reduced to the study of infinite systems of algebraic equations. Their regularity was proved and the corresponding estimates were obtained. The required number of terms of the polynomial in the expansion was established. The analysis of the results obtained made it possible to evaluate the influence of the rigidity characteristics of the filler and the inhomogeneity of the base on the distribution of internal force factors in the slabs.

1. Introduction

The article considers mathematical models, methods, and estimates of internal force factors in contact interactions of multilayer strip-slabs lying on an elastic inhomogeneous base.

A number of structural elements, such as foundations of buildings, slabs of hydro-technical structures, road and airfield pavements, rails and sleepers of railway tracks, and other elements work jointly with the subgrade, interacting with each other under various loads. Their soil base can be homogeneous, or, more often, inhomogeneous.

Today, the problem of determining the individual characteristics of multilayer structural elements interacting with inhomogeneous bases, taking into account mechanical, geometric, and other parameters of structural elements and bases remains unsolved.

Therefore, the development of models and new analytical methods for solving contact problems of multilayer elements of structures with an inhomogeneous base, taking into account their mechanical, structural features, as well as the assessment of their internal force factors is an urgent task of structural mechanics.

It should be noted that the solution to the problems of contact interactions of various elements of structures with the foundation is considered in fundamental publications [1–5], in which the main attention is paid to the analysis of the relationship of contacting structural elements.

To date, there are a sufficient number of published studies in which various issues of the contact of structural elements with the base are considered:

- in [6], the calculation of slabs on an elastic base with a variable coefficient of one-layer and two-layer beds is given. Calculations for a two-layer slab on an elastic base with a variable bed ratio are given for different heights of the upper layer using finite element methods;

- in [7], a mathematical model of the contact interaction of two plates made of materials with different moduli of elasticity is presented taking into account physical and structural nonlinearities. To study the stress-strain state of the mechanical structure, the method of variational iteration was used, which makes it possible to reduce the partial differential equations to ordinary differential equations;

- in [8], an axisymmetric quasi-static contact problem of the thermal and mechanical interaction of a circular punch and an inhomogeneous elastic half-space is considered, the mechanical and thermophysical properties of which are taken as arbitrary functions of the depth coordinate. The numerical implementation is performed for various dependences of material properties on the depth of the half-space;

- in [9], an analytical study of the contact problem of a multilayer elastic rigid body subjected to eccentric indentation by a rigid circular plate within the framework of classical elasticity is presented. An explicit expression for the solution for an elastic field in a multilayer rigid body is presented. The numerical results of checking the methods adopted in the study and the illustrations of the inhomogeneity effect of the layered material on the elastic field are presented;

- in [10], a mathematical model and a method for solving the problem for multilayer strip-slabs on a homogeneous elastic foundation under various static loads are developed. The problem under consideration was reduced (using the Chebyshev polynomial) to solving infinite systems of algebraic equations. The regularity of infinite systems of algebraic equations is proved and the corresponding estimates are obtained;

- in [11, 12], a detailed review of the history of development of mathematical modeling and methods of elastic analysis of inhomogeneous rigid bodies and a comprehensive review of various theoretical models of elastic and viscoelastic foundations in oscillatory systems are presented;

- in [13–15], dynamic problems for the structure – foundation were jointly solved, using artificial non-reflecting boundary conditions on the boundary of the finite area of the foundations.

A seismic analysis of the dam - base system using the finite element method is considered in [14]. The results show that when solving dynamic problems, the proposed artificial boundary conditions absorb the reflections of false waves quite well.

Along with these publications, there is a number of articles [16–23], devoted to the study of internal force factors and the behavior of inhomogeneous elastic and viscoelastic systems under various influences, taking into account their characteristics, operating conditions, and interaction with the environment.

When solving specific problems, each of these approaches has its own advantages and disadvantages; nevertheless, they are used in solving practical problems.

Here we have presented just a few articles devoted to solving various problems in the joint operation of structural elements with a deformable base, which show the incompleteness of research in this direction, especially in the field of obtaining analytical solutions. Therefore, this article is devoted to the development of mathematical models and analytical methods for studying the interaction of multilayer strip-slabs lying on an elastic inhomogeneous base.

2.   Methods

2.1. Mathematical models of the problem

We consider n layer strips-slabs $2l$ wide, h_1, h_2,..., h_n thick, respectively, having an arbitrary character in terms of geometrical and mechanical parameters. An elastic filler is arranged between the plates, and the lower plate fits tightly to an elastic inhomogeneous base. It is considered that the strip layers are loaded with external loads of q_1, q_2,..., q_n intensity, respectively, constant loads longwise the slab and arbitrary loads across it. We assume that the reaction of the elastic filler is proportional to the differences in deflections of connecting strips. The normal reactive pressures of the inhomogeneous base (Fig. 1) affect the lower strip, in addition to external loads, and the reaction of the filler of the upper strips.
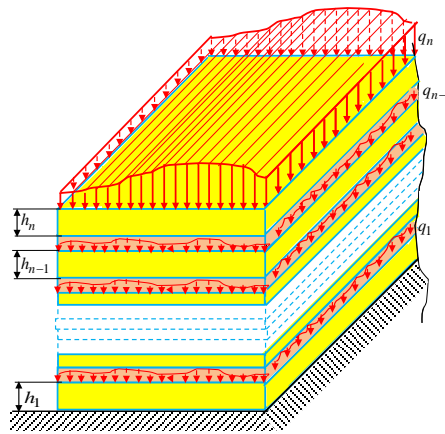
Figure 1. Design scheme of n-layer strip-slabs.

An n-layer slab beam cut out with a width equal to one is taken for mathematical modeling of the n-layer slab-strip deformation process. Under the above conditions, the calculation of n-layer strip-slabs is reduced to the calculation of n layer beam slabs $2l$ wide, h_1, h_2,..., h_n thick, respectively, with a width equal to one (Fig. 2). If we assume that the origin of the Cartesian coordinates is in the center of symmetry of the beam slabs, then the study along the abscissa axis is performed in a segment $\left[-l; l\right]$, i.e., $-l \le x \le l$, the ordinates of the slab deflection, y_1, y_2,..., y_n are functions of the variable x, i.e., $y_i = y_i\left(x\right)$, $i = 1, 2,..., n$, where y_i is the deflection of the i-th beam slab.
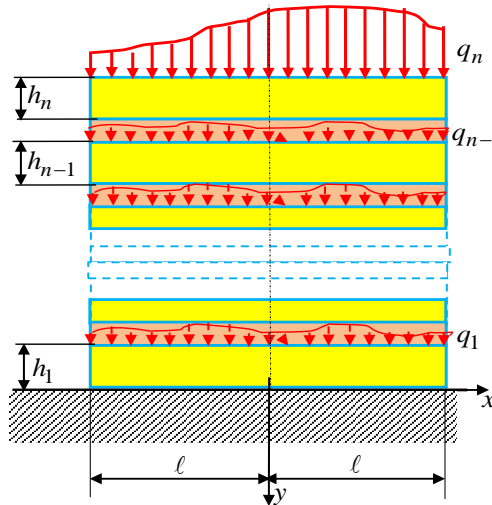
Figure 2. Design scheme of n layer beam slabs.

To simulate the deformation process of n layer beam slabs, one can write a system of differential equations for the unknown deflections of beam slabs in the following form:

$$\left.\begin{aligned}
D_n \cdot y_n^{IV} &= q_n - k_{n-1} \cdot \left(y_n - y_{n-1}\right) \\
D_{n-1} \cdot y_{n-1}^{IV} &= q_{n-1} + k_{n-1} \cdot \left(y_n - y_{n-1}\right) - k_{n-2} \cdot \left(y_{n-1} - y_{n-2}\right) \\
D_{n-2} \cdot y_{n-2}^{IV} &= q_{n-2} + k_{n-2} \cdot \left(y_{n-1} - y_{n-2}\right) - k_{n-3} \cdot \left(y_{n-2} - y_{n-3}\right) \\
&\cdots\cdots\cdots\cdots\cdots\cdots\cdots\cdots\cdots\cdots\cdots\cdots\cdots\cdots\cdots\cdots\cdots\cdots\cdots\cdots \\
D_1 \cdot y_1^{IV} &= q_1 + k_1 \cdot \left(y_2 - y_1\right) - p
\end{aligned}\right\}, \qquad (1)$$

where $D_i = \dfrac{E_i h_i^3}{12\left(1-v_i^2\right)}$; E_i, v_i are the modulus of elasticity and Poisson's ratio of the plate material;

k_i filler rigidity coefficients; $q_i = q_i(x)$ external loads of the i-th slab; $p = p(x)$ reactive normal pressure of the base.

An elastic inhomogeneous half-plane is taken as an elastic base, the deformation modulus of which changes according to the power law [4, 5]

$$E = E_m \cdot y^m, \ 0 \le m < 1,$$

where E_m is the constant; m is the inhomogeneity index.

The equation that determines the settlement $V(x)$ of an inhomogeneous base with reactive pressure $p(x)$ of the base under plane strain, according to the solution of the theory of elasticity [4], can be represented as

$$V = \frac{\theta_m}{m} \cdot \int_{-l}^{l} \frac{p(s)}{|x-s|^m}\, ds. \tag{2}$$

where $\theta_m = \dfrac{\left(1-v^2\right)\cdot\sin\dfrac{\gamma\pi}{2}\cdot\Gamma\left[1+(1-\gamma+m)/2\right]\cdot\Gamma\left[1+(1+\gamma+m)/2\right]}{\pi\cdot(1+m)\cdot E_m\cdot 2^{-1-m}\cdot\Gamma(m+2)}$; v is the Poisson's ratio of

homogeneous soil of the base; $\Gamma(x)$ is the Euler's gamma function.

The condition for the tight fit of the lower slab surface with the base is represented as

$$y_1(x) = V(x), \ -l \le x \le l. \tag{3}$$

Equation (3), as the contact conditions of the slab and the base, makes it possible to study the effect of base inhomogeneity on the internal forces of the slab.

The solution to the problem of the interaction of n-layer beam slabs with an inhomogeneous elastic base in the case of a two-way connection is reduced to solving systems of differential equations (1) and a singular integral equation (2) with condition (3). Equations (1), (2) and (3) constitute a closed system of equations for unknown functions, i.e., the number of the equations corresponds to the number of unknowns.

2.2. Solution method

To solve the problems posed (1)–(3), we use the expansion in the form [4]

$$\frac{1}{|x-s|^m} = \frac{2^{m-1}\cdot\Gamma\left(\dfrac{m}{2}\right)}{\Gamma(m+1)\cdot\cos\dfrac{m\pi}{2}} \cdot \sum_{n=0}^{\infty}\left(\frac{m}{2}+n\right)\cdot C_n^{\frac{m}{2}}(x)\cdot C_n^{\frac{m}{2}}(s), \tag{4}$$

where $C_n^{\frac{m}{2}}(x)$ is the orthogonal ultraspherical Gegenbauer polynomials [24] with weight functions

$$\rho(x) = \left(1-x^2\right)^{(m-1)/2}.$$

From expansion (4), it is seen that for singular integrals of type (2), the orthogonal Gegenbauer polynomials are eigenfunctions. This confirmation makes it possible to search for the unknown reactive pressure of an inhomogeneous base, in the following form

$$p(x) = \rho(x) \cdot \sum_{n=0}^{\infty} A_n \cdot C_n^{\frac{m}{2}}(x), \tag{5}$$

here A_n are the unknown constants.

In what follows, we use the dimensionless coordinates $"x"$ equal to the ratio of the absolute coordinate to the half-length of the beam l.

If the designations P and M are introduced for the sum of all vertical forces and the sum of their moments relative to the middle of the beam slabs, respectively, then the equilibrium equations for the beam slabs take the form

$$\int_{-1}^{1} p(x)\,dx = \frac{P}{l}; \quad \int_{-1}^{1} x \cdot p(x)\,dx = \frac{M}{l^2}. \tag{6}$$

After satisfying the equilibrium equations, i.e., substituting (5) into (6) and taking into account the orthogonality of the Gegenbauer polynomials, the value of the first two coefficients of series (5) is determined in the following form

$$A_0 = P \cdot \left(l \cdot \left\| C_0^{m/2} \right\| \right)^{-1}, \quad A_1 = M \cdot m \cdot \left(l^2 \cdot \left\| C_1^{m/2} \right\| \right)^{-1}, \tag{7}$$

where $\left\| C_0^{m/2} \right\|$, $\left\| C_1^{m/2} \right\|$ are the values of the norm of the orthogonal Gegenbauer polynomial determined by the following formula [24]

$$\left\| C_j^{\nu} \right\| = \frac{\pi \cdot 2^{1-2\nu} \cdot \Gamma(2\nu + j)}{\Gamma^2(\nu) \cdot j! \cdot (\nu + j)}. \tag{8}$$

If the remaining coefficients of series (5) are assumed zero, then we have the case of a rigid beam slab. The terms of series (5), starting from the values $n = 2$, represent a correction that differs from the distribution of reactive pressure for absolutely rigid beam slabs.

Substituting (5) into (2), and considering expansion (4) and the orthogonality of the Gegenbauer polynomials, for the base settlement, we obtain the following relationship

$$V = \alpha_m \cdot \sum_{n=0}^{\infty} A_n \cdot \left(\frac{m}{2} + n \right) \cdot \left\| C_n^{m/2} \right\| \cdot C_n^{\frac{m}{2}}(x), \tag{9}$$

where $\alpha_m = \dfrac{\theta_m \cdot 2^{m-1} \cdot \Gamma^2\left(\dfrac{m}{2}\right)}{\Gamma(m+1) \cdot \cos\dfrac{m\pi}{2}}.$

The resulting expression (9) allows us to determine the base settlement, i.e., the vertical displacement of the point of the inhomogeneous base.

3. Results and Discussion

Now, using the above results, we solve specific problems.

3.1. Problem

A two-layer beam slab interacting with an inhomogeneous elastic base is considered. The system of differential equations for the deflections of beam slabs (1) takes the form

$$\left.\begin{array}{l} \dfrac{D_2}{l^4} y_2^{IV} = q_2 - k_1(y_2 - y_1) \\[4mm] \dfrac{D1}{l^4} y_1^{IV} = q_1 + k_1(y_2 - y_1) - p \end{array}\right\} \qquad (10)$$

The general solution of the system of differential equations (10) is represented in the following form

$$y_1 = \frac{l^4}{D_1 + D_2} \cdot \left\{ \sum_{i=1}^{4} C_i \cdot x^{4-i} + f_q(x) - f_p(x) - \right.$$

$$\left. - D_2 \cdot \left[\sum_{i=1}^{4} B_i \cdot u_i(\alpha x) + \psi_q(x) + \varphi_p(x) \right] \right\}, \qquad (11)$$

$$y_2 = \frac{l^4}{D_1 + D_2} \cdot \left\{ \sum_{i=1}^{4} C_i \cdot x^{4-i} + f_q(x) - f_p(x) + \right.$$

$$\left. + D_1 \cdot \left[\sum_{i=1}^{4} B_i \cdot u_i(\alpha x) + \psi_q(x) + \varphi_p(x) \right] \right\}, \qquad (12)$$

where C_i, B_i are the integration constants determined from the boundary conditions of the problem under consideration:

$$\left.\begin{array}{ll} u_1(x) = chx \cdot \cos x; & u_2(x) = chx \cdot \sin x + shx \cdot \cos x; \\[2mm] u_3(x) = shx \cdot \sin x; & u_4(x) = chx \cdot \sin x - shx \cdot \cos x \end{array}\right\}; \qquad (13)$$

$$f_q^{IV}(x) = q_1(x) + q_2(x); \qquad (14)$$

$$f_p^{IV}(x) = p(x); \qquad (15)$$

$$\psi_q(x) = \frac{1}{4\alpha^3} \int_0^x \left[\frac{q_1(z)}{D_2} - \frac{q_2(z)}{D_1} \right] \cdot u_4 \left[\alpha(x-z) \right] dz; \qquad (16)$$

$$\varphi_p(x) = \frac{1}{4\alpha^3} \int_0^x \frac{p(z)}{D_1} \cdot u_4 \left[\alpha(x-z) \right] dz. \qquad (17)$$

Substituting (5) in (15) and (17), and performing the appropriate operations, we can write the following

$$f_p(x) = \sum_{n=0}^{\infty} A_n \cdot f_n(x), \qquad (18)$$

$$\varphi_p(x) = D_1^{-1} \cdot \sum_{n=0}^{\infty} A_n \cdot \varphi_n(x), \qquad (19)$$

where

$$f_n(x) = \frac{m(m+2)(m+4)(m+6)\left(1-x^2\right)^{\frac{m+7}{2}} C_{n-4}^{\frac{m}{2}+4}(x)}{n(n-1)(n-2)(n-3)(n+m)(n+m+1)(n+m+2)(n+m+3)} \quad n > 3, \qquad (20)$$

$$f_n'(x) = \frac{m(m+2)(m+4)\left(1-x^2\right)^{\frac{m+5}{2}} C_{n-3}^{\frac{m}{2}+3}(x)}{n(n-1)(n-2)(n+m)(n+m+1)(n+m+2)} \quad n > 2, \tag{21}$$

$$f_n''(x) = \frac{m(m+2)}{n(n-1)(n+m)(n+m+1)} \cdot \left(1-x^2\right)^{\frac{m+3}{2}} C_{n-2}^{\frac{m}{2}+2}(x) \quad n > 1, \tag{22}$$

$$f_n'''(x) = \frac{m}{n(n+m)} \cdot \left(1-x^2\right)^{\frac{m+1}{2}} C_{n-1}^{\frac{m}{2}+1}(x) \quad n > 0, \tag{23}$$

$$f_n^{IV}(x) = \left(1-x^2\right)^{\frac{m-1}{2}} C_n^{\frac{m}{2}}(x), \tag{24}$$

$$\varphi_n(x) = \frac{1}{4\alpha^3} \int_0^x u_4\left[\alpha(x-z)\right] \cdot \left(1-z^2\right)^{\frac{m-1}{2}} C_n^{\frac{m}{2}}(z)\,dz. \tag{25}$$

Identifying the explicit form of the function $f_n(x)$ at $n < 4$, we use the following formulas [24, 25]

$$C_n^\nu(x) = \sum_{j=0}^{\left[\frac{n}{2}\right]} (-1) \frac{2^{n-2j} \cdot \Gamma(\nu+n-j)}{\Gamma(\nu) \cdot j! \cdot (n-2j)!} \cdot x^{n-2j}, \tag{26}$$

$$\left(1-x^2\right)^{\frac{m-1}{2}} = \sum_{k=0}^{\infty} c_k \cdot x^{2k}, \tag{27}$$

where

$$c_k = \frac{\Gamma\left(\dfrac{1-m}{2}+k\right)}{\Gamma\left(\dfrac{1-m}{2}\right) \cdot k!}. \tag{28}$$

Introducing (5), (26), (27) into (15) and performing the appropriate mathematical operations, we obtain an explicit form for the function $f_n(x)$ at:

$$f_0(x) = \sum_{k=0}^{\infty} c_k \cdot \frac{x^{2k+4}}{(2k+1)(2k+2)(2k+3)(2k+4)}; \tag{29}$$

$$f_1(x) = \sum_{k=0}^{\infty} c_k \cdot m \cdot \frac{x^{2k+5}}{(2k+2)(2k+3)(2k+4)(2k+5)}; \tag{30}$$

$$f_2(x) = \sum_{k=0}^{\infty} c_k \cdot \left[\frac{m(m+2)}{2!} \cdot \frac{x^{2k+6}}{(2k+3)(2k+4)(2k+5)(2k+6)} - \frac{m}{2} \cdot \frac{x^{2k+4}}{(2k+1)(2k+2)(2k+3)(2k+4)}\right]; \tag{31}$$

$$f_3(x) = \sum_{k=0}^{\infty} c_k \cdot \left[\frac{m(m+2)(m+4)}{3!} \cdot \frac{x^{2k+7}}{(2k+4)(2k+5)(2k+6)(2k+7)} - \frac{m(m+2)}{2!} \cdot \frac{x^{2k+5}}{(2k+2)(2k+3)(2k+4)(2k+5)} \right].$$
(32)

Substituting (18) and (19) into (11) and (12), we obtain the following expressions for the deflections of beam slabs:

$$y_1 = \frac{l^4}{D_1 + D_2} \cdot \left\{ \sum_{i=1}^{4} C_i x^{4-i} + f_q(x) - \sum_{n=0}^{\infty} A_n \cdot f_n(x) - \right.$$
$$\left. -D_2 \cdot \left[\sum_{i=1}^{4} B_i \cdot u_i(\alpha x) + \psi_q(x) + \frac{1}{D_1} \cdot \sum_{n=0}^{\infty} A_n \cdot \varphi_n(x) \right] \right\},$$
(33)

$$y_2 = \frac{l^4}{D_1 + D_2} \cdot \left\{ \sum_{i=1}^{4} C_i x^{4-i} + f_q(x) - \sum_{n=0}^{\infty} A_n \cdot f_n(x) + \right.$$
$$\left. +D_1 \left[\sum_{i=1}^{4} B_i \cdot u_i(\alpha x) + \psi_q(x) + \frac{1}{D_1} \cdot \sum_{n=0}^{\infty} A_n \cdot \varphi_n(x) \right] \right\}.$$
(34)

Expressions (33) and (34), which determine the deflections of beam slabs, have a general character corresponding to an arbitrary law of distribution of external loads. In specific external loads with specific distribution laws, it will be possible to find the corresponding deflections of the beam slabs that satisfy the corresponding boundary conditions, i.e. the constant coefficients of integration B_i, C_i determined from the boundary conditions of the problems under consideration. It should be noted here that coefficients A_n in formulas (9), (33), and (34) are unknown. The contact conditions (3) are used to determine these unknown coefficients A_n. The deflection of the lower beam slabs satisfying the boundary conditions (33) and the settlement of the base (9) are determined by condition (3). Further, the equality obtained is multiplied by $(1-x^2)^{\frac{m-1}{2}} C_n^{\frac{m}{2}}(x)$, and then integrated between −1 and 1. As a result of integration with respect to unknown coefficients A_n, an infinite system of algebraic equations with infinite unknowns is obtained. An infinite system of algebraic equations is solved by the reduction method (the use of the reduction method will be justified strictly mathematically). Certain coefficients A_n are substituted in (5), (9), (33), (34) and the regularities of the reactive pressure, the settlement of the base, and the deflections of the beam slabs are found. Further, with determined deflections of the beam slabs, it is possible to define the change patterns of the internal forces of the slabs corresponding to a change in the inhomogeneity of the base.

3.2. Problem

Consider a two-layer beam slab loaded with uniformly distributed external loads, i.e.

$$q_1(x) = q_2(x) = q = const.$$

In this case, due to the symmetry property of the load in series (5), only even polynomials are taken into account

$$p(x) = (1-x)^{\frac{m-1}{2}} \cdot \sum_{n=0}^{\infty} A_{2n} \cdot C_{2n}^{\frac{m}{2}}(x).$$
(35)

From the equation of equilibrium (6), we obtain

$$A_0 = 4q \cdot \left\| C_0^{m/2} \right\|^{-1}.$$
(36)

Expression (3) describing the base settlement takes the following form

$$V(x) = \alpha_m \cdot \sum_{n=0}^{\infty} A_{2n} \cdot \left(\frac{m}{2} + 2n\right) \cdot C_{2n}^{\frac{m}{2}}(x), \tag{37}$$

expressions (14), (16) and (17), respectively, take the forms

$$f_q(x) = 2q \cdot \frac{x^4}{24}, \tag{38}$$

$$\psi_q(x) = \frac{1}{4\alpha^3} \cdot \frac{D_1 - D_2}{D_1 \cdot D_2} \cdot q \cdot \frac{1}{\alpha} \left[1 - u_1(\alpha x)\right], \tag{39}$$

$$\varphi_p(x) = \frac{1}{D_1} \cdot \sum_{n=0}^{\infty} A_{2n} \cdot \varphi_{2n}(x), \tag{40}$$

where

$$\varphi_{2n}(x) = \frac{1}{4\alpha^3} \int_0^x u_4\left[\alpha(x-z)\right] \cdot \left(1 - z^2\right)^{\frac{m-1}{2}} \cdot C_{2n}^{\frac{m}{2}}(z) dz. \tag{41}$$

In this case, the deflections of the slabs that satisfy the boundary conditions of the problem under consideration, take the following forms:

$$y_1 = \frac{l^4}{D_1 + D_2} \left\{ q \cdot C \cdot x^2 + C_4 + 2q \cdot \frac{x^4}{24} - \frac{D_1 - D_2}{D_1} \cdot \frac{q}{24} - \right.$$
$$\left. - \frac{D_2}{D_1} \sum_{n=0}^{\infty} A_{2n} \cdot \left[\phi_{1,2n} \cdot u_1(\alpha x) + \phi_{2,2n} \cdot u_3(\alpha x) + \varphi_{2n}(x) \frac{D_1}{D_2} \cdot f_{2n}(x)\right] \right] \tag{42}$$

$$y_2 = \frac{l^4}{D_1 + D_2} \cdot \left\{ q \cdot C \cdot x^2 + C_4 + 2q \cdot \frac{x^4}{24} + \frac{D_1 - D_2}{D_1} \cdot \frac{q}{24} + \right.$$
$$\left. + \sum_{n=0}^{\infty} A_{2n} \cdot \left[\phi_{1,2n} \cdot u_1(\alpha x) + \phi_{2,2n} \cdot u_3(\alpha x) + \varphi_{2n}(x) - f_{2n}(x)\right] \right\} \tag{43}$$

where

$$C = -\frac{1}{2} - \frac{2}{m+1} \cdot \left\| C_0^{m/2} \right\|^{-1} \tag{44}$$

$$\phi_{1,2n} = \frac{b^{-1}}{8\alpha^3} \cdot \int_0^1 \left\{2u_1(\alpha) \cdot u_1[\alpha(1-z)] + u_4(\alpha) \cdot u_2[\alpha(1-z)]\right\} \cdot (1-z^2)^{\frac{m-1}{2}} C_{2n}^{\frac{m}{2}}(z) dz \tag{45}$$

$$\phi_{2,2n} = \frac{b^{-1}}{8\alpha^3} \cdot \int_0^1 \left\{2u_3(\alpha) \cdot u_1[\alpha(1-z)] - u_2(\alpha) \cdot u_2[\alpha(1-z)]\right\} \cdot (1-z^2)^{\frac{m-1}{2}} C_{2n}^{\frac{m}{2}}(z) dz \tag{46}$$

The integration factor C_4 can be eliminated by proceeding to relative displacement.

Expressions (37) and (42) are substituted into (3), and then the obtained equalities are multiplied by

$$(1-x^2)^{\frac{m-1}{2}} \cdot C_{2k}^{\frac{m}{2}}(x), \quad k = 1, 2, 3, \ldots$$

and are integrated between −1 and 1.

In this case, considering the orthogonality of the ultraspherical Gegenbauer polynomials, we obtain the following infinite system with respect to unknown coefficients A_{2n}:

$$a_{2k} + \sum_{n=1}^{\infty} a_{2n,2k} \cdot A_{2n} = A_{2k} \cdot \alpha_m \cdot \left(\frac{m}{2} + 2k\right) \cdot \left\| C_{2k}^{m/2} \right\| \qquad k = 1, 2, 3, \ldots \qquad (47)$$

where

$$a_{2k} = \frac{l^4}{D_1 + D_2} \int_{-1}^{1} \left\{ q \cdot \left(\overline{C_2} \cdot x^2 + \frac{x^4}{24} \right) - \frac{D_2}{D_1} A_0 \cdot \left[\phi_{1,0} \cdot (u_1(\alpha x) - 1) + \right. \right.$$

$$\left. \left. + \phi_{2,0} \cdot u_3(\alpha x) + \varphi_0(x) + \frac{D_1}{D_2} \cdot (f_0(x) - f_0(0)) \right] \right\} \cdot (1 - x^2)^{\frac{m-1}{2}} \cdot C_{2k}^{\frac{m}{2}}(x) dx, \qquad (48)$$

$$a_{2n,2k} = -\frac{l^4}{D_1 + D_2} \cdot \frac{D_2}{D_1} \cdot \int_{-1}^{1} \left\{ \phi_{1,2n} \cdot [u_1(\alpha x) - 1] + \phi_{2,2n} \cdot u_3(\alpha x) + \right.$$

$$\left. + \varphi_{2n}(x) + \frac{D_1}{D_2} \cdot (f_{2n}(x) - f_{2n}(0)) \right] \right\} \cdot (1 - x^2)^{\frac{m-1}{2}} \cdot C_{2k}^{\frac{m}{2}}(x) d. \qquad (49)$$

By integrating (48), (49) by parts, it is possible to eliminate the singularities of the integrals and bring them to the following convenient form:

$$a_{2k} = \frac{l^4}{D_1 + D_2} \cdot \int_{-1}^{1} \left\{ 2q \cdot \left(\overline{C}_2 + \frac{x^2}{4} \right) - A_0 \cdot \frac{D_2}{D_1} \cdot \left[\phi_{1,0} \cdot u_1''(\alpha x) + \right. \right.$$

$$\left. \left. + \phi_{2,0} \cdot u_3''(\alpha x) + \varphi_0''(x) + \frac{D_1}{D_2} \cdot f_0''(x) \right] \right\} \cdot \alpha_{2k} \cdot (1 - x^2)^{\frac{m+3}{2}} \cdot C_{2k-2}^{\frac{m}{2}+2}(x) dx, \qquad (50)$$

$$a_{2n,2k} = -\frac{l^4}{D_1 + D_2} \cdot \frac{D_2}{D_1} \cdot \int_{-1}^{1} \left\{ \phi_{1,2n} \cdot u_1''(\alpha x) + \phi_{2,2n} \cdot u_3''(\alpha x) + \right.$$

$$\left. + \varphi_{2n}''(x) + \frac{D_1}{D_2} \cdot f_{2n}''(x) \right] \right\} \cdot \alpha_{2k} \cdot (1 - x^2)^{\frac{m+3}{2}} \cdot C_{2k-2}^{\frac{m}{2}+2}(x) d. \qquad (51)$$

where

$$\alpha_{2k} = \frac{m \cdot (m+2)}{2k \cdot (2k-1)(2k+m)(2k+m+1)} \qquad (52)$$

Thus, the considered problem is reduced to the study of infinite systems of algebraic equations with infinite unknowns for the coefficients A_{2n}.

Infinite systems of algebraic equations (47) can be solved by the reduction method. Based on the infinity reduction method, systems are limited by the first r equations corresponding to the first r unknowns. These conditions exactly correspond to the restriction in series (35) by the first r terms with unknown coefficients A_i at $i = 0, 1, 2, \ldots, r$.

3.3. Substantiation of the solution method

It is known that the reduction method is applicable only for regular infinite systems of algebraic equations.

Therefore, to apply the reduction method, it is necessary to prove the regularity or quasi-regularity of the system of infinite equations. To prove the regularity of system (47), the coefficients a_{2k} and $a_{2n,2k}$ are determined by formulas (50) and (51).

Research is performed as follows.

First, we estimate the coefficient a_{2k}. To estimate it, we take into account the following inequalities [24]:

$$\left|\int_a^b f_1(x) \cdot f_2(x)dx\right| \leq \left\{\int_a^b f_1^2(x)dx\right\}^{1/2} \cdot \left\{\int_a^b f_2^2(x)dx\right\}^{1/2} \qquad (53)$$

$$(1-x^2)^\alpha \leq (1-x^2)^\beta, \quad \alpha \geq \beta, \quad -1 \leq x \leq 1 \qquad (54)$$

Expressions (53) are called Cauchy-Bunyakovsky inequality.

Applying inequalities (53), (54) in (50), we obtain the following estimate

$$\left|a_{2k}\right| \leq \alpha \cdot \alpha_{2k} \cdot \left\|C_{2k-2}^{m/2+2}\right\| \qquad (55)$$

where

$$\alpha = \frac{l^4}{D_1 + D_2} \cdot \left\{\int_{-1}^1 \left[q \cdot \left(2\overline{C}_2 + \frac{x^2}{2}\right) - A_0 \cdot \frac{D_2}{D_1} \cdot \left(\phi_{1,0} \cdot u_1''(\alpha x)+\right.\right.\right.$$

$$\left.\left.\left.+ \phi_{2,0} \cdot u_3''(\alpha x) + \varphi_0''(x) + \frac{D_1}{D_2} \cdot f_0''(x)\right)\right]^2 dx\right\}^{\frac{1}{2}},$$

Substituting (8) and (52) into (55), we can see that

$$\left|a_{2k}\right| < \infty, \text{ at } k = 1,2,3,... \qquad (56)$$

Next, it is necessary to analyze the following infinite numerical series, consisting of coefficients $a_{2n,2k}$:

$$\sum_{n=1}^{\infty} \left|a_{2n,2k}\right|, \quad k = 1,2,3,... \qquad (57)$$

If conditions (56) are met for the infinite system (47) and the numerical series (57) converges and has a sum less than one for any, then the infinite system (47) will be quasiregular

$$\lim_{k \to \infty} \sum_{n=1}^{\infty} \left|a_{2n,2k}\right| = 0 \qquad (58)$$

Based on these results, the numerical series (57) is investigated. For this, the common terms of series (57) defined by formula (51) are rewritten in the following form

$$\phi_{2n}''(x)\, a_{2n,2k} = \frac{l^4}{D_1 + D_2} \cdot \frac{D_2}{D_1} \cdot \alpha_{2k} \cdot \left(u_{1,2k} \cdot \phi_{1,2n} + u_{3,2k} \cdot \phi_{2,2n} + \varphi_{2n,2k} + f_{2n,2k}\right) \qquad (59)$$

where

$$u_{1,2k} = \int_{-1}^1 u_1''(\alpha x) \cdot (1-x^2)^{\frac{m+3}{2}} \cdot C_{2k-2}^{\frac{m}{2}+2}(x)dx\,; \qquad (60)$$

$$u_{3,2k} = \int_{-1}^1 u_3''(\alpha x) \cdot (1-x^2)^{\frac{m+3}{2}} \cdot C_{2k-2}^{\frac{m}{2}+2}(x)dx\,; \qquad (61)$$

$$\phi_{2n,2k} = \int_{-1}^{1} \phi''_{2n}(x) \cdot (1-x^2)^{\frac{m+3}{2}} \cdot C_{2k-2}^{\frac{m}{2}+2}(x)dx \; ; \tag{62}$$

$$f_{2n,2k} = \int_{-1}^{1} f''_{2n}(x) \cdot (1-x^2)^{\frac{m+3}{2}} \cdot C_{2k-2}^{\frac{m}{2}+2}(x)dx \, . \tag{63}$$

With (13), and considering the inequalities (53), (54) in (58) and (59), we can obtain the following estimates

$$\left| u_{1,2k} \right| \le a_1 \cdot \left\| C_{2k-2}^{m/2+2} \right\|; \quad \left| u_{3,2k} \right| \le a_3 \cdot \left\| C_{2k-2}^{m/2+2} \right\|^{1/2} \tag{64}$$

where

$$a_1 = \left\{ \int_{-1}^{1} 4\alpha^4 \cdot u_3^2(\alpha x)dx \right\}^{1/2} ; \qquad a_3 = \left\{ \int_{-1}^{1} 4\alpha^4 \cdot u_1^2(\alpha x)dx \right\} \tag{65}$$

Now it is necessary to estimate the coefficients $\phi_{1,2n}$ and $\phi_{2,2n}$, determined by formulas (45) and (46), respectively. Integration by parts the coefficients are reduced to the following form

$$\phi_{1,2n} = \frac{b^{-1}}{8\alpha^3} \cdot (-2\alpha^2) \cdot \alpha_{2n} \cdot \int_{0}^{1} \{ 2u_1(\alpha) \cdot u_3[\alpha(1-z)] +$$

$$+ u_4(\alpha) \cdot u_4[\alpha(1-z)] \} \cdot (1-z^2)^{\frac{m+3}{2}} \cdot C_{2n-2}^{\frac{m}{2}}(z)dz \, , \tag{66}$$

$$\phi_{2,2n} = \frac{b^{-1}}{8\alpha^3} \cdot 2\alpha b \cdot \alpha_{2n} \cdot C_{2n-2}^{\frac{m}{2}}(0) - \frac{b^{-1}}{8\alpha^3} \cdot 2\alpha^2 \cdot \alpha_{2n} \cdot \int_{0}^{1} \{ 2u_3(\alpha) \cdot u_3[\alpha(1-z)] -$$

$$- u_2(\alpha) \cdot u_4[\alpha(1-z)] \} \cdot (1-z^2)^{\frac{m+3}{2}} \cdot C_{2n-2}^{\frac{m}{2}}(z)dz \, . \tag{67}$$

Taking inequalities (53) and (54) in (66), (67), we can obtain the following estimates

$$\left| \phi_{1,2n} \right| \le \phi_1 \cdot \alpha_{2n} \cdot \left\| C_{2k-2}^{m/2+2} \right\|^{1/2}; \quad \left| \phi_{2,2n} \right| \le \phi_2 \cdot \alpha_{2n} \cdot \left\| C_{2k-2}^{m/2+2} \right\|^{1/2} \tag{68}$$

where

$$\phi_1 = \frac{b^{-1}}{4\alpha} \cdot \left\{ \int_{0}^{1} \left[2u_1(\alpha) \cdot u_3(\alpha x) + u_4(\alpha) \cdot u_4(\alpha x) \right]^2 dx \right\}^{1/2} \tag{69}$$

$$\phi_2 \le \frac{1}{4\alpha^2} + \frac{b^{-1}}{4\alpha} \cdot \left\{ \int_{0}^{1} \left[2u_3(\alpha) \cdot u_3(\alpha x) - u_2(\alpha) \cdot u_4(\alpha x) \right]^2 dx \right\}^{1/2} \tag{70}$$

It is necessary to estimate the coefficient $\phi_{2n,2k}$ determined by formula (62). To do this, first, the function $\phi''_{2n}(x)$ participating in the integral (62), with (41), and by integrating by parts, is reduced to the following form

$$\varphi''_{2n} = \alpha_{2n} \cdot \left[(1-x^2)^{\frac{m+3}{2}} \cdot C_{2n-2}^{\frac{m}{2}+2}(x) - u_1(\alpha x) \cdot C_{2n-2}^{\frac{m}{2}+2}(0) - 4\alpha^4 \cdot \varphi_{2n}(x) \right]. \tag{71}$$

Substituting (71) into (62), we obtain

$$\phi_{2n,2k} = \alpha_{2n} \cdot \left(J_{1,2n,2k} + J_{2,2n,2k} + J_{3,2n,2k} \right) \tag{72}$$

where

$$J_{1,2n,2k} = \int_{-1}^{1} (1-x^2)^{\frac{m+3}{2}} \cdot C_{2n-2}^{\frac{m}{2}+2}(x) \cdot (1-x^2)^{\frac{m+3}{2}} \cdot C_{2n-2}^{\frac{m}{2}+2}(x)dx;$$ (73)

$$J_{2,2n,2k} = C_{2n-2}^{\frac{m}{2}+2}(0) \cdot \int_{-1}^{1} u_1(\alpha x) \cdot (1-x^2)^{\frac{m+3}{2}} \cdot C_{2k-2}^{\frac{m}{2}+2}(x)dx;$$ (74)

$$J_{3,2n,2k} = -4\alpha^4 \int_{-1}^{1} \phi_{2n}(x) \cdot (1-x^2)^{\frac{m+3}{2}} \cdot C_{2k-2}^{\frac{m}{2}+2}(x)dx.$$ (75)

Applying (53), (54) in (73), (74), (75) we obtain the following estimates

$$\left|J_{1,2n,2k}\right| \le 4\alpha^3 \cdot \left\|C_{2n-2}^{m/2+2}\right\|^{1/2} \left\|C_{2k-2}^{m/2+2}\right\|^{1/2},$$ (76)

$$\left|J_{2,2n,2k}\right| \le \overline{a}_1 \cdot \left\|C_{2n-2}^{m/2+2}\right\|^{1/2} \left\|C_{2k-2}^{m/2+2}\right\|^{1/2},$$ (77)

$$\left|J_{3,2n,2k}\right| \le 8\alpha^4 \cdot \left|\varphi_{2n}(1)\right| \cdot \left\|C_{2k-2}^{m/2+2}\right\|$$ (78)

where

$$\varphi_{2n}(1) = \frac{1}{4\alpha^3} \cdot \int_0^1 u_4[\alpha(1-z)] \cdot (1-z^2)^{\frac{m+3}{2}} \cdot C_{2n-2}^{m/2+2}(z)dz$$ (79)

Applying (53), (54) in (79), we obtain

$$\left|\varphi_{2n}(1)\right| \le \frac{1}{4\alpha^3} \cdot \left\{\int_{-1}^{1} u_4^2[\alpha(1-z)]dz\right\}^{1/2} \cdot \left\|C_{2k-2}^{m/2+2}\right\|^{1/2}$$ (80)

Substituting (80) into (78), we obtain the following estimate

$$\left|J_{3,2n,2k}\right| \le a_4 \cdot \left\|C_{2n-2}^{m/2+2}\right\|^{1/2} \cdot \left\|C_{2k-2}^{m/2+2}\right\|^{1/2}$$ (81)

where

$$a_4 = 2\alpha \left\{\int_{-1}^{1} u_4^2(\alpha x)dx\right\}^{1/2}.$$ (82)

Taking into account (76), (77), (77) in (72), we obtain the following estimates

$$\left|\varphi_{2n,2k}\right| \le \alpha_{2n} \cdot \left(4\alpha^3 + \overline{a}_1 + a_4\right) \cdot \left\|C_{2n-2}^{m/2+2}\right\|^{1/2} \cdot \left\|C_{2k-2}^{m/2+2}\right\|^{1/2}.$$ (83)

Substituting (22) into (63), then applying (53), (54), we obtain the following estimates

$$\left|f_{2n,2k}\right| \le \alpha_{2n} \cdot \left\|C_{2n-2}^{m/2+2}\right\|^{1/2} \cdot \left\|C_{2k-2}^{m/2+2}\right\|^{1/2}.$$ (84)

From equality (59), taking into account (64), (68), (83), (84), we obtain

$$\left|a_{2n,2k}\right| \le a \cdot \alpha_{2n} \cdot \left\|C_{2n-2}^{m/2+2}\right\|^{1/2} \cdot \alpha_{2k} \cdot \left\|C_{2k-2}^{m/2+2}\right\|^{1/2}$$ (85)

where

$$a = \frac{l^4}{D_1 + D_2} \cdot \frac{D_2}{D_1} \cdot \left(\phi_1 \cdot a_1 + \phi_2 \cdot a_3 + \overline{a}_1 + a_4 + 1\right).$$ (86)

Introducing (85) into (57), we obtain

$$\sum_{n=1}^{\infty}\left|a_{2n,2k}\right| \le a \cdot \alpha_{2k} \cdot \left\|C_{2k-2}^{m/2+2}\right\|^{1/2} \cdot \sum_{n=1}^{\infty} \alpha_{2n} \cdot \left\|C_{2n-2}^{m/2+2}\right\|^{1/2}. \tag{87}$$

In this inequality, the numerical series

$$\sum_{n=1}^{\infty} \alpha_{2n} \cdot \left\|C_{2n-2}^{m/2+2}\right\|^{1/2} \tag{88}$$

is absolutely convergent. This can be verified by substituting (52) and (8) in (88). If we denote the sums of series (88) by $S,$ then inequality (88) takes the form

$$\sum_{n=1}^{\infty}\left|a_{2n,2k}\right| \le S \cdot a \cdot \alpha_{2k} \cdot \left\|C_{2k-2}^{m/2+2}\right\|^{1/2}, \quad k = 1,2,3,... \tag{89}$$

Taking into account (8), (10), it can be shown that

$$\lim_{k \to \infty} \alpha_{2k} \cdot \left\|C_{2k-2}^{m/2+2}\right\|^{1/2} = 0. \tag{90}$$

Equality (90) shows that

$$\sum_{n=1}^{\infty}\left|a_{2n,2k}\right| \to 0, \text{ at } k \to \infty. \tag{91}$$

The proved limit values (91) state that conditions (56) and (91) are satisfied in the problem under consideration. As follows from the fulfillment of these conditions, the infinite system of algebraic equations (47) is quasiregular. Due to the quasiregularity of the system of infinite algebraic equations (47), it is possible to apply the reduction method to its solution.

3.4. Problem

Let a two-layer beam slab lying on an elastic inhomogeneous foundation be loaded with uniformly distributed external loads with the following characteristics of the soil material of the base

$$q(x) = q = const.$$

We take the following mechanical and geometrical parameters of the base and slabs:

For soil of the base:

$$\nu_0 = 0.3, \quad E_0 = 5 \cdot 10^2 \text{ kg/cm}^2.$$

For slabs:

$$l = 5\,m, \quad h_1 = h_2 = 0.45\,m, \quad \nu_1 = \nu_2 = 0.617$$

$$E_1 = E_2 = 1.25 \cdot 10^5 \text{ kg/cm}^2.$$

First, we determine the numerical values by solving the system (47), corresponding to the specific values of the coefficient of inhomogeneity m of the base and the values of the coefficient of rigidity k of the fillers. Solving the system (47), it is possible to determine the deflections of the slabs and the base, and the internal forces of the slab and the pressure of the inhomogeneous base according to the known formulas.

When solving this problem, we restrict ourselves to the first four terms in series (35). Then the system of infinite equations (47) turns into a system of three equations with three unknown coefficients A_2, A_4, A_6. The coefficient A_0 is considered known and its value is calculated by formula (36).

The numerical values of the coefficients A_0, A_2, A_4, A_6 for different values of the filler rigidity coefficient k and the base inhomogeneity coefficient $m,$ are given in Table 1.

Results of solving algebraic equations corresponding to different values of the filler rigidity (k) and the coefficient of inhomogeneity of the base (m).

Table 1.   A table of solutions of a system of algebraic equations.

$k\left(kg/sm^3\right)$	m	A_0/q	A_2/q	A_4/q	A_6/q
0.25	0.25	0.675059	−0.145148	0.097165	−0.008346
0.25	0.50	0.599070	−0.127346	0.065661	0.005514
0.25	0.75	0.543265	−0.115487	0.044763	0.002671
2.5	0.25	0.675059	−0.145148	0.097165	−0,008316
2.5	0.50	0.599070	−0.127346	0.065661	0.005514
2.5	0.75	0.543265	−0.115487	0.044763	0,002671
250	0.25	0.675059	−0.145148	0.097163	−0.008346
250	0.50	0.599070	−0.127346	0.065661	0.005514
250	0.75	0.543265	−0.115487	0.044763	0.002671

Analysis of the results given in Table 1 shows that:

- the change in the values of the filler rigidity coefficents does not substantially affect the change in the solution of system (47), it also does not affect the change in the reactive pressure of the base, determined by formula (35);
- the change in the values of the inhomogeneity coefficients of elastic base substantially affects the change in the solution of system (47), i.e., the absolute values of the solution to system (47) decrease due to an increase in the base inhomogeneity, which leads to a decrease in the reactive pressure of the base;
- the calculations of the internal force factors of the strip-slab can be limited to the first 4 terms of the series (35).

The maximum numerical values of the bending moments of the first $M_1(x)$ and second slabs $M_2(x)$ at $x=0,$ are given in Table 2.

The results of the maximum values of bending moments of the slabs corresponding to the values of the filler rigidity coefficient (k) and the base inhomogeneity coefficient (m).

Table 2. Table of values of bending moments of plates.

$k\left(kg/sm^3\right)$	m	The greatest value of bending moments of slabs, at $x=0$	
		$M_1(x)/(ql^2)$	$M_2(x)/(ql^2)$
	0.25	1.084615	1.067307
0.25	0.50	1.039137	1.031462
	0.75	0.994724	0.992371
	0.25	1.039906	1.036302
2.5	0.50	0.974743	0.974401
	0.75	0.922241	0.922186
	0.25	0.923714	0.923609
25	0.50	0.799507	0.798897
	0.75	0.699268	0.699260

Analysis of the results given in Table 2 shows that:

- an increase in the value of the filler rigidity coefficient (at a constant value of the base inhomogeneity), leads to a substantial decrease in the value of bending moments;
- with an increase in the values of the coefficients of inhomogeneity of the base (with a constant value of the filler coefficient), the values of bending moments are substantially reduced;

- with an increase in the values of the filler rigidity coefficient and the values of the coefficients of inhomogeneity of the base, the values of bending moments substantially decrease (down to 36 %);
- with an increase in the values of the filler rigidity coefficient, the values of the bending moments of the slabs approach each other.

The results obtained show the effectiveness of the technique in determining the internal force factors in multilayer slabs.

The results obtained show the effectiveness of the proposed model and the developed technique for solving contact problems on the interaction of multilayer slabs with elastic inhomogeneous bases.

It should be noted that the results obtained, when the coefficient of inhomogeneity (m) of the base tends to zero, are similar to the results obtained in [10] for a homogeneous base.

4. Conclusion

1. A mathematical model was developed to assess the internal force factors of multilayer strip-slabs on an elastic inhomogeneous base under various static loads.

2. To assess the internal force factors of multilayer strip-slabs interacting with an inhomogeneous base, an analytical method for solving the problem was proposed, based on the approximation of orthogonal polynomials.

3. A theoretically substantiated possibility of using the proposed method for solving contact problems on the interaction of multilayer slabs with elastic inhomogeneous bases is given.

4. The required number of terms of the Gegenbauer polynomial was established to obtain a result with satisfactory accuracy, and the efficiency of the method for solving the problem was shown by the example of solving test problems.

5. Analysis of the results obtained made it possible to establish that:

- an account of the rigidity characteristics of the filler leads to a redistribution of internal forces in the slabs;
- an account of the inhomogeneity of the base leads to a decrease in internal forces in the slabs;
- an account of the inhomogeneity of the base leads to a redistribution of the reactive pressures of the base.

References

1. Aleksandrov, V.M., Chebakov, M.I. Analiticheskiye metody v kontaktnykh zadachakh teorii uprugosti [Analytical methods in contact problems of elasticity theory]. Moscow: Fizmatlit, 2004. 304 p. (rus)

2. Butenko, Yu.I. Metod vozmushcheniy pri integrirovanii uravneniy izgiba mnogosloynykh konstruktsiy [Perturbation method in integrating the equations of bending of multilayer structures]. Izv. VUZ. Aviatsionnaya Tekhnika. 2002. No. 2. Pp. 3–6. (rus)

3. Starovoytov, E.I., Yarovaya, A.V., Leonenko, D.V. Deformirovaniye trekhsloynykh elementov konstruktsiy na uprugom osnovanii [Deformation of three-layer structural elements on an elastic foundation]. Moscow: Fizmatlit, 2006. 378 p. (rus)

4. Popov, G.Ya. Kontsentratsiya uprugikh napryazheniy vozle shtampov razrezov tonkikh vklyucheniy i podkrepleniy [Concentration of elastic stresses near stamps of sections of thin inclusions and reinforcements]. Moscow: Nauka, 1982. 342 p. (rus)

5. Shirinkulov, T.Sh., Zaretskiy, Yu.K. Polzuchest i konsolidatsiya gruntov [Creep and soil consolidation]. Tashkent: Fan, 1986. 392 p. (rus)

6. Barmekova, E.V. Strength analysis of variable rigidity slabs on elastic support with variable subgrade ratio. Vestnik Tomskogo gosudarstvennogo arkhitekturno-stroitel'nogo universiteta. Journal of Construction and Architecture. 2019. No. 1. Pp. 201–208. (rus)

7. Awrejcewicz, J., Krysko, V.A., Zhigalov, M.V. et al. Contact interaction of two rectangular plates made from different materials with an account of physical nonlinearity. Nonlinear Dynamics. 2018. No. 91. Pp. 1191–1211. DOI: 10.1007/s11071-017-3939-6

8. Krenev, L.I., Aizikovich, S.M., Tokovyy, Y.V., Wang, Y.-Ch. Axisymmetric problem on the indentation of a hot circular punch into an arbitrarily nonhomogeneous half-space. International Journal of Solids and Structures. 2015. Vol. 59. Pp. 18–28. DOI: 10.1016/j.ijsolstr.2014.12.017

9. Zhong, Q.Y. Elastic field for eccentrically loaded rigid plate on multilayered solids. International Journal of Solids and Structures. 1996. 33 (27). Pp. 4019–4049. DOI: 10.1016/0020-7683(95)00228-6

10. Mirsaidov, M., Mamasoliev, Q. Contact problems of multilayer slabs interaction on an elastic foundation. IOP Conference Series: Earth and Environmental Science. 2020. 614. Pp. 12089. DOI: 10.1088/1755-1315/614/1/012089

11. Younesian, D., Hosseinkhani, A., Askari, H., Esmailzadeh, E. Elastic and viscoelastic foundations: a review on linear and nonlinear vibration modeling and applications. Nonlinear Dynamics. 2019. 97 (1). Pp. 853–895. DOI: 10.1007/s11071-019-04977-9

12. Tokovyy, Y., Ma, C. Elastic Analysis of Inhomogeneous Solids: History and Development in Brief. Journal of Mechanics. 2019. 35(5). Pp. 613–626. DOI: 10.1017/jmech.2018.57

13. Takekawa, J., Mikada, H. An absorbing boundary condition for acoustic-wave propagation using a mesh-free method. GEOPHYSICS. 2016. 81 (4). Pp. T145–T154. DOI: 10.1190/geo2015-0315.1

14. Mandal, A., Maity, D. Finite Element Analysis of Dam-Foundation Coupled System Considering Cone-Type Local Non-Reflecting Boundary Condition. Journal of Earthquake Engineering. 2016. 20 (3). Pp. 428–446. DOI: 10.1080/13632469.20-15.1085464

15. Mirsaidov, M.M., Sultanov, T.Z., Rumi, D.F. An assessment of dynamic behavior of the system "structure – foundation" with account of wave removal of energy. Magazine of Civil Engineering. 2013. 39 (4). Pp. 94–105. (rus). DOI: 10.5862/MCE.39.10

16. Usarov, M., Salokhiddinov, A., Usarov, D.M., Khazratkulov, I., Dremova, N. To the theory of bending and oscillations of three-layered plates with a compressible filler. IOP Conference Series: Materials Science and Engineering. 2020. 869. Pp. 52037. DOI: 10.1088/1757-899x/869/5/052037

17. Usarov, M., Ayubov, G., Mamatisaev, G., Normuminov, B. Building oscillations based on a plate model. IOP Conference Series: Materials Science and Engineering. 2020. 883. Pp. 12211. DOI: 10.1088/1757-899x/883/1/012211

18. Sultanov, K.S. The attenuation of longitudinal waves in non-linear viscoelastic media. Journal of Applied Mathematics and Mechanics. 2002. 66 (1). Pp.115–122. DOI: 10.1016/S0021-8928(02)00015-1

19. Sultanov, K.S., Kumakov, J.X., Loginov, P.V., Rikhsieva, B.B. Strength of underground pipelines under seismic effects. Magazine of Civil Engineering. 2020. 93 (1). Pp. 97–120. DOI: 10.18720/MCE.93.9

20. Bakhodirov, A.A., Ismailova, S.I., Sultanov, K.S. Dynamic deformation of the contact layer when there is shear interaction between a body and the soil. Journal of Applied Mathematics and Mechanics. 2015. 79 (6). Pp. 587–595.
DOI: 10.1016/j.jappmathmech.2016.04.005

21. Mirsaidov, M. An account of the foundation in assessment of earth structure dynamics. E3S Web Conf. 2019. 97. Pp. 04015. DOI: 10.1051/e3sconf/20199704015

22. Mirsaidov, M.M., Toshmatov, E.S. Spatial stress state and dynamic characteristics of earth dams. Magazine of Civil Engineering. 2019. 89 (5). Pp. 3–15. DOI: 10.18720/MCE.89.1

23. Mirsaidov, M., Sultanov, T., Yarashov, J., Toshmatov, E. Assessment of dynamic behaviour of earth dams taking into account large strains. E3S Web Conf. 2019. 97. Pp. 05019. DOI: 10.1051/e3sconf/20199705019

24. Suetin, P.K. Klassicheskiye ortogonalnyye mnogochleny [Classical orthogonal polynomials]. Moscow: Fizmatlit, 2007. 480 p. (rus)

25. Abramowitz, M., Stegun, I.A. Handbook of Mathematical Functions with Formulas, Graphs, and Mathematical Tables. New York: Dover Publications, 1965. 1076 p.

Information about authors:

Mirziyod Mirsaidov, *Doctor of Technical Science*
ORCID: https://orcid.org/0000-0002-8907-7869
E-mail: theormir@mail.ru

Kazokboy Mamasoliev, *PhD in Physical and Mathematical Sciences*
ORCID: https://orcid.org/0000-0002-8853-8774
E-mail: q-mamasoliev@mail.ru

Resilient modulus model of asphalt mixture using steel slag

R.T. Bethary[1] ✉ 🆔 **, B.S. Subagio[2]**

[1] Sultan Ageng Tirtayasa University, province Banten, Indonesia

[2] Bandung Institute of Technology, Bandung, Indonesia

✉ rindutwidibethary @gmail.com

Abstract. The use of waste materials from road scrapping, called reclaimed asphalt pavement (RAP) and steel slag aggregates becomes more and more popular in road maintenance and road reconstruction. Those materials can replace and reduce the amount of virgin materials needed in the mixing process. In this research, the optimum bitumen content (OBC) of Marshall specimens has to be determined firstly, before the samples for resilient modulus test were prepared. The UMATTA equipment was used to determine the resilient modulus of each sample, which consist of: original mixture i.e., without slag and RAP materials, and the mixture with RAP and slag. The results showed that the mixture with RAP and slag materials has the higher resilient modulus, compared to the original mixture, and the most impactful parameters for the results are bitumen modulus, percentage of RAP materials, slag materials and void in mixture.

1. Introduction

In recent decades, the repair and reuse of waste materials from industrial activities and the construction sector have become very important to reduce the use of raw materials for road construction. For example, the use of Reclaimed Asphalt Pavement (RAP) plays an important role, because in addition to providing economic benefits, the environmental impact is also reduced [1–2]. Similarly, slag materials can also overcome the limited availability of rocks. The RAP material is obtained when the asphalt layer is removed for reconstruction, restoration of the surface layer and pavement removal due to utility installation, whereas the slag is a residue from the steel-making process. In the pavement rehabilitation, those materials were used in hot mix conditions and refer to the Indonesian specifications. Accordingly, the use of RAP [3] or slag materials [4–6] in hot-mix condition have given a good result compared to the conventional asphalt mixture.

Several studies show that the addition of RAP in the asphalt mixture indicates the changes in the physical behaviour of the mixture that affects its durability and structural performance [3, 7–8]. The use of 40–60 % RAP in hot mix asphalt can increase its Stiffness and Indirect Tensile Strength (ITS) value, and can produce the pavement which is resistant to rutting but prone to cracking and fatigue. It gives also a generally higher variability of hot-mix asphalt mixtures using RAP materials [3, 8]. Based on some study, the EAF slag on Stone Mastic Asphalt (SMA) mixture can increase its Stability value and its Marshall Quotient, which are indicators of high stiffness, resistance to permanent deformation, and higher durability [9–10]. The EAF slag also give better mechanical properties compared to the natural aggregates, considering that it is recommended as a reliable road material [11–13]. Meanwhile, another study shows a

decreasing value of the Marshall Stability [14]. This inconsistency can be attributed to the different test temperatures, size and percentage of slag [15].

The RAP material has significantly aged, which causing a reduction in the bonding between the aggregate and asphalt. The use of slag as an aggregate is expected to reduce the occurrence of this, due to the characteristic of slag material which has a high bonding with asphalt [16]. Based on a study of the resistance of asphalt mixture to fatigue, which using a combination of RAP and slag, the result shows that the asphalt mixture can increase its fatigue life and the damage is insignificant, in a mixture that containing RAP and slag than the control mixture [17]. Other results showed, that the asphalt mixture using slag and RAP without any rejuvenating material, can improve the overall performance of the mixture, compared to the control mixture [15]. The steel slag is more effective in improving the performance of asphalt mixtures, because one of the properties of steel slag is having the capacity to store heat, which causes higher energy consumption during the production of Hot Mix Asphalt (HMA), compared to the natural aggregate. Alternatively, the transportation of slag with RAP requires a longer time, starting from the production site to the layering site [18]. The time needed to increase the traffic, after completing the construction until it can be used, is around 5 to 10 minutes.

One important parameter in pavement design is the Stiffness Modulus, which represents the behaviour of mechanical properties that making possible to analyse structures with stress and strain distribution under wheel loads. Stiffness Modulus is a fundamental mechanical parameter that expresses synthetically the structural properties of asphalt mixtures, determined through non-destructive tests (NDT), and it is very useful for conducting statistical evaluations of the effects of one or more components in the mechanical response of a mixture [19]. Stiffness Modulus test on asphalt mixture is carried out by the Universal Material Testing Apparatus (UMATTA) test, where the main factors that need to be considered in the Stiffness Modulus testing are temperature and load frequency [20].

In general, the aims of this research are to determine the optimum performance and Stiffness Modulus of asphalt mixtures using RAP and Slag materials, with the target results are its Stiffness Modulus value that is greater than the original hot-mix asphalt mixture, which using the bitumen penetration (Pen) 60 / 70 and natural aggregates.

2. Experimental Methods

2.1. Materials

There are three aggregate materials used in this study: natural aggregate, RAP and steel slag. The natural aggregates were obtained from crushed stones from PT KADI International located in Klari, Karawang, Indonesia. While the RAP aggregate was from raking the National Road in Karawang, Indonesia. There are two types of steel slag that are commonly used in asphalt mixtures. The first one is Basic Oxygen Furnace (BOF), a steel-making process using converted furnace, and the second one is Electric Arc Furnace (EAF), a steel-melting process with electric arc [21]. In this study, the EAF slag type was used as a steel waste from steel-melting process. The tests result of physical and mechanical properties of the aggregates can be seen in Table 1.

Table 1. Physical and mechanical properties of aggregates and steel slag.

Test Type	Natural Aggregate	RAP Aggregate	Steel Slag
Coarse Aggregate Specific Gravity	2.642	2.496	3.488
Fine Aggregate Specific Gravity	2.614	2.442	3.086
with LA Machine	21.17	32.30	13.01
Sand Equivalent Value	76.35%	*	88.62%

Note: *) no measurement

The reference gradation used was the Asphalt Concrete – Binder Course (AC-BC) gradation which refers to the Indonesian General Specifications of Roads and Bridges [22], Meanwhile, the RAP aggregate gradation was laid within the upper and lower limits of the reference gradation. The determination of the slag aggregate gradation was the same as the reference aggregate gradation, because all filter sizes were available for slag aggregate. This curve can be seen in Fig. 1.
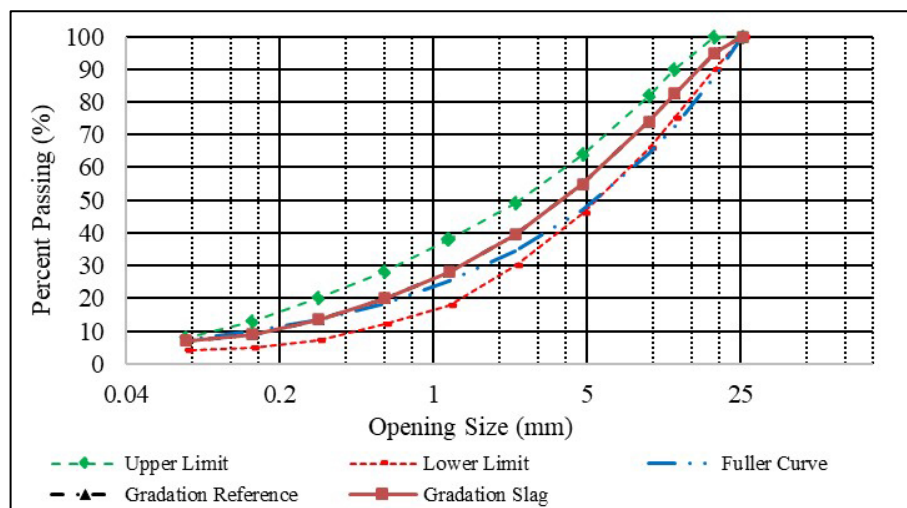
Figure. 1. Aggregate gradation of AC-BC mixture with RAP and slag.

The asphalt material used in this study was the oil asphalt Pen 60/70 produced by PT. Pertamina. Regarding the mixtures that using Pen 60/70, the results are more durable than that using the Pen 80/100 and RAP asphalt which obtained from extraction test using an evaporator with Tricholore Ethylene (TCE) fluid [25]. In order to make the characteristics of RAP asphalt close to control asphalt Penetration grade 60/70, a rejuvenating agent, namely Reclamite® of 23 %, was used to be mixed with the RAP asphalt [23–24]. The test results can be seen in Table 2.

Table 2. Asphalt and RAP asphalt characteristics.

Test	Pen60/70	RAP	RAP-Reclamite
Asphalt Level	–	5.15	–
Penetration	64.7	10	62.04
Softening Point	51	80	53
Ductility	100	38	100

a. Fine slag aggregate

b. Coarse slag aggregate
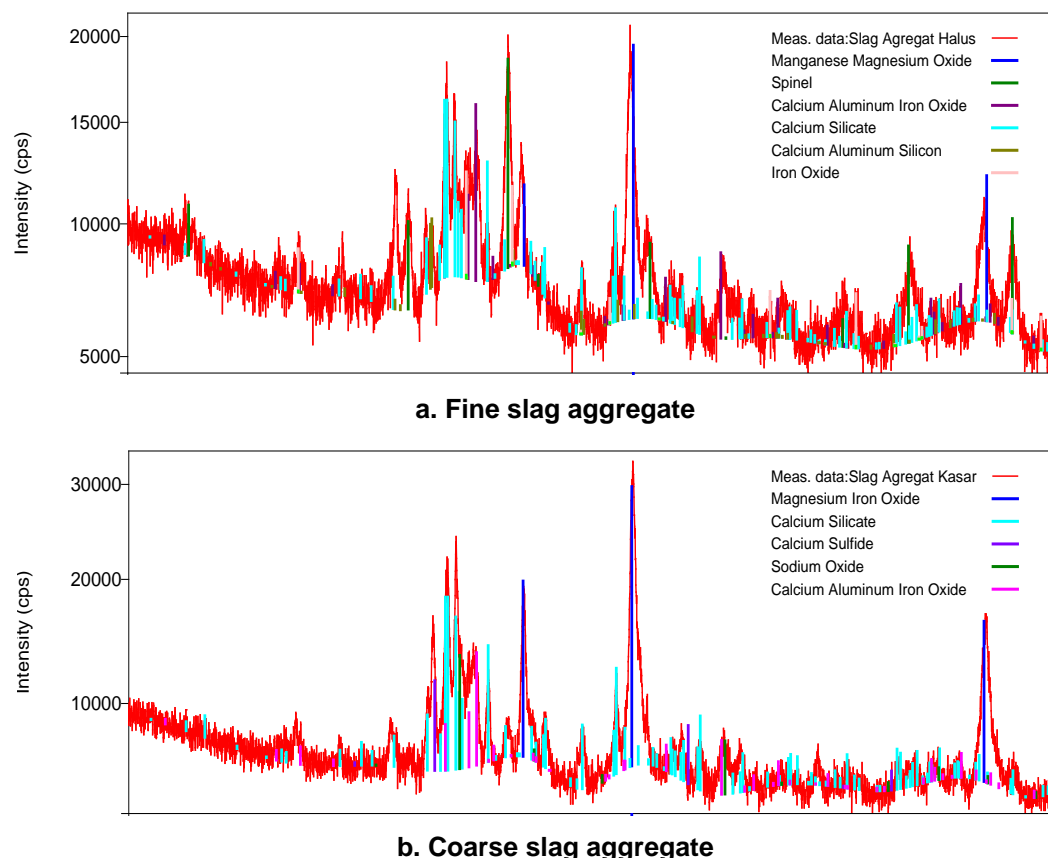
Figure 2. XRD spectrum test results for fine and coarse slag aggregates.

Slag material has a mineral and chemical composition characteristic that are different from other materials, so it needs to be tested by the X-ray fluorescence spectrometry (XRF) and X-ray diffraction (XRD). The working principle of this XRD is to use X-ray fraction scattered by the angle of the crystal being tested, so that the pattern that appears in the XRD pattern, represents a plane of crystal that has a certain orientation. The test results of XRD for fine and coarse aggregates can be seen in Fig. 2.

Based on the XRD test results it can be seen that for fine slag aggregate there are 4 dominant crystals, namely Manganese Magnesium Oxide (MGOMnO), Calcium Aluminium Iron Oxide (Ca2Fe140Al060O5), Calcium Silicate (Ca2SiO4), and Calcium Aluminium Silicon (Ca3Al2Si2), and for the coarse slag aggregate there are 3 dominant crystals: Calcium Silicate (Ca2SiO4), Sodium Oxide (NaO2) and Calcium Aluminum Iron Oxide (Ca2Fe140Al060O5). The Ca or Si ratio contained in fine and coarse slag aggregates is an indication of substantially alkaline, where this property affects the adhesion properties of slag aggregates in asphalt mixtures [25].

Meanwhile, the XRF is based on the identification and enumeration of X-ray characteristics that occur due to the photoelectric effect that can be analysed for the element content in slag material. The results can be seen in Table 3.

Table 3. Chemical composition of slag aggregate based on XRF test.

Slag Aggregate	Oxide Content (%)															
	Mg	Al	Si	P	S	Cl	K	Ca	Ti	MN	Fe	Sr	Zr	Na	V	Cr
Coarse	2.7	5.2	9.3	0.3	0.08	0.02	0.1	35.2	0.95	2.34	43.6	0.1	0.01			
Fine	3.0	5.8	7.7	0.3	0.1	0.02	0.1	30.8	0.8	2.9	47.3	0.1	0.1	0.08	0.6	0.3

Based on the Table 3, for fine slag aggregates and coarse slag aggregates, the most important elements are Fe, Ca, Si and Al. The content of aluminium oxide together with other metal elements in the slag result in a resistance to abrasion, while the Na element has a small percentage in the coarse slag aggregate (<12 %). So according to ASTM D5106-15, it is still permissible to use it in the asphalt mixtures up to 100 % use.

2.2. Morphology Characteristic

The Scanning Electron Microscope (SEM) is an equipment to evaluate and to compare the surface characteristics of the material, its pore dimensions and its crystal structure of natural slags and aggregates [26]. The SEM test was carried out with ± 0.5 cm test specimen, and then it was enlarged up to 6000 times. This result can be seen in Fig. 3.
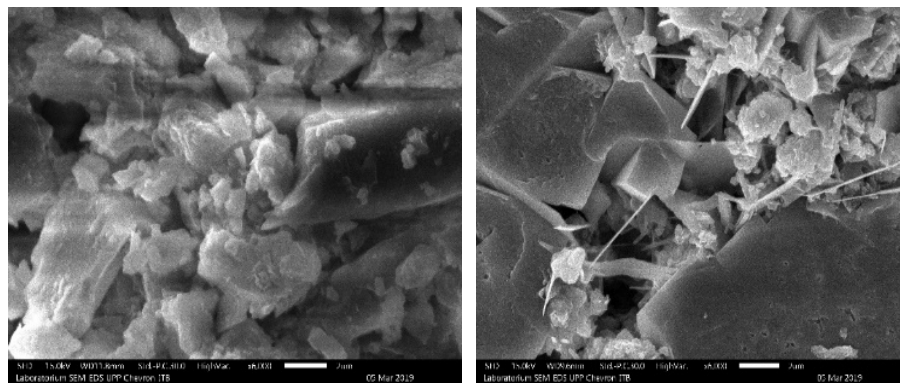
a. Natural Aggregate   **b. Slag Aggregate**

Figure. 3. Morphology of aggregate characteristics.

2.3. Asphalt Rheology

Mechanical asphalt rheology test (G^* and δ) was carried out using a DSR tool referring to AASHTO T315 with a test frequency of 10 rad/s and test temperature referring to the temperature range contained in the PG AASHTO M320 asphalt specification table. This test was carried out on three asphalt conditions: original, RTFOT and PAVT [24]. Based on these conditions, the asphalt stiffness modulus was obtained using the following formula:

$$S_{bit} = 2(1+\mu)\cdot G^*, \tag{1}$$

where S_{bit} is asphalt stiffness modulus, μ is Poisson ratio and G^* is complex shear modulus.

The DSR temperature sweep test is usually conducted to verify the grade of asphalt in the PG system, related to the mechanical behaviour of asphalt, the SUPERPAVE sets limits on the amount of G^* and δ on the flow parameters and the fatigue crack parameters, which are listed in Table 4.

Table 4. Performance grade of asphalt pen 60/70, RAP asphalt and RAP asphalt with reclamite.

Condition	SUPERPAVE Criteria	Test Result °C		
		Asphalt Pen 60/70	RAP Asphalt	RAP Asphalt (Reclamite)
Original Binder	Rutting	65.3	110.7	68.7
RTFOT	Rutting	63.6	120.2	68.9
PAVT	Fatigue	23.7	52.8	25.4

Based on Table 4, the performance grade can be determined based on the value of G^*/sin δ under the original conditions. The PG value is 64 for asphalt Pen 60/70, the PG value for RAP asphalt is 106, while the PG value for the RAP asphalt added with Reclamite rejuvenating materials is 64. The change in PG value on RAP asphalt with the addition of rejuvenating material shows a decrease in PG value, resulting in the same PG value with that of asphalt Pen 60/70. This indicates that there has been a good rejuvenation process in the RAP asphalt mixed with Reclamite.

2.4. Mixture Design

The resilient modulus test in the laboratory was carried out by the Indirect Tensile Modulus test, using the UMATTA equipment and referring to ASTM (1997) D4123-82, with a loading pulse width of 250 ms, and pulse repetition period of 3000 ms. It was carried out on the temperature variations with respect to fluctuations in temperature at the pavement, which were 35 °C and 45 °C. This type of test was a test that cannot damage the test specimen, because the load given was relatively small and it used a cylindrical specimens of the same size as the Marshall test specimen. The test specimens were loaded with a haversine or triangular pattern on its vertical diametrical plane through a loading bar.

The mixture design method uses Marshall method that referring to ASTM D6927 in order to obtain the value of Optimum Asphalt Content (OAC) that could be used for subsequent Resilient Modulus tests. The further discussion on the determination of OAC can be seen in another paper [27].
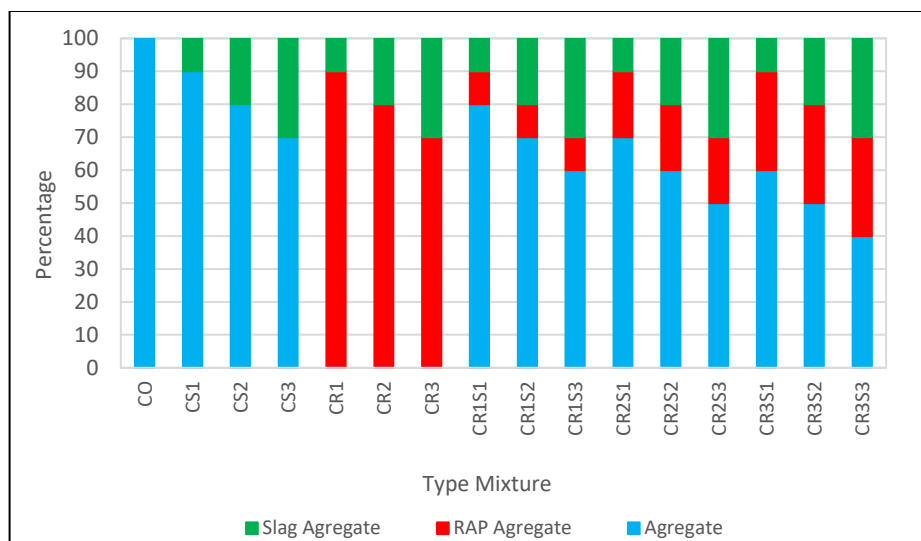

Figure. 4. The Combinations of Mixture Types.

This research used 16 combinations of mixture, in which there were variations of the percentage of slag and RAP materials. All variations can be seen in Fig. 4, with one mixture as a control mixture that using a natural aggregate and asphalt Pen 60/70 as a basic material.

3. Results and Discussion

3.1. Asphalt Stiffness Modulus

The value of asphalt stiffness modulus based on the results of the laboratory test using the DSR equipment, derived from the complex modulus $\left(G^* \right)$ value by using the equations (1), can be seen in Fig. 5.
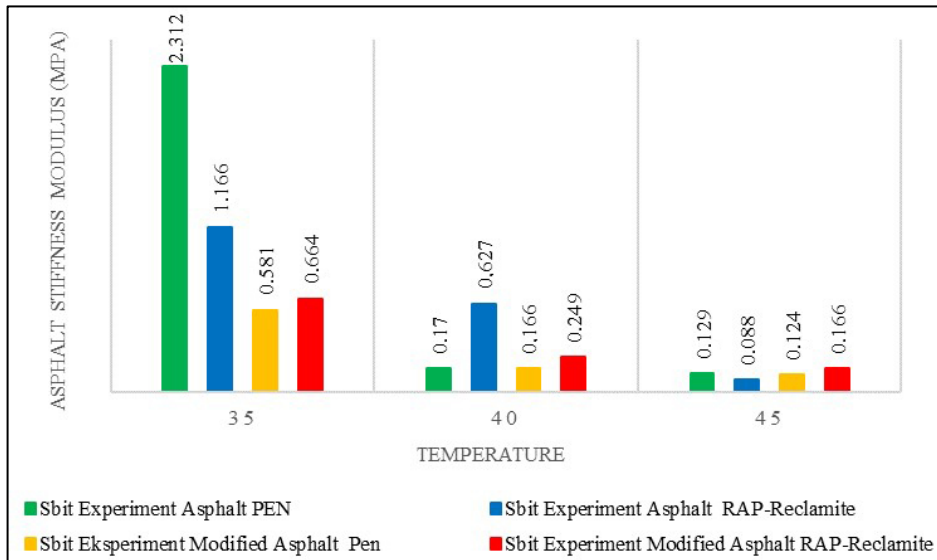

Figure. 5. Asphalt stiffness modulus.

Based on Fig. 5, the asphalt stiffness modulus value resulted from the DSR test, for asphalt penetration grade 60/70, is higher than that of RAP asphalt with Reclamite-added. Basically, this is due to the characteristics of the rejuvenating material that could make the condition of RAP asphalt returns into an original asphalt that is more "fresh" and liquid. The experimental testing makes it possible to use modified asphalt, where a calibration factor was needed. By using the statistical calculations, a calibration factor of 0.83 was obtained to apply the modified experimental Asphalt Stiffness Modulus.

3.2. Mixture Stiffness Modulus

Resilient modulus test of asphalt mixtures was carried out at 35 °C and 45 °C, based on an acceptable mean annual pavement temperature (MAPT) of 41 °C for the Indonesian climate. This test was carried out with the highest temperature, which was 45 °C, because at that temperature the asphalt has behaved like a viscous liquid with a little ability to return to normal condition. An increase in the test temperature affects the value of resilient modulus, where the higher the temperature the lower the modulus value. This is because at high temperatures, the asphalt will become a viscous material.

Based on Fig. 6, it can be seen that the asphalt mixture using RAP materials (CR1, CR2 and CR3) gives the largest modulus value while for the basic mixture, without slag and RAP (C0), the modulus value is the smallest. The aging process that occurs in the mixture can increase the modulus value of the mixture. This is shown in the mixture with RAP material, namely CR1, CR2 and CR3 mixtures. This is because the mixture contains aging RAP material was stiff, resulting in a higher modulus value. This phenomenon can be correlated to the increasing percentage of RAP in the mixture, with the higher asphalt aging rate, will increase the modulus value of the mixture at either 35 °C or 45 °C. The volumetric value will also affects the resilient modulus, where the void in mixture (VIM) value of CR3 mix is higher than that of CR1 mix, so that the increasing value of VIM will increase also the modulus value in the mixture.

	C0	CS1	CS2	CS3	CR1	CR2	CR3	CR1S1	CR1S2	CR1S3	CR2S1	CR2S2	CR2S3	CR3S1	CR3S2	CR3S3
■Temp 35	682.5	697.5	1057.5	843	738.5	1027.5	1231	729.5	775	781.5	838	901.5	852.5	1081.5	778	857.5
■Temp 45	284	293.5	294	293.5	275.5	363	452.5	261	289.5	316.5	357	289.5	274	364.5	329.5	341.5
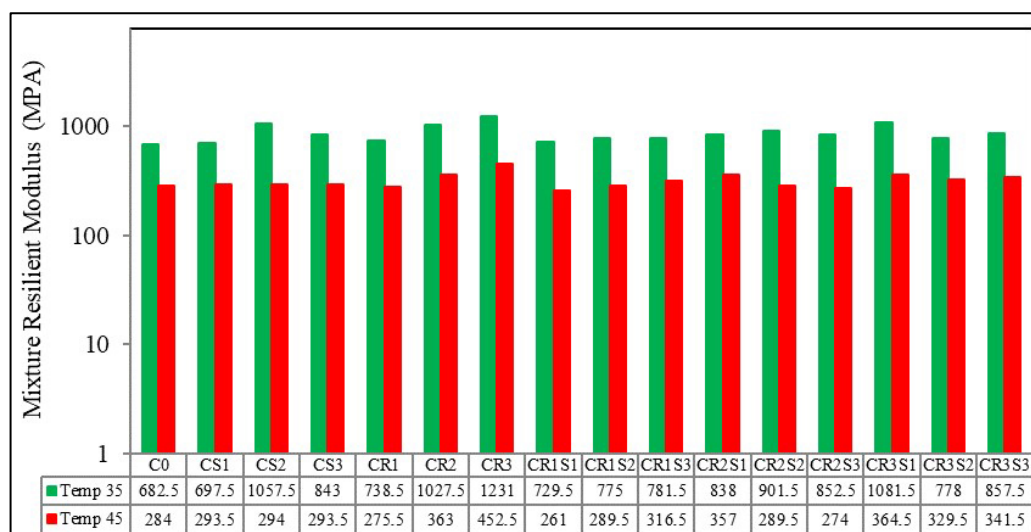
Figure. 6. Mixture Resilient Modulus.

The comparison of mixtures using slag (CS1, CS2, and CS3) shows that the increase in the percentage of slag will increase the resilient modulus value when it is related to the volumetric condition where the VIM value is greater on CR3 so the void mineral agregrate (VMA) CR3 value is smaller than the VMA CR1 so that the value increases VIM and reduced VMA values cause an increase in resilient modulus. This is also related to the surface roughness of the slag aggregate so that it gives a larger resilient modulus value. The results for the combination of slag mixtures with the addition of RAP (CR1S1, CR1S2, CR1S3, CR2S1, CR2S2, CR2S3, CR3S1, CR3S2, and CR3S3) showed an increase in the resilient modulus value seen from the higher VIM volumetric with the increase in the percentage of RAP in the mixture.

Value was found in the 30 % RAP mixture (CR3). This might be due to the asphalt contained in the RAP material had undergone aging at 35 °C and 45 °C test temperatures, compared to other mixtures, causing a greater mixture stiffness value. Increased stiffness was also seen when slag and RAP was combined. The results are greater when compared to the control mixture (C0). The optimum resilient modulus in the mixture of slag and RAP was in the mixture of RAP30Slag10 (CR3S1), this is shown when the percentage of RAP30 with the addition of slag indicates a smaller modulus value. In contrast, the smaller percentage of RAP with increasing slag causes a greater resilient modulus value. This is due to the high volumetric characteristics of the void in mix (VIM) with an increase in percentage of slag in the mixture.

### 3.3. Sensitivity of Resilient Modulus to Temperature Changes

Resilient modulus is very dependent on temperature, so it is necessary to analyse how the temperature sensitivity of Moduli at high temperatures (35 °C and 45 °C), where the asphalt characteristic are in viscous or visco-elastic conditions, as shown in Fig. 7 below.

a. RAP mixture

b. Slag mixture

c. Combination of RAP and slag
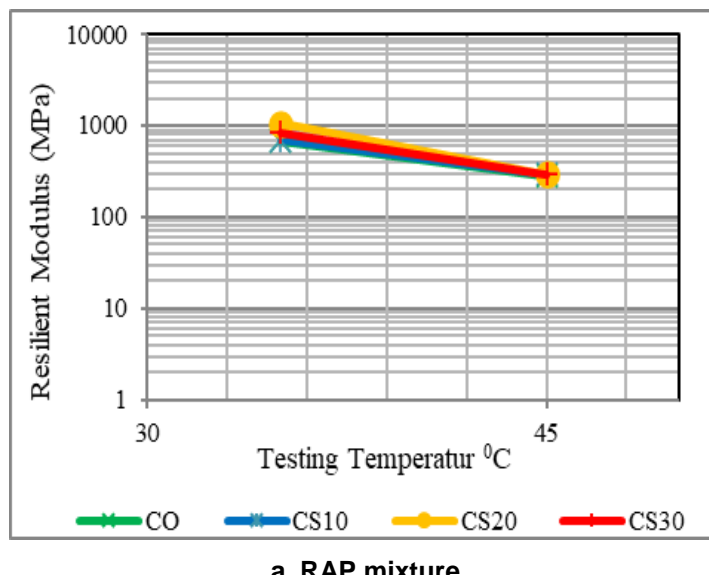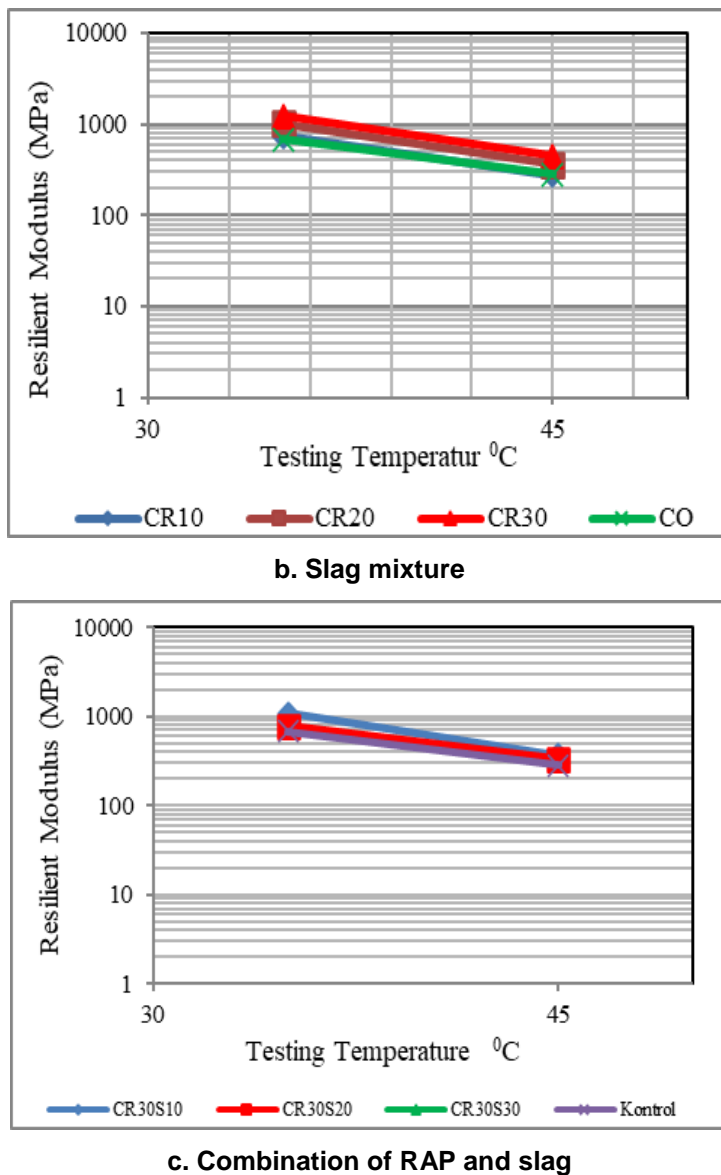
Figure 7. Temperature sensitivity of resilient modulus.

Based on Fig. 7a, at high temperatures (35 °C to 45 °C) and the increase in RAP percentage, it is shown that the line of the asphalt mixture using RAP is getting steep but almost coincide at one point. This presents that an increase in the RAP percentage at high temperatures tends to be insensitive to temperature changes. Meanwhile on Fig. 7b, the Modulus test with slag aggregate at same temperature of 35 °C to 45 °C, the increase in slag percentage shows a steeper slope, means the increasing sensitivity to temperature changes, compared to the control mixture without slag, where less sensitive to changes in temperature.

For overall combination in Fig. 7c, it can be seen that the addition of RAP in the slag mixture can reduce the sensitivity to temperature changes, especially at high-temperature conditions (35 °C – 45 °C). This condition can overcome the weakness of the slag aggregate which is sensitive to temperature changes. On the other hand, adversely the presence of RAP can increase the Stiffness Modulus using slag only.

3.4. Model of Mixture Resilient Modulus

The model of resilient modulus was developed based on tests conducted in the laboratory, under viscous conditions. The proposed regression models require another tests to determine whether the independent variables have an influence to the dependent variables. In this case, the classic assumption test was used cooperated with another several tests, such as multi-collinearity test, heteroscedasticity test, normality test, auto-correlation test and linearity test [28–30].

In this research, the proposed prediction model selected was a multi-linier regression model, composed with several models including some dependent variables and a combination of some

independent variables, such as model of the Nottingham University [31] and the Shell Model [32]. Table 6 presents the results of the model in viscous conditions for mixtures using RAP and slag, where the dependent variable is the Resilient Modulus of mixed (S_{mix}) and the independent variables are the Modulus of asphalt (S_{bit}), the void in mixture (VIM), and the percentage of RAP and slag materials.

Table 5. Analysis prediction resilient modulus model.

Test	Variable	Coefficient	DF	F	t	sig
Resilient modulus (Smix)	Constant	−112.603			−1.066	0.291
	S_{bit}	1140.587			16.320	0.000
	RAP	0.798	4	69.336	0.523	0.603
	Slag	0.555			0.347	0.729
	VIM	65.286			2.646	0.010
	R Square	0.825	R-Sq(adj)	0.813		

Based on the VIM Model, the value of R^2 is 0.825. This value is closed to 1.00, meaning that the independent variables provide almost all the requirement needed to predict the dependent variables. Based on the results of "one-way analysis of variance" (ANOVA), include with the F-test with a confidence level of 95 % (α = 0.05), it is obtained that the F-statistic value is greater than the F-value representing the relationship between independent variables. This is consistent with a p-value less than 0.05, which means that the resulted model is significant, and all regression coefficients significantly affect the Resilient Modulus of the mixture.

The VIM Model shows also that the dependent variable has a positive effect on Resilient Modulus. With the increasing value of Asphalt Modulus and the percentage of RAP, the Mixture Modulus becomes higher. This phenomenon can be related to aging process that occurs inside the asphalt of RAP. Meanwhile, the increase in percentage of slag contributes to an increase in the Resilient Modulus of mixture. This is due to the rough characteristic of the slag surface. Moreover, the selected model of Resilient Modulus needs to be validated, and compared with the value of Resilient Modulus measured in the laboratory. This correlation can be shown in Fig. 8.
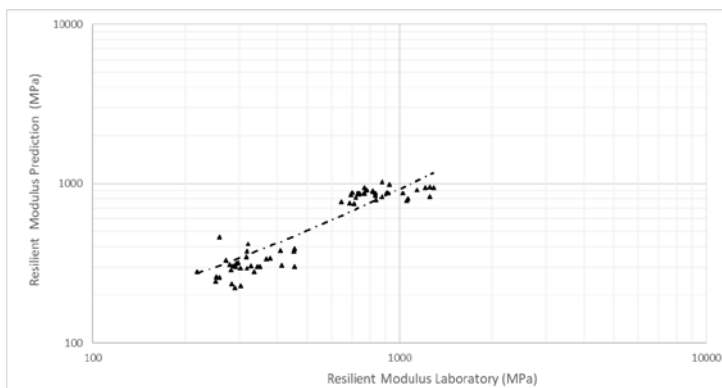

Figure 8. Comparison of laboratory and prediction model.

Based on Fig. 8, the "E" prediction model of resilient modulus, was selected, because besides that model can fulfilling all the classic assumption tests, it gave also a value of average ratio closed to 1.00. This condition concludes that the results of the prediction model of resilient modulus were closed to the results of the direct measurement using the UMATTA equipment.

4. Conclusion

Based on the analysis of the previous discussion, the following conclusions were obtained:

1. The morphology characteristics of slag aggregates used in this research, which is measured by using the XRD test, showed that the most important elements are Fe, Ca, Si and Al. Those elements in the slag will result in a resistance to abrasion.

2. The pen grade and softening point values of RAP asphalt with reclamite nearly same with that of the original pen grade asphalt 60/70. This condition approves the positive role of reclamite on the RAP asphalt only.

3. The value of stiffness modulus of RAP asphalt with reclamite, measured by DSR test at temperature of 35 °C and 45 °C, was nearly same with than that of asphalt modified pen 60/70. This condition approves also the positive role of reclamite on the RAP asphalt.

4. The maximum value of resilient modulus of asphalt mixture was obtained by a RAP percentage of 30 % (CR3), at both temperatures of 35 °C and 45 °C, whereas its optimum value was resulted from the combination mixture by 30 % RAP and 10 % slag (CR3S1).

5. The increase percentage of RAP in the asphalt mixture shows an insensitive trend with the increase of temperature, while the sensitive trend was obtained in the RAP mixture with slag. This combination of RAP and slag will obviously give an advantage in temperature sensitivity of the asphalt mixture.

6. The development of a resilient modulus model using RAP and slag materials under viscous conditions gives the optimum result of: SMix =1140,587 Sbit + 65,286 VIM +0.798 RAP + 0.555 slag - 122.603, where this equation was obtained by the combination of theoretical model from Shell and Nottingham.

References

1. Copeland, A. Reclaimed asphalt pavement in asphalt mixtures state of the practice. 2011. No. FHWA-HRT-11-021.

2. Modarres, A., Hosseini, Z. Mechanical properties of roller compacted concrete containing rice husk ash with original and recycled asphalt pavement material. Mater. Des. 2014. No. 64. Pp. 227–236. DOI: 10.1016/j.matdes.2014.07.072

3. Valdesa, G., Jimeneza, F.P., Miroa, R., Martineza, A., Botella, R. Experimental study of recycled asphalt mixtures with high percentages of reclaimed asphalt pavement (RAP). Construction and Building Materials. 2011. Pp. 1289–1297. DOI: 10.1016/j.conbuildmat.2010.09.016.

4. Hainina, M.R., Aziz, M.M.A., Alia, Z., Jayaa, R.P., El-Sergany, M.M., Yaacoba, H. Steel slag as a road construction material. Jurnal Teknologi (Sciences & Engineering). 2015. No. 73 (4). Pp. 33–38.

5. Oluwasola, E.A., Hainin, M.R., Aziz, M.M.A. Evaluation of asphalt mixtures incorporating electric arc furnace steel slag and copper mine tailings for road construction. Transportation Geotechnics. 2015. No. 2. Pp. 47–55. DOI: 10.1016/j.trgeo.2014.09.004

6. Wang, G., Wang, Y., Gao, Z. Use of steel slag as a granular material: Volume expansion prediction and usability criteria. Journal of Hazardous Materials. 2010. No. 184 (1-3). Pp. 555–560. DOI: 10.1016/j.jhazmat.2010.08.071

7. Al-Qadi, I.L., Aurangzeb, S.H., Carpenter, W.J., Pine., Trepanier, J. Impact of high RAP contents on structural and performance properties of asphalt mixtures. Technical Report FHWA- ICT-12-002, National Technical Information Service. 2012 Illinois Department of Transportation ICT R27-37 Springfield. Virginia.

8. Solaimanian, M., Savory, E. Variability analysis of hot-mix asphalt concrete containing high percentage of reclaimed asphalt pavement. Transp. Res. Rec. J. Transp. Res. Board, 1996. 1543 (1). Pp. 89–96. https://doi.org/10.1177/036119819615430-0111

9. Behnood, A., Ameri, M. Experimental investigation of stone matrix asphalt mixtures containing steel slag. Scientia Iranica A. 2012. No. 19 (5) 4. Pp. 1214–1219. https://doi.org/10.1016/j.scient.2012.07.007

10. Pasetto, M., Baldo, N. Performance comparative analysis of stone mastic asphalts with electric arc furnace steel slag A laboratory evaluation. Materials and Structures. 2012. Pp. 411–424. DOI: 10.1617/s11527-011-9773-2

11. Sofilic, T., Mladenovic, M., Sofilic, U. Defining of EAF steel slag application possibilities in asphalt mixture production. Journal of Environmental Engineering and Landscape Management. 2011. No. 19. Pp. 148–157. DOI: 10.3846/16486897.2011.580910

12. Hosseinzadeh, N., Rezaei, M.J., Hosseini, S.M. Investigation and performance improvement of hot mix asphalt concrete containing EAF slag. International Journal of Engineering and Technology. 2016. Vol. 8. No. 4. Pp. 260–264. DOI: 10.7763/IJET.2016.V8.895

13. Oluwasola, E.A., Hainin, M.R., Aziz, M.M.A., Warid, M.N.M. Volumetric properties and leaching effect of asphalt mixes with electric arc furnace steel slag and copper mine tailings. Sains Malaysiana. 2016. No. (45) 2. Pp. 279–287.

14. Hassan, H.F., Al-Jabri, K. Laboratory evaluation of hot-mix asphalt concrete containing copper slag aggregate. J Mater Civ.Eng. 2010. No. 6. Pp. 879–885. DOI: 10.1061/(ASCE)MT.1943-5533.0000246

15. Raposeiras, A.C., Vargas, A., Cerón, A., Quesada, D.M., Fresno, D.C. Effect of copper slag addition on mechanical behavior of asphalt mixes containing reclaimed asphalt pavement. Construction and Building Materials. 2016. No. 5. Pp. 268–276. DOI: 10.1016/j.conbuildmat.2016.05.081

16. Kavussi, A., Qazizadeh, M.J. Fatigue characterization of asphalt mixes containing electric arc furnace (EAF) steel slag subjected to long term aging. Construction and Building Materials. 2014. No. 72. 4. Pp. 158–166. DOI: 10.1016/j.conbuildmat.2014.08.052

17. Pasetto, M., Baldo, N. Fatigue behavior characterization of bituminous mixtures made with reclaimed asphalt pavement and steel slag. Social and Behavioral Sciences 53. 2015. No. 5. Pp. 297–306. DOI: 10.1016/j.sbspro.2012.09.882

18. Huang, L.S., Lin, D.F. Influence of cooling efficiency of basic oxygen furnace slag used in recycled asphalt mixtures. International Journal of Pavement Research and Technology. 2011. Vol. 4. No. 6, 3. Pp. 347–355.

19. Baldo, N., Manthos, E., Pasetto, M., Nikolaides, A.F. Comparative analysis of stiffness modulus and fatigue resistance of asphalt concretes containing RAP materials, in F. Canestrari, M.N. Partl (Eds.). Proceeding 8th RILEM International Symposium on Testing and Characterization of Sustainable and Innovative Bituminous Materials. 2016. RILEM Book Series. vol. 11. Pp. 915–926.

20. Suaryana, N., Subagio, B.S., Kosasih, D., Sjahdanulirwan. Development of a correlation model between resilient modulus and dynamic modulus for the mixture of stone mastic asphalt. Jurnal Teknik Sipil. 2014. Vol. 21 No. 2. Pp. 171–178.

21. Shaopeng, W., Yongjie, X., Qunshan, Y. Utilization of steel slag as aggregates for stone mastic asphalt (SMA) mixtures. Building and environment. 2007. No. 42. Pp. 2580–2585. DOI: 10.1016/j.buildenv.2006.06.008

22. Directorate General of Highways, Ministry of Public Works.General Specifications for Roads and Bridges. 2010. Indonesia.

23. Bethary, R.T., Subagio, B.S., Rahman, H., Suaryana, N. Effect of recycled materials on marshall performance of hot asphalt mixture (HMA–RAP). IOP Conf. Series, Materials Science and Engineering 508. 2019. DOI: 10.1088/1757-899X/508/1/012048

24. Bethary, R.T., Subagio, B.S. Rheological characteristics of reclaimed asphalt pavement (RAP) evaluation using reclamite rejuvenating material. In The 6th AMMSE Conference on Advanced Materials, Mechanics and Structural Engineering. 2019. Seoul. South Korea. DOI: 10.1088/1757-899X/739/1/012006

25. Kavussi, A., Qazizadeh, M.J., Hassani, A. Fatigue behavior analysis of asphalt mixes containing electric arc furnace (EAF) Steel Slag. Journal of Rehabilitation in Civil Engineering.2015. No. 3-1. Pp. 74–86. DOI: 10.22075/jrce.2016.364

26. Pasetto, M., Baldo, N. Experimental evaluation ofhigh performance base course and road base asphalt concrete with electric arc furnace steel slags. Journal of Hazardous Materials. 2010. Vol. 181. Pp. 938–948. DOI: 10.1016/j.jhazmat.2010.05.104

27. Bethary, R.T., Subagio, B.S., Rahman, H., Suaryana, N. Effect of Slag and Recycled Materials on the Performance of Hot Mix Asphalt (AC-BC). Journal of Civil Engineering. 2019. Vol. 26. No. 1. Pp. 1–9. DOI: 10.5614/jts.2019.26.1.1

28. Sarstedt, M., and Mooi, E. A Concise Guide to Market Research (The Process, Data, and Methods Using IBM SPSS Statistics) second edition. 2014. Springer-New York.

29. Subagio, B.S., Maha, I., Affandi, F., Rahman, H. Performance and development of resilient modulus and fatigue life predictive model of warm mix asphalt concrete binder course (AC-BC) containing reclaimed asphalt pavement (RAP). Eight International Conference on Maintenance and Rehabilitation of Pavements. 2016. Singapore.

30. Ainiyah, N., Deliar, A., Vitriana, R. Assumption test to driving factors of land cover change in the development region of northern part of west java the classica. The International Archives of the Photogrammetry, Remote Sensing and Spatial Information Sciences. 2016. Volume XLI-B6. XXIII ISPRS Congress. https://doi.org/10.5194/isprs-archives-XLI-B6-205-2016.

31. Brown, S.F., Brunton, J.M. An introduction to the analytical design of bituminous pavements. Second Edition. 1984. University of Nottingham, UK.

32. Shell. The Shell Bitumen Handbook Sixth Edition. 2015. Shell Bitumen, U.K.

Information about authors:

Rindu Twidi Bethary, *PhD*
ORCID: https://orcid.org/0000-0002-5094-9420
E-mail: rindutwidibethary@gmail.com

Bambang Sugeng Subagio, *PhD*
E-mail: bssubagio@yahoo.com

Stress-strain state of CFRD with a decrease in friction at the face-sidewall contact

M.P. Sainov ✉ iD

Moscow State University of Civil Engineering (National Research University), Moscow, Russia

✉ *mp_sainov@mail.ru*

Abstract. Friction forces arise at the contact between a concrete face and a rockfill dam body at deformations caused by hydrostatic pressure. They cause tensile and compressive longitudinal forces in the face which decrease the safety factor. In modern CFRD, a layer of emulsified asphalt is placed at the contact between the face and the sidewall made of low cement concrete to decrease the friction. Tests carried out in China permit determining shear characteristics of such a contact. They revealed the effect of increasing tangential stiffness with growth of compressive pressure. At high pressures the contact stiffness may reach 200÷500 MPa/m. The author refined the relationship describing the effect of increasing tangential stiffness and determined its parameters. Availability of the data on tangential stiffness and strength of the contact permitted the author to make a more precise model of the concrete face stress-strain state by the finite element method. The results of analyses showed that measures on decreasing the contact friction do not reach the required effect: considerable tensile longitudinal forces appear in the face. The contact tangential stiffness should be more decreased. Tentatively it may be recommended that in a 100m high dam to provide the face tensile strength the contact tangential stiffness should not exceed 50 MPa/m. However, for more justified conclusion it is necessary to carry out additional experimental studies of shear characteristics of the contact between face and the sidewall; and they should be conducted for conditions of very low shear rates typical for real dams.

Citation: Sainov, M.P. Stress-strain state of CFRD with a decrease in friction at the face-sidewall contact. Magazine of Civil Engineering. 2022. 115(7). Article No. 11506. DOI: 10.34910/MCE.115.6

1. Introduction

The urgent and debating issue in hydraulic engineering is refining the theory of concrete faced rockfill dams (CFRD). The dams of such a type are unique structures: in them a thin-wall and continuous structure of a concrete face perceiving hydrostatic pressure is subject to high deformations which are typical for earth fill. The concrete face (CF) thickness, as a rule does not exceed 1 % of the dam height and 0.5 % of the face length. Deflections of the face at high CFRD make up 0.1÷0.5 % of the dam height, i.e. they are comparable by value with the face thickness.

Debating is the theoretical concept of the concrete face stress-strain state (SSS) specific features. Traditionally it is considered that the face concrete mainly works in bending (in two planes) for perceiving pressive from its own weight.

However, one more specific feature of CF SSS was revealed bases on field measurements and with the aid of numerical modeling. For CF it is typical to have compressive stresses in direction from one bank to the other. The presence of these stresses is evidenced by formation of characteristic vertical cracks in faces of some ultra-high CFRD. The examples are dams Tianshengqiao-1 (China, dam height H = 178 m, the year of emergency situation is 1999), Barra Grande (Brazil, H = 185 m, 2005), Campos Novos (Brazil,

H = 202 m, 2005), Mohale (Lesotho, H = 145 m, 2006) [1–6]. By the results of field measurements, in Mohale dam face at the moment before crack formation the horizontal relative linear deformation amounted to 0.00065 [3]. The deformation of such a value corresponds to compressive stress amounting to about 20÷25 MPa, which is higher than concrete compressive strength.

The issue on the causes of appearing high compressive stresses in the face is debatable. It may be affirmed that the main cause is friction forces between the face and the body of the dam which appear at displacements of the dam body from the sides towards the valley floor. With the aid of numerical modeling it was obtained that the risk of appearing high compressive forces is characteristic for ultra-high dams in a narrow site [7].

It is evident that friction forces may act not only in horizontal direction but also in the direction along the slope. In this case they may present danger for the face strength. The hypothesis about considerable role of contact friction in formation of CF SSS was put forward in 2005 in paper [2] of P. Marques Filho and N. Pinto. They proposed that contact friction forces may cause high tensile stresses in the face in the direction along the slope. By their approximate calculations the tensile stresses in the face may reach 9 MPa. Such stresses are much higher than concrete tensile strength and may cause appearance of transversal cracks in the face.

Numerical modeling may give more precise evaluation of friction forces role in CF SSS formation. According to the studies conducted by Y. Arici (2011), formation of transversal cracks due to high tensile stresses may be expected in the lower part of high CFRD face in the direction along the slope [8]. The similar result was obtained by the author of this article in 2006 with the aid of numerical modeling [9]. It was shown that for CF SSS the characteristic feature is action of tensile longitudinal forces. Thus, there was confirmed the hypothesis about possible appearance of tensile longitudinal forces in CF due to contact friction. Consequently, CF works not only to perceive bending and transversal forces but also longitudinal forces.

In 2000 A. Marulanda and N. Pinto proposed special measures for decreasing friction between CF and the dam body. Their concept obtained the name "Bond Break"[1]. These measures were required because of changes in CFRD construction methodology. At construction of Ita dam (1999) there was used a new method of creating a plane surface for subsequent concreting of the face [10]. The method of Ita envisages to form the dam upstream slope using blocks made of low cement concrete. In technical literature such construction is called "extruded curb" or "extrusion-sidewall" (SW). The Ita method afterwards was used at construction of two dams and became a commonly-accepted method.

However, presence of stiff construction under CF increases friction, therefore, additional measures were required. Concept "Bond Break" envisages separation of CF from SW by an intermediate layer to decrease friction [11]. The role of this layer is played either by asphalt emulsion (about 2 mm thick) or a geomembrane. By recommendation of International Commission on Large Dams (ICOLD)[2] the antifriction measures were applied at the dams constructed in the XXIth century, but they were used at construction of Ita dam.

It should be noted that concept "Bond Break" has earlier analogs. Already in the first half of the XXth century the engineer Girand proposed the structure of a flexible laminated face where concrete slabs were separated from each other by bitumen layers. Such structural design was used in Chile at 85 m high Cogoti dam constructed in 1938. In 1943 the dam successfully withstood the earthquake with acceleration 0.2 g [12]. However, there were also flawed examples of using laminated concrete faces.

Therefore, it is important to evaluate the effectiveness of measures for decrease of friction. Studies of CFRD SSS conducted by the author [13, 14] with the aid of numerical modeling showed that the role of friction forces at the contact between the face and the dam body is high. Tangent stresses at the contact as a rule do not reach the limit values, nevertheless they may cause considerable tensile stresses in the face, especially in the face of an ultra- high dam.

However, the mentioned results of CFRD SSS numerical modeling may be doubtful. Many ultra-high CFRD are operating normally without loss of tensile strength and crack formation in the face. This may be explained by favorable effect of other factors (effect of spatial conditions of operation in a narrow river valley, relaxation of stresses in concrete, other reasons), but it also may be connected with overestimated in analysis characteristics of contact friction. In the studies of CFRD SSS carried out by the author the contact tangential stiffness was assumed to be equal to 50÷200 MPa/m.

---

[1] Marulanda, A., Pinto, N.L. de S. Recent Experience on Design, Construction, and Performance of CFRD Dams. J. Barry Cooke Volume, Concrete Face Rockfill Dams, ICOLD, 20th Congress, Beijing, China, September, 2000.

[2] ICOLD. Concrete Faced Rockfill dam: Concepts for design and construction, International Commission on Large Dams. 2010. Bulletin 141.

Therefore, the author fulfilled this study on revealing the effect of characteristics of contact friction between CF and SW.

2. Methods

The study of effect on CF SSS of tangential stiffness K_t value of the contact between CF and SW was conducted with the aid of numerical modeling. The idea of the study includes:

- use at analysis of experimental data on determining K_t;

- making calculations for a wide range of K_t values.

For this purpose, the author analyzed experimental data on shear characteristics of the contact between the face and the dam body.

Data of experimental studies of the contact shear characteristics.

Experimental tests of shear characteristics of contacts with concrete structures were carried out by different authors [15–20]. However, most of these studies were devoted to contacts of concrete structures with soils.

For the aims of our studies the most valuable is experimental data [19, 20], which was obtained in China at designing Shuibuya dam (2008), the highest CFRD in the world (H = 233 m). These tests were conducted with the aid of special equipment which permits conducting shear tests of coarse sample of constructions (25×25 cm) at downward pressure up to 2 MPa. The studies were conducted for several alternatives of contact surface along which a shear of a concrete slab occurs. Concrete slab shear tests were conducted against crushed stone as well as against the surface of low cement concrete provided there was an antifriction layer. For an antifriction layer there was used a 1 mm thick layer of emulsified asphalt, 0.2 mm thick polyethylene membrane and asphalt felt. The tests were conducted at several values of downward pressure (0.5; 1; 1.5; 2 MPa) at a rate of relative displacements about 0.1 mm per minute.

The results of tests fulfilled by W. Hou et al. [19, 20] are shown in Fig. 1 they are presented in a form of relationship between tangent stresses τ and relative displacement Δu of two contacting surfaces. By the results of the experiments there were determined the parameters of contacts shear strength and tangential stiffness.

It was established that the contact of concrete with crushed stone has the highest shear strength: the angle of internal friction φ makes up 41⁰. The contact shear strength with arrangement of interlayers of emulsified asphalt and polyethylene membrane is approximately one forth as less as the contact with crushed stone: $\varphi = 30°÷32°$. The lowest shear strength has the contact with a layer of asphalt felt: $\varphi = 4°$. Its shear strength is approximately 10 times as less as of the contact with crushed stone.

Of great interest are the results of contact stiffness studies. It was established experimentally that the contact of concrete with crushed stone has the highest tangential stiffness. Tangential stiffness K_t of the contact with layers of emulsified asphalt and a polyethylene membrane is nearly similar. Arrangement of an antifriction layer between CF and SW approximately by 5÷7 times decreases tangential stiffness K_t. Even lower is tangential stiffness of the contact with a layer of asphalt felt: it is approximately 20 as less as that of the contact with crushed stone.


a) concrete contact with emulsified asphalt   b) concrete contact with asphalt felt

σ: • 0.5 MPa   ■ 1 MPa   ◆ 1.5 MPa   ▲ 2 MPa
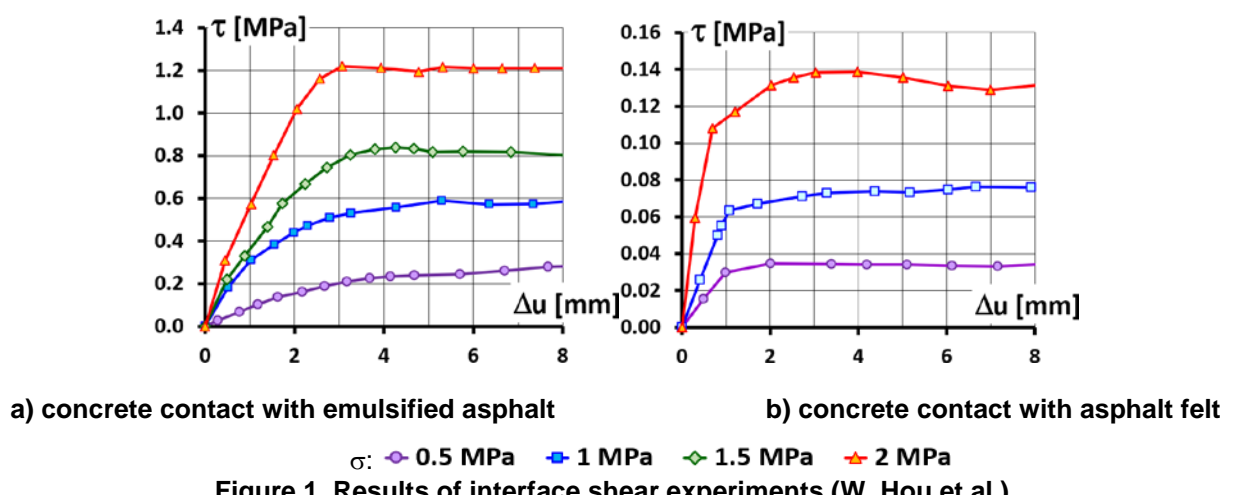
Figure 1. Results of interface shear experiments (W. Hou et al.).

It is noted that at approaching the limit state (slippage along the contact) the tangential stiffness decreases. At reaching the limit value by tangential stiffness the shear at the contact has unlimited increase.

The important result of tests was revealing the effect of relationship between tangential stiffness K_t of the contact and downward pressure σ (Fig. 1). For example, for the contact a layer of emulsified asphalt at $\sigma = 0.5$ MPa K_t does not exceed 100 MPa/m, and at $\sigma = 2$ MPa it reaches 600 MPa/m. As it is seen, at increase of σ the tangential stiffness increases intensively.

For the purpose of our study, we apply the range of stresses σ from 0 to 1 MPa. From the results of experiments it is evident that at $\sigma = 1$ MPa for the contact of concrete with crushed stone the tangential stiffness $K_t \approx 850$ MPa/m, at arrangement of the layer of emulsified asphalt it is equal approximately $180 \div 250$ MPa/m, and at arrangement of the layer of asphalt felt $K_t \approx 60$ MPa/m.

For description of non-linear relationship between K_t and σ W.Hou et al. [20] proposed to use power dependence in the form of:

$$K_t = K_0 p_a \left(\frac{\sigma}{p_a} \right)^n,$$

where K_0 is dimensionless modulus, p_a is atmospheric pressure, n is power index.

Similar relationship was used at numerical modeling of CFRD SSS by some authors [21, 22].

However, use of such a relationship means that at the absence of downward pressure ($\sigma = 0$) the contact has zero tangential stiffness, which contradicts the physical principles of the contact operation.

Therefore, the author proposed to use more full relationship with two components:

$$K_t = p_a \left[K_0 + K_\Delta \left(\frac{\sigma}{p_a} \right)^n \right],$$

where K_0 and K_Δ are dimensionless moduli.

The model parameters were obtained by the author from condition of maximum approximation of design relationship to the results of experiments. They are given in Table 1.

Table 1. Model parameters of shear along the contact.

Code of design alternative	Type of contact	K_0	K_Δ	n	φ
	filling material	4670	13.3	2.47	39°
alternative "A"	emulsified asphalt	41	58.4	1.48	31°
alternative "F"	asphalt felt	850	1.44	2.74	30°

The analysis shows that in the value of tangential stiffness of the contact between concrete with crushed stone and with a layer of asphalt felt the most part is presented by its constant part not depending on pressure σ.

The obtained relationships and their parameters were used at numerical modeling of the dam concrete face SSS. The alternative with a layer of emulsified asphalt was designated as alternative "A", and the alternative with a layer of asphalt felt as alternative "F". At SSS analysis of alternative "A" the modulus K_Δ was assumed equal to 72, i.e. it is somewhat increased as compared to experimental data for their better approximation in the range of σ from 0 to 1 MPa. It may be expected that at increase of emulsified asphalt layer to 2 mm the contact tangential stiffness will become 2 times as less, however, in this study the SSS analyses were conducted for the values obtained experimentally (for 1 mm thickness).

For comparison the SSS analyses were also conducted for the model with constant tangential stiffness K_t Three options of value K_t were considered: 5, 50, 300 MPa/m. They are designated as "a", "b", "c" respectively. The considered interval of tangential stiffness values includes stiffness of contacts with layers of emulsified asphalt and asphalt felt at $\sigma = 1$ MPa. The maximum value of the considered interval

K_t is somewhat higher than the value of the largest contact stiffness of alternative "A", and the minimum value is somewhat less than stiffness in alternative "F". In contrast to alternatives "A" and "F" in options with constant stiffness ("a", "b", "c") the contact was assumed to be absolutely strong at shear.

Principles of numerical modeling of concrete faced rockfill dam stress-strain state

Study of the contact tangential stiffness effect on CF SSS was conducted on the examples of an abstract dam (CFRD) 100 m high (Fig. 2). The dam has slopes were 1:1.4. The concrete face was of variable thickness: from 0.3 m at the top to 0.8 m in the lower part.
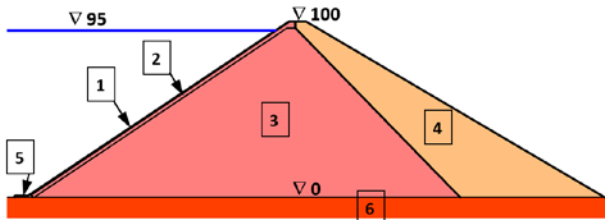

Figure 2. Scheme of the design of a concrete faced rockfill dam
1 – concrete face; 2 – filter zone; 3 – dam upper body; 4 – dam downstream body;
5 – plinth; 6 – dam foundation.

The dam body has a heterogenous structure. It was assumed that its upper part is less deformable than the lower part. The dam rock foundation was assumed to be absolutely stiff and was not included in the computational domain.

SSS analyses were conducted in 2D formulation for the dam cross section. A finite element model was developed and consisted of 500 finite elements of continuous medium and 40 contact finite elements. The sidewall structure was modeled in the form of a slab similar to [23]. Contact finite elements modeled contact interaction between CF with the dam and in the perimeter joint. There were used finite elements of high order with cubic approximation of displacements which provides high accuracy in distribution of stresses in a stiff thin-wall face. The total number of the model degrees of freedom comprised 4356.

Analyses were conducted taking into account the sequence of the dam construction and the reservoir impoundment: 28 design stages were considered. First 16 stages modeled the layered dam filling; one more stage modeled creation of the face. Then there were simulated gradual reservoir impoundment throughout 11 stages. At such a simple scheme the dam dead weight does not affect CF SSS: it is determined only by rockfill deformations under the action of hydrostatic pressure.

For description of the dam material deformation at SSS analyses a linear model was used where two parameters were applied: modulus of linear deformation E and Poisson's number ν. For the face concrete the following values were assumed: E_b = 29 GPa, ν_b = 0.2. For the extruded curb concrete based on the test results given in [24], E_b = 5 GPa.

SSS analyses were conducted for three alternatives of rockfill deformation. In alternative No. 1 modulus of linear deformation of the dam upstream part was taken equal E = 120 MPa, in alternative No. 2 E = 240 MPa, in alternative No. 3 E = 480 MPa. Rockfill modulus of deformation in the dam downstream part was assumed to be 2 times as less as that in the upstream part. Poisson's number in all the alternatives was assumed to be 0.2.

All in all, 15 design variants were considered. Their parameters are given in Table 1.

3. Results and Discussion

Analysis of CFRD SSS was conducted for the time moment of the reservoir impoundment up to ∇ 95 m. The results of CFRD SSS analysis are given in Fig. 2–4. They show distribution of displacements in the face height-wise Y. Extreme values of SSS parameters in all the alternatives are given in Table 2.

By the results or analyses the face is subject to bending deformations (Fig. 2). Maximum deflection U_n is observed at ∇ 45 m. Its value is determined by rockfill deformation. At rockfill modulus of deformation E = 120 MPa the face maximum deflection makes up 19.2 cm, i.e. 0.19 % of the dam height, at E = 240 MPa U_n = 9.6 cm, and at E = 480 MPa U_n = 5.3 cm.

The largest bending deformations occur at the lowest part of the face (below ∇ 6 m).

Table 2. Parameters of design alternatives.

Code of design alternative	A.1	A.2	A.3	F.1	F.2	F.2	a.1	a.2	a.3	b.1	b.2	b.3	c.1	c.2	c.3
Alternative or value of K_t [MPa/m]	A	A	A	F	F	F	300	300	300	50	50	50	5	5	5
E [MPa]	120	240	480	120	240	480	120	240	480	120	240	480	120	240	480
$\Delta U_{t,max}$ [mm]	2.3	1.7	0.8	6.1	4.0	1.1	7.2	4.6	1.0	4.1	3.3	1.5	1.0	1.0	0.5
$\Delta U_{t,min}$ [mm]	-3.7	-3.2	-2.4	-2.7	-2.3	-1.7	-7.2	-6.0	-4.5	-1.4	-1.2	-0.9	-0.3	-0.2	-0.2
$\sigma_{E,max}$ [MPa]	5.3	3.6	2.2	3.5	2.3	1.8	3.1	1.9	1.3	4.8	3.1	2.0	6.5	4.6	2.6
$\sigma_{E,min}$ [MPa]	-3.2	-2.2	-1.3	-2.7	-2.0	-1.5	-2.6	-1.6	-1.1	-3.1	-2.2	-1.7	-3.6	-2.4	-1.8

Designations:

ΔU_t is face displacement relative sidewall, σ_E is longitudinal stress in the face (in direction along the slope).
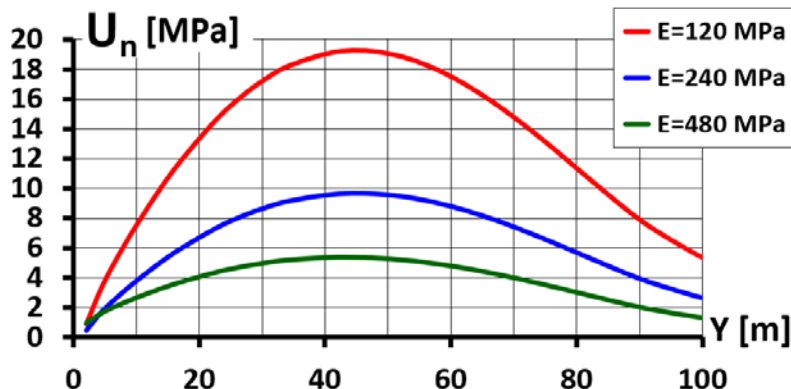
Figure 2. Height distribution of face deflections.

However, the dam body deformations occur not only in the direction perpendicular to the upstream slope (deflections), but along it also. Longitudinal displacements occur due to the fact that the dam horizontal displacements toward the downstream side are greater by value than its settlements. The result of longitudinal displacements of the face is opening of the perimeter joint between the CF and the plinth.

Presence of longitudinal displacements plays an important role for the concrete face SSS formation: they create friction forces between the face and the dam body. In the face these friction forces induce linear deformations (elongation-shortening) and longitudinal forces. Due to presence of antifriction layer between CF and SW the friction forces are partially compensated in the contact between them. This is reached due to relative displacements ΔU_t in the contact, i.e. displacements of the face (CF) relative to SW. they are shown in Fig. 3 and take into account displacements not only at perception of hydrostatic pressure but also under the action of face dead weight.

By the results of analyses the distribution of ΔU_t height-wise Y has a complicated pattern (Fig. 3). By value they may be both positive and negative. Positive displacements ΔU_t correspond to the case, when the face displaces upward along the slope relative to the sidewall (or SW displaces downward along the slope relative to the CF), and negative displacements take place at movement downward along the slope.

In most alternatives (alternative "F", options "a", "b", "c" with constant value of K_t) three sections are distinguished in distribution of relative displacements ΔU_t height-wise Y. In the lowest part of the contact (below ∇ 10m) the zone of the greatest by value positive displacements ΔU_t is observed. In alternative 1.F the maximum value of ΔU_t makes up 6 mm (Fig. 3), i.e. the difference between

displacements of the face and SW is great. At the section ∇ 10m ÷ ∇ 60m relative displacements ΔU_t are negative, and higher than ∇ 60 m they are again positive.

In alternative "A" (emulsified asphalt) there are only 2 characteristic sections for distribution of ΔU_t The face lower part (below ∇ 50÷60 m) displaces downward along the slope, and the upper part displaces upward (Fig. 3). Thus, the face «expands» in direction along the slope striving to compensate longitudinal deformations transferred to it.
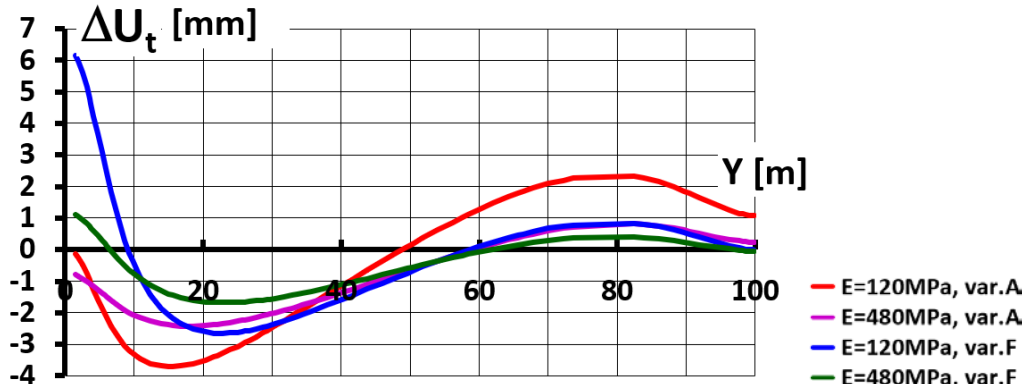

Figure 3. Height distribution of face offsets relative to sidewall.

Distribution of displacements ΔU_t conditions the direction of tangent stresses τ between the face and SW. Relative to CF and CW the tangent stresses are applied in opposite directions. Positive τ correspond to the case when they are directed relative to CF from the top downward along the slope. The sign of tangent τ corresponds to the sign of ΔU_t Positive τ are observed at the section below ∇ 20 m, and higher on the most part of the contact length they are negative.

Such distribution of tangent stresses causes appearance of compressive and tensile forces in the face. In the lower section (below ∇ 30 m) the face is subject to tensile longitudinal forces and in the upper section it is subject to compressive forces. The evidence of this is distribution height-wise the face of medium (with respect to the face thickness) values of longitudinal stresses σ_E, shown in Fig. 4. At high contact stiffness the tensile σ_E exceeds the concrete tensile strength.
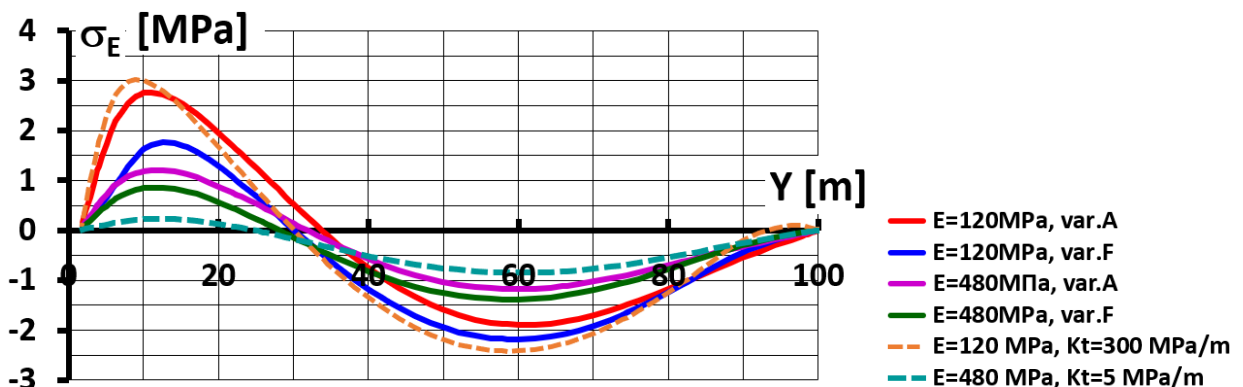
Figure 4. Height-wise distribution of mean values of longitudinal stresses in the face.

The analysis shows that induced by friction longitudinal forces play the decisive role in formation of longitudinal stresses σ_E in the face (Fig. 5). Non-uniform distribution of stresses σ_E between the upstream and downstream edges of the face caused by bending demonstrates considerably less effect. The exclusion is the lowest section of the face where bending deformations are greatly developed.
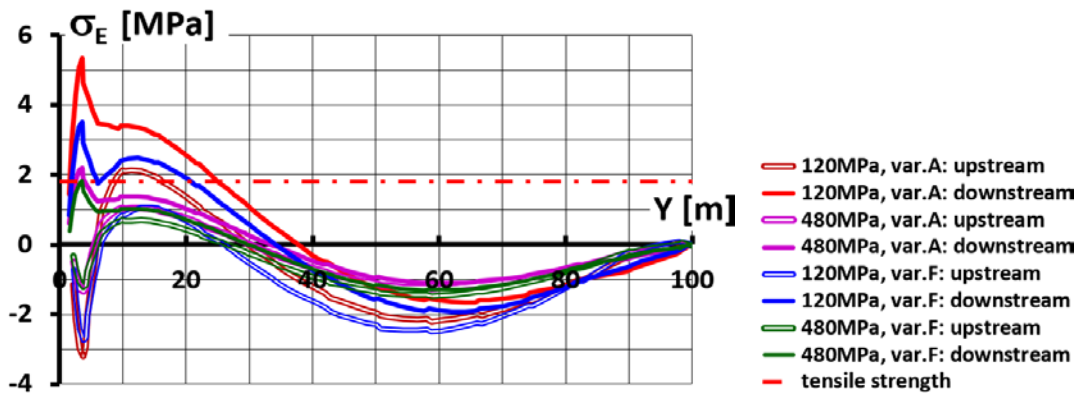
Figure 5. Distribution of longitudinal stresses on the upstream and downstream edges of the face.

The pattern of concrete face SSS described above is characteristic for all the considered alternatives not depending on the value of rockfill modulus of deformation E and tangential stiffness K_t of the contact between CF and SW. However, E and K_t determine quantitative size of deformations and stresses. Their impact may be evaluated from Fig. 6, showing maximum and minimum parameters of CF SSS. It permits evaluation of effectiveness of antifriction measures in regulation of CF SSS.

Fig. 6a permits evaluation of E and K_t effect on relative displacements ΔU_t between the face and the sidewall. It is evident that the lower is stiffness K_t, the higher is ΔU_t Therefore, in the options of alternative "F" (a layer of asphalt felt) displacements ΔU_t are greater than those in the options of alternative "A" (a layer of emulsified asphalt). At using a layer of asphalt felt the maximum value of displacements ΔU_t is approximately 1.5÷3 as much as at using a layer of emulsified asphalt. Rockfill deformation E has great effect on the value of ΔU_t. At high values of E the effect of K_t on ΔU_t decreases.

It may be noticed that by values ΔU_t the options of alternative "F" (a layer of asphalt felt) are closer to options of series "c" (K_t = 50 MPa/m), and the options of alternative "A" (a layer of emulsified asphalt) to the options of series "a" (K_t = 300 MPa/m).

Maximum values of tangent stresses τ at the contact CF-SW considerably depend on tangential stiffness K_t. At stiff contact (K_t = 300 MPa/m, alternative "A") they reach 0.2÷0.4 MPa, and at the most flexible one (K_t = 50 MPa/m) they do not exceed 0.05 MPa (Fig. 6b). It is necessary to note that for the moment of the reservoir impoundment completion in all the alternatives the tangent stresses do not exceed the contact shear strength: shear strength is maintained at the whole length of the contact. However, in alternative No. 1.F at the intermediate stages of the reservoir impoundment the failure of shear strength of the contact lower part was recorded.

By maximum values of tangent stresses (Fig. 6b) the options of alternative "A" (a layer of emulsified asphalt) are close to options of series "a" (K_t = 300 MPa/m), and options of alternative "F" (a layer of asphalt felt) are in the intermediate position between options of series "c" (K_t = 5 MPa/m) and "b" (K_t = 50 MPa/m).

From Fig. 6b it may be noticed that decrease of tangential stiffness K_t by an order (10 times) the tangent stresses are only approximately 4 times as less.
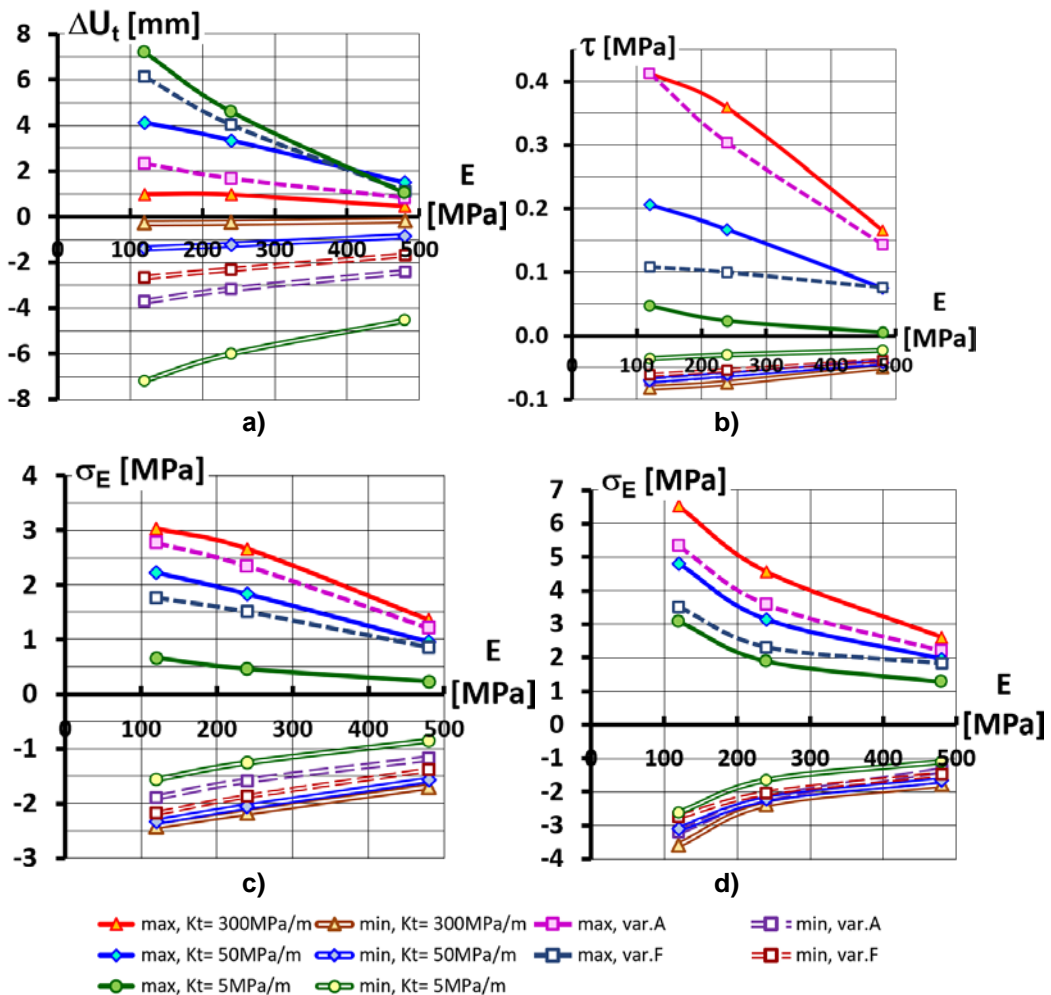
Figure 6. Variation of maximum and minimum values of concrete face SSS parameters depending on rockfill modulus of deformation E
a – CF displacements relative to SW; b – longitudinal stresses.

By maximum values of longitudinal tensile forces (Fig. 6c) the options of alternative "A" (a layer of emulsified asphalt) are closer to options of series "a" (K_t = 300 MPa/m), and options of alternative "F" (a layer of asphalt felt) to options of series "b" (K_t = 50 MPa/m), but are somewhat "behind". Thus, account of the contact tangential stiffness K_t variation led to decrease of tensile forces in the face, however, this improvement is not very significant.

To more extent the account of the contact tangential stiffness K_t variability effected the values of maximum tensile longitudinal stresses σ_E (Fig. 6d). In many options the tensile stresses decreased approximately by 1 MPa. Nevertheless, this change is not sufficient for guaranteed provision of the face concrete tensile strength.

The results obtained in this study contribute to the study of the SSS formation of a concrete face, taking into account the application of the "extrusion-sidewall" technology. This issue is controversial, there are different opinions about the role of SW in the formation of SSS of the concrete face of the rock fill dam. For example, in works [25–26], based on numerical simulations, it is argued that the SW device improves the strength of CF. However, the article [27] states that the influence of SW on SSS of the concrete face is small, except for its end sections. Similar results were obtained by the author of this article in [14]. It was found that the presence of an antifriction layer between CF and SW plays a more significant role. The important role of this layer in the formation of SSS CF is also noted in [28]. G. Zhang and J.-M. Zhang in publication [29] it was shown that the arrangement of the asphalt layer between CF and SW significantly changes the stress state of the screen. This is consistent with the results of the study presented in this article. The magnitude of stresses in the screen depends on the magnitude of the tangential stiffness of the CF and SW contact, this is demonstrated by the results of the study carried out in this article. In addition, it can be noted that the presence of an antifriction layer is important for the formation of a face (CF) under temperature influences. This is stated in [30].

4. Conclusion

1. Tangential stiffness of the contact between the concrete face (CF) with the sidewall (SW) made of thin-cement concrete, where it is envisaged to arrange a layer of asphalt emulsion of 1 mm thickness, by the results of experiments, may reach considerable values 200÷500 MPa/m. Such value of tangential stiffness does not provide decrease of friction forces on this contact to be sufficient to prevent appearance of tensile stresses in the face. At increase of emulsion thickness to 2 mm it may be expected that tangential stiffness will decrease but still will be considerable.

2. The important effect is increase of the contact tangential stiffness depending on downward pressure. Therefore, in ultra-high dams at the contact between the face with the dam the greater friction forces are acting and they present greater danger. The author proposed empirical relationship between tangential stiffness and a downward pressure; and it is also a possibility to take into account the presence of stiffness even at the absence of downward pressure.

3. Consideration at numerical modeling of stress-strain state of the fact that at small downward pressure the tangential stiffness is decreased, permits obtaining more favorable stress state of the face than at using constant value of stiffness. However, this change is not determining: it does not change the earlier made conclusions about specific features of CFRD SSS.

4. SSS analyses fulfilled for a wide range of tangential stiffness values of the contact between CF and SW and with consideration of its variable value, permits affirming that for CF SSS the presence of tensile longitudinal forces is a specific feature. It is confirmed by the fact that in all CFRD the perimeter joint between the face and the foundation is open. It was revealed that decrease of tangential stiffness by an order decreases longitudinal tensile forces in the face by 2-3 times. Therefore, to improve the face stress-strain state it is necessary to decrease considerably the tangential stiffness. It may be recommended that tangential stiffness of the contact should not exceed 50 MPa/m.

5. For more precise quantitative predictions of CFRD SSS it is required to carry out additional studies of shear characteristics of the contact between CF and SW, having antifriction layers. Necessary studies should include determination of the contact characteristics at very low shear rates. It may be expected that in these conditions the forces of internal friction in emulsified asphalt will be low, accordingly tangential stiffness will be considerably lower than that which was used in analyses. On the other hand, it should be expected that in real conditions the surface of the contact between CF and SW may have large roughness and irregularities, which results in increase of tangential stiffness. It also requires additional studies.

References

1. Ma, H., Chi, F. Technical progress on researches for the safety of high concrete-faced rockfill dams. Engineering. 2016. 2. Pp. 332–339.
2. Marques Filho, P., Pinto, N.L.S. CFRD dam characteristics learned from experience. International Journal on Hydropower and Dams. 2005. 12 (1). Pp. 72–76.
3. Johannesson, P., Tohlang, S.L. Lessons learned from Mohale. The International Water Power & Dam Construction. 2007. 59 (8). Pp. 16-18+20-22+24-25
4. Freitas, M.S.Jr. Concepts on CFRDs Leakage Control – Cases and Current Experiences. ISSMGE Bulletin. 2009. 3 (4). Pp. 11–18.
5. Xavier, L.V., Albertoni, S.C., Pereira R.F., Antunes J. Campos Novos dam during second impounding. The International Journal on Hydropower & Dams. 2008. 15. Pp. 53–58.
6. Sainov, M., Zatonskikh, M. Structural cracks initiation in reinforced concrete faces of rockfill dams. Construction of Unique Buildings and Structures. 2018. 10 (73). Pp. 16–27. DOI: 10.18720/CUBS.73.2
7. Sainov, M.P. Impact of dam site configuration on 3D stress-strain state of concrete faced rockfill dam. Magazine of Civil Engineering. 2016. 63(3). (rus). Pp. 16–39. DOI: 10.5862/MCE.63.2
8. Arici, Y. Investigation of the cracking of CFRD face plates. Computers and Geotechnics. 2011. 38. Pp. 905–916. DOI: 10.1016/j.compgeo.2011.06.004
9. Sainov, M.P. Osobennosti raschetov napriazhenno-deformirovannogo sostoianiia kamennykh plotin s zhelezobetonnymi ekranami [Features of the calculations of the stress-strain state of rockfill dams with reinforced concrete faces]. Vestnik MGSU [Proceedings of oscow State University of Civil Engineering]. 2006. 2. Pp. 78–86.
10. Materon, B., Resende F. Construction Innovations for the Itapebi CFRD. International Journal on Hydropower & Dams. 2001. 8(5). Pp. 66–70.
11. Pinto, N.L.D.S. Questions to ponder on designing very high CFRDs. International Journal on Hydropower and Dams. 2001. 8.(5). Pp. 61–65.
12. Wieland, M. CFRDs in highly seismic regions. International Water Power and Dam Construction. 2010. 62(3). Pp. 28–31.
13. Sainov, M.P. Strength of ultra-high rockfill dam concrete face. Magazine of Civil Engineering. 2021. 101(1). Article No. 10113. DOI: 10.18720/MCE.101.13
14. Sainov, M. Formation and peculiarities of stress-strain state of rockfill dam. Construction of Unique Buildings and Structures. 2020. 87. DOI: 10.18720/CUBS.87.2
15. Shakir, R.R., Zhu, J.-G. Mechanical behavior of soil and concrete interface. Proceedings of SPIE – The International Society for Optical Engineering. 2009. 7375,73756R. DOI: 10.1117/12.839390

16. Wang, Y.-L., Rao, X.-B., Pan, J.-J., Zuo, Y.-Z., Gao, P. Mechanical behaviors of interface between sand-gravel cushion material and concrete face slab by large-scale simple shear tests. Yantu Gongcheng Xuebao/Chinese Journal of Geotechnical Engineering. 2019. 41 (8). Pp. 1538–1544.

17. Haeri, H., Sarfarazi, V., Zhu, Z., Marji, M.F., Masoumi, A. Investigation of shear behavior of soil-concrete interface. Smart Structures and Systems. 2019. 23 (1). Pp. 81–90. DOI: 10.12989/sss.2019.23.1.081

18. Rehman, Z.U., Luo, F., Wang, T., Zhang, G. Large-Scale Test Study on the Three-Dimensional Behavior of the Gravel-Concrete Interface of a CFR Dam. International Journal of Geomechanics. 2020. 26 (6). 04020046.

19. Zhou, X.-W., Gong, B.-W., Ding, H.-S., Rao, X.-B. Large-scale simple shear test on mechanical properties of interface between concrete face and gravel underlayer. Yantu Gongcheng Xuebao/Chinese Journal of Geotechnical Engineering. 2005. 27 (8). Pp. 876–880.

20. Hou, W.-J., Zhang, G., Zhang, J.-M. Behavior of interface between extrusion-sidewall and slab face of CFRD. Yantu Gongcheng Xuebao/Chinese Journal of Geotechnical Engineering. 2008. 30(9). Pp. 1356–1360.

21. Xu, B., Zou, D., Liu, H. Three-dimensional simulation of the construction process of the Zipingpu concrete face rockfill dam based on a generalized plasticity model. Computers and Geotechnics. 2012. 43. Pp. 143–154. DOI: 10.1016/j.com-pgeo.2012.03.002

22. Ye, Z., Lu, L. Nonlinear Static Analysis of Shuibuya Dam in China-World's Highest CFRD. The Electronic Journal of Geotechnical Engineering. 2016. 21 (4). Pp. 1527–1537.

23. Peng, C., Guo, D., Wang, Q., Lu, Y. Application of extrusion-sidewall technology to the project of rock fill dam with face slab. Rock and Soil Mechanics. 2008. 29. Pp. 201–203.

24. Zhang, G., Zhang, J.-M. Modeling of low-cement extruded curb of concrete-faced rockfill dam. Canadian Geotechnical Journal. 2011. 48 (1). Pp. 89–97.

25. Luo, X.-Q., Wu, X.-M., Tong, F.-G., Li, C.-C. Research on the stress-strain of Shuibuya concrete face rockfill dam based on the concrete crushing-type side wall technology. Yanshilixue Yu Gongcheng Xuebao/Chinese Journal of Rock Mechanics and Engineering. 2005. 24 (13). Pp. 2342–2349.

26. Xu, C.-D., Wang, Y., Hou, H.-M., Li, H.-C. Study on application of extrusion concrete side wall in concrete face rock fill dam. Advanced Materials Research. 2011. 287–290. Pp. 3002–3006. DOI:10.4028/www.scientific.net/AMR.287-290.3002

27. Hou, W.-J., Zhang, G., Zhang, J.-M. Influence on stress and deformation of concrete faced rockfill dam using extrusion-sidewall. Yantu Lixue/Rock and Soil Mechanics. 2009. 30 (7). Pp. 2147–2152.

28. Del Olmo, D., Bermejo, M. Bond-breaker impact on slab behaviour in concrete face dams. Dams and Reservoirs. 2017. 27 (3). Pp. 102–110. DOI:10.1680/jdare.16.00046

29. Zhang, G., Zhang, J.-M. Numerical modeling of soil-structure interface of a concrete-faced rockfill dam. Computers and Geotechnics. 2009. 36 (5). Pp. 762–772. DOI: 10.1016/j.compgeo.2009.01.002

30. Zhou, W., Hua, J.-J., Chang, X.-L., Cao, Y.-H. Cause analysis of cracking of concrete slab for high CFRD based on concrete crushing-type side wall technology. Yantu Lixue/Rock and Soil Mechanics. 2008. 29 (8). Pp. 2037–2042.

Information about author:

Mikhail Sainov*, PhD of Technical Science*
ORCID: https://orcid.org/0000-0003-1139-3164
E-mail: mp_sainov@mail.ru

Complex modified additive for concrete based on industrial waste

R.E. Lukpanov [iD] *, D.S. Dyussembinov* [iD] *, D.V. Tsygulyov* [iD] *, S.B. Yenkebayev* [iD]

L.N. Gumilyov Eurasian National University, Astana, Kazakhstan

✉ *Rauan_82 @mail.ru*

Abstract. The article presents the results of studies of concretes with the use of additives developed based on industrial waste: ash, post-alcoholic bard, and soapstock. The aim of the research was to improve the physical and mechanical characteristics of concrete without increasing its cost. The research was carried out for samples of different ash concentrations and the corresponding percentage of the additive. The material quality was assessed by comparing the results of laboratory tests of the binder and concrete: strength, bending strength, setting time (for the binder); cube strength, water absorption, frost resistance (for concrete). The test results showed the effectiveness of the additive, which can compensate for the losses of physical and mechanical characteristics due to the inclusion of ash into the concrete (to reduce costs). The optimum concentration of the additive is 0.004% by weight of cement, with a cement ash replacement rate of 5%. At these proportions, the investigated parameters, albeit insignificantly, exceed the samples of the traditional composition of concrete without additive, and at a lower concentration of ash, they exceed them to a large extent. The obtained results of the study are of practical value, can be used in construction without reference to the region, as the applied wastes belong to the standard industrial sectors.

1. Introduction

Today, reinforced concrete structures and products are among the most demanded materials in both civil and industrial construction [1]. Surrounding buildings and structures do not make do without the use of concrete, even in road construction concrete has widespread use [2].

The history of the development of concrete dates back to ancient times, but to this day has active development. Modern technology favors the future prospect of the development of technology for the use and production of concrete in construction [3]. New types of concrete find application in modern practice, such as fiber concretes, self-compacting concretes, carbon concretes, nanoconcretes, and others [4–7].

However, most of the transformation process of concrete as a building material does not involve the development of new materials, but the use of additives to improve its physical and mechanical properties. An additive can be selected, for example, depending on the technological application of concrete or to improve certain concrete properties: setting or hardening rate, an increase of strength, water absorption, frost resistance, etc. [8–10].

This article deals with increasing the strength of concrete through the use of additives. It can be informed that today the construction market has enough specialized additives to improve the strength of concrete [11]. However, this approach to solving the problem will affect the cost of concrete, so the proposed additives are developed from the wastes of industrial production in the region where the research was conducted. In this case, the used waste is not a localized feature of a particular region, but rather an integral part of a particular technological production [12]. Thus, solving the problem of increasing the strength of concrete partially closes the urgent environmental issue of industrial waste disposal [13].

The technical solution to increase the strength of concrete (as well as the accompanying reduction of water absorption and increase in frost resistance) is achieved by using the following components represented by industrial production wastes: post-alcoholic bard (refers to the alcohol production waste), soapstock (refers to the category of fat production waste return), an alkali (caustic soda, NaOH) [14]. In addition to the developed composition, in order to save the binder it was decided to include in the composition of the additive – fly ash [15, 16]. The addition of ash helps to reduce the cost of concrete, as a building product, by reducing the amount of cement [17, 18]. Acceptable addition of ash to the composition of concrete mixture is up to 5 %, while the changes in the characteristics of concrete are minimal, strength losses are insignificant, but they take place. Compensation, and in our case even an increase in strength is due to the use of additives, in particular post-alcohol bard [19]. Post-alcohol bard essentially has plasticizing and hydrophobic properties due to the presence of polymeric components in its composition [20]. Bard has a relatively small plasticizing effect, but sufficient to compact the concrete mixture (by filling the pore structure of ash). The hydrophobizing effect of bard refers to the infrastructural hydrophobization of concrete [21]. The polymer, in the composition of bard, is inherently hydrophobic, that is after curing does not react with water [22]. In the process of mixing, the polymeric component is distributed throughout the entire volume, and during setting, it fills the pore (micropore) structure of the concrete. This leads to a loss of the chemical contact area of water and the inherently hydrophilic concrete, thus increasing the hydrophobicity of the material [23]. Soapstock is a fatty product that forms a convex meniscus when it interacts with water. In contrast to the bard, the non-wettability of soapstock with water contributes to the concrete's volumetric hydrophobicity. However, a positive effect can be achieved only by including caustic soda in the composition of the additive, which brings the soapstock into contact with water. However, once in the concrete mixture, caustic soda reacts chemically with the concrete mixture, restoring the primary hydrophobic properties of soapstock. Thus, the output is concrete with enhanced hydrophobic properties [24, 25].

The aim of the study is to determine the optimal composition of concrete using industrial waste to improve the physical and mechanical characteristics of the material. The optimality of the composition consists in determining such a quantity of components, in which there is no reduction in the strength of the concrete due to the replacement of cement binder by ash. The latter is made in order to reduce the cost of concrete and recycling of industrial waste.

2. Methods

To produce a complex modified additive it is necessary to have a rational ratio of all the components according to their characteristics, taking into account their impact on the qualitative indicators of the heavy concrete. The ratio of the components of the complex modified additive by weight are post-alcohol bard (48 %), soapstock (47 %) and caustic soda (5 %).

The technological process of preparation of the additive is shown schematically in Fig. 1.
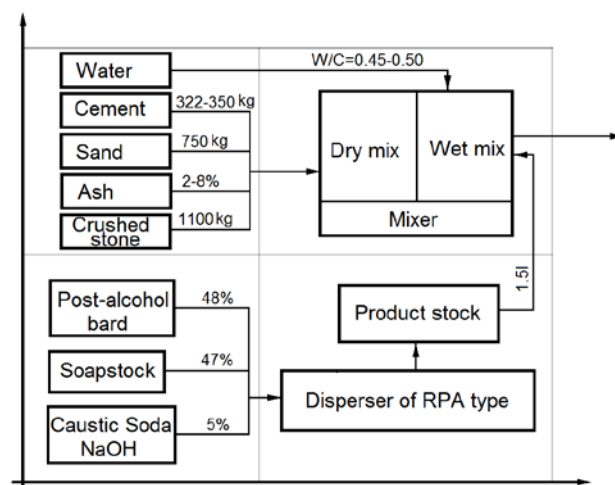

Figure 1. Technological process of additive production.

The combination process should be carried out in the following sequence: caustic soda is combined with soapstick until complete dissolution at a temperature not below 60 °C; next the resulting solution is passed through the rotary pulsation apparatus (RPA dispersant) to accelerate the chemical reaction with soapstick; then the resulting water-soluble emulsion is combined with post-alcohol bard and repeatedly passed through RPA. The resulting emulsion is readily soluble in water, thus providing a set of properties of both hydrophobization and plasticization. The technological process allows for a homogeneous emulsion easily soluble in water without the formation of oil spots, which cannot be achieved with the usual combination of the same components by mechanical agitation without despergation. The whole production process should be carried out at a temperature of not less than 60 °C. The percentage of complex modified additive in concrete mortar varies depending on the percentage of the binder, ranging from 0.5 to 0.8 %.

Determination of the composition of industrial waste to assess their suitability in the cement binder in the production of a complex additive was carried out by chemical analysis. Soapstock has the following composition: fat 38–40 % neutral fat 7–11 %, nonfat components (proteins and carbohydrates) 55–50 % in water, unreacted NaOH and NaCl 0.001-1 %. Post distillery stillage used as an additive has the following composition: crude protein 2.0 %, non-fatty substances 3.0 %, fat 0.5 %, cellulose 0.5 %, the rest is a liquid phase (mostly water with dissolved substances of proteins, cellulose, fats, casein, lignin). Hydrotreatment ashes include: silicon dioxide (SiO_2) – up to 52 %, aluminum oxide (Al_2O_3) – up to 18 %; quicklime (CaO) – up to 13 %, magnesium oxide (MgO) – up to 2 %, iron scale (Fe_2O_3) – up to 7 %, sulfur dioxide (SO_3) – up to 3 %, alkali metals – up to 2 %, ash residue – up to 7 %.

Research on the effect of a complex modified additive on the improvement of physical and mechanical properties of concrete as a building material was carried out in two stages. At the first stage, the performance of the binder with ash was evaluated in comparison with the standard cement binder of the classic technology of concrete production. The first phase aims to evaluate the impact of ash in the composition of the binder on its physical and mechanical properties. The quantitative composition of ash in the composition of the binder is presented in Table 1, the increment of ash component concentration is a multiple of 2 %. In the second phase, the evaluation of concrete as a building material was carried out. The evaluation was also carried out in comparison with the classic technology of production of concrete, standard composition. The purpose of the second stage is to evaluate the effect of the complex modified additive on improving the physical and mechanical properties of concrete. That is, if the component of the first stage contributes to the deterioration of the qualities of the material, the component of the second stage compensates for these losses. Thus, at the output, we get a quality similar to the classical technology of concrete, but with a lower cost, due to the replacement of the components in the composition of the concrete waste industry. Studies are a complex of laboratory tests related to the basic methods of assessing the properties of building materials. Qualitative and quantitative composition of the components of the compared binders and compared samples of concrete are presented in Table 1, where type 1, in both cases, refers to the classical method of production of concrete.

Table 1. Qualitative and quantitative composition of binders and concrete.

Type, number	Cement (PC400 D0), kg	Sand, kg	Ash, kg	Water/Cement	Crushed stone, kg	Additive, l
Step 1 – Examination of the binder						
Type 1	1.00	3.00	0	0.30	–	–
Type 2	0.98	3.00	0.02 (2%)	0.31	–	–
Type 3	0.96	3.00	0.04 (4%)	0.33	–	–
Type 4	0.94	3.00	0.06 (6%)	0.37	–	–
Type 5	0.92	3.00	0.08 (8%)	0.45	–	–
Step 2 – Examination of the concrete						
Type 1	350	750	–	0.45	1100	–
Type 2	343	750	7 (2%)	0.40	1100	1.5
Type 3	336	750	14 (4%)	0.42	1100	1.5
Type 4	329	750	21 (6%)	0.45	1100	1.5
Type 5	322	750	28 (8%)	0.50	1100	1.5

A complex of basic laboratory tests of the binder, Fig. 2A:

- Determination of strength according to Interstate Standard GOST 6139-2003 EN 196-1;
- Determination of the bending strength of Interstate Standard GOST 6139-2003 EN 196-1;
- Determination of the setting time in accordance with Interstate Standard GOST 30744-2001.

A set of basic laboratory tests of concrete samples, Fig. 2B:

- Determination of cubic strength according to Interstate Standard GOST 10180-2012;
- Determination of water absorption according to Interstate Standard GOST 12730.3-78;
- Determination of frost resistance according to Interstate Standard GOST 10060-2012.

A

B
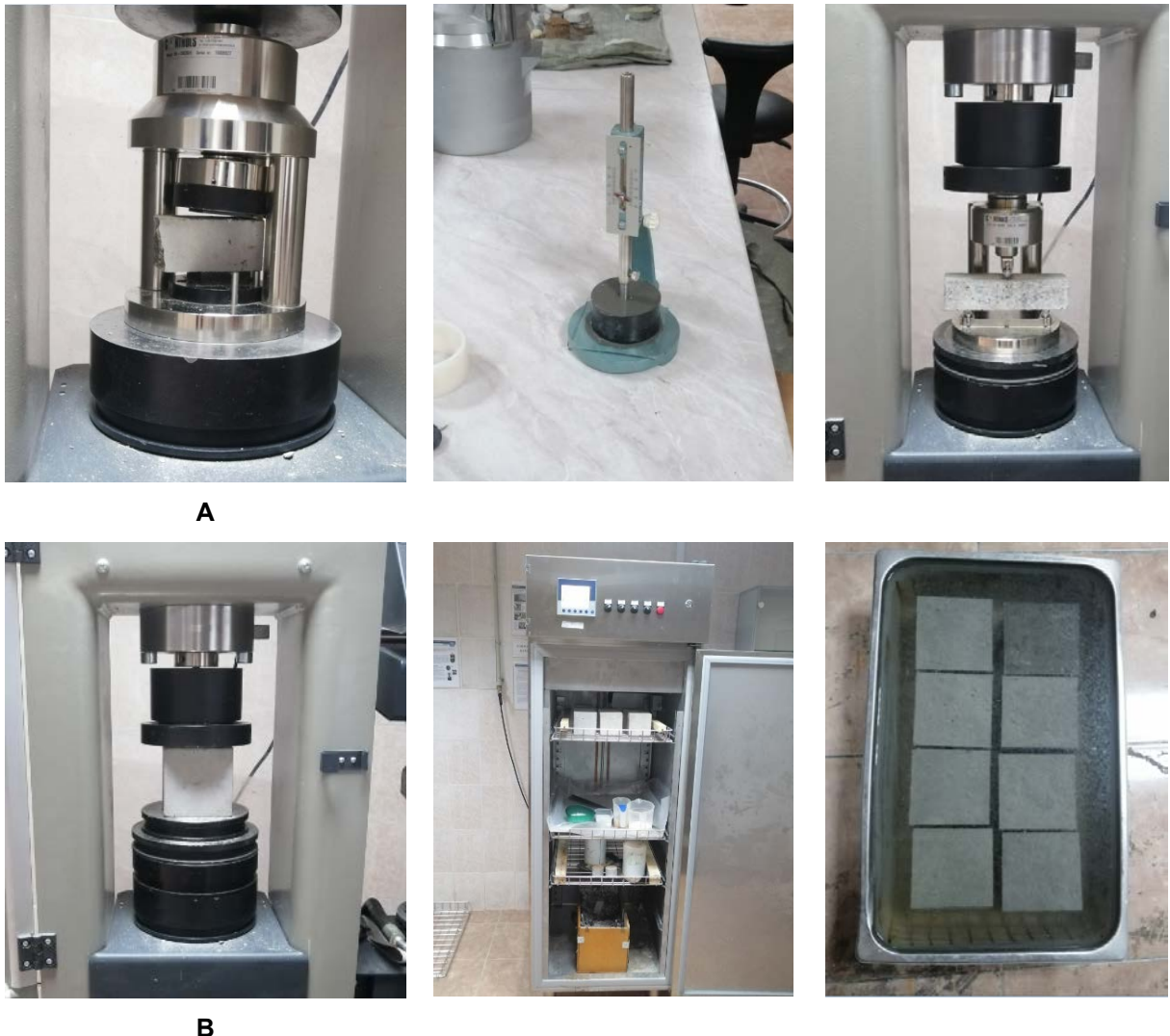
Figure 2. A set of laboratory tests.

Tests were conducted for standard samples: prismatic specimens (beams), dimension 40×40×160 mm; cubic specimens (cubes), dimension 100×100×100 mm. Each test was performed for 5-8 samples, to evaluate the average performance of the compared types of materials.

3.   Results and Discussion

3.1. The results of determining the strength of the binder

The test results of the strength of the binder are shown in Fig. 3. Fig. 3A shows the dependence of the average values of compressive strength by type of sample, Fig. 3B shows the progression of strength reduction from the percentage of ash in the composition of the binder.
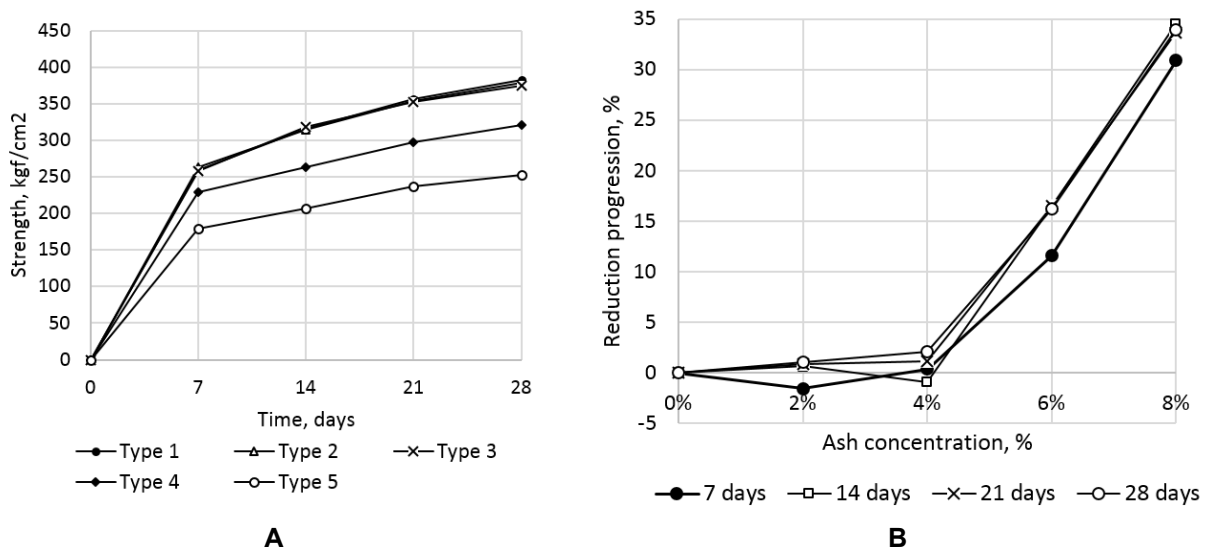
Figure 3. Results of strength tests.

According to the test results, the reduction of strength properties is not linear, despite the proportional replacement of the cement component by ash. Reduction of compressive strength at 2 % substitution with ash was up to 1.0 %, at 4 % substitution it was 1.2–1.7 %, at 6 % substitution it was 11.5–16.4 %, at 8 % substitution it was 30.8–34.5 %. The obtained average values of strength of the eight individual values have good statistical indices: Type 1 – quadratic deviation is 5.77 with an average value of 383 kgf/cm^2 (28 days), coefficient of variation is 2.33 %; Type 2 – deviation – 3.71 with an average value of 379 kgf/cm^2, coefficient of variation – 1.17 %; Type 3 – deviation – 4.07 with an average value of 375 kgf/cm^2, the coefficient of variation – 1.14 %; Type 4 – deviation – 5.81 with an average value of 321 kgf/cm^2, the coefficient of variation – 1.51 %, Type 5 – deviation – 3.14 with an average value of 252 kgf/cm^2, the coefficient of variation – 1.51 %. From the above data we can conclude about the close relationship of individual values within each type of material, as well as a high degree of reliability of the results obtained.

The test results of the strength tests showed a non-linear character of strength reduction by the equivalent replacement of cement by ash, multiple of 2 % by mass. The cause of the progression may be the low density of ash due to its friability, which partially persists even at mixing with additives having plasticizing properties.

3.2. The results of the determination of the setting time

The results of the setting time tests of the compared samples are shown in Fig. 4. Fig. 4A shows the results of the average and individual values of the beginning and end of the setting (beginning of hardening) according to the type of specimen. Fig. 4B shows the results of the changes in the same times depending on the concentration of the ash component. The results of the mixture setting time do not contradict the results of similar studies, in which the ash was also used [26].
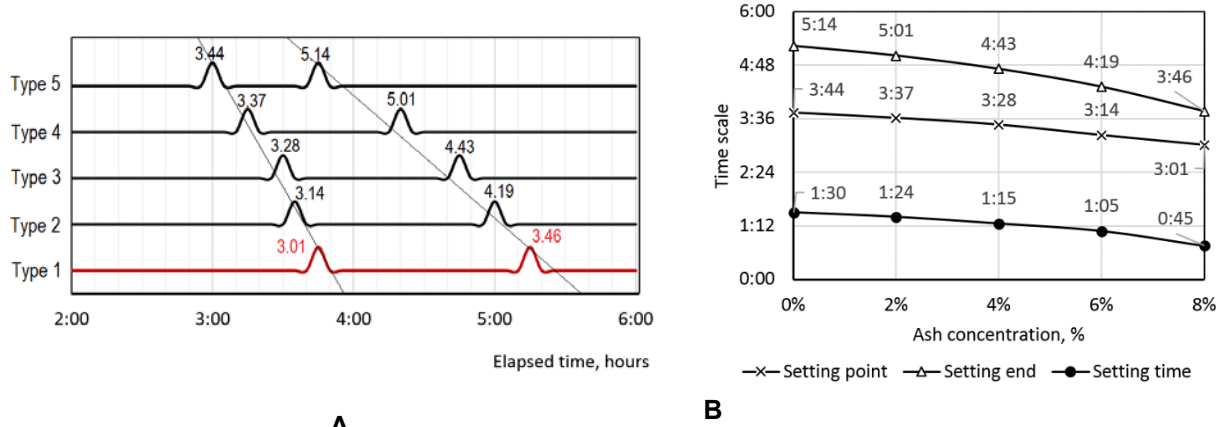

Figure 4. Results of strength tests.

In this case, there is a relatively stable variation at the beginning of the setting time depending on the ash content. The difference of the end-setting times has a greater variation concerning the beginning of setting depending on the type of specimen. This is confirmed by comparing the angles of deviation from

the standard cement-sand mortar (without ash) shown in Fig. 4A. In addition, when the concentration of the ash component increases, the setting time decreases due to the absorption capacity of the ash. Compared to the standard cement-sand mortar, the percentage reduction in setting time is as follows: for 2 % replacement of cement with ash – 6.7 % reduction in time, for 4 % – 16.7 %, for 6 % – 27.8 %, for 8 % – 50.0 %. At the same time, there is a nonlinear increase in the percentage reduction in terms according to the linear increase in concentration.

The average values are shown in Fig. 4B also confirm the effect of the ash component on the setting time. According to the statistical processing of the data, all individual values of the setting values have a close relationship and high reliability of the results: Type 1 – maximum quadratic deviation (end of setting) is 4.74, coefficient of variation is 2.8 %; Type 2 – quadratic deviation (end of setting) is 7.48, coefficient of variation is 2.3 %; Type 3 – quadratic deviation (beginning of setting) is 4.18, coefficient of variation is 3.2; Type 4 – quadratic deviation (end of setting) is 7.32, coefficient of variation is 5.29; Type 5 – quadratic deviation (end of setting) is 6.21, coefficient of variation is 6.31.

The decrease of the setting time (beginning and end) with the increase of the ash component can be explained by the absorption capacity of the ash. At the same time according to water-binding ratio tests obtained by measuring the flowability of ash-cement-sand mortar, the absorption effect is accompanied during the whole setting period. Consequently, the depletion of water necessary for hydration and workability (mobility) occurs in geometric progression.

3.3. The results of determining the bending strength of the binder

The results of the bending strength tests of the beams are shown in Fig.5. Fig. 5A shows the results of private and average values of bending strengths depending on the type of material, Fig. 5B shows the results of progression of changes in the average values of bending strengths according to the percentage of ash component. The results obtained do not contradict, but, on the contrary, correspond to the results of similar studies of the bending strength of specimens using ash [17, 27].
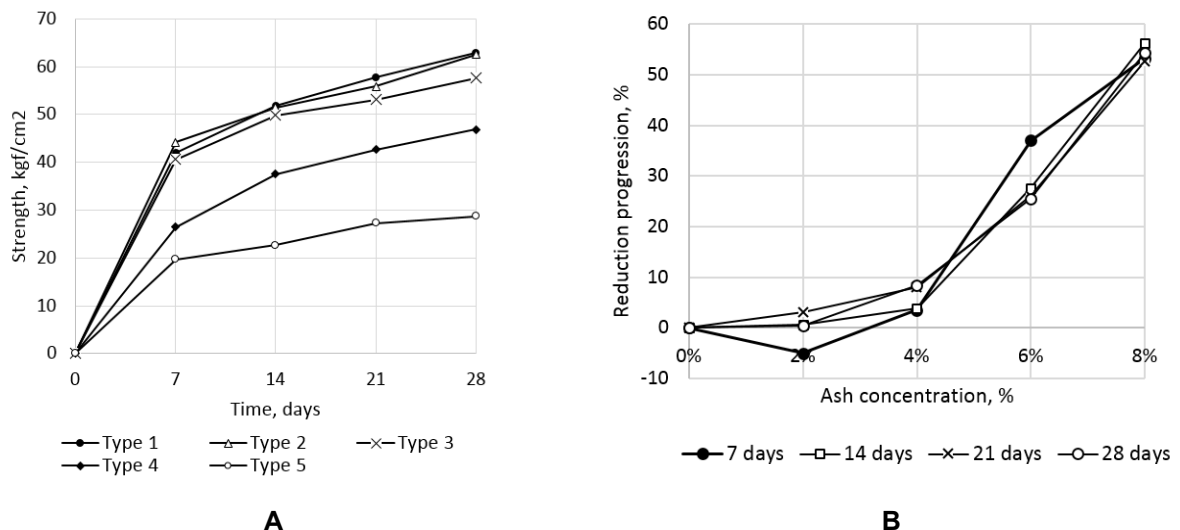

Figure 5. Bend test results.

There is also a non-linear progression of strength change with a uniform increase of ash components in the composition of the binder. The decrease in flexural strength at 2 % substitution with ash is up to 4.9 %, at 4 % substitution it is 3.5–8.4 %, at 6 % substitution it is 25.4–37.1 %, at 8 % substitution it is 52.7–56.2 %. Compared with the strength of the mass, there are a greater relative progression of the reduction of the bending strength (exceeding 1.5 times) quantitative indicators with the increase in the ash component. The obtained average bending strength values also have good statistical indices: Type 1 – quadratic deviation is 2.11 with an average value of 62.9 kgf/cm^2 (28 days), coefficient of variation is 3.35 %; Type 2 – deviation – 1.98 with an average value of 62.6 kgf/cm^2, coefficient of variation – 3.16 %; Type 3 – deviation – 2.05 with an average value of 57.6 kgf/cm^2, coefficient of variation – 3.55 %; Type 4 – deviation – 1.27 with an average value of 46.9 kgf/cm^2, coefficient of variation – 2.71 %; Type 5 – deviation – 1.03 with an average value of 28.7 kgf/cm^2, coefficient of variation – 3.59 % Therefore, we can conclude about the close relationship of individual values within each type of material and the high degree of reliability of the results.

The increase in the progression of the decrease in the bending strength compared to the strength of the grade may be due to an increase in the brittleness of the material, that is, the low resistance to tangential stresses as a result of the increased porosity of the material.

3.4. The results of determining the cube strength of concrete

Fig. 6 shows the results of cube strength tests of concrete specimens using the additive. Fig. 6A shows the results of average strength values as a function of ash concentration, Fig. 6B shows the progress of percent strength reduction by specimen type. The results of the strength test are consistent with similar studies to determine the optimal waste content [17, 27, 28].
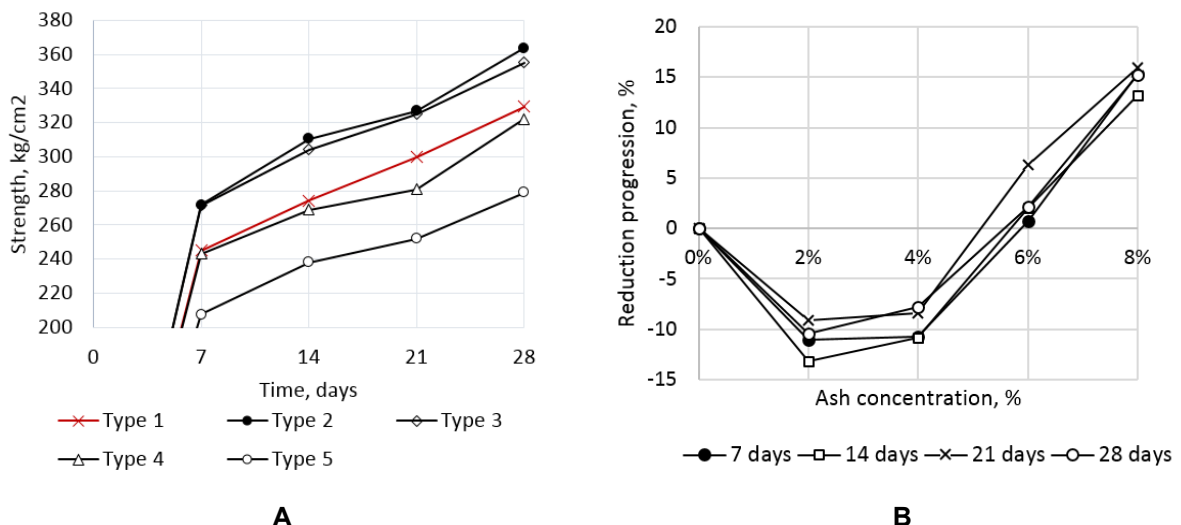

Figure 6. Compressive strength test results.

Non-linear progression of percentage change of strength in comparison with the samples of type 1 (classical technology) is: at 2 % substitution of ash – 9.1÷13.2 %, at 4 % substitution – 7.8–10.9 %, at 6 % substitution – 0.7–6.3 %, at 8 % substitution – 13.2–15.9 %. That is the most approximate, but not satisfactory (since all the values below the samples of type 1) have shown the results of type 4 (which corresponds to 6 % of ash concentration). The obtained values of compressive strength of the concrete also have good statistical indices: Type 1 – quadratic deviation is 2.11 with an average value of 62.9 kgf/cm^2 (28 days), coefficient of variation is 3.35 %; Type 2 – deviation – 1.98 with an average value of 62.6 kgf/cm^2, coefficient of variation – 3.16 %; Type 3 – deviation – 2.05 with an average value of 57.6 kgf/cm^2, coefficient of variation – 3.55 %; Type 4 – deviation – 1.27 with an average value of 46.9 kgf/cm^2, coefficient of variation – 2.71%; Type 5 – deviation – 1.03 with an average value of 28.7 kgf/cm^2, coefficient of variation – 3.59 % Therefore, we can conclude about the close relationship of individual values within each type of material and the high degree of reliability of the results.

3.5. The results of determination of frost resistance

Fig. 7 shows the results for frost resistance of concrete specimens. Fig. 7A shows the results of private and average strength values depending on ash concentration after cyclic freezing of specimens (150 cycles), Fig. 6B shows the progress of percentage reduction of strength by specimen type.
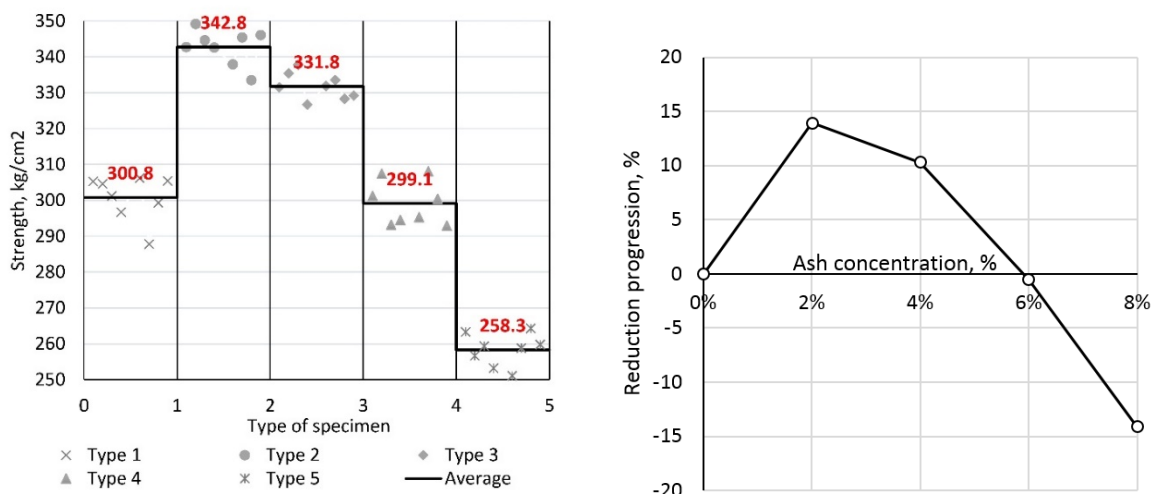

Figure 7. Results of frost resistance tests.

In this case, the non-linear progression of percentage change in strength after freezing is as follows relative to type 1 sample (also after freezing): at 2 % substitution with ash up to 13.94 %, at 4 % substitution up to 10.29 %, at 6 % substitution up to 0.56 %, at 8 % substitution up to 14.12 %. According to the results of statistical processing of data, the obtained values have a close connection and a high degree of reliability, in all cases, the coefficient of variation of individual values does not exceed 9 % (according to the requirements of GOST 100060-2012): Type 1 – quadratic deviation is 6.25 with an average value of 301 kgs/cm^2 (28 days), coefficient of variation is 2.07 %; Type 2 – deviation – 4.96 with an average value of 343 kgs/cm^2, coefficient of variation – 1.44%; Type 3 – deviation – 3.72 with an average value of 332 kgf/cm^2, the coefficient of variation – 1.12 %; Type 4 – deviation – 6.15 with an average value of 299 kgf/cm^2, the coefficient of variation – 2.05%, Type 5 – deviation – 4.55 with an average value of 258 kgf/cm^2, the coefficient of variation – 1.76 %.

3.6. The results of water absorption determination

Fig. 8 shows the results of water absorption tests of concrete specimens. Fig. 8A shows the results of the individual parameter values for assessing the water absorption capacity of concrete as a function of ash concentration, Fig. 8B shows the progress of the percentage reduction in water absorption by type of specimen.
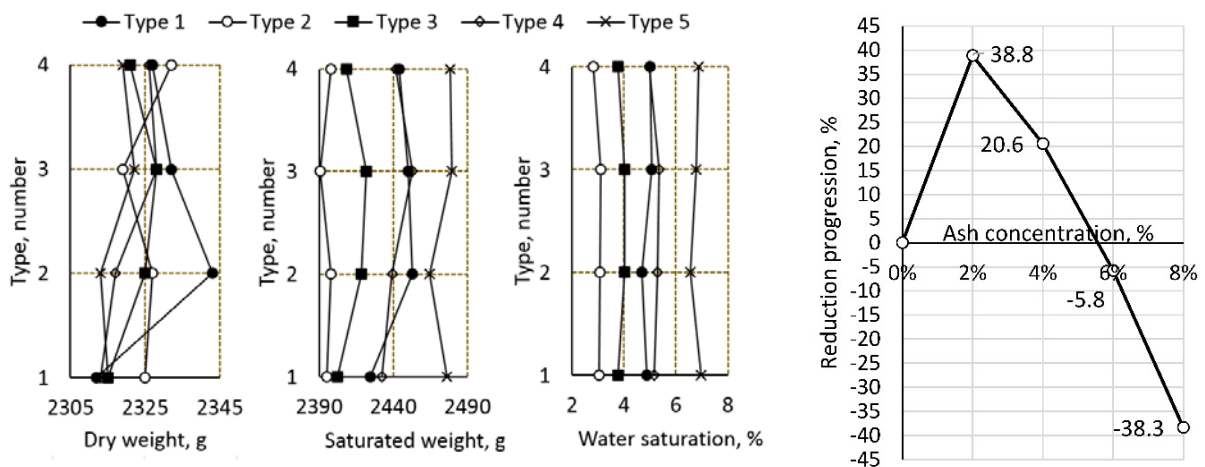

Figure 8. Water absorption test results.

In this case, the non-linear progression of percent change in water absorption capacity is: at 2 % substitution by ash to 38 %, at 4 % substitution to 21 %, at 6 % substitution to 9 %, at 8 % substitution to 41 %. According to the results of statistical processing of the data, the values obtained are also closely related and have a high degree of reliability: Type 1 – quadratic deviation is 0.17, coefficient of variation is 3.42 %; Type 2 – quadratic deviation is 0.12, coefficient of variation is 3.92 %; Type 3 – quadratic deviation is 0.14, coefficient of variation is 3.70 %; Type 4 – quadratic deviation is 0.17, coefficient of variation is 3.20 %, Type 5 – quadratic deviation is 0.18, coefficient of variation is 2.62 %. The close relationship of the coefficients of variation indicates a high degree of validation of the test method and the purity of the experiment. Comparing the results of different types of specimens one can conclude about the effect of the additive on the hydrophobic properties of concrete, and the relatively insignificant difference of weights in the dry state indicates its plasticizing properties (reduction of natural porosity of ash). A significant difference in water absorption capacity of different types is visually traceable by the nature of divergence of the curves of Fig. 8. If in the diagram of dry masses the curves overlapped in places, as a result of random arrangement of the results, in the diagram of water absorption the same curves are distant from each other. Moreover, the curvature and flatness of the water absorption curves indicate the absence or presence of a pattern of influence of the additive on the water absorption capacity of the material. The obtained results of water absorption have a similar relationship to the studies where cement substitution with ash was used [26].

3.7. The evaluation of the optimal composition of the concrete mixture

Fig. 9 shows summary evaluation diagrams, based on which a sample of the optimal composition of the concrete mixture is made. Each of the diagrams represents the dynamics of change of one of the evaluation criteria (previously defined physical-mechanical characteristics of concrete) depending on the type of sample relative to the classical concrete production technology (Type 1). Fig. 9A presents a general comparative diagram of the percentage changes in the physical and mechanical parameters of concrete, Fig. 9B compares the changes in the binder strength and cube strength of concrete, 9C compares the strengths without freezing and after cyclic freezing, 9D compares the strength after cyclic freezing and water absorption capacity.
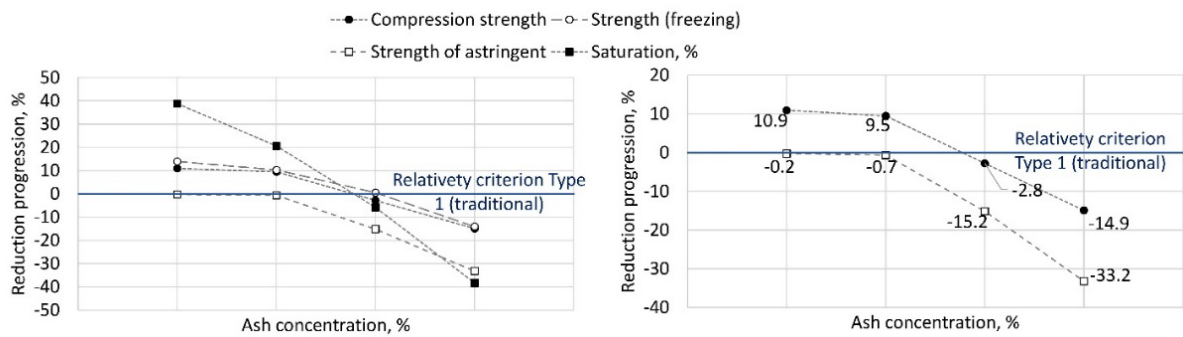
Figure 9. Comparative diagrams of concrete evaluation criteria.

Comparing the percentage progression of strength changes of binder and concrete samples, it can be concluded about the influence of the additive on the improvement of strength characteristics. The dynamics of progression in both cases is identical, the percentage increase in cube strength of concrete from the initial strength of the binder is: for type 1 – 11.1 %, type 2 – 11.2 %, type 3 – 12.4 %, type 4 – 18.3 %, corresponding to a positive correlation coefficient (x_i – ash content with addition, y_i – strength gain) 0.861. Thus, the loss of strength when adding the ash component is compensated by the introduction of a modified additive. Comparing percentage progression of strength change of specimens before and after cyclic freezing, we can conclude about the influence of additive on concrete durability, since strength loss after freezing in percentage ratio is for type 1 – $100\%\left(1-\dfrac{301}{329}\right)=8.58\%$, type 2 – $100\%\left(1-\dfrac{364}{343}\right)=5.83\%$, type 3 – $100\%\left(1-\dfrac{332}{355}\right)=6.54\%$, type 4 – $100\%\left(1-\dfrac{299}{322}\right)=7.11\%$, type 5 – $100\%\left(1-\dfrac{258}{279}\right)=7.41\%$ At the same time, there is a trend of gradual increase in strength loss depending on the content of the ash component. Theoretically, the results of frost resistance should correlate with the results of water absorption, since the former depends directly on the latter, that is, the loss of strength from the degree of water saturation of the sample. Nevertheless, the percentage progression of water absorption has a sharper character in relation to strength (by frost resistance), the difference is: for type 1 – 24.9 %, type 2 – 10.3 %, type 3 – 5.8 %, type 4 – 24.2 %, which corresponds to a negative correlation coefficient (x_i is ash content with additive, y_i is strength increase) –0.998. Which is directly related to the perceptibility of the absorption effect of ash with the increase of its concentration. Despite the character, the general tendency of the curve propagation indicates the relative influence of the additive on the water absorption capacity of concrete, depending on the ash concentration.

According to the results of comparisons, the optimal composition in all cases will be that composition in which the physical and mechanical characteristics are not inferior to the traditional concrete, in our case, it is the concentration of the ash component between type 3 and 4. The minimum of the three interpolated criteria will be 5.7 %. As the recommended ash concentration (without loss of physical and mechanical properties of concrete) of the concrete composition can be taken a concentration equal, for reliability, to 5 % of the mass of cement, provided the proposed modified additive is used.

4. Conclusion

1. A complex modified additive for improving the strength and reducing the water absorption of concrete has been developed and tested. Full solubility of the additive in water allows it to react effectively with a cement binder without the formation of micropores with reduced water-cement ratio and thereby improve the physical and mechanical, and construction-technical properties of concrete.

2. The complex of laboratory studies was carried out in two stages: the first stage assessed the impact of the ash concentrate on reducing the strength properties; the second stage assessed the impact of the additive on increasing the strength. The results of the research represent the composition of concrete mixture with a rational concentration of ash and additive, without any loss of concrete strength.

3. According to the results of the measurement of the binder, a pattern of decrease in physical and mechanical properties of the binder depending on the concentration of ash from 2 to 8 % by mass of cement was obtained. In all cases, a non-linear progression of the decrease of the compared characteristics was observed despite the proportional replacement of the cement component by ash. The reduction of strength ranged from 1.0 % to 34.5 %, the reduction of setting time from 6.7 % to 50.0 %, the reduction of flexural

strength from 4.9 % to 56.2 %. The above figures indicate a significant impact of the ash component, despite its insignificant percentage in the composition of the binder, on its characteristics.

4. According to the results of measurements of concrete, the dependence of the effect of additive on the increase of its physical and mechanical properties at the same concentration of ash binder was obtained. Nonlinear progression of percentage change in strength is from 0.7 to 15.9 %, change in strength after 150 cycles of freezing is from 0.56 to 14,12 %, change in water absorbency is from 4 to 41 %, depending on the percentage of ash content. The patterns obtained testify to the influence of the additive on the physical and mechanical properties, in particular strength and durability.

5. According to the results of comparisons according to the evaluation criteria (previously determined physical and mechanical characteristics of concrete), the optimal composition of cement-ash binder and complex modified additive was determined. In most cases, the dynamics of progression of changes in characteristics by changing the concentration of ash component has a similar gradual pattern. The optimum composition is the concentration of ash component between type 3 and 4, but satisfying the condition of identical properties of concrete of traditional composition (not lower). In general, the confidence concentration of the ash component replacing the cement binder is 5 %, the modified additive – 0.004 % by mass of cement.

References

1. Castañeda-Saldarriaga, D.L., Alvarez-Montoya, J., Martínez-Tejada, V., Sierra-Pérez, J. Toward Structural Health Monitoring of Civil Structures Based on Self-Sensing Concrete Nanocomposites: A Validation in a Reinforced-Concrete Beam. International Journal of Concrete Structures and Materials. 2021. 15 (1). DOI: 10.1186/s40069-020-00451-8.

2. Prathap, M.G., Balaji, N., Sudarsan, J.S. Experimental study on usage of industrial waste in road construction. AIP Conference Proceedings. 2020. 2277 (November). DOI: 10.1063/5.0025309

3. Tkach, E. Improvement of the modified heavy concrete properties based on the use of activated silica fume. E3S Web of Conferences. 2019. 135. Pp. 03028. DOI: 10.1051/e3sconf/201913503028.

4. Sasanipour, H., Aslani, F. Effect of specimen shape, silica fume, and curing age on durability properties of self-compacting concrete incorporating coarse recycled concrete aggregates. Construction and Building Materials. 2019. 228. Pp. 117054. DOI: 10.1016/j.conbuildmat.2019.117054.

5. Neef, T., Müller, S., Mechtcherine, V. 3D-Druck mit Carbonbeton: Technologie und die ersten Untersuchungsergebnisse. Beton- und Stahlbetonbau. 2020. 115 (12). Pp. 943–951. DOI: 10.1002/best.202000069.

6. He, K., Chen, Y., Mei, M. Study on influencing factors of photocatalytic performance of CdS/TiO 2 nanocomposite concrete. Nanotechnology Reviews. 2020. 9 (1). Pp. 1160–1169. DOI: 10.1515/ntrev-2020-0074.

7. Gonzalez, M., Tighe, S.L., Hui, K., Rahman, S., de Oliveira Lima, A. Evaluation of freeze/thaw and scaling response of nanoconcrete for Portland Cement Concrete (PCC) pavements. Construction and Building Materials. 2016. 120. Pp. 465–472. DOI: 10.1016/j.conbuildmat.2016.05.043.

8. Wan, Z., Chen, J., Li, J. Probability density evolution analysis of stochastic seismic response of structures with dependent random parameters. Probabilistic Engineering Mechanics. 2020. 59. Pp. 103032. DOI: 10.1016/j.probengmech.2020.103032.

9. Deepasree, S., Venkatraman, V., Srividya, R. Comparative investigation of internal curing agent incorporated with cenosphere. 2020. Pp. 030009. DOI: 10.1063/5.0019406.

10. Hu, C., Weng, X., Yan, X., Liu, P., Guo, T. Study on frost resistance and abrasion resistance of fiber mesh reinforced concrete. E3S Web of Conferences. 2020. 206. Pp. 02020. DOI: 10.1051/e3sconf/202020602020.

11. Lang, L., Duan, H., Chen, B. Experimental Investigation on Concrete Using Corn Stalk and Magnesium Phosphate Cement under Compaction Forming Technology. Journal of Materials in Civil Engineering. 2020. 32 (12). Pp. 04020370. DOI: 10.1061/(ASCE)MT.1943-5533.0003487.

12. Behera, M., Bhattacharyya, S.K., Minocha, A.K., Deoliya, R., Maiti, S. Recycled aggregate from C&D waste & its use in concrete – A breakthrough towards sustainability in construction sector: A review. Construction and Building Materials. 2014. 68. Pp. 501–516. DOI: 10.1016/j.conbuildmat.2014.07.003.

13. Teara, A., Shu Ing, D. Mechanical properties of high strength concrete that replace cement partly by using fly ash and eggshell powder. Physics and Chemistry of the Earth, Parts A/B/C. 2020. 120. Pp. 102942. DOI: 10.1016/j.pce.2020.102942.

14. Lukpanov, R., Dyussembiniv, D., Sabitov, Y., Yenkebayev, S. Complex modified additive for heavy concrete. Patent. 33533. 2017.

15. Berenguer, R., Lima, N., Valdés, A.C., Medeiros, M.H.F., Lima, N.B.D., Delgado, J.M.P.Q., Silva, F.A.N., Azevedo, A.C., Guimarães, A.S., Rangel, B. Durability of Concrete Structures with Sugar Cane Bagasse Ash. Advances in Materials Science and Engineering. 2020. 2020. Pp. 1–16. DOI: 10.1155/2020/6907834.

16. Rivera, J.F., Mejía de Gutiérrez, R., Ramirez-Benavides, S., Orobio, A. Compressed and stabilized soil blocks with fly ash-based alkali-activated cements. Construction and Building Materials. 2020. 264. Pp. 120285. DOI: 10.1016/j.con-buildmat.2020.120285.

17. Che Amat, R., Nizar Ismail, K., Mohamad Ibrahim, N., Liza Rahim, N. Recycling Municipal Solid Waste Incineration Bottom Ash as Cement Replacement in Concrete. IOP Conference Series: Earth and Environmental Science. 2020. 616. Pp. 012062. DOI: 10.1088/1755-1315/616/1/012062.

18. Hilal, N.N., Rajab, N.A., Faraj, R.H. Fresh Behavior and Hardened Properties of Self-Compacting Concrete Containing Coal Ash and Fly Ash as Partial Replacement of Cement. IOP Conference Series: Materials Science and Engineering. 2020. 978. Pp. 012005. DOI: 10.1088/1757-899X/978/1/012005.

19. Yaowarat, T., Horpibulsuk, S., Arulrajah, A., Mohammadinia, A., Chinkulkijniwat, A. Recycled Concrete Aggregate Modified with Polyvinyl Alcohol and Fly Ash for Concrete Pavement Applications. Journal of Materials in Civil Engineering. 2019. 31(7). Pp. 04019103. DOI: 10.1061/(ASCE)MT.1943-5533.0002751.

20. Allahverdi, A., Kianpur, K., Moghbeli, M.R. Effect of polyvinyl alcohol on flexural strength and some important physical properties of Portland cement paste. Iranian Journal of Materials Science and Engineering. 2010. 7 (1). Pp. 1–6.

21. Arulrajah, A., Mohammadinia, A., Horpibulsuk, S., Samingthong, W. Influence of class F fly ash and curing temperature on strength development of fly ash-recycled concrete aggregate blends. Construction and Building Materials. 2016. 127. Pp. 743–750. DOI: 10.1016/j.conbuildmat.2016.10.049

22. Pakravan, H.R., Jamshidi, M., Asgharian Jeddi, A.A. Combination of ground rice husk and polyvinyl alcohol fiber in cementitious composite. Journal of Environmental Management. 2018. 215. Pp. 116–122. DOI: 10.1016/j.jenvman.2018.03.035.

23. Thong, C.C., Lee Teo, D.C., Ng, C.K. Durability Characteristics of Polyvinyl Alcohol–Treated Oil Palm Shell Concrete. Journal of Materials in Civil Engineering. 2017. 29 (10). Pp. 04017200. DOI: 10.1061/(ASCE)MT.1943-5533.0002066.

24. Ma, Z., Liu, M., Duan, Z., Liang, C., Wu, H. Effects of active waste powder obtained from C&D waste on the microproperties and water permeability of concrete. Journal of Cleaner Production. 2020. 257. Pp. 120518. DOI: 10.1016/j.jclepro.2020.120518.

25. Bao, J., Li, S., Zhang, P., Xue, S., Cui, Y., Zhao, T. Influence of exposure environments and moisture content on water repellency of surface impregnation of cement-based materials. Journal of Materials Research and Technology. 2020. 9 (6). Pp. 12115–12125. DOI: 10.1016/j.jmrt.2020.08.046.

26. Damodhara Reddy, B., Aruna Jyothy, S., Kiran Kumar, N., Hemanth kumar, K. An Experimental Investigation on Concrete by Partial Replacement of Cement by Fly Ash and Fine Aggregate by Quarry Dust. IOP Conference Series: Materials Science and Engineering. 2020. 1006. Pp. 012033. DOI: 10.1088/1757-899X/1006/1/012033.

27. Solai Mathi, S., Johnpaul, V., Riyas, P. Mechanical Properties of Concrete with Bottom Ash as Partial Replacement of Fine Aggregate. IOP Conference Series: Materials Science and Engineering. 2020. 1006. Pp. 012011. DOI: 10.1088/1757-899X/1006/1/012011.

28. Venkateswara Rao, J., Rajesh, S., Shankar, G. An Experimental Study on Partial Replacement of Cement and Fine Aggregate with Industrial Waste in Concrete Paver Blocks. IOP Conference Series: Materials Science and Engineering. 2020. 1006. Pp. 012014. DOI: 10.1088/1757-899X/1006/1/012014.

Information about authors:

Rauan Lukpanov, PhD
ORCID: https://orcid.org/0000-0003-0085-9934
E-mail: Rauan_82@mail.ru

Duman Dyussembinov, PhD of Technical Science
ORCID: https://orcid.org/0000-0001-6118-5238
E-mail: dusembinov@mail.ru

Denis Tsygulyov, PhD of Technical Science
ORCID: https://orcid.org/0000-0002-7061-699X
E-mail: denis_riza_72@mail.ru

Serik Yenkebayev, PhD
ORCID: https://orcid.org/0000-0002-5984-9346
E-mail: yenkebayev-serik@mail.ru

Topology design of plane bar systems
based on polygonal discretization

A.V. Alekseytsev[a]* ✉ 🆔 *, N.S. Kurchenko[b]* 🆔

[a] Moscow State University of Civil Engineering (National Research University), Moscow, Russia

[b] Bryansk State University of Engineering and Technology, Bryansk, Russia

*E-mail: aalexw@mail.ru

Abstract. A topology formation method for frame and truss structures, which is relevant for use in computer-aided design, is proposed. A flat figure discretized into polygonal primitives is used as a basic structure. This structure is presented in the form of a finite element model and is assumed redundant. Its elements are excluded using the principle of maximizing the intensity of the force flow during the initial calculation and the shortest path of this force flow between the points that reflect force and kinematic connections. At the same time, the heuristic principle implemented in the ACO algorithms was used. Registration of geometrically variable systems is performed based on an estimate of the infinite norm of the stiffness matrix of the finite element model. For flat trusses and frames, examples of the formation of rational topologies under given force and kinematic constraints are considered. Comparison with the method of redundant structure, which implements the exclusion based on the genetic algorithm, is performed. It has been shown that the proposed technique allows one to effectively select both one and several alternative variants of the topology of bearing systems.

1. Introduction

One of the key issues in designing plane bar systems is the formation of the initial object structure. Usually, the structure is formed notionally, while the constructor refers mainly to his/her background experience or generic solutions. Partial algorithmic presentation and mathematical implementation of this process with rapid development become possible. Certain steps have already been made in terms of selecting sustainable geometry of structures for plane bar systems. In this vein, it has been proposed to synthesize the plane bar system structure in works [1–4] based on metaheuristic algorithms, approaches are known [5–7] when the initial topology was developed using patterning the groups of geometrically invariable bars, kinematic chains and solid bodies. The following structure forming methods have been developed and improved by several authors:

- excluding elements from the basic structure, which is in certain cases deemed to be excessive [8–11];

- formation of topology on a range of produced joints via triangulation, construction of Voronoi's diagrams, etc. [12–15];

- design of topology based on transformations of system rigidity matrix and analytical equations of structure shape [16–20].

The issue of structure shape design has often been addressed in common iterative optimisation procedures for bearing structures both in normal operations and emergency actions, while genetic algorithms [21–26], in which all of the mentioned forming methods can be used have gained ground. In some works [27–29] the search for the rational topology of plane bar systems has been proposed to be made based on excluding the groups of plate elements from the continuous area, on the borders of which load and kinematical limitations are established. Such an approach is feasible in addressing one-criterion tasks upon the criterion of minimum mass for this area in a variety of plane thickness in some of its sub-areas. However, the wide application of this approach has been inhibited by the high labour input of the computational process.

Works are widespread for the topological design of frames considering the type, calculation and structure designing peculiarities. Algorithms set forth for reinforced concrete frames [30], steel trusses and [31–34], as well as wood and other bar systems [35–37] are fundamental algorithms.

The purpose of the research is to obtain topologies of bar-bearing structures that are rational in terms of material consumption. For this, an approach is used that involves the exclusion of elements from some redundant structure. The article provides the method for the design of plane bar systems based on combined heuristic strategy including the basic principle of optimisation algorithm ACO (ant colony optimization) [38] and FE analysis of the area and volume meshed on bar elements. This method was tested on the formation of flat frames and trusses topologies. The obtained results are compared with the topology optimization method based on genetic algorithms. The proposed method makes it possible to obtain guaranteed topologies that are geometrically invariable.

2. Methods

2.1. Formulation of the topology optimization problem

Let us consider a plane area in which the bar pattern structure will be formed. According to the fundamental provisions of the ACO-algorithm, the topology is formed along the shortest path of the colony between the base points. In this case, the points of application of forces and points of support are considered. Load and kinematical constraints will be input at the area boundary. The minimum bar length will be considered as the search criterion. According to the ACO algorithm basic principle, the minimum length of insects travels way is determined by the preservation of the pheromone they emit on this way that disseminates if a long or irrational way is selected. Drawing an analogy, the stress flow, which is delivered by the path of application of load to supports, will be taken as the pheromone. At the same time, considering the integral plane body modelled using plate elements, the stress flow will have various intensities similarly to the pheromone dissipation degree Fig. 1a.

a)   b)   c)
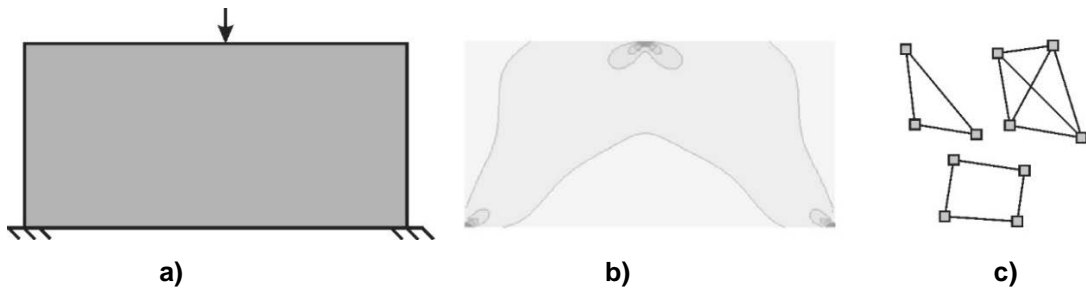
**Figure 1. Initial data for topology design: integral body (a),
arrangement of vertical compressive stress (b), shapes for sampling, composed of bars (c).**

Let us split the area into shapes so that the obtained bar construction has applied forces and supports in bar nodes at the area boundary. Wherein, the patterns shown in Fig. 1 will be used as splitting shapes. Wherein, the stability of geometrical shape should be provided. The obtained bar pattern will contain some possible stress flow paths of various intensities. Thus, we obtain one criterion for the optimisation of the gross-force task.

$$L_s(Y) \rightarrow \min, \tag{1}$$

where L_s is the overall bar length; Y is the set of bar groups, consecutively excluded from the initial framework formed in splitting the plane area.

2.2. Boundary conditions of the task

In respect to the task of obtaining the bearing structure pattern, the following constraints should be obtained:

1. Stability of geometrical shape of the framework at each stage of its formation. For relatively simple splitting and small areas to evaluate this criterion the procedure for evaluating the FE model stiffness matrix determinant can be used effectively. The system is invariable provided that the matrix is positive-definite. If a time-consuming task is solved, then the algorithm will be relevant based on the material solidification hypothesis (links weakening). Considering the results of this work the following analytical signs of stability of the geometrical shape of the system is used:

$$\det[K] \neq 0; \tag{2}$$

$$\alpha_{cond} = cond_\infty [K] \big/ e^m , \tag{3}$$

where $[K]$ is the global stiffness matrix of the finite element model; $cond_\infty [K] = \left\| [K] \right\|_\infty \times \left\| [K]^{-1} \right\|_\infty$ is the matrix of condition number $[K]$; $\left\| \bullet \right\|_\infty$ is the endless matrix norm symbol; m is the number of discs in the system.

The value $\alpha_{cond} < 10^3$ is responsible for the stability of the object's geometrical shape; if $\alpha_{cond} > 10^{100}$ then calculating is interrupted due to obtaining $\det[K] = 0.$ If the determinant of the stiffness matrix is zero, then the topology is geometrically variable. Intermediate results can be interpreted as instant instability of the examined system.

1. The structure calculations are made by the linear finite element (FE) analysis. At the same time, if the frame construction is searched, only bar elements of the bent should be used in the framework (three degrees of freedom in the node), and if a truss is synthesized, then truss finite elements are used (two degrees of freedom in the node).

2. The stiffness of all bars is described correspondingly and accepted the same for all members. The value of the assigned stiffness and loads should enable to perform effective arranging of groups of bars by the intensity of stresses arising in them.

2.3. Algorithm of design topology for plane bar systems

The following sequence of actions is performed:

1. Select primitives, in which the area will be split. Select the shape of the splitting area. The rectangular area is the first preference. At the same time, it is recommended to use splitting shapes of similar type and size. Split the area to obtain a bar pattern.

2. Overlay load and kinematical limitations on the obtained plane model. Forces and stiffness values are set correspondingly. Calculate the stress-strain state of the object to obtain initial forces distribution. In calculating the stresses, bending and compression strains are considered.

3. Rank the stress values. Split the range of stress values into 15–20 intervals. Create a list of groups of bars occurring in each range.

4. Take attempts to exclude any groups of bars with low stresses (making less than 15–20 % from maximal) and groups with the least number of bars. Upon excluding each group, the stability of the geometrical shape of the system is checked (see constraint one). If the system becomes alterable, then group exclusion is not allowed. It has been established empirically that in the first implementation of this stage the number of excluded groups of bars should not exceed 3. Late in framework forming, it is possible to try excluding one or several groups with relatively high stress. If the number of groups in which exclusion the system does not pass into a geometrically invariable state equals zero, then one may talk about the ultimate pattern.

In excluding the groups in externally statistically indeterminate systems with supports in a form of rigid restraints, it may prove that the framework degenerates: splits into parts, each of which has shortest paths from the load to its support Fig. 1b. For solving this problem, the fundamental propositions of graph theory are used. Let us present the sampled bar structure as a directed graph $G(B, N),$ consisting of

several vertices N and edges B. In this case, it is considered that the vertex is a nodal joint, and the edge is a bar. The presence of at least one path in the graph from one supporting node to another is checked. If there is only one such path, the exclusion of the group of bars passing through the supporting nodes is not allowed. The condition of path existence is formalised by the construction of the incident matrix and reachability matrix for the graph $G\left(B,N\right)$.

5. Calculate the system obtained at stage 4 by the FE analysis to obtain a new stress arrangement. Then continue with stage 4.

2.4. Forming trusses topology

In designing the truss patterns there are stages implemented for task solving similar to that of the rigid frames with the following differences:

- in splitting the area, the truss bar elements are used, only stresses from axial forces are used. The splitting grid should be formed in such a way so that one side of the spiting primitive is not smaller in size than any structural element, that is the structural element of the future framework should contain one finite element of the calculation model.
- in implementing the exclusion attempts at each stage of framework formation, only one group of bars should be excluded, in which the priority is first given to small stress values, then to the number of bar elements in the group. The Search condition for paths in this graph $G\left(B,N\right)$ is not applied.

2.5. FE analysis for topology design

To determine the components of the stress-strain state of elements in the redundant topology of the rod system, a linear static calculation is used. For the design of flat frames, bar elements are used with three degrees of freedom each in the node. This is a vertical, horizontal displacement and rotation in the plane of the frame. For the topology of trusses, a bar element with two degrees of freedom (linear displacements in a plane) is used. In the topology, all bars can be excluded or groups of boundary elements can be formed that cannot be excluded. If boundary elements are present in the topology, then their stiffnesses are set for 2-3 orders of magnitude higher than for the rest of the bars. This technique makes it possible to avoid their exclusion in the search process.

The FE mesh for trusses must be formed so that one finite element corresponds to one bar of the truss. There is no such restriction for frame structures. The size of the FE mesh significantly affects the amount of computation during the search. When a group of elements is excluded from the topology, the FE model is rebuilt. In this case, the element is excluded not by creating zero stiffnesses for it, but by removing the topology matrix of the FE model. The reason for this is related to the estimation of the determinant of the stiffness matrix.

3. Results

3.1. Design frame topology for the symmetrically loaded area. Example 1

Let us consider the design of the framework on the given rectangular area at the given load and the kinematical limitations shown in Fig. 2a. Sample this area to elementary triangles composed of plane bar finite elements (Fig. 2b). Force P is applied in the middle of the span. P force and stiffness value is set in due form: P = 500 kN, the bar cross-section area A = 0.4 m², central moment of inertia lx = 1.3E10⁻⁴ m⁴. The X-axis is perpendicular to the longitudinal axis Z of the bar and the plane of the frame (Fig. 2c). Consider the axial force values as one of the criteria to estimate the possible exclusion of bar groups. For all bars in this and the following examples, a material with an Young's modulus E = 70000 MPa, and density of 27 kN/m³ was assigned.
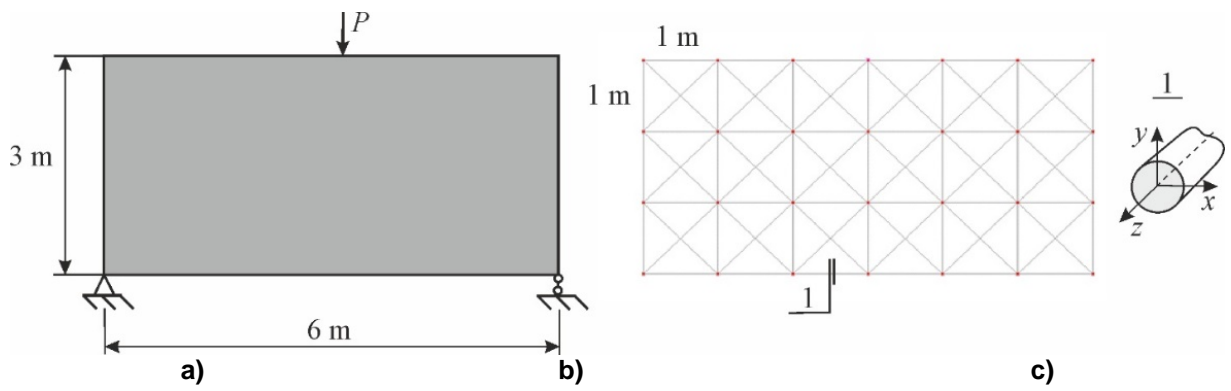
Figure 2. Baseline data for frame structure design.

Upon system calculation, rank the obtained stress components by splitting the obtained values into 16 equal intervals. A different number of bars may occur in each of such intervals. These data are presented in Fig. 3, via a colour-coded indication. The grey lines show the bar's excluded at the current stage of the search.

In implementing attempts to exclude bars for each iteration, one or several groups of bars were excluded. At the same time, to determine what groups are to be excluded from the available, the criterion of Eq. (1) was used. The intermediate results at the third iteration of the structure search are shown in Fig. 3b. Eventually, at the last iteration, the configuration shown in Fig. 3c is obtained. The result of structure design accurately coincided with the precise analytical solution by Goldstein [39], obtained in solving the task of the optimal search for elastic lines of bar systems based on the calculus of variations.
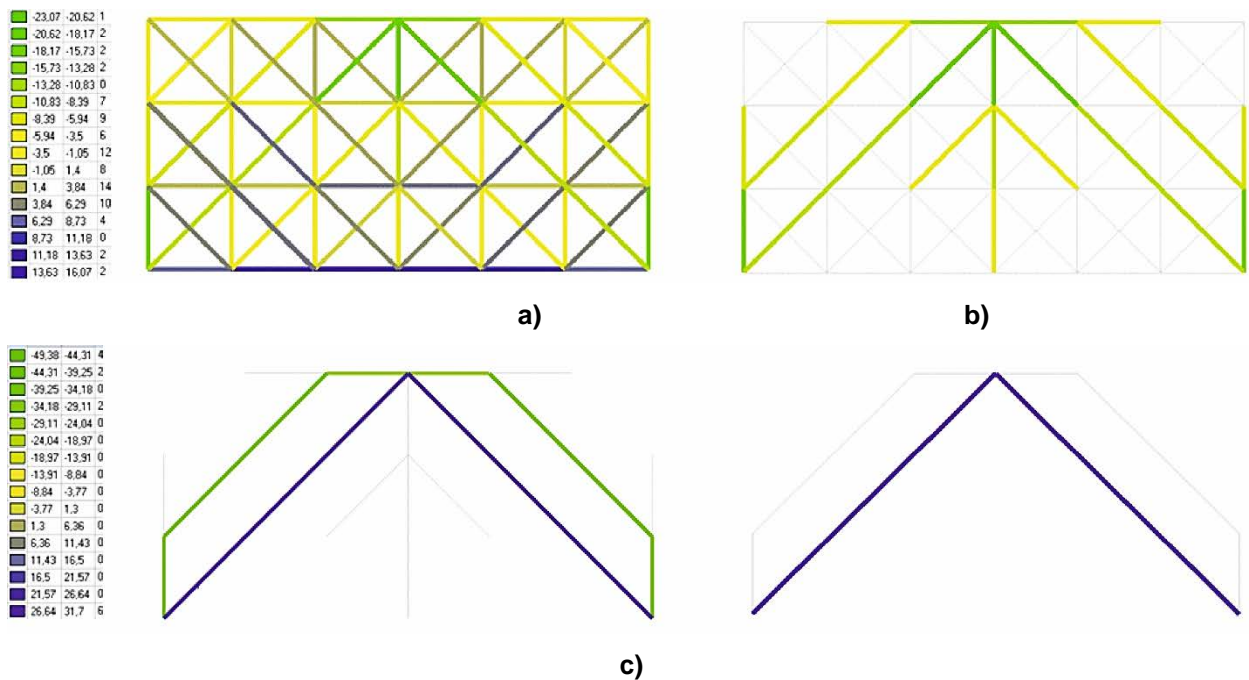
Figure 3. Results of single-span system design loaded by one force in the span centre: the first and second columns in the color legends show the boundaries of the intervals for the values of axial forces (tonnes). The third column is the number of bars in this interval.

3.2. Design frame topology for an asymmetrically loaded area. Example 2

Synthesize the frame construction topology on the rectangular area with limiting conditions shown in Fig. 4a. Split this area into triangle primitives consisting of frame bar elements, see Fig. 4b. The value of forces and geometric characteristics of bars are taken the same as in Example 1.

a)   **b)**
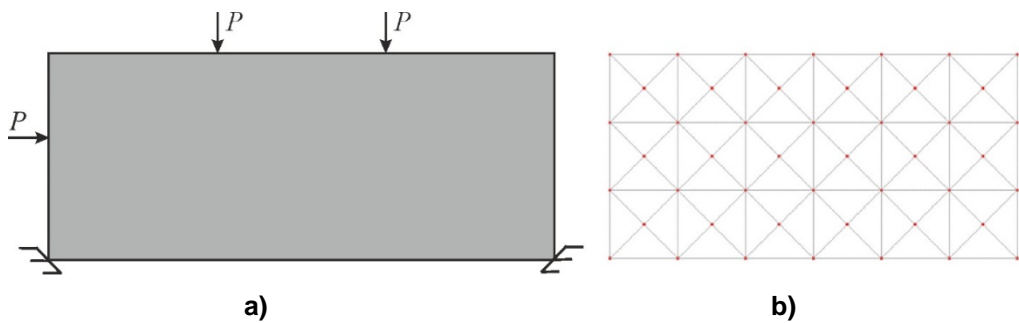
Figure 4. Load diagram for frame topology design.

Solutions are searched similarly to Example 1. The process of topology design was performed in 9 iterations presented in Fig. 5. At the same time, at each iteration, several attempts were taken to exclude the groups with the preliminary evaluation of the possibility of such an exclusion.

Considering the kinematical limitations of Example 2, shown in Fig. 4, a situation is possible when the least length structure is discrete for each support. So, to obtain the ultimate framework shown in Fig. 6, an additional knockout criterion is used according to the arrangement of the existing continuous path between bearing summits in the oriented unweighted graph $G(B,N)$. It should be emphasized that it was not necessary to use the additional criterion of continuous path existence in the topology graph between bearing nods in Example 1, as parts of the framework in abruption of topology between supports turned out to be sub static.

9
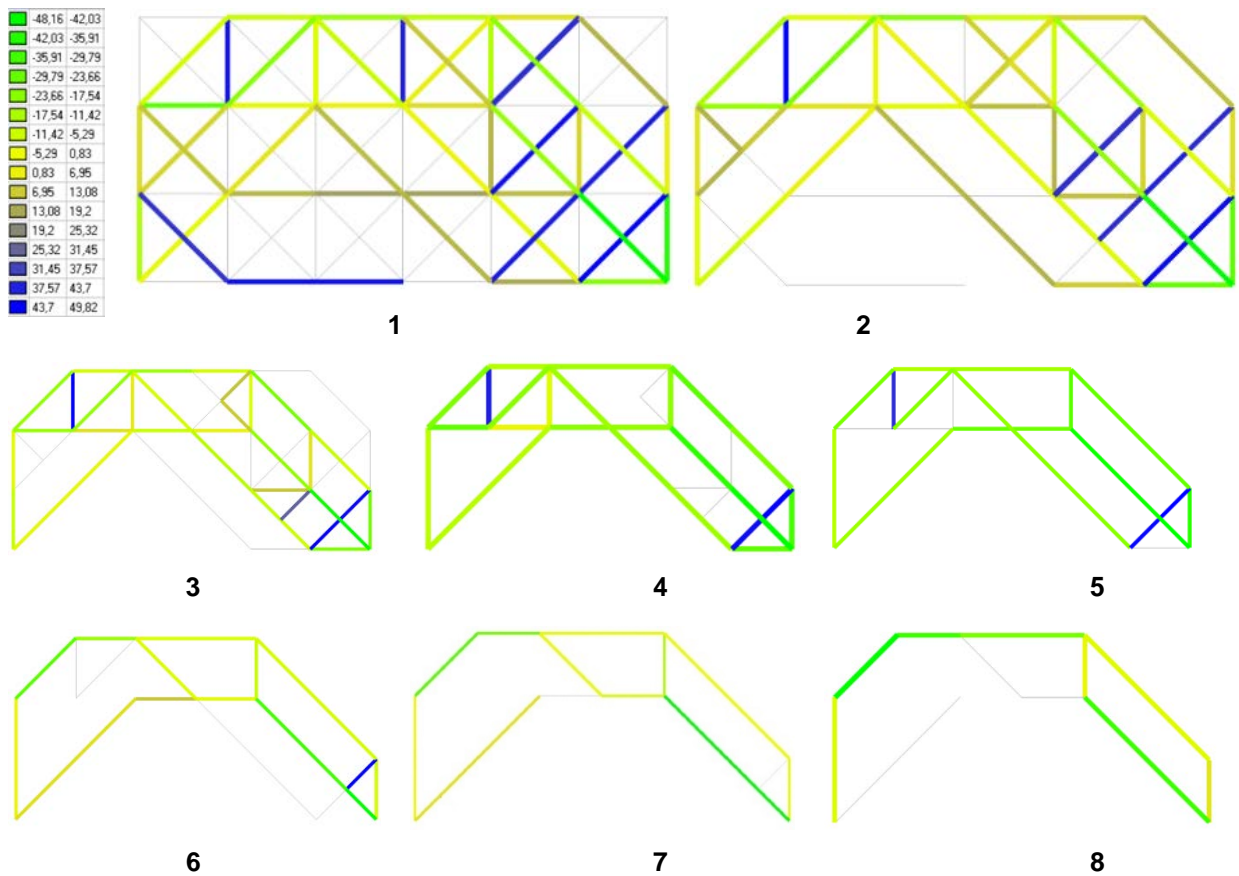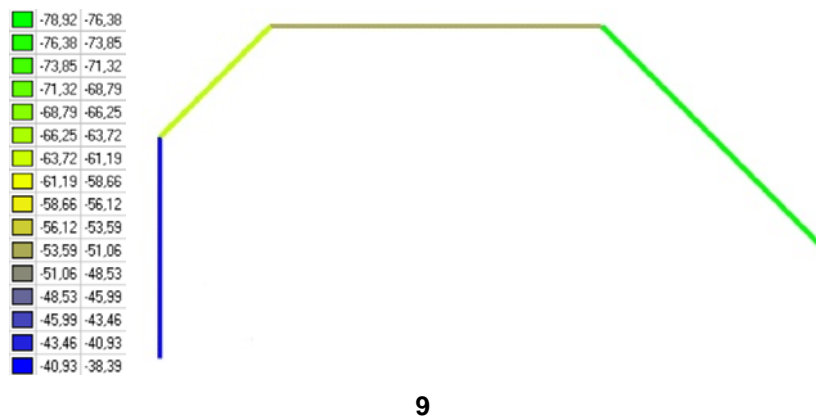
**Figure 6. Stages of frame topology design: the colours shown the levels
of axial forces in the bars**.

3.3. Truss structure design. Example 3

Let us consider an example of a rectangular area design (Fig. 7). The supports are taken as the hinged-fixed. The area has dimensioned a = 4.064 m (160 in.), b = 0.762 m (30 in.). The value of point forces and geometric characteristics of truss bar elements were accepted from Example 1. Solution search stages are shown in Fig. 8.

Initially, braces in the middle truss area were excluded with axial force values [–0.34; 6.4] (see scheme I on Fig. 8). In attempting to exclude additionally one more group of three rods at this stage, for which the value of the force belongs to the interval [–0.34; –7.32], the system becomes geometrically invariable. Upon calculating the framework obtained at stage I, perform finite element analysis and new force distribution to be analysed at stage II. At the second stage in the provision of stability of geometrical shape condition and the minimum length of the output, structure bars only one group of the two bars of side plates was excluded with the axial forces in the interval [27.84; 34.69]. In the attempt to exclude more groups, these limitations were not put into effect. Further, the calculation was performed and axial force distribution at stage III was obtained. At this stage, the exclusion of any single group resulted in the violation of limitations, so efforts were taken to exclude 2 and more bar groups. This resulted in the exclusion of two groups. The first group consists of five bars including end and middle pickets and end panel upper strake bars. Axial forces for these bars belong to the range [–7.77; 0.43] (see scheme I Fig. 8). The second group consists of two bars of middle panel lower core with the axial forces range of [8.62; 16.81]. This resulted in the topology shown in Fig. 9.

4. Discussion

The solution obtained in Fig. 9, accurately coincides with Kirsch truss structural design result (Fig. 10a) [8, 11], where based on the genetic algorithm 19 topology variants were obtained. The three of such variants are shown in Fig. 10b-d. The analysis of all the 19 topologies [8] shows that the solution given in Fig. 9 is the only one of all the solutions according to the geometrically invariable topology. The rest of the solutions are either geometrically unstable or have large length bars. The absence of bars was simulated by setting fragility elements but not the full removal from the topology; hence system alterability was not recorded. The use of Eqs. (2) and (3) in the proposed algorithm ensures the registration and removal from consideration of such topologies.
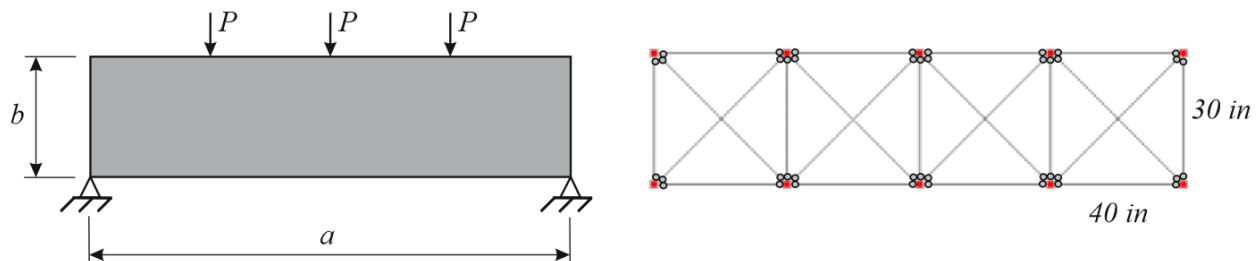
Figure 7. Rectangular area and its sampling for truss topology formation.
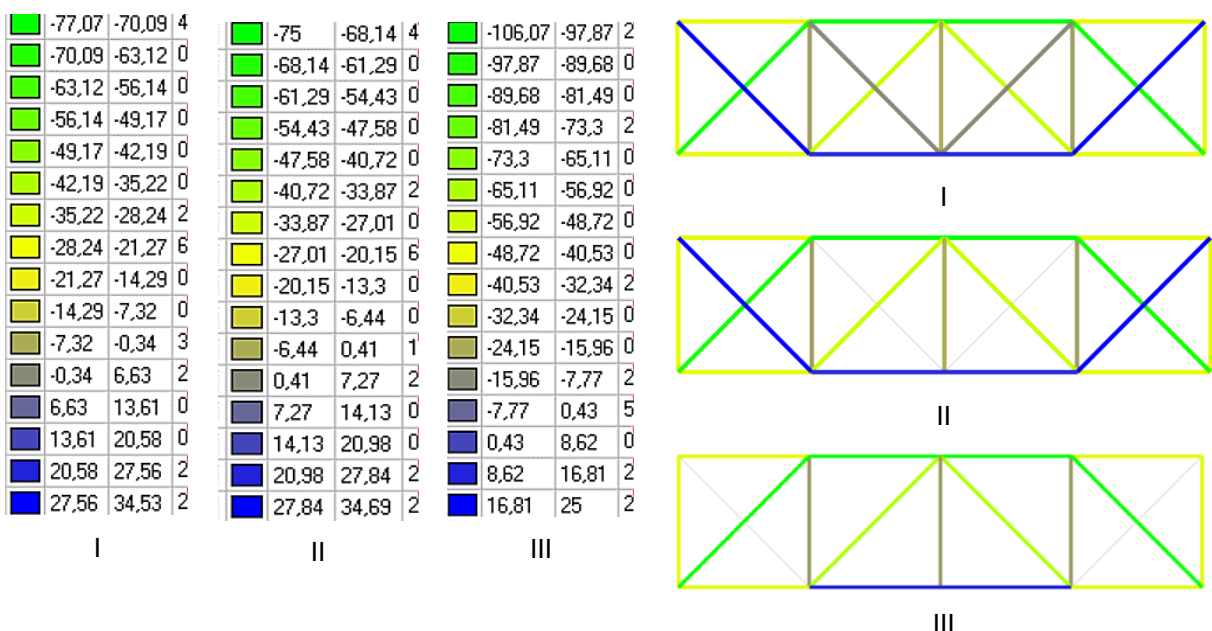
Figure 8. Truss topology formation process: I-III – search steps.
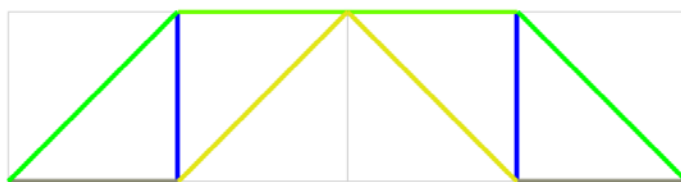
Figure 9. Resulting truss topology.
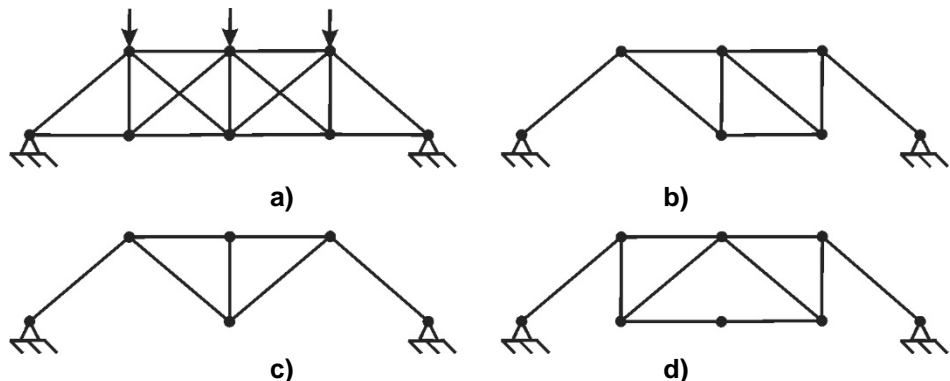
Figure 10. Some solutions for optimisation of Kirsch truss topology.

5. Conclusion

The method of plane bar systems rational topology design has been developed based on sampling the rectangular area to bar primitives. Basic principles of ant colony imitation and search for ways in oriented graphs have been taken as a basis. The efficiency of the proposed method has been proved based on the coincidence of the obtained results with the common solutions for standard test tasks. Such an approach for frameworks design can be recommended to be used in forming layout arrangements for frame buildings and structural systems.

References

1. Wang, L., Zhang, H., Zhu, M., Chen, Y.F. A new Evolutionary Structural Optimization method and application for aided design to reinforced concrete components. Structural and Multidiscipli-nary Optimization. 2020. 62 (5). Pp. 2599–2613. DOI: 10.1007/s00158-020-02626-z

2. Xia, Y., Langelaar, M., Hendriks, M.A.N. A critical evaluation of topology optimization results for strut-and-tie modeling of rein-forced concrete.Computer-Aided Civil and Infrastructure Engi-neering. 2020. 35 (8). Pp. 850–869. DOI: 10.1111/mice.12537

3. Kociecki, M., Adeli, H. Shape optimization of free-form steel space-frame roof structures with com-plex geometries using evolu-tionary computing. Engineering Applications of Artificial Intelli-gence. 2015. 38. Pp. 168–182. DOI: 10.1016/j.engappai.2014.10.012

4. Degertekin, S.O., Lamberti, L., Ugur, I.B. Sizing, layout and topology design optimization of truss structures using the Jaya algorithm. Applied Soft Computing Journal. 2018. 70. Pp. 903–928. DOI: 10.1016/j.asoc.2017.10.001

5. Wang, H., Yu, W., Chen, G. An approach of topology optimization of multi-rigid-body mechanism. CAD Computer Aided Design. 2017. 84. Pp. 39–55. DOI: 10.1016/j.cad.2016.12.002

6. Shahabsafa, M., Fakhimi, R., Lei, W., He, S., Martins, J.R.R.A., Terlaky, T., Zuluaga, L.F. Truss to-pology design and sizing optimization with guaranteed kinematic stability. Structural and Mul-tidisciplinary Optimization. 2021. 63(1). Pp. 21–38. DOI: 10.1007/s00158-020-02698-x

7. Pozhbelko, V. A unified structure theory of multibody open-, closed-, and mixed-loop mechanical systems with simple and multiple joint kinematic chains. Mechanism and Machine Theory. 2016. 100. Pp. 1–16. DOI: 10.1016/j.mechmachtheory.2016.01.001

8. Balling, R.J., Briggs, R.R., Gillman, K. Multiple optimum size/shape/topology designs for skeletal structures using a genetic algorithm. Journal of Structural Engineering-ASCE. 2006. 132(7). Pp. 1158–1165. DOI: 10.1061/(ASCE)0733-9445(2006)1-32:7(1158)

9. Li, Z., Luo, Z., Zhang, L.C., Wang, C.H. Topological design of pentamode lattice metamaterials using a ground structure method. Materials and Design. 2021. 202 . DOI: 10.1016/j.matdes.2021.109523

10. Chen, M., Zhao, Y., Xie, Y. Topology optimization and additive manufacturing of nodes in spatial structures. Tumu Gongcheng Xuebao/China Civil Engineering Journal. 2019. 52(2). Pp. 1–10.

11. Serpik, I.N., Alekseytsev, A.V., Balabin, P.Y. Mixed approaches to handle limitations and execute mutation in the genetic algorithm for truss size, shape and topology optimization. Periodica Polytechnica Civil Engineering. 2017. 61(3). DOI: 10.3311/PPci.8125

12. Cucinotta, F., Raffaele, M., Salmeri, F. A stress-based topology optimization method by a Voronoi tessellation Additive Manufacturing oriented. International Journal of Advanced Manufacturing Technology. 2019. DOI: 10.1007/s00170-019-03676-4

13. Radhi, A., Iacobellis, V., Behdinan, K. Manipulation of topologically optimized structures using graphic statics. Materials and Design. 2021. 198. DOI: 10.1016/j.matdes.2020.109286

14. Kirsanov, M.N. Analytical calculation of deflection of a multi-lattice truss with an arbitrary number of panels. International Journal for Computational Civil and Structural Engineering. 2020. 16(3). Pp. 23–29. DOI: 10.22337/2587-9618-2020-16-3-23-29

15. Spinos, A., Carroll, D., Kientz, T., Yim, M. Topological Reconfiguration Planning for a Variable To-pology Truss. Journal of Mechanisms and Robotics. 2021. 13(4). DOI: 10.1115/1.4050530

16. Fukada, Y. Support-free robust topology optimization based on pseudo-inverse stiffness matrix and eigenvalue analysis. Structural and Multidisciplinary Optimization. 2020. 61(1). Pp. 59–76. DOI: 10.1007/s00158-019-02345-0

17. Kirsanov, M.N. Installation diagram of the lattice truss with an arbitrary number of panels. Magazine of Civil Engineering. 2018. 81(5). Pp. 174–182. DOI: 10.18720/MCE.81.17

18. Brütting, J., Fivet, C., Senatore, G. Struct. Archit. Bridg. Gap Crossing Borders – Proc. 4th Int. Conf. Struct. Archit. ICSA. 2019. Pp. 221–228. DOI: 10.1201/9781315229126-27

19. Choi, S.-K., Patel, J. Optimal design of cellular structures under random fields. Journal of En-gineering Design. 2011. 22 (9). Pp. 651–668. DOI: 10.1080/09544828.2010.505185

20. Kirsanov, M.N. Analytical dependence of the deflection of the spatial truss on the number of panels. 2020. Magazine of Civil Engineering. 96 (4), pp. 110–117. DOI: 10.18720/MCE.96

21. Abdi, M., Ashcroft, I., Wildman, R. Topology optimization of geometrically nonlinear structures using an evolutionary optimization method. Engineering Optimization. 2018. 50(11). Pp. 1850–1870. DOI: 10.1080/0305215X.2017.1418864

22. Alekseytsev, A.V., Akhremenko, S.A. Evolutionary optimization of prestressed steel frames. Magazine of Civil Engineering. 2018. 81(5). DOI: 10.18720/MCE.81.4

23. Tamrazyan, A., Alekseytsev, A. Evolutionary optimization of reinforced concrete beams, taking into account design reliability, safety and risks during the emergency loss of supports. E3S Web Conf. 2019. DOI: 10.1051/e3sconf/20199704005

24. Forman, P., Gaganelis, G., Mark, P. Optimization-based design | Optimierungsgestützt entwerfen und bemessen.Bautechnik. 2020. 97(10). Pp. 697–707. DOI: 10.1002/bate.202000054

25. Prokurov, M., Indykin, A., Alekseytsev, A. Increasing the reliability of the soil slopes design using evolutionary modelling. MATEC Web Conf. 2018. DOI: 10.1051/matecconf/201825104017

26. Serpik, I.N., Alekseytsev, A.V. Optimization of frame structures with possibility of emergency ac-tions. Magazine of Civil Engineering. 2013. 44 (9). DOI: 10.5862/MCE.44.3

27. Jain, N., Saxena, R. Effect of self-weight on topological optimization of static loading structures. Alexandria Engineering Journal. 2018. 57 (2). Pp. 527–535. DOI: 10.1016/j.aej.2017.01.006

28. Niu, C., Zhang, W., Gao, T. Topology optimization of continuum structures for the uniformity of con-tact pressures.Structural and Multidisciplinary Optimization. 2019. 60(1). Pp. 185–210. DOI: 10.1007/s00158-019-02208-8

29. Alekseytsev, A.V., Al Ali, M. Optimization of hybrid I-beams using modified particle swarm method. Magazine of Civil Engineering. 2018. 83(7). DOI: 10.18720/MCE.83.16

30. Resmy, V.R., Rajasekaran, C. Topology Optimization of Concrete Dapped Beams Under Multiple Constraints. 2020. DOI: 10.1007/978-981-15-3215-3_5

31. Kazemi, H., Norato, J.A. Topology optimization of lattices with anisotropic struts. Structural and Multidisciplinary Optimization. 2021. 63(4). Pp. 1653–1668. DOI: 10.1007/s00158-020-02822-x

32. Zinkova, V.A. Optimization of the structure of flat metal tube trusses. Innovations and Technologies in Construction. BUILDINTECH BIT 2020. Lecture Notes in Civil Engineering, vol 95. Springer, Cham. DOI: 10.1007/978-3-030-54652-6_32

33. Hooshmand, A., Campbell, M.I. Truss layout design and optimization using a generative synthesis approach. Computers and Structures. 2016. 163. Pp. 1–28. DOI: 10.1016/j.compstruc.2015.09.010

34. Zhao, X., Shea, K. Intelligent generation and design of spatial truss structures. Jianzhu Jiegou Xuebao/Journal of Building Structures. 2010. 31(9). Pp. 63–69.

35. Dzwierzynska, J. Multi-objective optimizing curvilinear steel bar structures of hyperbolic paraboloid canopy roofs. Buildings. 2020. 10(3). DOI: 10.3390/buildings10030039

36. Mam, K., Douthe, C., Le Roy, R., Consigny, F. Shape optimization of braced frames for tall timber buildings: Influence of semi-rigid connections on design and optimization process. Engineer-ing Structures. 2020. 216. DOI: 10.1016/j.engstruct.2020.110692

37. Alekseytsev, A., Botagovsky, M., Kurchenko, N. Cost minimization for safety enhancing of timber beam structures in historical buildings. E3S Web Conf. 2019. Vol. 97. Art. No. 03002. DOI: 10.1051/e3sconf/20199703002

38. Ribeiro, S.F., Bastos-Filho, C.J.A. (2020) Assessing Ant Colony Optimization Using Adapted Net-works Science Metrics. Hybrid Intelligent Systems. HIS 2018. Advances in Intelligent Systems and Computing. 2019. Vol. 923. DOI: 10.1007/978-3-030-14347-3_13

39. Goldshteyn, Yu.B., Solomeshch, M.A. Variatsionnyye zadachi statiki optimalnykh sterzhnevykh sistem [Variational problems of statics of optimal bar systems]. L.: Izd-vo LGU, 1980. 208 p. (rus)

Information about authors:

Anatoly Alekseytsev, *Doctor of Technical Science*
ORCID: https://orcid.org/0000-0002-4765-5819
E-mail: aalexw@mail.ru

Natalya Kurchenko, *PhD of Technical Science*
ORCID: https://orcid.org/0000-0002-5434-4277
E-mail: ms.kurchenko@mail.ru

Workability of warm mix asphalt additives
and mechanical property characterization of asphalt concrete

S.Yu. Obukhova[1] ✉ iD **, E.V. Korolev[2]** iD **, A.N. Novikov[3], A.G. Shevtsova[4]**

[1] *Moscow State Civil Engineering University (National Research University), Moscow, Russia*

[2] *St. Petersburg State University of Architecture and Civil Engineering, St. Petersburg, Russia*

[3] *Orel State University, Orel, Russia*

[4] *V.G. Shukhov Belgorod State Technological University, Belgorod, Russia*

✉ *SHehovtsovaSYU@mgsu.ru*

Keywords: warm mix additives, mechanical properties, rheology, activation energy, workability

Abstract. Warm mix asphalt (WMA) technology offers a promising solution to address the ecological concern of asphalt mixtures. Warm asphalt (WA), is expected to be a sustainable paving technology that integrates energy conservation, noise reduction, and performance optimization. This study aims to characterize and compare the engineering properties of WA mixture prepared with various WMA additives. To achieve this goal, WA mixtures were prepared with seven different WMA additives, including Adgezol 3-TD, DAD-TA2, Azol 1007, Cecabase RT 945, DAD-TA, Doros-T and Amdor TS-1. Comprehensive laboratory tests were conducted to characterize their workability and engineering properties, including penetration, fragility and softening temperature of bitumen, and dynamic viscosity. According to the experimental results, WMA additives including Adgezol 3-TD, DAD-TA2, Doros-T and Azol 1007 provided a 30% reduction in dynamic viscosity of modified bitumen; however, with such WMA additives as DAD-TA, Cecabase RT 945 and Amdor TS-1 no reduction in dynamic viscosity of modified bitumen was observed. Coefficients that consider the complex of physical, mechanical, technological and economic properties, as well as a generalized criterion (Fk) for the technical and economic efficiency of chemical additives were developed. It was proposed to divide warm mix additives into two groups: additives that improve the efficiency of bitumen by 5% (Fk≥1.05) or more, as well as additives that do not improve the efficiency of bitumen by more than 5% (Fk≤1.05), that is, have no significant effect on the properties. Comprehensive laboratory tests were conducted to characterize their workability and mechanical properties, including moisture susceptibility. According to the experimental results, only with Cecabase RT 945 and DAD-TA one can achieve compliance with regulatory requirements for hot asphalt concrete. The influence of warm mix additives on the structure of bitumen was studied. Using the Arrhenius equation, the change in the activation energy required to overcome the potential (kinetic) barrier of the bitumen with the surfactants had been calculated. The workability of warm mix additives was investigated, on the basis of which their classification was proposed.

1. Introduction

The use of technologies of warm asphalt concrete, based on an initially lower preparation temperature, allows you to ensure both the achievement of an economic effect and the reduction of environmental pressure in the process of manufacturing the road surface [1]. Thus, French researchers have found that the use of warm asphalt-concrete mixtures can reduce greenhouse gas emissions by 12 % and flue gas emissions by 25 % [2]. Modern technology for the production of warm asphalt concrete is based on the use of technological, physical and chemical methods that ensure the achievement of the required viscosity of bitumen at low temperatures for the production of road asphalt pavement [2, 3].

There are several possible options for producing warm asphalt concrete mixtures: bitumen foaming by means of foaming additives (zeolites) or mechanical foaming systems; organic plasticizing additives containing wax and / or paraffin; chemical additives (surfactants); combined technologies, including the simultaneous use of several of the above methods [4–12].

Bitumen foaming technologies that use water as the foaming component are currently considered cost-effective. However, they are associated with high initial equipment costs and are limited by the lower operating temperature due to the condensation temperature of water vapor. In addition, residual moisture may enter the asphalt concrete to be laid, which will contribute to the destruction of the road surface [4, 5].

The use of organic additives or waxes leads to a decrease in the melting point of bitumen, which allows the production of mixtures at lower temperatures [6, 7]. However, the use of wax in the composition of bitumen reduces the crack resistance of both the binder and asphalt concrete based on it, and may not be effective in areas with low temperatures [8].

Emergence of warm-mix additives has alleviated the high demand for heat energy in asphalt plant producer or in the paving process itself. Given this development, several studies have reported that warm mix asphalt (WMA) additives in asphalt mixture could reduce the required temperatures for mixing and compaction of asphalt mixtures by up to 20–40 °C through a reduction in binder viscosity and chemical interaction between WMA additives and neat asphalt binder [13, 14]. The use of chemical additives does not require additional costs for upgrading the equipment, and as a rule the additives had mixes with bitumen in the tanks of the mixing plant or are introduced by means of existing automatic equipment for the introduction of conventional adhesive additives [15–22]. This determines the prevalence of such a technological solution in the global construction industry, which is confirmed by foreign researches. The method of preparation of the asphalt concrete sample depends on the type of tests. Nevertheless, it is worth noting that better performance of warm asphalt concrete is achieved with rotational compaction on the gyrator [15, 16], because this method simulates the impact of the roller during compaction in real operating conditions. The authors of [18] studied the influence of chemical additives on the tensile strength coefficient (TSR) which is an indicator that characterizes the effect of moisture on the properties of asphalt concrete. The authors in [19] considered whether all types of asphalt concrete mixtures are suitable for the preparation of warm asphalt concrete mixtures. It has been found that asphalt mixes with a high binder content, such as AR-AC-13, are not suitable for the preparation of warm asphalt mixes. In [20] the influence of the compaction temperature on the bulk properties of asphalt concrete was studied. It is established that in the temperature range of 122–135 °C, an improvement in the bulk properties of asphalt concrete is observed. The authors in [21, 22] investigated the effect of chemical additives on the physical and mechanical properties of asphalt concrete containing recycled asphalt pavement (RAP). It was found that additives for warm asphalt concrete, which is containing RAP, do not allow improving the moisture resistance (TSR). The authors of [23, 24] indicated that the use of binder's viscosity is not sufficient to quantify the production temperatures or the overall workability, specifically for modified asphalt binders and RAPM containing asphalt mixtures. Eventually, direct evaluation of production temperature based on workability should be used for WMA. Several factors, including additive type and dosage, the grade of asphalt binder, and aggregate gradation affect the strength characteristics WMA [25–27].

Moreover, insufficient data for the computation of mixing and compaction temperature with the utilization of workability devices entails rigorous research to form a concrete conclusion. The analysis of the available scientific literature shows that the works are mainly aimed at studying the influence of chemical additives on the properties of warm asphalt concrete mixtures, and there are no research articles aimed at studying their influence on the properties and structure of bitumen, the main structure-forming component of asphalt concrete that determines its properties. However, it is worth noting that the occurrence of fatigue defects and low-temperature cracking of asphalt concrete by 60–90 % depend on bitumen, and the formation of plastic track by 40 % [29–31]. Therefore, the study of the effect of warm additives on the properties of bitumen will make it possible to predict the properties of asphalt concrete at the early stages of the study. This makes this study relevant. Therefore, the main purpose of the study is to establish the workability of chemical warm-mix additives. To do this, it is necessary to solve the problems of determining the influence of various chemical warm-mix additives on the properties and structure of bitumen 70/100.

This study is expected to provide extensive information for the established workability of chemical warm additives, which will allow predicting the mechanical properties of asphalt concrete modified with warm mix additives at an early stage.

2. Materials and Methods

The study of the effect of chemical additives on bitumen was carried out on chemical additives presented on the Russian market and recommended for the production of warm asphalt concrete mixtures:

- Adgezol 3-TD which is an organic composition obtained on the basis of the products of the interaction of tall oil with polyalkyl polyamine compounds, production by LLC "Basis";
- Azol 1007 which is a surfactant of the ampholytic type with a complex of plasticizing additives, production by LLC "Kotlas Chemical Plant";
- Cecabase RT 945, the information about the composition is not available in the public domain, production by Arkema (France);
- DAD-TA which is a highly active liquid composition of surfactants based on polyamines, production by Selena LLC;
- DAD-TA2 which is a specially modified amphoteric surfactant, production by Selena LLC;
- Doros-T, the information about the composition is not available in the public domain, production by Doros LLC,
- Amdor TS-1 that is a mixture of cationic surfactants, production by Uralkhimplast-Amdor LLC.

As a binder, bitumen of the BND 70/100 brand, production by Lukoil LLC, was considered. The properties of BND 70/100 are presented in Table 1.

Table 1. Physical and mechanical properties of BND 70/100.

Indicator name	Requirement of Russian State Standard GOST 33133	Actual value
The depth of penetration of the needle at a temperature of 25 °C, mm $^{-1}$	71–100	72
The depth of penetration of the needle at a temperature of 0 °C, mm $^{-1}$, no less than	21	24
Ring and ball softening temperature, °C, no less than	+ 47	+ 50
Fraass fragility temperature, °C, no more than	− 18	− 19

Mineral powder MP-1 (an inactive carbonate rock dolomite), crushed granite of 5–20 mm size and stone mineral (crushed granite screenings of 0–5 mm size) were used as mineral materials for the preparation of asphalt concrete type B according to Russian State Standard GOST 9128.

For this type of asphalt concrete, samples must be formed in according with Russian State Standard GOST 12801. However, this method is based on the formation of asphalt concrete sample under constant vertical load from a hydraulic press. Whereas in real conditions of road construction in the process of compaction of asphalt concrete pavement, the load from the roller is rotational and variable. The main property that characterizes the processability of a warm asphalt concrete mixture at low temperatures is its ability to achieve the required density with minimal effort during the compaction process. The method of compaction of asphalt concrete mixture (ACM) samples using the device of rotational (gyration) compaction, which is achieved by combining the shear force during rotation and the vertical resulting force, allows simulating to the process of compaction of asphalt concrete mixtures in the road surface in the laboratory as close to the real conditions as possible. The device "Laboratory gyratory compactor Cooper CRT-GYR" (hereinafter – gyrator) provides a record of the number of rotations (revolutions) required to achieve a given density of asphalt concrete. Therefore, this method was chosen for scientific research.

The studies considered asphalt concrete of type B with a given density of 2380 ± 10 kg/m^3, the consumption of chemical additives corresponded to the manufacturers' recommendations. The asphalt concrete mixture was prepared at a temperature of 150 °C; then, the mixture was kept in a drying cabinet at a temperature of 110 °C for 2 hours to stabilize the temperature of the mixture by volume. Compaction of mixtures with various chemical additives was carried out at a temperature of 110 °C until the specified density of asphalt concrete was reached. At the same time, for ACM containing the chemical additive under

study, the number of the gyrator revolutions required to achieve the given density of asphalt concrete at a sample height of 115 mm was recorded.

When evaluating the effectiveness of the chemical additives used, their influence on the physical, mechanical and technological properties of the bitumen binder, as the main structure-forming component of asphalt concrete, was evaluated according to the following properties:

- The depth of penetration of the needle, at a temperature of 25 °C and 0 °C, according to Russian State Standard GOST 33136;
- Ring and ball softening temperature, °C, according to Russian State Standard GOST 33142;
- Fraass fragility temperature, °C, according to Russian State Standard GOST 33143;
- Dynamic viscosity at a shear rate of 100 s^{-1} according with Russian State Standard GOST 33137, on the Anton Paar Modular Compact Rheometer Physical MCR 101.

Three samples were prepared for each investigated chemical additive. No less than three measurements were made for each test method according to the requirements of Russian State Standard. The results are presented as an average value.

Based on the multi criteria optimization method [32], quality and efficiency criteria were developed. The effectiveness of the surfactant was evaluated according to the generalized criterion of technical and economic efficiency $\left(F_k\right)$, which takes into account both the set of operational properties and economic indicators, calculated by the formula:

$$F_k = K_q \cdot K_{ec}. \tag{1}$$

The coefficient of economic efficiency $\left(K_{ec}\right)$ was determined by the formula:

$$K_{ec} = \dfrac{1}{1 + P_{cd} \cdot \dfrac{C_{hd}}{C_b}}, \tag{2}$$

where P_{cd} and C_{hd} are consumption, kg/t, and cost, rub/t, of the chemical surfactant, respectively; C_b is the cost of oil bitumen, rub/t.

Operational properties were evaluated by a generalized quality coefficient $\left(K_q\right)$, which takes into account the complex of physical, mechanical and technological properties of bitumen and asphalt concrete mixture:

$$K_q = \sqrt[6]{k_{compaction} \cdot k_{P_{25}} \cdot k_{P_0} \cdot k_{T_{fr}} \cdot k_{T_{softening}} \cdot k_\eta}, \tag{3}$$

where $k_{compaction} = \dfrac{N_{compaction}}{N'_{compaction}}$ is a criterion that takes into account the effect of a chemical additive on the compaction of an asphalt concrete mixture equal to the ratio of the number of revolutions required for compacting an asphalt concrete mixture without a chemical additive to the number of revolutions required for compacting an asphalt concrete mixture with a chemical additive;

$k_{P_{25}} = \dfrac{P_{25}}{P'_{25}}$ is a criterion that takes into account the effect of a chemical additive on the conditional viscosity equal to the ratio of the depth of penetration of the needle at 25 °C into bitumen without a chemical additive to the depth of penetration of the needle at 25 °C into bitumen with a chemical additive;

$k_{P_0} = \dfrac{P'_0}{P_0}$ is a criterion that takes into account the effect of a chemical additive on the conditional viscosity equal to the ratio of the depth of penetration of the needle at 0 °C in bitumen with a chemical additive to the depth of penetration of the needle at 0 °C in bitumen without a chemical additive;

$k_{T_{fr}} = \dfrac{T'_{fr}}{T_{fr}}$ is a criterion that takes into account the effect of a chemical additive on the crack resistance of bitumen equal to the ratio of the fragility temperature of bitumen with a chemical additive to the fragility temperature of bitumen without a chemical additive;

$k_{T_{softening}} = \dfrac{T_{softening}}{T'_{softening}}$ is a criterion that takes into account the effect of a chemical additive on the heat resistance of bitumen equal to the ratio of the softening temperature of bitumen without a chemical additive to the softening temperature of bitumen with a chemical additive;

$k_{\eta} = \dfrac{\eta'}{\eta}$ is a criterion that takes into account the effect of a chemical additive on the initial dynamic viscosity of bitumen at a temperature of 70 °C, at a shear rate of 100 s^{-1} equal to the ratio of the dynamic viscosity of bitumen with a chemical additive to the dynamic viscosity of bitumen without a chemical additive.

At the stage of studying the effect of chemical additives on the properties of bitumen and the compaction of asphalt concrete mixture, the most rational additives are selected for further study of their effect on the properties of asphalt concrete, which were evaluated according to the following properties:

- average density, kg/m^3, not rated;
- water saturation, %, according with Russian State Standard GOST 9128;
- compressive strength, MPa, at 20 and 50 °C, according with Russian State Standard GOST 9128;
- water resistance, according with Russian State Standard GOST 9128;
- water resistance under long-term water saturation, according with Russian State Standard GOST 9128.

No less than three measurements were made for each test method according to the requirements of Russian State Standard GOST 9128. The results are presented as an average value.

The influence of temperature on the viscosity of the system "bitumen/bitumen with surfactant" under study was evaluated using the parameters a and U of the dependence $\eta = f(T)$ described by the Arrhenius equation [33]:

$$\eta = a \cdot e^{\frac{-U}{(RT)}}, \qquad (4)$$

where η is bitumen viscosity, Pa*s; a is a constant whose unit of measurement is similar to the unit of viscosity measurement; U is activation energy of the flow process, J/mol; R is a universal gas constant ($R = 8.314$ J/(mol·K)); T is the absolute temperature, K.

The activation energy U is an important parameter equal to the amount of energy that must be brought from the outside to start the flow, that is, to overcome the physical barrier that characterizes the parameters of the melt structure for the systems under consideration. Thus, U characterizes the excess energy in relation to the average energy of the particles at a given temperature. Obviously, the change in U during the introduction of additives will characterize the structural changes that occurred as a result of their introduction.

The physical meaning of the constant a becomes apparent only when:

$$e^{\frac{-U}{(RT)}} = 1.$$

This equality holds when $T \rightarrow \infty$:

$$\eta(\infty) = \lim_{T \to \infty} a \cdot e^{\frac{-U}{(RT)}} = a.$$

Thus, the constant a is also a structural parameter that characterizes the effect of additives (surfactants) on the absence of temperature influence.

3. Results and Discussion

To establish the effectiveness of chemical additives at the first stage, their effect on the manufacturability (compacting) of a warm asphalt concrete mixture (WACM) compacted at a low temperature of 110 °C was studied, the results are presented in Table 2.

Table 2. The effect of various additives on the compaction of WACM.

Name of warm-mix additive	Additive consumption, % by weight of bitumen	Compaction temperature, °C	Number of revolutions of the gyrator, units
without warm-mix additive	–	150	53
		110	110
Adgezol 3-TD	1.0	110	65
DAD-TA2	1.0	110	66
Azol 1007	1.0	110	65
Cecabase RT 945	0.3	110	50
DAD-TA	0.3	110	50
Doros-T	0.6	110	69
Amdor TS-1	0.3	110	62

The analysis of the results presented in Table 2 allowed us to establish that all the considered additives reduce the required number of gyrator revolutions by 38... 55 % in order to achieve a given density of asphalt concrete at a reduced temperature. The use of the additive Cecabase RT 945 and DAD-TA allows you to reduce the compaction temperature of the asphalt concrete mixture by 40 °C without compromising its manufacturability, obtained under standard conditions – the compaction temperature of 150 °C.

At the second step of evaluating the effectiveness of the studied chemical additives (surfactants), their effect on the physical, mechanical and technological properties of bitumen was studied. The main indicators that reflect their behavior under operating conditions are: the conditional viscosity characteristics which are the depth of penetration of the needle (penetration at 25 °C and 0 °C) and the plasticity interval (softening temperature and brittleness temperature). The dynamic viscosity is an indicator that determines the technological characteristics of the binder. The results of the determination of physical, mechanical and technological properties are presented in Table 3 and in Fig. 1 and 2.

Table 3. The effect of various additives on the penetration of BND 70/100.

Name of warm-mix additive	Additive consumption, % by weight of bitumen	The depth of penetration of the needle, mm $^{-1}$, at a temperature of, °C	
		0	25
without warm-mix additive	–	24	72
Adgezol 3-TD	1.0	26	82
DAD-TA2	1.0	28	80
Azol 1007	1.0	28	89
Cecabase RT 945	0.3	29	76
DAD-TA	0.3	28	76
Doros-T	0.6	28	81
Amdor TS-1	0.3	28	73

As can be seen from Table 3, all the studied additives have a plasticizing effect on bitumen, but do not change its mark, in accordance with Russian State Standard GOST 33133. The modified bitumen is in the conditional viscosity range of 70/100 mm^{-1}. It should be noted that the greatest plasticizing-diluting effect is observed in additives with a recommended concentration of 0.6–1 %, which is 20 % on average, while in additives with a concentration of 0.3 %, the plasticizing effect is 0.3–6 % on average.
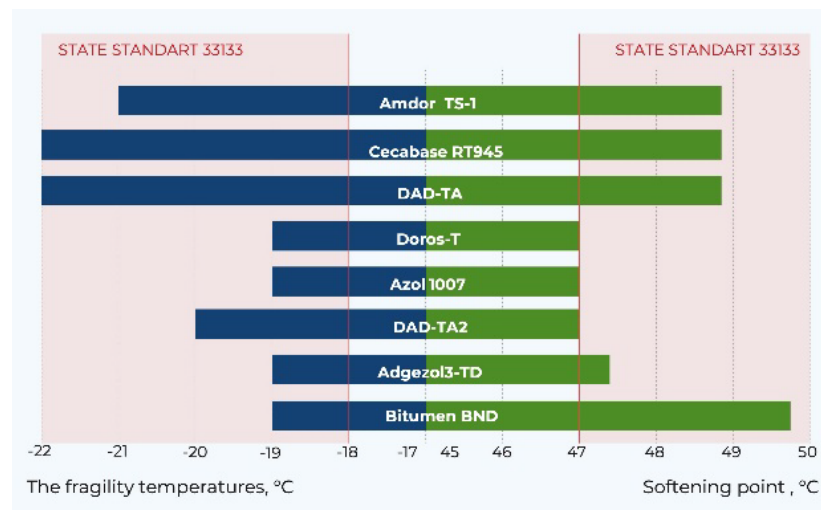
**Figure 1. The effect of additives (surfactants)
on the fragility and softening temperature of bitumen.**

During the study of the effect of additives on the range of plasticity of bitumen (the combination of softening temperature and fragility) as shown in Fig. 1, it was found that the additives Doros TS-1, Azol 1007 and DAD-TA2 with a concentration of 0.6–1 % did not pass the tests for the softening temperature of binders, the obtained indicators are at the tolerance limit. It is also important to note that the additives Azol 1007 and Adgezol 3-TD did not affect the fragility temperature. At the same time, all additives with a recommended consumption of 0.3 % (Cecabase RT 945, DAD-TA and Amdor TS-1) showed results close to bitumen in terms of softening temperature, which indicates the absence of a plasticizing effect in bitumen in the operating temperature range. At the same time, bitumen with additives has improved low-temperature characteristics: additives Cecabase RT945 and DAD-TA showed an improvement of up to 16 %.
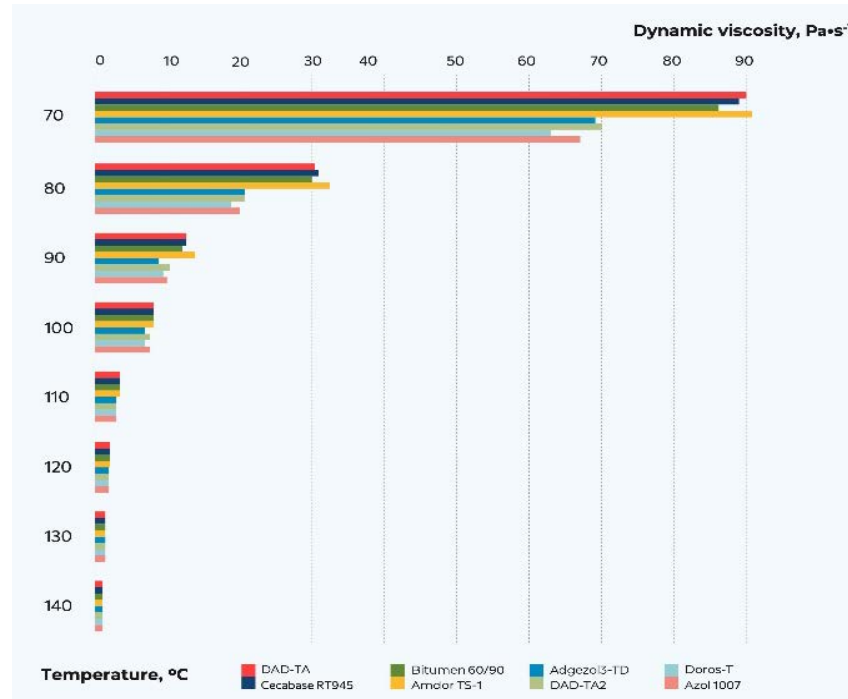
Figure 2. Dynamic viscosity of bitumen with additives (surfactants) at a shear rate of 100 s^{-1}.

Analysis of the results of the dynamic viscosity of modified bitumen (Fig. 2) shows that Adgezol 3-TD, DAD-TA2, Doros-T and Azol 1007 reduce the viscosity of bitumen by up to 30 % over the entire measured temperature range (T = 70–140 °C), which correlates with the data on the softening temperature (Fig. 1), and will have a negative impact on the deformative parameters of asphalt concrete prepared with their use. The additives DAD-TA, Cecabase RT 945 and Amdor TS-1 do not significantly affect the initial viscosity of bitumen, while maintaining the processability of the binder in the entire temperature range during the preparation of asphalt concrete mixture and, in accordance with Table 1, during its compaction.

To determine the generalized criterion of technical and economic efficiency (F_k) of the considered additives for warm asphalt concrete mixtures, the economic efficiency coefficients and operational efficiency coefficients were calculated according to the formula (2). The calculation results are presented in Table 4.

Table 4. Criteria and coefficient of economic and operational efficiency of chemical additives (surfactants).

Name of warm mix additive	Economic efficiency coefficient K_{ec}	Authors' quality criteria						Generalized quality factor K_q
		$k_{compaction}$	$k_{P_{25}}$	k_{P_0}	k_{Tfr}	$k_{T_{softening}}$	k_η	
Adgezol 3-TD	0.88	1.69	0.85	1.08	1.00	1.05	0.8	1.04
DAD-TA2	0.93	1.67	0.90	1.17	1.05	1.06	0.8	1.08
Azol 1007	0.93	1.69	0.79	1.17	1.00	1.06	0.8	1.04
Cecabase RT 945	0.92	2.20	0.90	1.21	1.16	0.98	1.0	1.19
DAD-TA	0.94	2.08	0.92	1.17	1.16	0.98	1.1	1.19
Doros-T	0.92	1.59	0.86	1.17	1.00	0.94	0.7	1.02
Amdor TS-1	0.94	1.77	0.96	1.17	1.11	0.98	0.7	1.08

The K_{ec} coefficient shows how much the cost of bitumen increased when a chemical additive was introduced into it taking into account its consumption. The K_q coefficient shows the contribution of the chemical additive to improving the complex of physical, mechanical and technological properties of bitumen and asphalt concrete mixture.

Based on the results obtained by calculating the coefficients of economic and operational efficiency (Table 4), a generalized criterion for the technical and economic efficiency of the use of the chemical additives in question was calculated (Fig. 3).
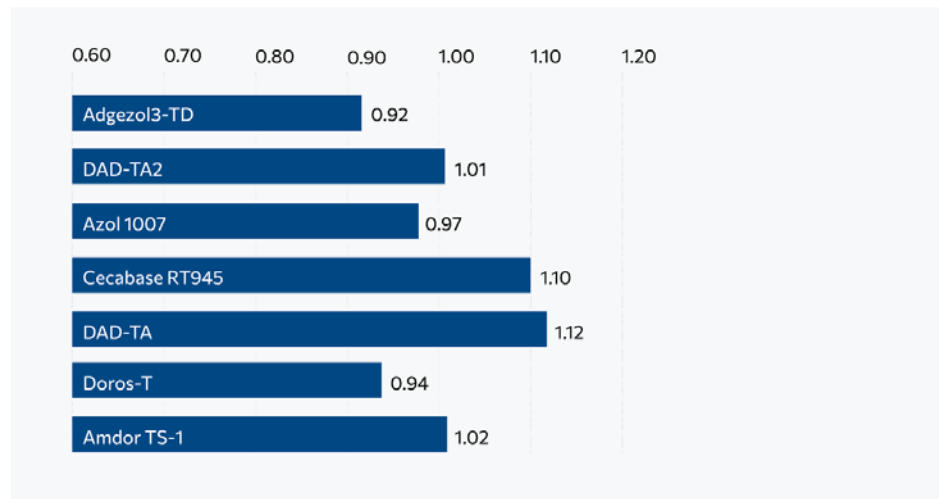
Figure 3. Generalized criterion of technical and economic efficiency of the use of chemical additives (surfactants), F_k.

The analysis of the values of the criterion for the rationality of the use of chemical additives (Fig. 3) allows us to suggest the division of the additives into two groups: additives that improve the efficiency of bitumen by 5 % ($F_k \geq 1.05$) or more, as well as additives that do not improve the efficiency of bitumen by more than 5 % ($F_k \leq 1.05$), that is, do not significantly change the properties.

To determine the effect of additives (surfactants) in the composition of bitumen on the properties of asphalt concrete, additives from two different groups of effectiveness were selected: DAD-TA and Cecabase RT945 from the first group, Azol 1007 and Adgezol 3-TD from the second group. The obtained results of the properties are presented in Table 5.

Table 5. Physical and mechanical properties of asphalt concrete type B compacted at a temperature of 110 °C.

Indicator name	Requirement of Russian State Standard GOST 9128-2013	Actual indicators of asphalt concrete prepared with the use of				
		without	DAD-TA	Cecabase RT945	Azol 1007	Adgezol 3-TD
Average density, g/cm ^{3}	–	2.31	2.38	2.38	2.34	2.33
Water saturation, %	1.5…4.0	3.46	1.68	1.72	2.53	2.55
Compressive strength, MPa at temperature:						
- 20 °C	no less than 2.5	3.18	4.83	4.62	4.28	4.30
- 50 °C	no less than 1.2	1.18	1.75	1.63	1.15	1.15
Water Resistance	no less than 0.9	0.80	0.98	0.97	0.80	0.80
Water resistance under long-term water saturation	no less than 0.85	0.78	0.97	0.95	0.78	0.78

The study of the physical and mechanical properties of asphalt concrete prepared on bitumen modified with additives with a recommended concentration of 0.3 % showed that they do not have a negative effect on its properties. Samples of asphalt concrete compacted at a temperature of 110 °C meet the requirements of Russian State Standard GOST 9128-2013 for traditional hot asphalt concrete mixtures, Table 5.

Asphalt concrete prepared without additives and asphalt concrete prepared using the additives Azol 1007 and Adgezol 3TD, with the recommended concentration of 1 %, is not sufficiently compacted, as evidenced by a lower average density. This naturally contributed to an increase in water saturation and an unsatisfactory value of the water resistance index of the samples <12 % than the State Standard requirements, and the compressive strength at 50 °C < 5 % than the State Standard requirements. This will negatively affect the performance of the road surface made with it. Asphalt concretes prepared using additives DAD-TA and Cecabase RT945 exceed the requirements of State Standard. Thus, the compressive strength at 20 °C is 93 % of the requirements of State Standard, the compressive strength at 50 °C is 45 % of the requirements of State Standard, and the water resistance is 9 % of the requirements of State Standard.

To explain the effect of various surfactant additives on the structure of bitumen, the authors calculated the change in the activation energy required to overcome the potential (kinetic) barrier of the bitumen binder with the studied surfactants (according to formula 4) relative to the bitumen using the Arrhenius equation, Table 6.

Table 6. Effect of additives (surfactants) on the activation energy and the viscosity constant.

Name of warm mix additive	Additive consumption, % by weight of bitumen	The activation energy, U		The viscosity constant, a	
		U/R	$\dfrac{(U/R)}{(U/R)_b}$	a	a/a_b
Without warm mix additive	–	11736	1.00	$9.39 \cdot 10^{-14}$	1.00
Adgezol 3-TD	1.0	15272	1.30	$3.14 \cdot 10^{-18}$	$3.3 \cdot 10^{-5}$
DAD-TA2	1.0	15452	1.32	$1.89 \cdot 10^{-18}$	$2.0 \cdot 10^{-5}$
Azol 1007	1.0	15745	1.34	$7.8 \cdot 10^{-19}$	$8.3 \cdot 10^{-6}$
Cecabase RT 945	0.3	12143	1.03	$3.13 \cdot 10^{-14}$	0.33
DAD-TA	0.3	12146	1.03	$3.08 \cdot 10^{-14}$	0.33
Doros-T	0.6	16609	1.42	$6.01 \cdot 10^{-20}$	$6.4 \cdot 10^{-7}$
Amdor TS-1	0.3	12098	1.03	$3.58 \cdot 10^{-14}$	0.38

Note: the index "b" indicates bitumen.

The data presented in Table 6 shows that all the additives used make a change in the structure of the bitumen melt. However, the studied additives can be classified into two groups:

1. Additives inducing a slight change in the parameters of the structure of the bitumen melt. For such additives, the potential barrier increases slightly, and after the termination of the structuring factor of the temperature the decrease in viscosity does not exceed 2 times.

2. Additives inducing a significant increase in the activation energy (up to 40 %) and a significant decrease in viscosity after the termination of the influence of temperature (up to 10^{+7} times).

Evaluation of the influence of the structuring factor on the behavior of bitumen modified by the presented additives requires additional research and determination of the dependence of the melt viscosity on the shear rate. By obtaining data that confirms the presented classification of additives and studying the effect of the shear rate on the viscosity of bitumen melts, it is possible to construct a structural model of the effect of additives on the rheological properties of these systems.

4. Conclusion

1. It is found that the additives (surfactants) under consideration can reduce the required number of gyrator revolutions by 38 ... 55 %, to achieve a given density of asphalt concrete at a sample height of 115 mm and a reduced temperature of 110 °C. This allows you to reduce the temperature of production and laying of asphalt concrete mix by 40 °C.

2. It is found that all the studied additives (surfactants) have a plasticizing effect on bitumen, but do not change its grade. It was found that Adgezol 3-TD, DAD-TA2, Doros-T and Azol 1007 reduce the dynamic viscosity of bitumen by up to 30 % over the entire measured temperature range (T = 70–140 °C), which correlates with the data on the softening temperature. DAD-TA, Cecabase RT 945 and Amdor TS-1 additives slightly affect the initial viscosity of bitumen, maintaining the processability of the binder in the entire temperature range during the preparation of asphalt concrete mixture, and also improve the fragility temperature of bitumen by up to 16 %.

3. To determine the complex technical and economic criterion of the effectiveness F_k of the studied additives for warm asphalt concrete mixtures, the following coefficients were developed and proposed: economic efficiency coefficient K_{ec}, which shows how much the cost of the bitumen binder increased when a chemical additive was introduced into it, taking into account its consumption; generalized quality factor K_q, which shows the contribution of the chemical additive to improving the complex of physical, mechanical and technological properties of bitumen and asphalt concrete mixture.

4. Based on the results obtained by calculating the F_k criterion, it is proposed to divide the additives into two groups: the first group includes additives Cecabase RT945, DAD-TA and Amdor TS-1, which improve the efficiency of bitumen by 5 % (F_k ≥ 1.05 and more); the second group includes additives Adgezol 3-TD, DAD-TA2, Azol 1007, Doros-T, which do not improve the efficiency of bitumen by more than 5 % (F_k ≤ 1.05), that is, do not make any significant change in the properties. It is established that the use of additives of the second group in the composition of warm asphalt concrete leads to an increased water saturation value and an unsatisfactory value for water resistance and long-term water resistance of asphalt concrete samples. This is 12 % lower than stated in the requirements of State Standard for the ultimate compressive strength at 50 °C, which is 5 % lower than the values in the requirements of State Standard. The use of additives of the first group in the composition of asphalt concrete compacted at a reduced temperature of 110 °C causes an increase in the compressive strength at 20 °C, the compressive strength at 50 °C, water resistance by 93 %, 45 %, and 9 % of the requirements of State Standard, respectively.

5. It is established that all the additives used make a change in the structure of the bitumen melt. However, the studied additives can be classified into two groups: 1. Additives leading to a slight change in the parameters of the structure of the bitumen melt; the potential barrier increases slightly, and after the termination of the structuring factor of the temperature the decrease in viscosity does not exceed 2 times. 2. Additives leading to a significant increase in the activation energy (up to 40 %) and a significant decrease in viscosity after the termination of the influence of the temperature (up to 10+7 times).

References

1. Saad, I.S. Behavior of Warm Mix Asphalt Concrete under Moisture Damage. International Journal of Engineering Papers. 2018. 3 (1). Pp. 21–28.
2. Julien, M., Benoît, B. Environmental assessment of France. 2020. 64 p.
3. Huang, W., He, P., Long, X., Tian, J., Yu Z., Ma, H., Hu.S. Design of a skeleton-stabilized warm mix asphalt mixture and investigation of its fatigue and fracture performance. Construction and Building Materials. 2020. 248 (10). 118618. DOI: 10.1016/j.conbuildmat.2020.121781

4. Shekhovtsova, S.Yu. Features of the formation of properties of stone-mastic asphalt concrete based on a warm polymer modified binder. Materials Science Forum. 2020. 992. Pp. 200–205. DOI: 10.4028/www.scientific.net/MSF.992.200

5. Iwański, M.M. Chomicz-Kowalska, A., Maciejewski, K. Resistance to Moisture-Induced Damage of Half-Warm-Mix Asphalt Concrete with Foamed Bitumen. Materials. 2020. 13 (3). 654 p. DOI: 10.3390/ma13030654

6. Harrison, T., Christodulaki, L. Innovative process in asphalt production and application – strengthening asphalt's position in helping build a better world. First International Conference of Asphalt Pavements. Sydney. 2000.

7. Silva, H.M.R.D., Oliveira, J.R.M., Peralta, J., Zoorob, S.E. Optimization of warm mix asphalts using different blends of binders and synthetic paraffin wax contents. Construction and Building Materials. 2010. 24 (9). Pp. 1621–1631. DOI: 10.1016/j.conbuildmat.2010.02.030

8. Carlina, S., Subagio, B.S., Kusumawati, A. The performance of warm mix for the asphalt concrete–wearing course (AC-WC) using the asphalt pen 60/70 and the Sasobit additives. Civil Engineering Journal ITB. 2019. 26 (1). Pp. 11–16. DOI: .org/10.5614/jts.2019.26.1.2

9. Diefenderfer, S.D., McGhee, K.K., Donaldson, B.M. Installation of warm mix asphalt projects in virginia. Final report. 2007. Pp .1–34.

10. Wang, H., Liu, X., Apostolidis, P., Scarpas, T. Review of warm mix rubberized asphalt concrete: Towards a sustainable paving technology. Journal of Cleaner Production. 2018. 177 (10). Pp. 302–314. DOI: 10.1016/j.jclepro.2017.12.245

11. Oliveira, J.R., Silva, H.M., Abreu, L.P., Fernandes, S.R. Use of a warm mix asphalt additive to reduce the production temperatures and to improve the performance of asphalt rubber mixtures. Journal of Cleaner Production. 2013. 41. Pp. 15–22. DOI: 10.1016/j.jclepro.2012.09.047

12. Rodríguez-Alloza, A.M., Gallego, J. Mechanical performance of asphalt rubber mixtures with warm mix asphalt additives. Materials. Structures. 2017. 50 (2). 147. DOI: 10.1617/s11527-017-1020-z

13. Pasquini, E., Canestrari, F., Cardone, F., Santagata, F.A. Performance evaluation of gap graded Asphalt Rubber mixtures. Construction and Building Materials. 2011. 25 (4). Pp. 2014–2022. DOI: 10.1016/j.conbuildmat.2010.11.048

14. Pouranian, M.R., Shishehbor, M. Sustainability assessment of green asphalt mixtures: a review. Environments. 2019. 6. 73 p. DOI: 10.3390/environments6060073

15. Rubio, M.C., Martínez, G., Baena, L., Moreno, F. Warm mix asphalt: an overview. J. Clean. Prod. 2012. 24. Pp. 76–84. DOI: 10.1016/j.jclepro.2011.11.053

16. Cucalon, L.G., Yin, F., Martin, A.E., Arambula, E., Estakhri, C., Park, E.S. Evaluation of moisture susceptibility minimization strategies for warm-mix asphalt: Case study. Journal of Materials in Civil Engineering. 2015. 28 (2). 05015002. DOI: 10.1061/(ASCE)MT.1943-5533.0001383

17. Rodríguez-Alloza, A.M., Saiz-Rodríguez, L. Evaluation of Warm Rubberized Stone Mastic Asphalt Mixtures through the Marshall and Gyratory Compactors. Materials. 2020. 13 (2). 265. DOI: 10.3390/ma13020265

18. Khedmati, M., Khodaii, A., Haghshenas, H. F. A study on moisture susceptibility of stone matrix warm mix asphalt. Construction and Building Materials. 2017. 144. Pp. 42–49. DOI: 10.1016/j.conbuildmat.2017.03.121

19. Xu, S., Xiao, F., Amirkhanian, S.N., Singh, D. Moisture characteristics of mixtures with warm mix asphalt technologies – A review. Construction and Building Materials. 2017. 42. Pp. 148–161.

20. Wang, Y., Zhu, J., Liu, L., Sun, L. Gradation Evaluation of Asphalt Rubber Mixture with Warm-mix Additive. Procedia – Social and Behavioral Sciences. 2013. 96. Pp. 31–38. DOI: 10.1016/j.sbspro.2013.08.007

21. Akisetty, C.K., Lee, S.J., Amirkhanian, S.N. Effects of Compaction Temperature on Volumetric Properties of Rubberized Mixes Containing Warm-Mix Additives. Journal of Materials in Civil Engineering. 2009. 21 (8). DOI: 10.1061/(ASCE)0899-1561(2009)21:8(409)

22. Guo, N., You, Z., Zhao, Y., Tan, Y., Diab, A. Laboratory performance of warm mix asphalt containing recycled asphalt mixtures. Construction and Building Materials. 2014. 64. Pp. 141–149. doi.org/10.1016/j.conbuildmat.2014.04.002

23. Frigio, F., Stimilli, A., Virgili, A., Canestrari, F. Performance Assessment of Plant-Produced Warm Recycled Mixtures for Open-Graded Wearing Courses. Transportation Research Record Journal of the Transportation Research Board. 2017. 2633 (1). Pp. 16–24.

24. Stimilli, A., Virgili, A., Canestrari, F. Warm recycling of flexible pavements: Effectiveness of Warm Mix Asphalt additives on modified bitumen andmixture performance. Journal of Cleaner Production. 2017. 156. Pp. 911–922.

25. Wang, C., Hao, P., Ruan, F., Zhang, X., Adhikari, S. Determination of theproduction temperature of warm mix asphalt by workability test. Construction and Building Materials. 2013. 48. Pp. 1165–1170.

26. Bairgi, B.K., Tarefder, R.A., Ahmed, M.U. Long-term rutting and strippingcharacteristics of foamed warm-mix asphalt (WMA) through laboratory andfield investigation. Construction and Building Materials. 2018. 170. Pp. 790–800.

27. Sangsefidi, E., Ziari, H., Mansourkhaki, A. The effect of aggregate gradation oncreep and moisture susceptibility performance of warm mix asphalt. Int. J.Pavement Eng. 2012. 15. Pp. 133–141.

28. Sebaaly, P.E., Hajj, E.Y., Piratheepan, M. Evaluation of selected warm mixasphalt technologies. Road Mater. Pavement Des. 2015. 16. Pp. 475–486.

29. Pan, P., Yi, K., Xiaodi, H., Xiao, Zh. A Comprehensive Evaluation of Rejuvenator on Mechanical Properties, Durability, and Dynamic Characteristics of Artificially Aged Asphalt Mixture. Materials. 2018. 11 (9). 1554. https://doi.org/10.3390/ma11091554

30. Shekhovtsova, S., Korolev, E., Inozemtcev, S., Jiangmiao, Yu., Huayang, Yu. Method of forecasting the strength and thermal sensitive asphalt concrete. Magazine of Civil Engineering. 2019. 05. Pp. 129–140. DOI: 10.18720/MCE.89.11

31. Ki, H.M., Augosto, C.F., Di, W., Yun, S.K. Experimental Investigation on Fatigue and Low Temperature Properties of Asphalt Mixtures Designed with Reclaimed Asphalt Pavement and Taconite Aggregate. Transportation Research Record Journal of the Transportation Research Board. 2019. 2673 (3). Pp. 472–484.

32. Bazhenov, Yu.M., Garkina, I.A., Danilov, A.M., Korolev E.V. System analysis in building materials science. 2012. 152 p.

33. Liu, H.W., Zeiada, G.G., Al-Khateeb, A., Shanableh, M. Characterization of the shear-thinning behavior of asphalt binders with consideration of yield stress. Materials and Structures. 2020. 53 (4).105 p.

Information about authors:

Svetlana Obukhova, *PhD of Technical Science*
ORCID: https://orcid.org/0000-0002-4268-7897
E-mail: SHehovtsovaSYU@mgsu.ru

Evgeniy Korolev, *Doctor of Technical Science*
ORCID: https://orcid.org/0000-0003-0815-4621
E-mail: korolev@nocnt.tu

Alexander Novikov, *Doctor of Technical Science*
E-mail: novikovan@ostu.ru

Anastasia Shevtsova, *PhD of Technical Science*
E-mail: shevcova-anastasiya@mail.ru

Magazine of Civil Engineering

journal homepage: http://engstroy.spbstu.ru/

High performance lightweight concretes for 3D printing

A.S. Rassokhin[1] ✉ iD **, A.N. Ponomarev**[2] iD **, S.L. Shambina**[2] iD **, A.I. Karlina**[3] iD

[1] *Peter the Great St. Petersburg Polytechnic University, St. Petersburg, Russia*

[2] *Peoples' Friendship University of Russia, Moscow, Russia*

[3] *Moscow State University of Civil Engineering (National Research University), Moscow, Russia*

✉ *rassokhinaleksandr@gmail.com*

Keywords: high-performance concrete, 3D printing, compressive strength, fine-grained concrete, basalt fiber, silica fume

Abstract. The paper is devoted to developing high-performance nanostructured concrete for 3D printing and studying its strength and operational characteristics. The research addresses issues related to the use of modern concrete chemistry, such as plasticisers and concrete hardening accelerators, and nanomodification by two types of nanocarbon: nanotores (Astralene) and sulphur graphene (Ugleron). The designed lightweight concrete for 3D printing has a compressive strength of about 70 MPa and 9 MPa after extrusion at a density of about 1.55–1.6 kg/m³. Pozzolan additives from industrial waste in concrete are used, such as silica fume and oil shale ash. Microspheres, which are also industrial wastes, are used as lightweight aggregate and thixotropy regulators. As a result, lightweight, high-performance concrete for 3D printing was developed, which allows the disposal of industrial waste inside it.

1. Introduction

The rapid development of a digital economy requires an equally quick transition of industrial production to robotic technologies with digital control [1, 2]. This also applies to such an inertial sector of the industry as construction is.

Such a tool can be the introduction of 3D printing technology in construction [3, 4].

The introduction of 3D printing in construction will reduce labour costs by automatization [5]. In this case, for the manufacturing of concrete walls, for example, there is no need to work with several masons teams, but the operator who will monitor the building process and prepare the concrete mixture is enough. Moreover, it is possible to reduce the number of materials used in construction due to optimizing the geometry of structures[6]. In addition, account must be taken of that automatization of construction is not only a matter of cost reduction. It is a hard and traumatic job, where there are not rarely fatalities. Automatization of even a part of the processes will reduce injuries and even save human lives.

These actions will significantly increase the environmental friendliness of construction and relieve the environmental burden from the construction region. It is worth pointing out that cement production is responsible for 5–9 % CO_2 emissions [7]. Moreover, massive waste is formed in construction, especially when utilizing old buildings [8, 9].

With the advent and development of 3D printers and their penetration into the technology of forming products made of polymers and metals [10, 11], 3D printing in construction technologies also began to

develop [12, 13]. However, each such transition becomes possible only after the creation and development of the industry producing the related specialized materials such as unique thermoplastics for digital printing of plastic parts and special powders [14], tapes, and wires for the technology of printing metal parts [15]. The same new materials are also required for printing structures in construction. It would seem that the properties of the traditional compositions based on mineral binders (concretes) are very close to the tasks of 3D printing in construction technologies [16–18]. Industrial concretes based on Portland cement, aluminous (high alumina), sulphoaluminate and slag-portland cement binders according to the current regulatory and technical base, do not have (in their majority) the ability to set quickly (in less than 30 minutes) [19]. Also, they cannot promptly gain hardness, providing an intensive increase in crack resistance and stability of the shape of the cross-section of the concrete jet which is being laid.

In this regard, it is advisable to use concrete hardening accelerators that accelerate the concrete setting and contribute to an accelerated set of strength in the first hours of hardening. However, hardening accelerators should not lead to cracking and other problems when used [20]. The cause of cracks in such situations is typically the unequal start of hardening or overheating of concrete. In the case of concrete printing 3D, you should not fear overheating concrete. When using this technology, massive monolithic structures of tens of cubic meters of concrete are not formed. Multilayer structures in 3D printing are used that allow excess heat to leave the concrete.

As a result of the information given above, it becomes a highly urgent task to develop and organize materials (dry admixes of raw materials) for concrete mixtures intended for industrial 3D printing of reliable and safe buildings and structures.

The primary purposes of this work and tasks of its experimental part were as follows:

- select suitable additive materials to develop concrete formulations for 3D printing;
- to develop some variants of working formulations of concrete mixtures for 3D printing;
- to conduct studies on the workability and effectiveness of the selected base materials in the composition of experimental working formulations of concrete mixtures for 3D printing;
- to determine mechanical and operational characteristics, as well as strength gain dynamics.

2. Methods

2.1. Used materials

In this research, the authors are focused on Portland cement as a primary binder which is the most affordable and relatively cheap in mass production. Still, they took it without additives, with a minimum amount of free alkalis in Na_2O (not more than 0.8 % of the mass). Such cement is currently represented in Russia only by Portland cement CEM I 42.5 N, produced by PJSC Mordovcement and portland cement CEM I 42.5 N produced by LLC Asia-Cement (Penza). All other cement manufacturers cannot provide a high quality of the composition and characteristics of their products, especially in terms of exceeding the permissible amount of free alkalis, which adversely affects the freeze and thaw resistance of concrete and on their longevity.

However, in this research, the choice was favouring cement manufactured by PJSC Mordovement since it is more accessible in Russia's northern and central regions.

Active microcrystalline silica fume manufactured by pilot production of the Irkutsk National Research Technical University (IRNITU) and electro filter slate fly ash "Zoles Bet" obtained from State District Electric Station (SDES) in Narva were used as pozzolanic and fine-grained additives. Modified basalt microfiber by TC 5761-014-13800624-2004 was used for dispersal reinforcement. Carbon torus-like nanoparticles of the fulleroid type Astralenes® by TC 2166-001-13800624-2003 were used to control the properties of cement stone crystallization and its micro-dispersion self-reinforcement. Ash aluminosilicate cenospheres (from Kemerovskaya CHPP) with average diameters of 100-130 microns were used to control the thixotropy of the concrete mixture. High-efficiency antifreeze additive NitCal® was used as an accelerator for setting and obtaining high strength values. The water quantity was reduced with the help of the carboxylate plasticizer REOMAX PC 3901P manufactured by KUBAN-POLYMER LLC with admix of hydrophilic sulphur adduct carbon nanoclusters Ugleron® (TC 2166-049-91957749-2011), which has been used for these purposes in [21].

Aluminosilicate cenospheres were used to control the thixotropy of the concrete mixture. Aluminosilicate hollow microspheres are glass-crystalline aluminosilicate cenospheres that are formed during the high-temperature flaring of the coal. They are the most valuable components of ash waste from thermal power plants. They are hollow, almost ideal in shape silicate balls with a smooth surface, with a diameter of 10 to several hundred micrometers, on average about 100 micrometers. The microspheres walls are

solid non-porous with a thickness of 2 to 10 microns, a melting point of 1400–1500 °C, a density of 580–690 kg/m³. The inner cavity of the particles is filled mainly with nitrogen and carbon dioxide.

2.2. Preparation of concrete samples and determination of their characteristics

Laboratory mixing of concrete according to Russian State Standard GOST 10180-2012 was carried out according to the following recipes:

Table 1. Concrete recipe No. 1

Components	recipe No. 1	recipe No. 1
	Kg per m³	
Portland Cement CEM I 42.5 N manufactured by JSC Mordovcement	552	
Gabbro diabase manufactured by Lysaya Gora Ltd. (fraction of 0 – 2.5 mm)	405	397
Dry admix of:		
Silica fume manufactured by pilot production of the INRTU [22]		
Shale ash Zolest-bet manufactured by PCV LLC		
Modified basalt microfiber manufactured by NTC of Applied Nanotechnologies	396	
Aluminosilicate cenospheres (from Novo-Kemerovo CHPP)		
Plasticizing agent REOMAX PC 3901P manufactured by KUBAN-POLYMER LLC		
Carbon nanoparticles Astralene manufactured by NTC of Applied Nanotechnologies		
Antifreeze additive NitCal®		
Modified basalt microfiber manufactured by NTC of Applied Nanotechnologies	–	8
The water of mixing according to GOST 23732-2011	220	220

The concrete was mixed as follows. Water, binding materials and plasticizing agent were first incorporated in the concrete gravity batch mixer Eco CM-71 for one minute. After that, fine aggregates were introduced and mixing lasted another minute. Fiber and Astralene were introduced last into the concrete mixture. The final mixing also lasted for one minute.

Nanomodifiers (Astralene) were introduced into concrete by serial dilution method [23]. An aqueous suspension of Astralenes was made, which was added to the concrete mixture using the laboratory homogenizer I100-840 LLC Ultrasonic Technique.

The volume of each batch of concrete mixing was 35 litres.

Concrete density was determined according to Russian State Standard GOST 10181-2014.

Concrete cubes with dimensions of 100×100×100 mm in the quantity of 15 pieces and concrete prisms with dimensions of 100×100×400 mm in the amount of 3 samples were made according to Russian State Standard GOST 10180-2012.

The concrete samples were prepared in moulds and removed from the moulds after 1-day curing at room temperature. All the samples (and the control samples) have been hardened in thermo-humidity conditions according to Russian State Standard GOST 10180-2012.

The compressive strength test of concrete cubes with dimensions of 100×100×100 mm was carried out on the hydraulic laboratory testing machine MP-1000 «Nutcracker» according to Russian State Standard GOST 10180-2012.

Waterproofing of concrete control samples by air permeability was determined by the device AGAMA-2 according to Russian State Standard GOST 12730.5-2018.

Figure 1. Extrusion Equipment.

The extrusion was carried out using the construction syringe Long Blast and the Injection screw pump KRIN-706 PRO.

Control samples of extrusion concrete were made as follows: fine-grained concrete was fed into the pump funnel. Concrete was pumped through a flexible pipe with a diameter of 3 cm and a length of 2 meters. Extrusion was performed through a rectangular nozzle of 2.5 cm × 0.5 cm. Extrusion was carried out by the "layer by layer" method [24]. Prisms were filled with concrete perpendicular to the application of the load during the mechanical testing.

Moreover, in samples with fiber, this was also done to create the effect of fiber orientation [25]. Next, the forms with concrete were compacted using vibration according to Russian State Standard GOST 10181-2014. During concrete compacting, additional concrete was supplied to fill the resulting space using the construction syringe Long Blast.

The test load was applied perpendicular to the direction of laying.

3. Results and Discussion

The main concrete properties are given in Table 2. And Table 2 shows how extrusion, fiber, concrete hardening accelerators influence the main concrete properties.

Table 2. Main properties of concrete.

Properties	Units	Without Nitcal	Without fiber		With fiber	
			Before extrusion	After extrusion	Before extrusion	After extrusion
Compressive strength (12 hours)	MPa	9.8	15.9	17.5	16.4	17.9
Compressive strength (1 day)	MPa	30.1	39.6	42.4	40.4	43.1
Compressive strength (2 days)	MPa	43.1	48.3	51.2	48.7	52
Compressive strength (3 days)	MPa	46.8	51.9	54.3	52.3	55.1
Compressive strength (7 days)	MPa	51.4	56.3	60.1	56.7	61
Compressive strength (21 days)	MPa	60.7	62.1	66.2	62.6	66.8
Compressive strength (28 days)	MPa	65.4	64.8	69.6	65.7	70.9
Flexural strength (28 days)	MPa	7.3	7.1	8.9	7.7	10.2
Fresh concrete density	kg/m³	1568	1573	1609	1587	1621
Concrete density (28 days)	kg/m³	1521	1529	1554	1541	1572
Waterproofing	Class	W18	W18	W20	W20	W20
Flowability	Class	Self-Compacting				

The use of basalt microfiber led to an increase in the strength of concrete before extrusion. The compression strength of concrete increased from 64.8 MPa to 65.7 MPa (+ 1.4 %), and the flexural strength from 7.1 MPa to 7.7 MPa (+ 8.4 %).

It can be seen from Table 2 the concrete strength enhancement after extrusion. The compression strength of concrete without fiber increased from 64.8 MPa to 69.6 MPa (+ 7.4 %), and the flexural strength from 7.1 MPa to 8.9 MPa (+ 25 %). The compressive strength of fiber reinforced concrete increased from 64.8 MPa to 70.9 MPa (+ 9.4 %), and the flexural strength from 7.1 MPa to 10.2 MPa (+ 42 %). It should be noted that the concrete was placed in the molds perpendicular to the direction of application of the load during the tests, which led to the orientation of the fibers in the direction of extrusion [25]. This explains such a significant increase in flexural strength with a relatively low fiber content in concrete.

The extrusion improves the structure of concrete rock, leading to an increase in its strength. The basalt microfiber serves as a dispersed micro-reinforcement, leading to the concrete strength enhancement, especially flexural strength enhancement. During concrete extrusion, the fiber is oriented in the extrusion direction. It led to a significant increase in the strength of the concrete in the plane perpendicular to the extrusion direction. The orientation of the fiber during extrusion has also been established by other researchers [26–28].
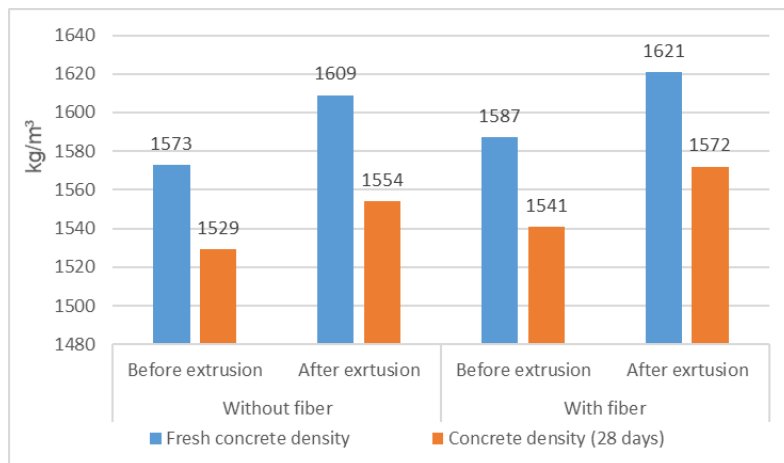
Figure 2. The concrete density.

In the Fig. 2, it can be seen that the density of concrete after extrusion increases by about 35 kg/m³. During extrusion, air bubbles are removed, which are involved in the concrete mixture during the mixing process. This suggests that after extrusion, the string-round of concrete is improved and the interaction between the matrix and the inert aggregate is improved. Also worth noting is that after extrusion, the waterproofing of concrete increased by the next class (from W18 up to W20) and reached the highest class W20. This also indicates that the structure of the concrete after extrusion is improved as its permeability is reduced. In turn, it should lead to an increase in the durability and operational properties of concrete.
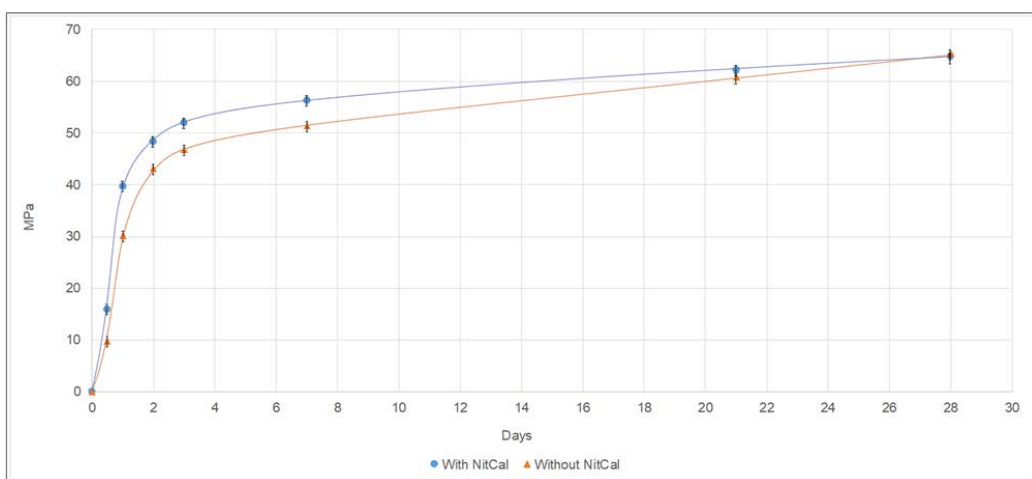

Figure 3. Concrete hardening dynamic.

Fig. 3 shows that the strength of concrete in the presence and absence of a hardening accelerator agent differs, especially in the first two days. The concrete gains 24 % of the class strength (28 days of hardening) in the first 12 hours when using a strength gain accelerator. And without Nitcal using the concrete gains only 15 % of class strength. After a day of hardening, concrete gains 61 % of class strength by using a hardening accelerator and only 46 % of class strength when no hardening accelerators were used. The gap between values in the process of time is reduced, and on the 28th day, the strength of concrete without Nitcal slightly exceeds the value of concrete strength with NItcal. The authors of this research [20] also concluded in favour of using a concrete hardener based on calcium nitrite, since alternative versions led to the appearance of cracks or other defects.

4. Conclusions

1. Nanostructured concrete formulations with high mechanical and operational characteristics were developed, and strength gain dynamics were investigated.

2. The use of a calcium nitrite hardening accelerator has resulted in the accelerated hardening of concrete in the early stages. In addition, this did not lead to any defects in concrete, such as cracking. This is consistent with the results of other researchers who have concluded that it is advantageous to use a concrete hardening accelerator based on calcium nitrite [20].

3. On day 28, the strength of concrete without fiber before extrusion was 64.8 MPa, 65.7 MPa and 65.4 MPa using a hardening accelerator (Nitcal).

4. It has been found that after extrusion, the strength of concrete increases significantly. This is because excess air is removed from the concrete mixture. There was an increase in concrete strength in the current research by 7.4 % (from 64.8 MPa to 69.6 MPa), and when using fiber by 7.9 % (from 65.7 MPa to 70.9 MPa).

5. The developed concrete can be safely called eco-friendly since it has many industrial waste products, such as silica fume, shale ash, aluminosilicate cenospheres. This reduces the impact of industrial waste on the region.

6. In terms of strength and operational properties, the developed concrete surpasses most founded analogues with a similar density. For example, this research [27] developed a concrete with similar strength values but with higher density values (1.7 – 1.8 t/m³).

7. The developed concrete is suitable for extrusion and further development of lightweight concrete structures for 3D printing.

References

1. Giftthaler, M., Sandy, T., Dörfler, K., Brooks, I., Buckingham, M., Rey, G., Kohler, M., Gramazio, F., Buchli, J. Mobile robotic fabrication at 1:1 scale: the In situ Fabricator. Construction Robotics. 2017. DOI: 10.1007/s41693-017-0003-5

2. Willmann, J., Knauss, M., Bonwetsch, T., Apolinarska, A.A., Gramazio, F., Kohler, M. Robotic timber construction – Expanding additive fabrication to new dimensions. Automation in Construction. 2016. DOI: 10.1016/j.autcon.2015.09.011

3. Buswell, R.A., Leal de Silva, W.R., Jones, S.Z., Dirrenberger, J. 3D printing using concrete extrusion: A roadmap for research. Cement and Concrete Research. 2018. 112 (October 2017). Pp. 37–49. DOI: 10.1016/j.cemconres.2018.05.006.

4. De Schutter, G., Lesage, K., Mechtcherine, V., Nerella, V.N., Habert, G., Agusti-Juan, I. Vision of 3D printing with concrete — Technical, economic and environmental potentials. Cement and Concrete Research. 2018. 112 (November 2017). Pp. 25–36. DOI: 10.1016/j.cemconres.2018.06.001.

5. Ngo, T.D., Kashani, A., Imbalzano, G., Nguyen, K.T.Q., Hui, D. Additive manufacturing (3D printing): A review of materials, methods, applications and challenges. Composites Part B: Engineering. 2018. 143 (December 2017). Pp. 172–196. DOI: 10.1016/j.compositesb.2018.02.012.

6. Mechtcherine, V., Bos, F.P., Perrot, A., da Silva, W.R.L., Nerella, V.N., Fataei, S., Wolfs, R.J.M., Sonebi, M., Roussel, N. Extrusion-based additive manufacturing with cement-based materials – Production steps, processes, and their underlying physics: A review. Cement and Concrete Research. 2020. 132 (March). Pp. 106037. DOI: 10.1016/j.cemconres.2020.106037.

7. Boesch, M.E., Hellweg, S. Identifying improvement potentials in cement production with life cycle assessment. Environmental Science and Technology. 2010. 44 (23). Pp. 9143–9149. DOI: 10.1021/es100771k

8. Roussat, N., Dujet, C., Méhu, J. Choosing a sustainable demolition waste management strategy using multicriteria decision analysis. Waste Management. 2009. 29 (1). Pp. 12–20. DOI: 10.1016/j.wasman.2008.04.010.

9. Dosho, Y. Development of a sustainable concrete waste recycling system: Application of recycled aggregate concrete produced by aggregate replacing method. Journal of Advanced Concrete Technology. 2007. 5 (1). Pp. 27–42. DOI: 10.3151/jact.5.27

10. Kietzmann, J., Pitt, L., Berthon, P. Disruptions, decisions, and destinations: Enter the age of 3-D printing and additive manufacturing 2015.

11. Thomas, D.J., Claypole, T.C. 3-D Printing. Printing on Polymers: Fundamentals and Applications 2015.

12. Wu, P., Wang, J., Wang, X. A critical review of the use of 3-D printing in the construction industry 2016.

13. Mpofu, T.P., Mawere, C., Mukosera, M. The Impact and Application of 3D Printing Technology. International Journal of Science and Research (IJSR). 2014.

14. Biron, M. Plastics Solutions for Practical Problems. Thermoplastics and Thermoplastic Composites 2018.

15. Frazier, W.E. Metal additive manufacturing: A review 2014.

16. Upadhyay, M., Sivarupan, T., El Mansori, M. 3D printing for rapid sand casting – A review 2017.

17. De Schutter, G., Lesage, K., Mechtcherine, V., Nerella, V.N., Habert, G., Agusti-Juan, I. Vision of 3D printing with concrete — Technical, economic and environmental potentials. Cement and Concrete Research. 2018. 112 (June). Pp. 25–36. DOI: 10.1016/j.cemconres.2018.06.001.

18. Panda, B., Unluer, C., Tan, M.J. Investigation of the rheology and strength of geopolymer mixtures for extrusion-based 3D printing. Cement and Concrete Composites. 2018. DOI: 10.1016/j.cemconcomp.2018.10.002

19. Hu, C., De Larrard, F. The rheology of fresh high-performance concrete. Cement and Concrete Research. 1996. DOI: 10.1016/0008-8846(95)00213-8

20. Meagher, T., Shanahan, N., Buidens, D., Riding, K.A., Zayed, A. Effects of chloride and chloride-free accelerators combined with typical admixtures on the early-age cracking risk of concrete repair slabs. Construction and Building Materials. 2015. 94. Pp. 270–279. DOI: 10.1016/j.conbuildmat.2015.07.003.

21. Nizina, T.A., Ponomarev, A.N., Kochetkov, S.N., Nizin, D.R., Kozeev, A.A. Analysis of influence nanomodified polycarboxylate plasticizers on strength and rheological characteristics of cementitious composites. Scientific Israel - Technological Advantages. 2014. Vol.16. No. 3. Pp. 6.

22. Rassokhin, A.S., Ponomarev, A.N., Figovsky, O.L. Silica fumes of different types for high-performance fine-grained concrete. Magazine of Civil Engineering. 2018. No. 78(2). Pp. 151–160. doi: 10.18720/MCE.78.12.

23. Ben-David, A., Davidson, C.E. Estimation method for serial dilution experiments. Journal of Microbiological Methods. 2014. DOI: 10.1016/j.mimet.2014.08.023

24. Le, T.T., Austin, S.A., Lim, S., Buswell, R.A., Gibb, A.G.F., Thorpe, T. Mix design and fresh properties for high-performance printing concrete. Materials and Structures/Materiaux et Constructions. 2012. 45 (8). Pp. 1221–1232. DOI: 10.1617/s11527-012-9828-z

25. Ding, T., Xiao, J., Zou, S., Zhou, X. Anisotropic behavior in bending of 3D printed concrete reinforced with fibers. Composite Structures. 2020. 254. Pp. 2021. DOI: 10.1016/j.compstruct.2020.112808

26. Arunothayan, A.R., Nematollahi, B., Ranade, R., Bong, S.H., Sanjayan, J.G., Khayat, K.H. Fiber orientation effects on ultra-high performance concrete formed by 3D printing. Cement and Concrete Research. 2021. 143 (November 2020). Pp. 106384. DOI: 10.1016/j.cemconres.2021.106384.

27. Wang, P., Zou, B., Ding, S., Huang, C., Shi, Z., Ma, Y., Yao, P. Preparation of short CF/GF reinforced PEEK composite filaments and their comprehensive properties evaluation for FDM-3D printing. Composites Part B: Engineering. 2020. 198 (January). Pp. 108175. DOI:10.1016/j.compositesb.2020.108175.

28. Pham, L., Tran, P., Sanjayan, J. Steel fibres reinforced 3D printed concrete: Influence of fibre sizes on mechanical performance. Construction and Building Materials. 2020. 250. Pp. 118785. DOI: 10.1016/j.conbuildmat.2020.118785.

Information about authors:

Aleksandr Rassokhin,
ORCID: https://orcid.org/0000-0001-7416-927X
E-mail: rassokhinaleksandr@gmail.com

Andrey Ponomarev, PhD of Technical Science
ORCID: https://orcid.org/0000-0003-2803-8281
E-mail: 9293522@gmail.com

Svetlana Shambina, PhD of Technical Science
ORCID: https://orcid.org/0000-0002-9923-176X
E-mail: shambina_sl@mail.ru

Antonina Karlina, PhD of Technical Science
ORCID: https://orcid.org/0000-0003-3287-3298
E-mail: karlinat@mail.ru

Durable concrete in sewerage using non-grinded rice husk ash and water-permeable mould

R.N. Uwazuruonye ✉ iD

Yokohama National University, Hodogaya-ku, Yokohama, Japan

✉ *uwazuruonyeraphael@yahoo.com*

Abstract. There are increasing interests in using natural pozzolans as partial replacements for ordinary Portland cement (OPC) in concrete due to the benefit to the environment, low-carbon footprint, and durability improvement potentials. In the present research, open-air-burnt non-grinded rice husk ash (RHA) samples from Ganawuri-Plateau State, Nigeria, were used as a partial replacement for OPC in concrete. A water-permeable form (controlled permeability formwork – CPF) was utilized to counter the adverse effects of high-water demand. The combined effects of CPF and RHA on the cover-zone microstructure/porosity were analysed by the mercury intrusion porosimetry (MIP) test. Water sorptivity and sulphuric acid resistance properties were measured by Surface Water Absorption Test (SWAT) and accelerated sulphuric acid resistance test, respectively, to study the suitability of the concrete mixtures for sewerage concrete structures. Compared to Portland cement concrete, the RHA with CPF samples had relatively low permeability and low water sorptivity while the RHA without CPF samples showed the highest resistance to sulphuric acid attack, exhibiting no weight loss, no gypsum formation at the surface with the least surface discolouration.

1. Introduction

The quest for sustainability has led to the massive utilization of natural pozzolans and various agricultural by-products in concrete production. Rice husk ash (RHA) is a good partial replacement for ordinary Portland cement for reducing permeability and increasing the acid resistance properties of concrete [1–3]. In several ways, it has been shown that RHA can be used to improve the strength and durability of concrete [2, 4, 5]. It has also been established by several researchers that due to the high siliceous content of RHA, it can resist acid attack to a significant degree [6].

Sulphate attack is the major cause of concrete deterioration in the sewerage environment. The attack generates microbial induced corrosion [7]. The formation of sulphuric acid in a sewerage environment can simply be expressed as:

sewage + sulphur reducing bacteria (SRB) + anaerobic condition= hydrogen sulphide (H_2S)   (1)

H_2S + aerobic condition + oxygen= sulphuric acid (H_2SO_4)   (2)
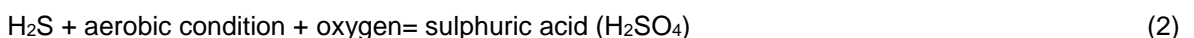
Microbial induced corrosion that results from the interaction of hydrogen sulphide and thiobacillus bacteria [2, 3] damages concrete structures, especially sewerage collection systems [9]. Olmstead and Hamlin (1900) wrote the first literature that brought the knowledge of this form of concrete corrosion to the limelight [9]. Wei et al (2010) explained the understanding that they termed the biological and physiochemical processes associated with microbiologically induced concrete corrosion. Sulphur-oxidizing microbes colonize the concrete in the presence of sufficient moisture and nutrient [10]. Sewerage provides the sulphur-oxidizing microbes with sufficient moisture and nutrients in wastewater treatment plants. Several microbes participate in this early stage of colonization due to the high pH value (pH 12) of the surface of a non-deteriorated concrete. Alkaline-tolerant microbes are one of the early participant microbes. The biogenic oxidation of sulphur on the concrete lowers the surface pH creating more palatable conditions for further microbial colonization [10]. According to Ramezanianpour (2010), "sulphate attack is one of the most aggressive environmental deteriorations that affects the long term durability of concrete structures" [11]. The SO_4^{2-} ions from H_2SO_4 reacts with Ca $(OH)_2$ and transform into gypsum $(CaSO_4.2H_2O)$. It then attacks the cement matrix leading to expansion and further cracking of the interior concrete structure [2]. This leaves the concrete more susceptible to direct and further attacks by H_2SO_4 [2].

An increase in pozzolanic reaction and fixing of $Ca(OH)_2$ by RHA yields additional C-S-H [12], increases density and resistance to penetration of deleterious substances [2]. Nonetheless, RHA decreases the workability of concrete due to high surface area [3] and require more water for proper mixing and adequate compaction than Portland cement concrete. This effect could harm the durability properties of concrete if not controlled. Chindaprasirt et al. (2007) could only attain the same workability in OPC mortar of 0.55 water-to-cement ratio using 0.68 water-to-binder ratio when 20 % OPC was replaced with RHA [3]. Moreover, investigations have shown that RHA increases water demand in fresh concrete [1–4]. A greater percentage of the water is primarily for workability, placement, and compaction. It is important to seek a method for expelling excess water from fresh RHA concrete after achieving proper placement and compaction.

The production of high-performance concrete by blending RHA has been widely established and adopted in construction but not yet appreciated by many agricultural-based developing countries like Nigeria because of requirements in technology and cost for controlled incineration and grinding. Location, type of burning and grinding affect the chemical composition of RHA and the resultant properties of concrete. Therefore, advances in research for the utilization of RHA for different purposes are localized. "In particular, durability of concrete structures depend primarily on the permeability of the outer concrete cover, which generally is a result of production standard, casting conditions, compaction in heavily reinforced areas and curing conditions"[13]. Therefore, several studies are being carried out on how the resistance to mass transfer at the cover zone of concrete can be improved.

Controlled permeability formwork (CPF) - first developed in Japan in the early 1980s [14] is one of the techniques that could be used to improve the quality of concrete at the cover zone [13–15]. CPF is primarily composed of a textile liner that is tensioned on a conventional formwork allowing the drainage of excess water while retaining the cement paste and at the same time expelling air bubbles from freshly placed concrete[13, 15]. CPF can reduce up to 20 % water-to-cement ratio at the cover zone [14], thus, improving the durability of the concrete by reducing the permeability [14, 16]. Nonetheless, this does not prevent the problem resulting from poor compaction where applicable or aggregate nesting induced by lack of paste [13].

The objective of the paper is to evaluate the effects of RHA and CPF on the microstructure, resistance to water ingress, and sulphuric acid resistance properties of the cover-zone of concrete blended with different amounts of an open-air-burnt non-grinded rice husk ash from Nigeria (RHA) for possible utilization in the durability and sustainability designs of sewerage concrete structures.

2.   Materials and Methods

2.1. Materials and specifications

A total of 48 samples consisting of 12 concrete types were prepared with OPC blended with RHA at 0 %, 10 % and 20 % by weights of the OPC. The 12 mix designs were selected from among the commonly used concrete in Nigeria and the mix proportions are shown in Table 1a.

The rice husk was obtained from a local rice mill in Ganawuri town, Riyom Local Government Council of Plateau State, Nigeria. It was dried in the open air and burnt under atmospheric conditions. RHA that passed through a 6 µm laboratory sieve with chemical properties shown in Table 1b was utilized for the concrete. The steps for processing the RHA are simplified in Fig. 1a. ED-XRF chemical analysis showed that the RHA could be classified as Type N pozzolanic material as per ASTM C618 classification because the percentage sum of SiO_3, Al_2O_3 and Fe_2O_3 components is greater than 70. Also, the SO_3 component of the RHA is not higher than 4 %.

Fine aggregate used was natural silica pit sand. It was sieved with a 5 mm aperture experimental sieve and washed to remove impurities it might contain. Surface dry density of the sand is 2.635 gcm^3. Crushed granite coarse aggregate was used. The aggregate size ranges from 5 mm to 20 mm with a surface dried density ~ 2.690 gcm^3, an absolute dried density ~ 2.663 gcm^3 and a water absorption rate of 1.00. The aggregate was used at a surface saturated condition and the water used was tap water.

Two types of moulds – conventional metal mould (N) and controlled permeability formwork (CPF) measuring 100 mm×100 mm×100 mm (Fig. 1b) were used. Three w/b ratios – 0.40, 0.50 and 0.60 were used and denoted as 40, 50 and 60 respectively. Water permeable sheets were used to construct the 100 mm×100 mm×100 mm CPF mould (Fig. 1b).

Table 1a. Concrete mix proportion.

Name of specimen	Binder type [1]	Mould type [2]	W/B (%)	RHA (%)	Mix composition (kg/m^3)			
					OPC	RHA	Coarse aggregate	Fine aggregate
40N *	O	N	40	–	437	–	977	767
50N *	O	N	50	–	437	–	911	716
50CPF	O	CPF	50	–	437	–	911	716
50RHA1-N	O-RHA	N	50	10	393.3	43.7	910	714
50RHA1-CPF	O-RHA	CPF	50	10	393.3	43.7	910	714
50RHA2-N *	O-RHA	N	50	20	349.6	87.4	908	713
50RHA2-CPF *	O-RHA	CPF	50	20	349.6	87.4	908	713
60CPF	O	CPF	60	–	437	–	847	665
60RHA1-N	O	N	60	10	393.3	43.7	845	663
60RHA1-CPF	O-RHA	CPF	60	10	393.3	43.7	845	663
60RHA2-N	O-RHA	N	60	20	349.6	87.4	844	662
60RHA2-CPF	O-RHA	CPF	60	20	349.6	87.4	844	662

Binder type [1] – O: ordinary Portland cement, RHA: open-burnt non-grinded rice husk ask
Mould type [2] – N: conventional metal mould, CPF: controlled permeability formwork
Asterisk (*): Samples used for MIP test

Table 1b. ED-XRF Chemical analysis of the properties of OPC and RHA.

| Binder	SiO$_2$ (%)	Fe$_2$O$_3$ (%)	Al$_2$O$_3$ (%)	SO$_3$ (%)	CaO (%)	NiO (%)	CuO (%)	MnO (%)	K$_2$O (%)	Na$_2$O (%)
OPC	20.36	3.04	5.33	2.13	64.09	–	–	–	0.36	0.28
RHA	67.75	2.75	–	0.53	4.51	0.01	0.14	1.46	7.62	–
	MgO (%)	ZnO (%)	P$_2$O$_5$ (%)	TiO$_2$ (%)	Rb$_2$O (%)	BaO (%)	V$_2$O$_5$ (%)	Eu$_2$O$_3$ (%)	Cr$_2$O$_3$ (%)	Re$_2$O$_7$ (%)
OPC	1.50	–	–	–	–	–	–	–	–	–
RHA	–	0.10	11.70	0.39	0.09	0.01	0.01	0.08	0.04	0.03
	Specific gravity		Surface area (g/cm^2)							
OPC	3.16		3310							
RHA	2.11		–							

Figure 1. Preparation of RHA material and moulds.
(a) Open-air burning and processing of RHA (b) metal and water permeable (CPF) moulds.

The curing condition applied was sealed curing for 28 days in the mould after casting the concrete. After curing, five sides of the specimen except for the side for measurements were sealed with aluminium tape and epoxy resin. Then, the specimens were kept in a controlled room condition (temperature – 20 °C and relative humidity – 60 %) and monitored until the time for measurements.

2.2. Test methods

Non-destructive and destructive tests were performed to measure porosity and transport properties of cover-zone of concrete and evaluate the durability in sewerage environment.

2.2.1 Surface moisture content

Surface moisture content was measured with a non-destructive electric-resistance type of moisture meter (model HI-100 of Kett Electric Laboratories Tokyo Japan) by pressing the device on the surface of the concrete for outputs expressed as count values. Appropriate initial surface moisture content has previously been confirmed by the author [17] and the upper threshold for the count values of the HI-100 moisture meter was established as 210 count values.

Moisture contents at the surfaces of the concretes that were not sealed with aluminium tape and epoxy resin were monitored until sufficiently dried cover zones that will ensure proper evaluations of the resistance to water ingress were attained. All the concrete samples (kept in a controlled room environment of a temperature of 20 °C and 60 % relative humidity) showed proper initial surface moisture contents at the age of 84 days.

2.2.2 Surface water absorption test (SWAT)

Surface water absorption test - SWAT (by Yokohama National University/Maruto Testing Company, Japan) [18] was used to measure the resistance to surface water ingress. SWAT measurements were conducted on the specimens 84 days after casting. The measurements were conducted in 20 °C and 60 % RH room condition. Coefficient of Surface Water Absorption- *CSWA* is the water sorptivity index used in the analysis. *CSWA* is the slope of an approximate linear regression between water absorption amount and the square root of time. The average value from four samples was used for the analysis.

SWAT (Fig. 2a) is a simple non-destructive device that evaluates the quality of the covercrete at 10 minutes under natural dominant water suction [18, 19]. SWAT has proven to be effective in detecting the influence of curing conditions and the effects of microcracks in covercrete quality within 10–20 mm, which is the most affected by concreting works [19–24]. The rate of surface water absorption at 10 minutes (in which the time for pouring water is 10 seconds) by SWAT is termed p_{600} (in ml/m^2/s). Moreover, the new SWAT index (CSWA in ml/m^2/s$^{1/2}$) was recently introduced by the author and was found to be correlated with the JSCE standard sorptivity test results [23].

2.2.3 Mercury intrusion porosimetry (MIP) test

Mercury intrusion porosimetry (MIP) test was conducted on selected concrete specimens to evaluate the porosity and pore size distribution at the cover zone. Samples from the specimens marked with asterisks (*) in Table 1a were carefully selected for the MIP tests to evaluate pore size changes relating to CPF, metal mould, w/b ratio and RHA. After the SWAT test, a 100 mm concrete cube was used for the MIP test. The test was conducted at Denki Kagaku Kogyo (Co.) laboratory, Tokyo – Japan. The specimens were cut at a depth of 15 mm – 20 mm from the exposed surface. The cut samples were coarsely pulverized and subjected to acetone to stop further hydration of un-hydrated particles. Final test samples 2.5 mm – 5 mm squares weighing 2.3025 g, 2.3023 g, 2.5004 g, and 2.5008 g for 40N, 50N, 50RHA2-N and 50RHA2-CPF respectively were used. The volume of cement pastes and cement + RHA pastes in the test samples were 0.300658 ml for 40N, 0.354783 ml for 50N, 0.40139 ml for 50RHA2-N, and 0.40146 ml for 50RHA2-CPF. An AutoPore IV 9500 V1.09 was used for the test.

2.2.4 Accelerated sulphuric acid resistance test

Accelerated sulphuric acid resistance tests were conducted on 3 samples for each mix design to study the effect of partial replacement of OPC with RHA. Besides, the test measured the effect of CPF on the resistance to H_2SO_4 attack. Immediately after SWAT, the 3 samples used for the accelerated sulphuric acid resistance test were immersed in tap water for 4 days to avoid possible effects of concrete dryness on the test and to simulate real conditions in sewerage structures where water ingress occurs before H_2SO_4 forms and the later acid attack. After, the specimens were transferred into a 5 % solution of H_2SO_4 by water weight (Fig. 2b). The H_2SO_4 used was 98.08 % concentration. The parameters investigated were the time and weight changes of fully immersed concrete specimens with only one surface exposed to the acid solution. Weight changes of the concrete specimens were measured at 3, 7, 14, 21, 28, 56 days and the depth of scaling from the surface after 56 days following immersion.


(a) (b)
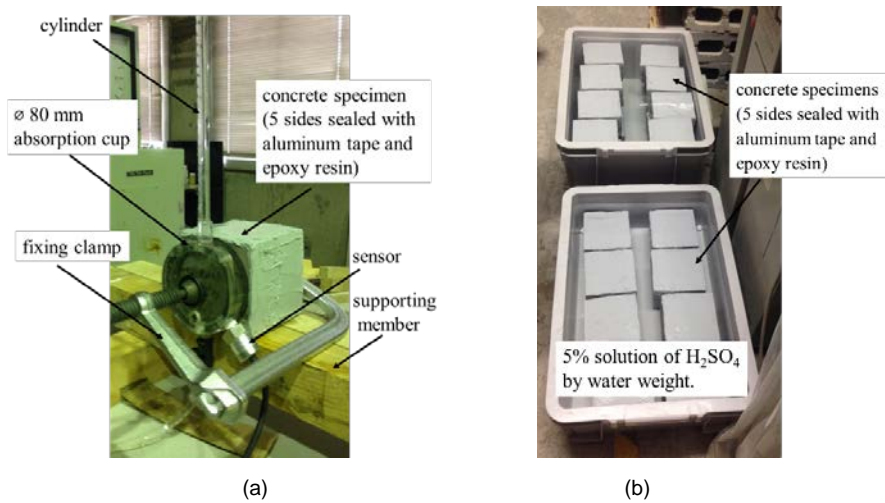
Figure 2. Test setups (a) Surface water absorption test (b) Accelerated H2SO4 test.

3. Results and Discussion

3.1. Water sorptivity of concrete

The influence of types of mould on time-dependent cumulative water absorption per unit area for the concrete cubes is presented in Fig. 3a while the water sorptivity at 10 minutes (CSWA in ml/m^2/s$^{1/2}$) is presented in Fig. 3b. Also, the initial surface moisture contents before the water absorption tests are shown in Fig. 3b.

Initial surface moisture contents measured by HI-100 moisture meter for the tested concrete samples range from 175 to 206 count values. As earlier mentioned, 210 count value of the HI-100 moisture meter has previously been established by the author as the upper threshold moisture content for effective evaluation of the resistance to water ingress property of concrete by SWAT [17]. It can be seen in Fig. 3b that before SWAT measurement, the surface moisture contents are slightly higher for samples cast with CPF than those cast with metal moulds. This indicates that CPF improved the quality by densifying the cover zone, reducing both the total pore volume and the pore diameters, thereby inhibiting rapid loss of moisture at the cover zone. Significant improvement in the resistance to water ingress for concrete cubes produced with CPF is observed as can be seen in Fig. 3b. A fifty-two per cent reduction in water sorptivity was observed for 50 % w/c OPC concrete. The water sorptivity results for 50N and 60-CPF specimens

showed that CPF could effectively eliminate the 10 % w/c difference. Even with an additional 9 % reduction in sorptivity resulting from the use of CPF. For the RHA blended specimens, the maximum and minimum reduction in water sorptivity resulting from the use of CPF was 38 % and 19 % respectively.

The addition of RHA improved the resistance to water ingress properties of the concrete. This could be evidence that RHA yielded more C-S-H leading to an increase in the density and producing lower permeability. Just as expected, 50 % w/b contents revealed lower surface water absorption than 60 % w/b contents. Twenty per cent RHA showed slightly higher resistance to water absorption than 10 % RHA while combining RHA and CPF significantly improved the resistance to water absorption.
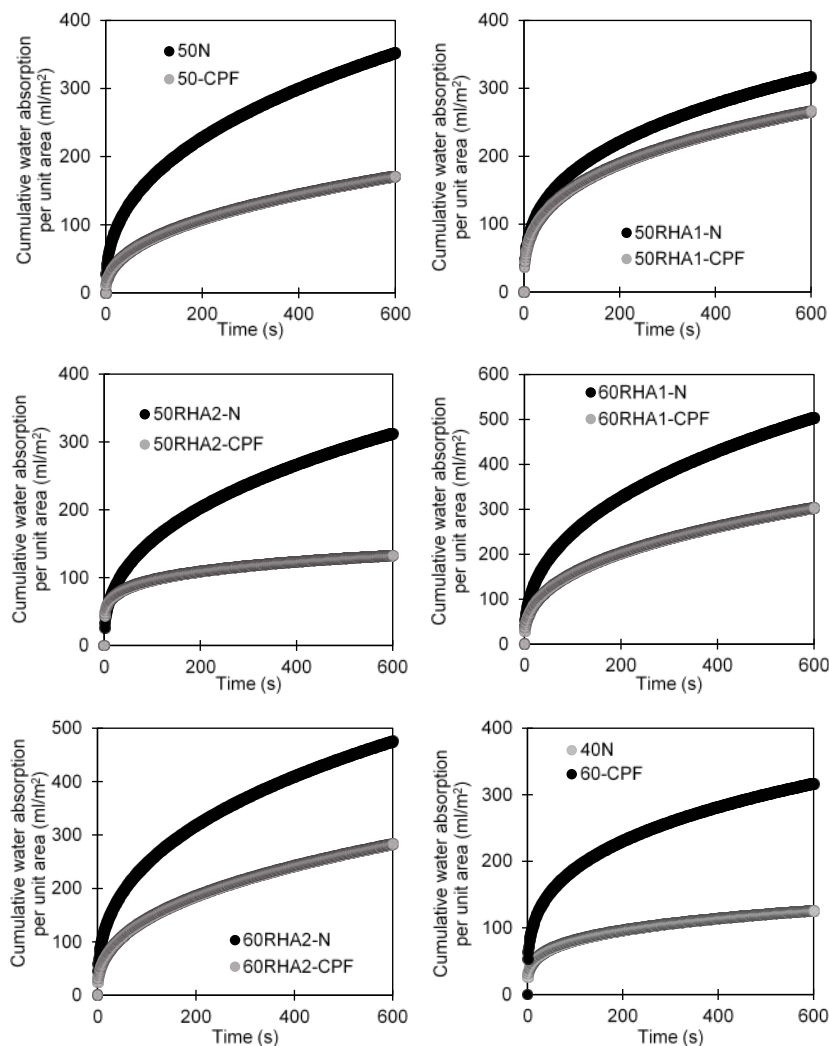
Figure 3a. Influence of type of mould on time-dependent cumulative water absorption per unit area for the concrete cubes.
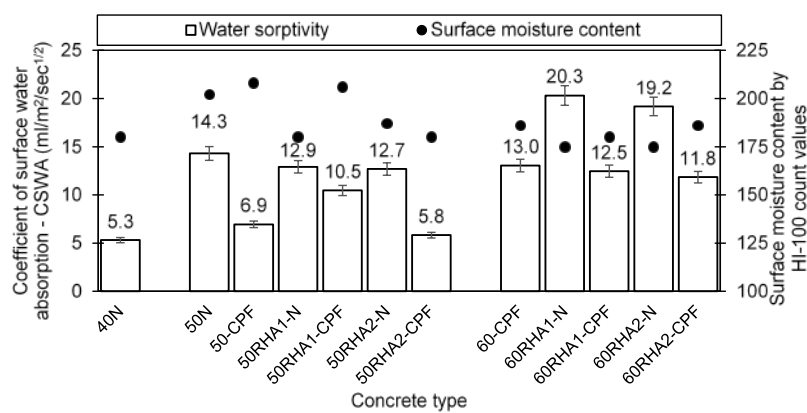
Figure 3b. Water sorptivity and initial surface moisture content of the concrete cubes.

3.2. Porosity and pore size distribution of concrete

A plot of cumulative pore volume against the pore diameter from the MIP measurements is presented in Fig. 4a while the pore size distribution is presented in Fig. 4b. It can be inferred from the results that intrudable porosity for the four concrete types is nearly the same pore diameter. They are 3.556 nm for 40 N, 50 N and 50RHA2-CPF and 3.889 nm for 50RHA2-N. Intrudable porosity $\left(\phi_{in}\right)$ is obtained as the smallest equivalent pore diameter that corresponds to the highest point on the cumulative porosity curve [24]. The quantitative threshold pore diameter $\left(d_{th}\right)$ is calculated using the popular tangent method and confirmed with the Sakai C. et al novel method that derived its "basis on the empirical critical volume fraction for percolation"[25]. The method assumes that when 16 % of the cement paste is filled with mercury during the MIP test, the corresponding pore radius is the threshold pore radius [25]. Quantitative threshold pore diameter $\left(d_{th}\right)$ is the largest pore diameter above which a comparatively little mercury intrusion occurs and below which a large volume of mercury intrusion starts [24]. The threshold pore radius for the concrete samples is 16.41 nm for 40 N, 41.11 nm for 50 N, 5.33 nm for 50RHA2-N and 5.93 nm for 50RHA2-CPF. The total porosity (in %) for 40N is 6.7888, 50N is 13.3998, 50RHA2-N is 9.8040 and 50RHA2-CPF is 10.2262. Threshold pore radius is defined as "the minimum pore size through which a mass has to pass for penetration to be possible" [25].

The addition of RHA significantly reduced the porosity and the threshold pore radius obtained from the cover zone of the concrete. Replacing 20 % of OPC with RHA reduced the total porosity by ~ 27 % for 50RHA2-N and ~ 24 % for 50RHA2-CPF compared to 50N. Also, the threshold pore radius improved about seven times. It is seen that the porosity for the 50RHA2-CPF sample increased by ~ 5 % because of CPF. Likewise, the threshold pore radius for the 50RHA2-CPF sample increased by ~ 10 %. Nevertheless, the increase in porosity and threshold pore radius are insignificant owing to heterogeneity of concrete and other major factors such as pore continuity/connectivity that affects permeability. The shift in the pore size distribution for the RHA blended specimens is reflected in the calculated threshold pore radius $\left(r_{th}\right)$. The range of capillary pores that define continuity/connectivity of the pore system (ϕ10 nm to ϕ100 nm), which is the main indicator of the durability of concrete [26, 27], are dominant in 50N specimen. When the volume of pores in this range is high, it could indicate more interconnectivity and continuity of the pores and could translate into a higher permeability. Furthermore, large capillary pores (above ϕ100 nm) that have a direct influence on mass transfer [26–28] are seen more in specimens without RHA. These are evident in the water sorptivity values obtained from these specimens.
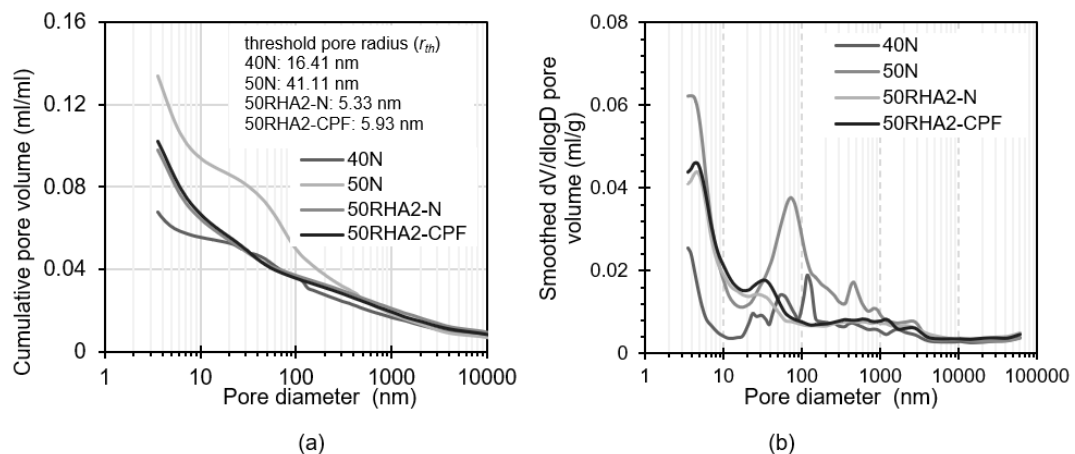

Figure 4. (a) Cumulative pore volume vs pore diameter (b) Pore size distribution.

3.3. Accelerated sulphuric acid resistance

The results of the accelerated H_2SO_4 resistance tests are presented in Fig. 5. Fig. 5a shows the time-dependent weight change of concrete in 5% H_2SO_4 solution while Fig. 5b shows the depth of scaling after 56 days of immersion. A value of $R^2 = 0.8537$ was obtained in the linear regression analysis between the two indices.

As the percentage change in weight of the concrete specimens is analysed, it is inferred that the addition of RHA influences this parameter. The first clear trend is the reduction in the percentage of weight loss shown in Fig. 5a. Second, the inclusion of RHA reduced the depth of scaling (Fig. 5b). Regardless of the RHA dosage, its addition significantly improved the resistance to sulphate attack. Specimens with 60 % w/b contents showed the lowest weight loss. The lesser attack of H_2SO_4 on RHA blended concrete

specimens could be resulting from a reduction in tricalcium aluminate (C_3A) and tricalcium silicate (C_3S) contents of the concrete and the lower sulphate adsorption by C-S-H. High C_3A in cement proves less resistance to sulphate attack, evident in the British Standards (BS 4027) stipulating a maximum of 3.5 % C_3A content in Portland cement for sulphate resistance. Besides, the reaction that causes concrete deterioration occurs between the sulphate and hydrates from calcium hydroxide (CH). CH is significantly generated by tricalcium silicate (C_3S) [11], and it is known that RHA reduces the C_3S content, which is the main cause of the low early age strength of RHA blended concretes. Visual evaluations revealed no gypsum formation on the surfaces of the RHA blended concretes. This suggests that the RHA countered to a significant value, the sulphate attack that reduces the stiffness of the hydrated pastes that could have been followed by large expansion and scaling due to ettringite formation.
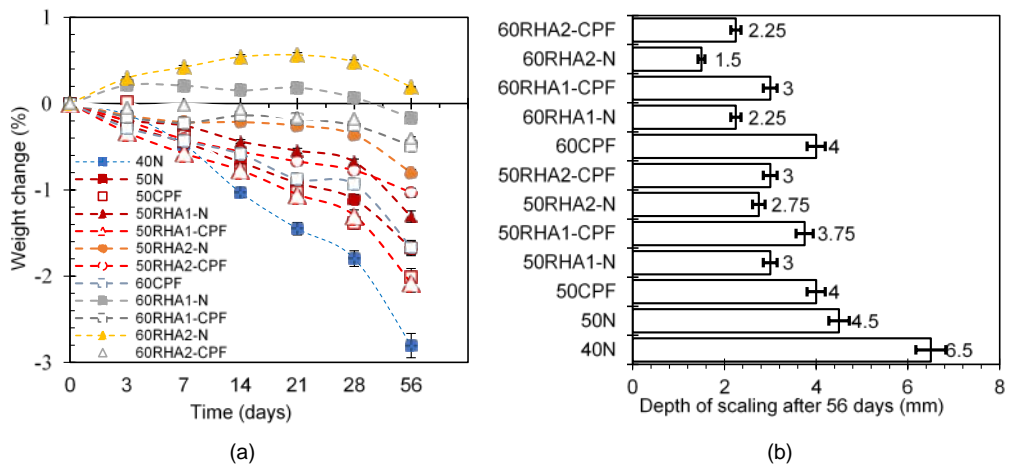

Figure 5. (a) Time-dependent weight change of concrete in 5% H_2SO_4 solution (b) Depth of scaling after the 56 days of immersion

4. Conclusions

In this study, durability performance of OPC concretes blended with 10 % and 20 % open-air-burnt non-grinded rice husk ash (RHA) and cast with conventional metal mould and water permeable mould (CPF) was investigated to evaluate potential utilization for sewerage concrete structures. From the result of the ED-XRF chemical analysis of the RHA, the MIP test, water sorptivity and accelerated acid resistance results of concretes with 40 %, 50 % and 60 % water-to-binder contents, the following conclusions are obtained:

1. The open-air burnt non-grinded RHA in this research could be classified as a Type N pozzolanic material as per ASTM C618 classification because the percentage sum of SiO_3, Al_2O_3 and Fe_2O_3 components is greater than 70. In addition, the SO_3 component of the RHA is not higher than 4 %.

2. The combination of 10 % OPC replaced with RHA and conventional metal mould did not significantly improve the water-resistance properties of the cover concrete, like for the combination of 20 % OPC replaced with RHA and a conventional metal mould. However, the water resistance properties of the 10 % and 20 % RHA concrete could be significantly improved by introducing CPF.

3. The replacement of 10 % and 20 % OPC with RHA provided significant resistance to sulphuric acid attack, to a greater extent than the conventional OPC concretes. These were applicable when cast with both conventional metal mould and CPF. Nonetheless, RHA concretes produced with conventional metal mould could provide greater resistance to H_2SO_4 attack than the ones produced with CPF.

4. A significant reduction of porosity and threshold pore diameter of concrete could be achieved by replacing OPC with 10 % or 20 % open-air-burnt non-grinded rice husk ash (RHA).

5. Open-air-burnt non-grinded rice husk ash from Nigeria (RHA) is a good Supplementary Cementitious Material (SCM) and could effectively be utilized in durability and sustainability designs of sewerage concrete structures.

References

1. Ramasamy, V. Compressive strength and durability properties of rice husk ash concrete. KSCE Journal of Civil Engineering. 2012. 16 (1). Pp. 93–102. DOI: 10.1007/s12205-012-0779-2

2. Chatveera, B., Lertwattanaruk, P. Durability of conventional concretes containing black rice husk ash. Journal of Environmental Management. 2011. 92 (1). Pp. 59–66. DOI: 10.1016/j.jenvman.2010.08.007

3. Chindaprasirt, P., Kanchanda, P., Sathonsaowaphak, A., Cao, H.T. Sulfate resistance of blended cements containing fly ash and rice husk ash. Construction and Building Materials. 2007 21 (6). Pp. 1356–1361. DOI: 10.1016/j.conbuildmat.2005.10.005

4. Givi, A.N., Rashid, S.A., Aziz, F.N.A., Salleh, M.A.M. Assessment of the effects of rice husk ash particle size on strength, water permeability and workability of binary blended concrete. Construction and Building Materials. 2010. 24 (11). Pp. 2145–2150. DOI: 10.1016/j.conbuildmat.2010.04.045

5. Habeeb, G.A., Mahmud, H.B. Study on properties of rice husk ash and its use as cement replacement material. Materials Research. 2010. 13 (2). Pp. 185–190. DOI: 10.1590/S1516-14392010000200011

6. Chatveera, B., Lertwattanaruk, P. Evaluation of sulfate resistance of cement mortars containing black rice husk ash. Journal of Environmental Management. 2009. 90 (3). Pp. 1435–1441. DOI: 10.1016/j.jenvman.2008.09.001

7. Shook, W.E., Bell, L.W. Corrosion control in concrete pipe and manholes. Proceedings of Water Environmental Federation, Florida. 1998. [Online]. System requirements: Adobe Acrobat Reader. URL: https://citeseerx.ist.psu.edu/viewdoc/download?doi=10.1.1.500.7182&rep=rep1&type=pdf (date of application: 16.04.2021)

8. De Muynck, W., De Belie, N., Verstraete, W. Effectiveness of admixtures, surface treatments and antimicrobial compounds against biogenic sulfuric acid corrosion of concrete. Cement and Concrete Composites. 2008. 31 (3). Pp. 163–170. DOI: 10.1016/j.cemconcomp.2008.12.004

9. Roberts, D.J., Nica, D., Zuo, G., Davis, J.L. Quantifying microbially induced deterioration of concrete: initial studies. International Biodeterioration & Biodegradation. 2002. 49 (4). Pp. 227–234. DOI: 10.1016/S0964-8305(02)00049-5

10. Wei, S., Sanchez, M., Trejo, D., Gillis, C. Microbial mediated deterioration of reinforced concrete structures. International Biodeterioration & Biodegradation. 2010. 64 (8). Pp. 748–754. DOI: 10.1016/j.ibiod.2010.09.001

11. Ramezanianpour, A.A., Pourbeik, P., Moodi, F. Sulfate resistance of concrete containing rice husk ash. Amirkabir Journal of Civil Engineering. 2013. [Online]. System requirements: Adobe Acrobat Reader. URL: https://www.sid.ir/en/journal/ViewPaper.aspx?id=401439 (date of application: 18.04.2021)

12. Neville, A.M. Properties of Concrete, 4th Edition. Pearson Education Limited. 2004.

13. Figueiras, H., Nunes, S., Coutinho, J.S., Figueiras, J. Combined effect of two sustainable technologies: Self-compacting concrete (SCC) and controlled permeability formwork (CPF). Construction and Building Materials. 2009. 23 (7). Pp. 2518–2526. DOI: 10.1016/j.conbuildmat.2009.02.035

14. Harrison, T. Introducing controlled permeability formwork, increase concrete durability in the cover zone. Publication of Concr. Constr. 1991. [Online] URL: https://www.concreteconstruction.net/how-to/materials/introducing-controlled-permeability-formwork_o (date of application: 18.04.2021)

15. Sousa C.J. The combined benefits of CPF and RHA in improving the durability of concrete structures. Cement and Concrete Composites. 2003. 25 (1). Pp. 51–59. DOI: 10.1016/S0958-9465(01)00055-5

16. Liu, J., Miao, C., Chen, C., Liu, J., Cui, G. Effect and mechanism of controlled permeable formwork on concrete water adsorption. Construction and Building Materials. 2013. 39 (1). Pp. 129–133. DOI: 10.1016/j.conbuildmat.2012.05.005

17. Uwazuruonye. R.N., Hosoda, A. Investigation of the effects of saturation degree of permeable pore voids for appropriate covercrete quality evaluation by SWAT. Internet Journal of Society for Social Management Systems. 2020. 12 (2). [Online]. System requirements: Adobe Acrobat Reader. URL: http://ssms.jp/img/files/sms19_2361%281%29.pdf

18. Hayashi, K., Hosoda, A. Development of surface water absorption test applicable to actual structures. Proceedings of Japan Concrete Institute. 2011. 33 (1). Pp. 1769-1774. (in Japanese)

19. Hayashi, K., Hosoda, A. Fundamental study on evaluation method of covercrete quality of concrete structures by surface water absorption test. Journal of Japan Society of Civil Engineers, Ser. E2, Materials and Concrete Structures. 2013. 69 (1). Pp. 82–97. DOI: 10.2208/jscejmcs.69.82

20. Komatsu, S., Tajima, R., Hosoda, A. Proposal of quality evaluation method for upper surface of concrete slab with surface water absorption test. Concrete Research and Technology. 2018. 29 (1). Pp. 33–40. DOI: 10.3151/crt.29.33

21. Ngo, V.T., Hosoda, A., Komatsu, S., Ikawa, N. Effect of moisture content on surface water absorption test and air permeability test. Proceedings of Japan Concrete Institute. 2018. 40 (1). Pp. 1725–1730.

22. Nam, H.P., Hosoda, A. Improvement of water and chloride penetration resistance of slag concrete by using high alite cement. Proceedings of Japan Concrete Institute. 2015. 37 (1). Pp. 661–666.

23. Uwazuruonye, R.N., Hosoda, A. Investigation on correlation between surface water absorption test and JSCE sorptivity test. Proceedings of Japan Concrete Institute. 2020. 42 (1). Pp. 1726–1731.

24. Ma, H. Mercury intrusion porosimetry in concrete technology: tips in measurement, pore structure parameter acquisition and application. J Porous Mater. 2014. 21 (2). Pp. 207–215. DOI: 10.1007/s10934-013-9765-4

25. Sakai, Y., Nakamura, C., Kishi, T. Threshold pore radius of concrete obtained with two novel methods. Proceedings of RILEM International workshop on performance-based specification and control of concrete durability. 2013. ISBN: 978-2-35158-135-3. Pp. 109–116.

26. Uwazuruonye, R.N., Hosoda, A. Numerical simulation of water sorptivity of concrete measured by Surface Water Absorption Test. Proceedings of Japan Concrete Institute. 2021. 43 (1). Pp. 1295–1300.

27. Uwazuruonye, R.N. Effects of pore void saturation degree on nondestructive tests for durability assessment of concrete structures. PhD Dissertation. Yokohama National University. 2020. DOI: 10.18880 / 00013481

28. Rucker-Gramm, P., Beddoe, R.E. Effect of moisture content of concrete on water uptake. Cement and Concrete Research. 2010. 40 (1). Pp. 102–108. DOI: 10.1016/j.cemconres.2009.09.001

Information about author:

Raphael Uwazuruonye, PhD
ORCID: *https://orcid.org/0000-0002-4707-9946*
E-mail: *uwazuruonyeraphael@yahoo.com*

Research article

UDC 625

Compressive strength prediction model of lightweight high-strength concrete

L.N. Zhang[1] (iD) **, D.P. He[1]** (iD) **, W.Y. Xu[1]** (iD) **, Q.Q. Zhao[2]** ✉ (iD) **, S.B. Teng[3]** (iD)
[1] Northeast Forestry University, Harbin, Heilongjiang, China
[2] Northeast Agricultural University, Harbin City, Heilongjiang Province, China
[3] Heilongjiang Transportation Investment Group Co., Harbin City, Heilongjiang Province, China

✉ 492954791@qq.com

Keywords: concrete, numerical model, regression analysis, optimization, mechanical performance

Abstract. A reasonable prediction of the compressive strength of lightweight high-strength concrete is an important basis for determining concrete strength. Through cluster analysis, the key factors affecting the compressive strength of lightweight high-strength concrete are found, and the degree of influence of each factor on the compressive strength is analyzed. We applied linear regression analysis of the relationship between the above factors and the compressive strength using SPSS, and performed multiple non-linear regression to establish a prediction model for the compressive strength of lightweight high-strength concrete using MATLAB. Using RMSE, we tested the simulated and actual values of the model, to determine the applicable conditions of the model through response surface analysis. The results of the study show that: cylinder compressive strength, water-binder ratio, cement dosage, coarse aggregate particle size and sand ratio are the key factors affecting the compressive strength. The R^2 values of the single-factor prediction models are all greater than 0.9, and the corresponding coefficients of the lightweight high-strength concrete compressive strength prediction models are 1.46, 18.31, 21.6, –3.28, –71.12, 1.36 and 20.48 respectively; The root mean square error RMSE is all lower than 1.05 MPa. The applicable condition of the prediction model shows that the cylinder compression strength is between 3.2 MPa and 4.9 MPa. When the coarse aggregate particle size is 15 mm~25 mm, the sand ratio is 26 %~35 %, the cement dosage is 450 Kg/m³~500 Kg/m³, and the water-binder ratio is 0.34~0.4, the parameter value range is the optimal prediction space of the model. When the 5 parameters are simultaneously in the optimal prediction interval, the prediction level of the model is the best and the prediction accuracy of the proposed compressive strength prediction model is higher. The model is of great significance to the study of the mechanical properties of lightweight high-strength concrete.

1. Introduction

Lightweight high-strength concrete has become a hot spot in the industry: it has the characteristics of strong durability, good corrosion resistance and high compressive strength, and its performance and quality can be used for high-rise buildings [1]. As the basis to determine the strength grade of concrete, compressive strength has become a necessary index to determine the quality and production control evaluation of concrete [2, 3].

Most of the research on the compressive strength of lightweight high-strength concrete at home and abroad focuses on the qualitative analysis of the factors affecting the compressive strength and the detection of the compressive strength. For example, Cheng [4] conducted an indoor unconfined uniaxial compression test and believed that admixtures had a significant influence on the early compressive strength of lightweight high-strength concrete. Slonski [5–7] has completed a number of mix ratio tests, and obtained the optimal mix ratio that makes the compressive strength of lightweight high-strength concrete relatively high. Akbari [8] observed the microstructure of lightweight high-strength concrete with scanning electron microscope and determined that the appropriate curing conditions had significant influence on the compressive strength. Based on the cement-based material test, Sobhani [9–11] found that the type of micro beads would affect the density of the material, thus affecting the compressive strength. Costa [12–14] proved through sampling test that proper reduction of cement dosage and corresponding increase of coarse aggregate dosage can ensure concrete strength and prolong concrete service life. Although the above research has confirmed that some factors have influence on the compressive strength of lightweight high-strength concrete, the research object is one-sided and lacks a comprehensive analysis of the compressive strength of concrete in practical engineering.

The testing methods of compressive strength are mainly divided into two categories. One is to use mathematical statistics software to conduct theoretical calculation on the influence parameters of concrete strength, that is, to predict concrete compressive strength by analyzing the concrete mix ratio. For example, Lee [15, 16] used Boromi's formula to predict the compressive strength, and Malachanne [17] established the BP neural network model to predict the compressive strength. The second is the use of tests or instruments for detection, that is, based on the actual mixing in the field through the early strength prediction of late strength method, such as ultrasonic rebound synthesis method, fresh concrete on-site detection method. In the relevant literatures, Boukli [18] proposed the relation formula of fly ash concrete strength, Zhang [19] proposed the bivariate strength formula of fly ash concrete, and Bingol [20] established the strength model of fly ash concrete at different ages by using Statistical Package for Social Sciences (SPSS) software. Although the above prediction methods can predict the compressive strength of lightweight high-strength concrete, the prediction accuracy is not high, because the formulated prediction cannot be applied to all types of lightweight high-strength concrete, the parameters in the prediction model are not comprehensive, and the field detection is not predictable.

In conclusion, the compressive strength prediction method of lightweight high-strength concrete needs to be further improved. In this paper, the relevant research content of the compressive strength of lightweight high-strength concrete is combined with theory and practice, through analysis, the main factors that affect the lightweight high-strength concrete are found out, and the influence degree of the factors is analyzed. The prediction model of 28 days strength of lightweight high-strength concrete is established, and the model is tested. The applicable conditions of the model are determined by surface analysis method. The prediction model of compressive strength of lightweight high-strength concrete can accurately predict the change of compressive strength. The model can provide reference for the design of mix ratio of lightweight and high-strength concrete, and provide experimental basis and theoretical guidance for the mechanical properties of lightweight aggregate concrete. Therefore, the research on the prediction model of compressive strength of lightweight high-strength concrete is of great significance.

2. Methods

2.1. Influence factor extraction

In order to extract the factors that affect the compressive strength of lightweight high-strength concrete in seasonal freezing areas, the existing research results of domestic and foreign literature are analyzed. Mehta [21] used numerical analysis methods to perform regression analysis on factors such as concrete component dosage, curing conditions, admixtures, early strength, water absorption and bulk density, and predicted 28 days compressive strength. Hung [22–24] used 7 variables including the maximum particle size of crushed rock, sand ratio, cement label, slump, water, cement, sand and gravel consumption as input parameters for network training, and 28 days compressive strength as output parameters. Chithra [25, 26] pointed out that the strength of high-strength high-performance concrete is related to many factors such as cement type, aggregate particle size, admixtures and curing conditions. Ambily [27] further advanced the water-cement ratio theory and proposed a strength formula based on the hydrocolloid ratio. Yoon [28] added antifreeze to lightweight high-strength concrete to improve the compressive strength according to the climatic characteristics of seasonal freezing areas.

According to the above analysis, the concrete compressive strength, curing conditions, early strength, water absorption, bulk density, cement type, coarse aggregate particle size, water-binder ratio, cement dosage, sand ratio, water reducing agent and admixture of coarse aggregate concrete etc., the above factors may affect the compressive strength of lightweight high-strength concrete in seasonal freezing areas. In view of the two factors of water absorption and bulk density, since coarse aggregates are

pre-wet before mixing to reach a saturated surface dry state, water absorption is not considered in the factors affecting the strength of lightweight high-strength concrete; bulk density as the physical properties of aggregate, it is not considered. Haile [29–31] et al. proposed that water reducers can reduce the water consumption of mixed concrete, thereby increasing the strength of concrete. Since mineral admixtures and water-reducing agents have a recommended dosage before use, the impact of water-reducing agents on the compressive strength of lightweight high-strength concrete is not considered.

The cluster analysis method is used to extract the above factors affecting the compressive strength of lightweight high-strength concrete, as shown in Fig. 1. The 12 influencing factors are numbered, and the numbers are F1 to F12, as shown in Table 1.

Table1. Factors and numbers affecting the compressive strength of lightweight high-strength concrete.

No.	Influencing factors	No.	Influencing factors	No.	Influencing factors
F1	Cylinder compressive strength of coarse aggregate	F5	Water reducing agent	F9	Maintenance conditions
F2	Coarse aggregate size	F6	Early strength	F10	Water absorption
F3	Bulk density	F7	Cement varieties	F11	Sand rate
F4	Water-binder ratio	F8	Admixture	F12	Cement consumption

In Fig. 1, the abscissa is the standard value of influence Z (RIV), and the ordinate is the standard value of influence Z (SDV). The larger influencing factors of the Z (RIV) and Z (SDV) values are F2 (coarse aggregate particle size), F11 (sand rate) and F12 (cement amount) in cluster 2, cluster 3 contains F1 (the barrel compressive strength of coarse aggregate) and F4 (water-binder ratio), indicating that the five factors included in these two clusters have a wide range of influence on the compressive strength of lightweight high-strength concrete, so these five factors It is a key factor. The 7 factors included in the other 2 clusters have a smaller range and degree of influence than the 5 factors in cluster 2 and cluster 3, so they are secondary factors. According to the analysis in Fig. 1, the barrel compressive strength of coarse aggregate, coarse aggregate particle size, water-binder ratio, cement dosage and sand ratio are the key factors affecting the compressive strength of lightweight high-strength concrete.
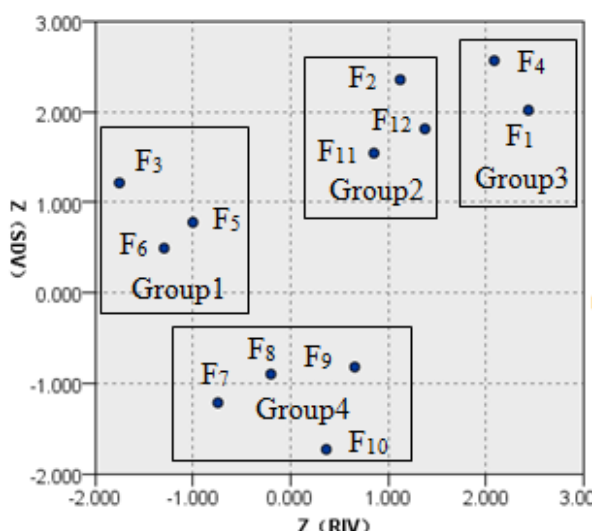

Figure 1. Cluster analysis of influencing factors.

2.2. Analysis of influencing factors

In order to further analyze the degree of influence of the above factors on the compressive strength of lightweight high-strength concrete, establish different amounts of coarse aggregate particle size, water-binder ratio, cement dosage, sand ratio, admixtures and different barrel compressive strengths. The change of compressive strength under the same age conditions, so as to determine the influence of the above factors on the compressive strength by comparing experiments. It adopts China's current national standard GB/T 50081-2002 "Standard for Test Methods of Mechanical Properties of Ordinary Concrete". The size of the test piece is 150 mm×150 mm×150 mm, and the water-permeable concrete specimens composed of different aggregate particle sizes are prepared for comparison test. According to the design principles of ordinary concrete, a set of initial mix ratios are designed, in which the water-cement ratio is 0.35, the sand

ratio is 0.3, and the amount of cement per cubic meter of concrete material is 485.71 kg, the amount of sand is 280.09 kg, and the amount of stones is 666.87 kg, the amount of water used is 170 kg. The water-binder ratios selected are 0.3, 0.35 and 0.4 respectively; the sand content is from 35 % to 45 %. The amount of cement is 225 g, 250 g, 275 g, 325 g and 350 g respectively. The coarse aggregate particle size is 5 mm~25 mm. The cylinder compressive strength is 5.7 MPa and 3.2 MPa respectively. The specimens are cured in the curing room, and the curing conditions are temperature 20±2 °C and relative humidity above 95 %.

In order to verify the impact of cylinder compressive strength on the compressive strength, two sets of comparative test pieces were established, each with 5 test pieces, and the same condition of the coarse aggregate particle size, water-binder ratio, cement dosage, sand ratio and admixture was established. The cylinder compressive strength is 3.2 MPa and 5.7 MPa respectively, the comparative analysis of compressive strength is carried out, as shown in Fig. 2. In Fig. 2, the concrete specimen with a cylinder compressive strength of 5.7 MPa is 22.2 %, 21.5 %, 20.5 % and 25.0 % higher than the specimen with a cylinder compressive strength of 3.2 MPa at ages of 5 d, 10 d, 15 d, and 20 d. Indicating that the cylinder compressive strength has a significant influence on the compressive strength of lightweight high-strength concrete. The reason for the analysis is that the strength of lightweight aggregate is significantly lower than that of mortar. The external force is mainly borne by the mortar. When the particle size in the aggregate is large, the mortar skeleton surrounding the aggregate will become weaker, which will result in a decrease in the strength of the concrete. And as the particle size of the lightweight aggregate decreases, its specific surface area increases, and the bonding force with the cement mortar increases. At the same time, the smaller the particle size, the smaller the probability of internal cracks and the increase in resistance to deformation. This allows the particle shape coefficient to be optimized, stress concentration is reduced, and the strength of concrete is improved. From the above analysis, it can be concluded that the cylinder compressive strength is an important factor in determining the strength of lightweight aggregate concrete.
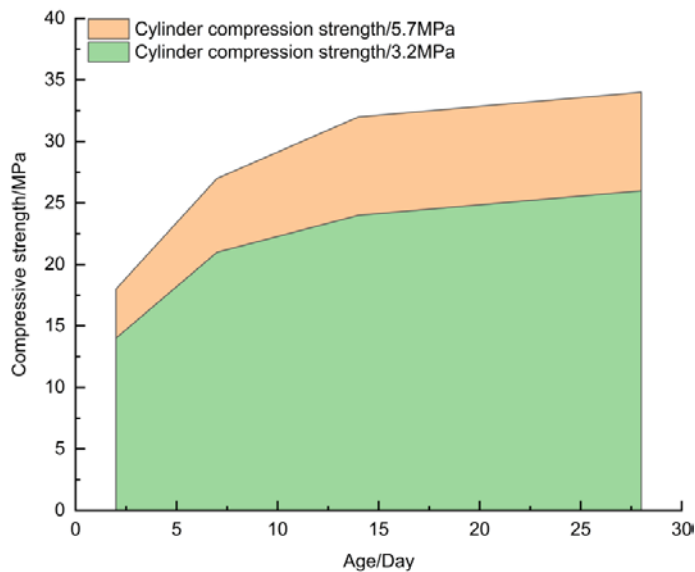

**Figure 2. Influence of cylinder compressive strength
on concrete compressive strength of different ages.**

In order to verify the influence of the particle gradation of coarse aggregate on the compressive strength of lightweight high-strength concrete, four sets of comparative specimens were established under the condition that the cylinder compressive strength, water-binder ratio, cement dosage and sand ratio remain unchanged. 5 pieces for comparison test. Choose four different coarse aggregate particle sizes, which are 5~10 mm, 5~15 mm, 5~20 mm and 5~25 mm, as shown in Fig. 3. According to the analysis in Fig. 3, as the age increases, the compressive strength of each particle size continues to increase, but the compressive strength of 5~15 mm is the largest, and the impact of coarse aggregate particle size on concrete strength is relatively low. The slight difference in compressive strength at the same age is controlled within the range of 5 MPa. The above analysis proves that with the increase of aggregate particle size, the strength of high-strength concrete first increases and then decreases. The aggregate particle size should not exceed 20 mm, and the best particle size is 5~15 mm. The reason for the analysis is that the particle size of the coarse aggregate has an impact on the compressive strength. The larger the particle size of the aggregate, the greater the probability that there will be defects in the concrete component. At this time, the bonding strength of the interface is lower, which will cause the interior of the concrete. The uneven distribution of particles induces a decrease in the strength of the hardened concrete.
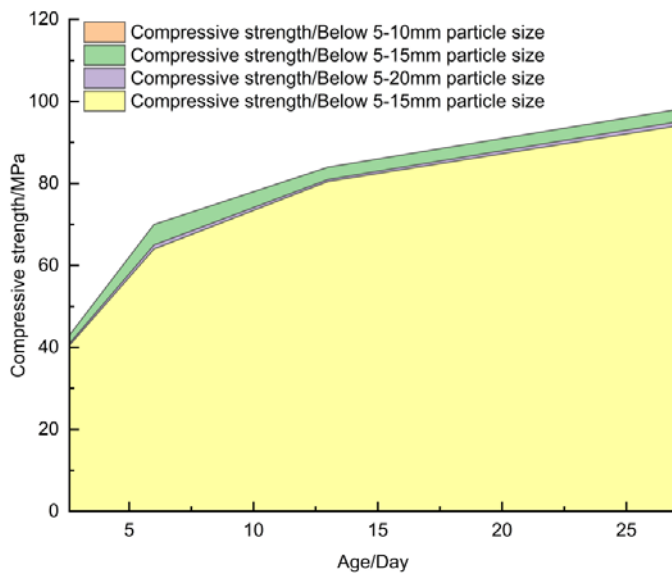
**Figure 3. Influence of coarse aggregate size
on compressive strength of concrete at different ages.**

The size of the sand ratio directly affects the ratio of aggregate to cement stone in the concrete. When the sand ratio is increased, the ratio of light aggregate will decrease and the strength of concrete will increase. So lightweight high-strength concrete needs to increase the sand rate. According to the cluster analysis, sand ratio is an important factor affecting the compressive strength of fine aggregates. In order to further study and determine the impact of sand ratio on compressive strength, concretes with different sand ratio contents were selected. The sand content is 35 %, 37 %, 39 %, 41 %, 43 %, 45 %. When the ages are 3 days, 7 days, 14 days and 28 days, the changes in compressive strength of different ages are analyzed. The situation is shown in Fig. 4. It can be seen from Fig. 4 that the sand ratio has a very obvious influence on the compressive strength of concrete. The greater the sand ratio, the smaller the proportion of light aggregate in the concrete, and the higher the strength of the concrete. When the sand ratio is 39 %, the compressive strength was 35 MPa, 56 MPa, 58 MPa and 64 MPa at the age of 3 days, 7 days, 14 days and 28 days respectively. However, when the sand ratio increases to 39 %, continuing to increase the sand ratio will reduce the compressive strength of the concrete. Compared with the sand ratio of 39 %, the compressive strength of the sand ratio of 45 % decreased by 8.6 %, 5.4 %, 4.3 % and 4 % at the age of 3 days, 7 days, 14 days and 28 days. The main reason is that the sand rate is too large and the concrete is easy to segregate, which leads to uneven formation of the concrete structure, and the concrete damage is easy to break from the part where the aggregate is concentrated.
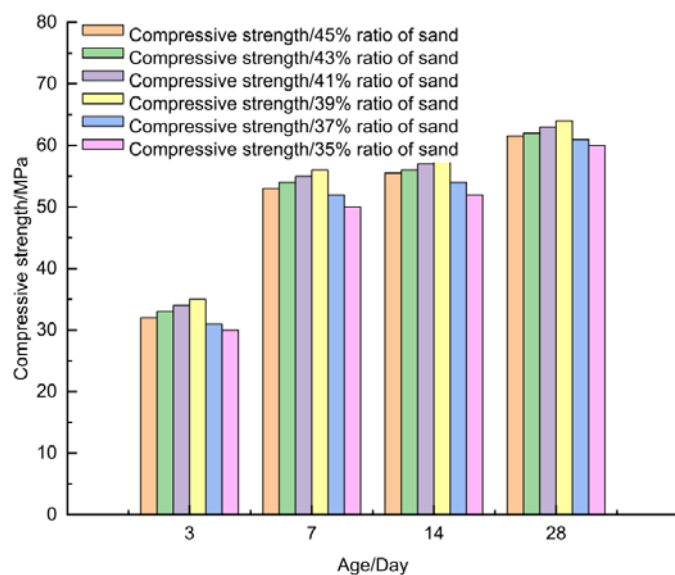


Figure 4. Influence of sand ratio on compressive strength of concrete at different ages.

In order to verify the influence of different cement dosages on compressive strength, the changes in compressive strength at different ages were established when the cement dosages were 225 g, 250 g, 275 g, 300 g, 325 g and 350 g, as shown in Fig. 5. In Fig. 5, when the concrete age is 3 days and the

amount of cement is 300 g, the maximum compressive strength of concrete is 34 MPa. When the concrete age is 7 days, the cement dosage with the highest compressive strength of concrete is 325 g, and the pressure value at this time is 56 MPa. In other words, for certain preconditions, there is a cement amount that maximizes the compressive strength of the concrete cube. For the same water-cement ratio, the compressive strength of concrete gradually increases as the amount of cement increases, and when the strength reaches the maximum, it begins to slowly decrease to a certain fixed value. This rule also applies to different ages of concrete.
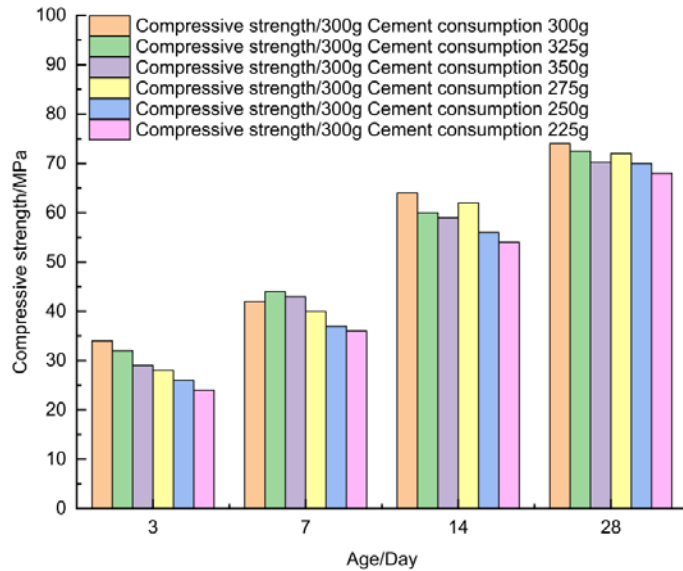

Figure 5. The influence of different cement content on the compressive strength of concrete.

In order to verify the influence of different water-binder ratios on compressive strength, under the condition that the cylinder compressive strength, coarse aggregate particle size, sand ratio and cement dosage remain unchanged, concrete blocks with fly ash content of 35 % were selected [29], compare the compressive strength under different water-binder ratio conditions, as shown in Table 2. It can be seen from Table 2 that the selected fly ash content is 35 %, each of the 3 groups of test pieces is 5, and the water-binder ratio is 0.3, 0.35 and 0.4 respectively. The three groups of concrete blocks A, B, and C have a faster rate of increase in strength during 0 to 7 days of curing, while the rate of strength increase of concrete blocks with a large water-binder ratio slows down. In the early stage of curing of concrete blocks, the water-binder ratio has a significant impact on the strength. The water-binder ratio is negatively correlated with the growth of the compressive strength of the concrete blocks. In the later stage of the curing of concrete blocks, the water-binder ratio and the strength increase are positively correlated. The reason is that concrete blocks with a small water-binder ratio are fully hydrated in the early stage of cement hydration, so the strength increases quickly, but the strength increase is small in the later period of curing. It can be seen that the water-binder ratio can make the lightweight concrete blocks have Stable strength.

Table 2. Influence of water-to-binder ratio on compressive strength.

No.	Fly ash content/%	Water glue ratio	Compressive strength/MPa			
			3d	7d	14d	28d
A	35	0.3	2.61	5.84	8.33	9.53
B	35	0.35	2.79	8.06	7.59	9.08
C	35	0.4	1.92	3.82	6.48	8.78

2.3. Establish a prediction model for the compressive strength of lightweight high-strength concrete

Before establishing a multi-factor regression model, use SPSS software to establish a curve regression model between each factor and the compressive strength of lightweight high-strength concrete, and judge according to the decisive coefficient R^2 value. The functional relationship between a single index and compressive strength, thereby completing a multivariate nonlinear compressive strength prediction model. The cylinder compressive strength, water-binder ratio, cement dosage, coarse aggregate particle size and sand ratio were used as independent variables, and the compressive strength was used as the dependent variable for regression analysis. The regression function and deterministic coefficient R^2 of the influencing factors and compressive strength are shown in Table 3.

Table 3. Regression function and coefficient of determination R².

Influencing factors	Correspondence function	R²
Cylinder compression strength	Logarithmic function	0.991
Aggregate size	Quadratic function	0.972
Sand rate	Linear function	0.975
Water glue ratio	Exponential function	0.999
Cement consumption	Logarithmic function	0.997

In Table 3, each R² value is greater than 0.9, which proves that the regression correlation is significant. According to the analysis in Table 3, the smaller the water-binder ratio, the greater the compressive strength; the effect of the amount of cement on the compressive strength of lightweight high-strength concrete increases linearly in the early stage, but the compressive strength is also constrained by aggregate strength. Therefore, the impact of the two compressive strengths rises to a certain maximum point and tends to be stable; the impact of cylinder compressive strength on the compressive strength of lightweight high-strength concrete, after the rapid growth in the early stage reaches a certain maximum, is affected by the strength of cement stone It tends to be stable after the restriction of the particle size; the impact of the particle size on the compressive strength of the coarse aggregate first increases and then decreases; the impact of the sand rate on the compressive strength, increase the sand rate, and sand on the basis of a reasonable sand rate If the ratio value is too large, the amount of coarse aggregate in the concrete will decrease and the concrete strength will decrease accordingly. On the contrary, if the sand ratio value is too small, the concrete strength will increase.

In section 2.2, the coarse aggregate particle size, water-binder ratio, cement dosage, sand ratio, external admixture and different coarse aggregate barrel compressive strengths with different dosages were studied, and the compressive strengths at different ages were analyzed changing trend. The curve regression model between each factor and the compressive strength of lightweight and high-strength concrete was established by SPSS software, and the functional relationship between a single index and the compressive strength could be judged according to the R² value of the decisive coefficient, as shown in Table 3. The analysis in Table 3 shows that the above factors will affect the strength of lightweight high-strength concrete. Therefore, the establishment of the strength prediction model of lightweight high-strength concrete requires comprehensive consideration of multiple factors that affect its strength. According to the functional relationship between a single factor and 28 days strength of lightweight high-strength concrete obtained from the analysis, each specific mathematical model can be obtained, and then these models are superimposed to establish a multivariate nonlinear mathematical model. Coarse aggregate barrel compressive strength, coarse aggregate particle size, water-binder ratio, cement dosage and sand ratio are used as separate indicators, and combined with the various influencing factors in Table 3 and the regression function of compressive strength, the relationship is established. In order to simplify the methods and steps in the regression analysis of nonlinear equations, the logarithmic function method is adopted to linearly transform the equations. Finding the natural logarithm of both sides of the equation at the same time, we can get formula 1:

$$y = b_0 + \log_{b1}^{x1} + b_2 x_2^2 + b_3 x_2 + b_4 x_3 + b_5^{-x_4} + \log_{b_6}^{x_5}, \tag{1}$$

where: x_1 is the cylinder compressive strength; x_2 is the aggregate particle size; x_3 is the sand ratio; x_4 is the water-binder ratio; x_5 is the amount of cement; b_k is the regression coefficient, (k = 0, 1, 2, 3, 4, 5, 6)

Use the nonlinear analysis command in Matrix Laboratory to solve the above model, choose the nlinfit command to solve the regression coefficients in the multiple nonlinear model, and establish the parameter estimation of the multiple nonlinear regression model as shown in Table 4. In Table 4, the observed value t of the statistic in the significance test of the regression coefficient of the five variables is greater than the significance level Sig., so the null hypothesis is rejected. The partial regression coefficient is significantly different from 0. The linear relationship between the four explanatory variables and the explained variables is significant, so the independent variables are kept in the equation and are not eliminated.

Table 4. Parameter estimation of multiple nonlinear regression model.

parameter	Parameter Estimation	Standard error	t	Sig.
intercept	1.46	0.03	143.25	0
x_1	18.31	2.93	6.26	0.03
x_2^2	21.6	0.01	3.01	0.04
x_2	−3.28	1.10	2.99	0.06
x_3	−71.12	12.50	5.70	0.05
x_4	1.36	4.73	4.32	0.04
x_5	20.48	6.30	3.25	0.02

According to the parameters in Table 4, the predictive model of the compressive strength of the multivariate nonlinear lightweight high-strength concrete is obtained as formula 2:

$$y = 1.46 + 18.31\ln^{x_1} + 21.6x_2^2 - 3.28x_2 - 71.12x_3 + 1.36^{-x_4} + 20.48\ln^{x_5} . \tag{2}$$

In the formula: x_1 is the cylinder compressive strength; x_2 is the aggregate particle size; x_3 is the sand ratio; x_4 is the water-binder ratio; x_5 is the amount of cement.

3. Results and Discussion

3.1. Model validation

The RMSE (Root Mean Square Error) is used to evaluate the difference between the simulated value and the measured value to verify the rationality of the prediction model for the compressive strength of lightweight high-strength concrete. The RMSE is expressed as formula 3, and the comparison between the measured strength value and the model simulation value is shown in Table 5.

$$RMSE = \sqrt{\frac{\sum_{i=1}^{n}(p_i - o_i)^2}{n}}. \tag{3}$$

In the formula: n is the total number of data points; p_i is the simulated value; o_i is the measured value.

According to Table 5, the maximum and minimum RMSE of the compressive strength value predicted by the model and the measured value are 1.05 MPa and 0.96 MPa. 15 sets of data are randomly selected from 30 sets of tests for verification. the R^2 values are 0.96 and 0.92 respectively, which are both higher than 0.9, indicating that the corresponding relationship between the measured value and the simulated value is good, the error is small, and the prediction accuracy of the model is high. Therefore, the proposed compressive strength prediction model.

Table 5. Model simulation compressive strength value and RMSE of measured value.

No.	RMSE/MPa	R^2
1	1.02	0.96
2	1.05	0.93
3	0.97	0.92
4	1.01	0.93
5	0.96	0.96

3.2. Comparison between prediction models

In order to verify the accuracy of the prediction model for compressive strength and the superiority of prediction compared with other models, experiments are needed. In the indoor test, in order to avoid the contingency of the measured values of the compressive strength, 18 standard specification specimens were made, each with a side length of 150 mm. Every 3 specimens are a group, and the average value of the compressive strength of the 3 specimens is taken as the actual measured value of compressive strength. In the test, choose the same cylinder compressive strength, aggregate particle size, sand ratio, water-binder ratio and cement dosage, and the test environment temperature is 20 °C. Compare the

measured value of compressive strength and the predicted value of the compressive strength of lightweight high-strength concrete. And J. Shen's [31] concrete compressive strength prediction model prediction value, as shown in Fig. 6 (the figure number will be changed in the following), the abscissa is the number of the 6 groups of specimens, and the ordinate is the compressive strength $f_{cu.k}$, draw the compressive strength value curve under different test piece numbers. It can be seen from Fig. 6 that the predicted model compressive strength curve is closer to the actual measured compressive strength curve than the J. Shen model compressive strength curve. The predictive model has better practicability. At the same time, because the cylinder compressive strength, aggregate particle size, sand ratio, water-binder ratio and the amount of cement in the 6 groups of specimens have different effects on the compressive strength, the predicted value of the compressive strength of the proposed model will be low. In the case of the actual measured value or higher than the actual measured value. To obtain more accurate prediction results, response surface analysis is required to determine the precise applicable conditions of the proposed model. That is, the proposed model predicts the most accurate when the cylinder compressive strength, aggregate particle size, sand ratio, water-binder ratio and cement dosage are used.
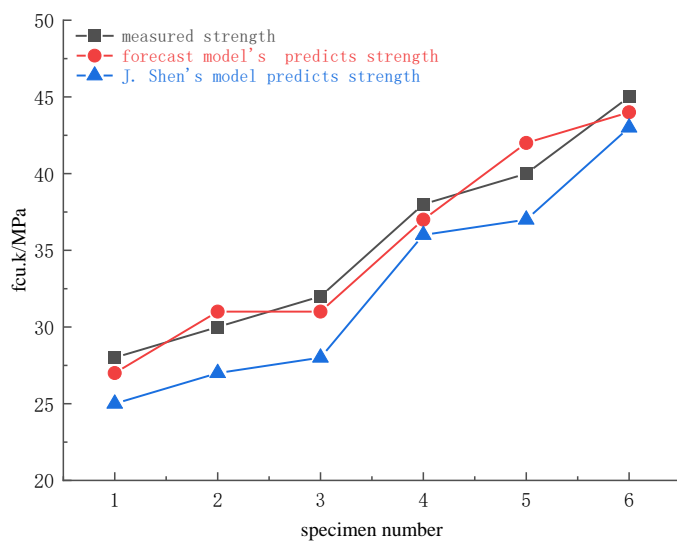

Figure 6. Comparison of predicted compressive strength

3.3. Determination of the applicable conditions of the model

In order to make the model have a higher evaluation accuracy, the surface analysis method is used to determine the applicable conditions of the model. Based on domestic and foreign experience and the characteristics of lightweight high-strength concrete, the value ranges of the five parameters in the model are set as followed: the cylinder compressive strength range is 3.2 MPa~6.6 MPa; the coarse aggregate particle size is 5 mm~25 mm The range of sand ratio is 26 %~44 %; the amount of cement is 450 Kg/m³ ~550 Kg/m³ ; the water-binder ratio is within 0.28~0.4.

In order to facilitate the drawing of test records, the cylinder compressive strength, coarse aggregate particle size, sand ratio, cement dosage and water-binder ratio are represented by symbols in order: CSS, AS, SR, CC and WGR; the codes in the response surface test are in order A, B, C, D, E. According to the number and range of the parameters, select the response surface test with 5 factors and 3 levels. The coding levels and values are shown in Table 6.

Table 6. Coding level and value.

Coding level	A（CSS/ MPa）	B（AS/mm）	C（SR/%）	D（CC/Kg/m³）	E（WGR）
-1	3.2	5	26	450	0.28
0	4.9	15	35	500	0.34
1	6.6	25	44	550	0.4

When the coding level of sand ratio, cement dosage and water-binder ratio is 0, the response surface of design cylinder compressive strength (MPa) and coarse aggregate particle size (mm) against compressive strength is shown in Fig. 7. In Fig. 7, CCS stands for Cylinder compression strength, AS stands for Aggregate size. When the cylinder compressive strength is between 3.2 MPa and 4.9 MPa, the compressive strength increases faster than 4.9 MPa or more. The reason is that in high-strength concrete, after the cylinder compressive strength reaches a certain value, the compressive strength is restricted by the strength of light aggregates and continues to increase. High cylinder compressive strength has little

effect on changes in compressive strength, so when the cylinder compressive strength is above 4.9 MPa, the response of compressive strength is low. As the particle size of the coarse aggregate increases, the compressive strength gradually decreases, and the larger the particle size, the faster the rate of decrease. The reason is that the larger the particle size, the faster the particles move in the concrete mixture, resulting in the uneven distribution of particles seriously affects the compressive strength. Therefore, when the particle size is 15 mm or more, the response to compressive strength is more sensitive.

When the coding level of cylinder compressive strength, coarse aggregate particle size and water-binder ratio is 0, the response surface of design sand ratio (%) and cement dosage (Kg/m³) compressive strength is shown in Fig. 8. In Fig. 8, CC stands for Cement consumption, and SR stands for Sand rate. As the sand ratio increases, the compressive strength gradually increases. When the sand ratio exceeds 35 %, the increase in compressive strength tends to be flat, and the sand ratio begins to decrease after it exceeds 39 %. The reason is the larger sand ratio. The proportion of lightweight aggregates can be reduced, thereby increasing the compressive strength. If the sand ratio is too large, the concrete will be easily segregated and its structure will be uneven. At this time, the compressive strength will decrease and the concrete will easily collapse. Therefore, when the sand ratio is below 35 %, the response to compressive strength is higher. Increasing the amount of cement can increase the compressive strength, but after 500 Kg/m³, the increase in compressive strength becomes smaller. The reason is that the excessive amount of unilateral cement will increase the heat of hydration, causing the internal temperature difference of the concrete to be too large, and cracks may occur. Which affects the improvement of compressive strength, at this time the response of cement dosage to compressive strength is low.
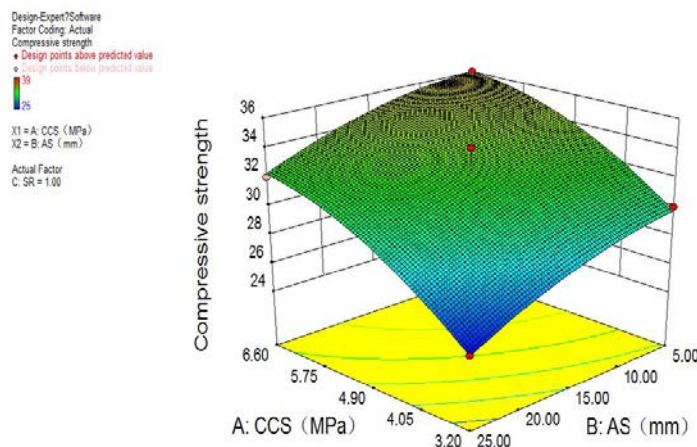

Figure 7. Response surface of A and B compressive strength.
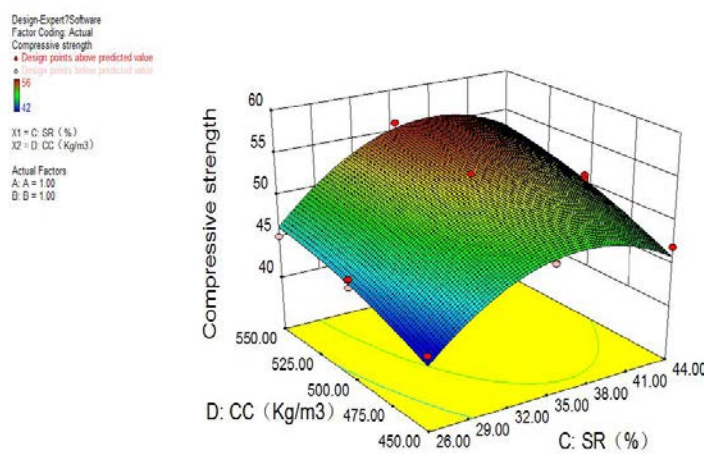

Figure 8. Response surface of C and D compressive strength.

When the coding level of cylinder compression strength, coarse aggregate particle size and sand ratio is 0, the response surface of the designed cement dosage (Kg/m³) and water-binder ratio to the compression strength value is shown in Fig. 9. In Fig. 9, CC represents Cement consumption, WGR represents Water glue ratio. As the water-to-binder ratio increases, the compressive strength gradually decreases, and the larger the water-binder ratio, the faster the strength decreases. The reason is that a larger water-binder ratio will significantly increase the fluidity of the cement paste and cause the slurry to drip severely. The adhesion between the aggregates becomes poor, resulting in a rapid decrease in

compressive strength. Therefore, when the water-binder ratio is greater than 0.34, the response to compressive strength is higher.
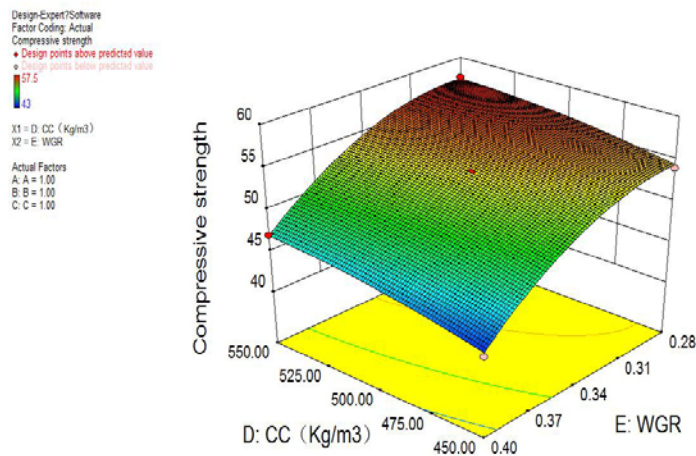

Figure 9. Response surface of D and E compressive strength.

Combining the analysis of the response surface above, it can be seen that if the response surface tends to be flat, it means that within the parameter value range corresponding to the surface, the compressive strength cannot change synchronously with the parameter value, and the compressive strength has a low response to parameter changes. At this time, the prediction accuracy of the compressive strength prediction model of lightweight high-strength concrete is low. If the slope of the response surface is large, the compressive strength will change significantly, and the corresponding parameter value range will be more suitable for model prediction. According to the results of response surface analysis, the cylinder compressive strength is between 3.2 MPa～4.9 MPa, the coarse aggregate particle size is between 15 mm～25 mm, the sand ratio is between 26 %～35 %, the amount of cement is between 450 Kg/m³ ～500 Kg/m³ , and the water-binder ratio is between the parameter value range from 0.34 to 0.4 is the optimal prediction space of the model. When the five parameters are in the optimal prediction space at the same time, the prediction level of the model is the best.

4. Conclusions

1. Using cluster analysis method, it is proposed that the cylinder compressive strength, water-binder ratio, cement dosage, coarse aggregate particle size and sand ratio in clusters 2 and 3 are the five key factors that affect the compressive strength.

2. The R^2 value of the single-factor prediction model for the compressive strength of lightweight high-strength concrete is greater than 0.9, which proves that the regression analysis of the compressive strength, water-binder ratio, cement dosage, coarse aggregate particle size, sand ratio and compressive strength is reasonable.

3. A multivariate nonlinear lightweight high-strength concrete compressive strength prediction model is established, and the corresponding coefficients of the model are 1.46, 18.31, 21.6, –3.28, –71.12, 1.36 and 20.48.

4. In the comparison between the model prediction and the measured value, the root mean square error RMSE is lower than 1.05 MPa, and the prediction accuracy of the proposed compressive strength prediction model is higher.

5. The applicable conditions of the prediction model are determined. The cylinder compressive strength is between 3.2 MPa~4.9 MPa, the coarse aggregate particle size is between 15 mm~25 mm, the sand ratio is between 26 %~35 %, and the amount of cement is between 450 Kg/m³~500 Kg/m³. The parameter value range when the water-binder ratio is 0.34~0.4 is the optimal prediction space of the model. When the 5 parameters are in the optimal prediction space at the same time, the prediction level of the model is the best.

References

1. Shahmansouri, A.A., Bengar, H.A., Ghanbari, S. Compressive strength prediction of eco-efficient GGBS-based geopolymer concrete using GEP method. Journal of Building Engineering. 2020. 31. Pp. 101326. DOI: 10.1016/j.jobe.2020.101326.

2. Klyuev, S.V., Klyuev, A.V., Vatin, N.I. Fiber concrete for the construction industry. Magazine of Civil Engineering. 2018. 84 (8). Pp. 41–47. DOI: 10.18720/MCE.84.4

3. Klyuev, S.V., Khezhev, T.A., Pukharenko, Y.V., Klyuev, A.V. Experimental study of fiber-reinforced concrete structures. Materials Science Forum. 2018. 945. Pp. 115–119. DOI: 10.4028/www.scientific.net/MSF.945.115

4. Cheng, M., Chou, J., Roy, A.F. V, Wu, Y. Automation in Construction High-performance Concrete Compressive Strength Prediction using Time-Weighted Evolutionary Fuzzy Support Vector Machines Inference Model. Automation in Construction. 2012. 28. Pp. 106–115. DOI: 10.1016/j.autcon.2012.07.004.

5. Słoń, M. A comparison of model selection methods for compressive strength prediction of high-performance concrete using neural networks q ´ ski. Computers and Structures. 2010. 88 (21–22). Pp. 1248–1253. DOI: 10.1016/j.compstruc.2010.07.003.

6. Beycioğlua, A., C. Başyiğit. Rule-Based Mamdani-Type Fuzzy Logic Approach to Estimate Compressive Strength of Lightweight Pumice Concrete. ACTA PHYSICA POLONICA A. 2015. 128 (2). Pp. 424–426. DOI: 10.12693/APhysPolA.128.B-424

7. Tanyildizi, H. Prediction of the Strength Properties of Carbon Fiber-Reinforced Lightweight Concrete Exposed to the High Temperature Using. Advances in Civil Engineering. 2018. Pp. 1–11.

8. Akbari, M., Deligani, V.J. Data driven models for compressive strength prediction of concrete at high temperatures. Frontiers of Structural and Civil Engineering. 2020. Pp. 1–11. DOI: 10.1007/s11709-019-0593-8

9. Sobhani, J., Najimi, M., Pourkhorshidi, A.R., Parhizkar, T. Prediction of the compressive strength of no-slump concrete : A comparative study of regression, neural network and ANFIS models. Construction and Building Materials. 2010. 24 (5). Pp. 709–718. DOI: 10.1016/j.conbuildmat.2009.10.037.

10. Wu, T., Wei, H., Zhang, Y., Liu, X. Axial compressive behavior of lightweight aggregate concrete columns confined with transverse steel reinforcement. Advances in Mechanical Engineering. 2018. 10 (3). Pp. 1–14. DOI: 10.1177/168781401876-6632

11. Fediuk, R.S., Mochalov, A.V., Bituev, A.V., Zayakhanov, M.E. Structuring Behavior of Composite Materials Based on Cement, Limestone, and Acidic Ash. Inorganic Materials. 2019. 55 (10). Pp. 1079–1085. DOI: 10.1134/S0020168519100042

12. Costa, H., Carmo, R.N.F., Júlio, E. Influence of lightweight aggregates concrete on the bond strength of concrete-to-concrete interfaces. Construction and Building Materials. 2018. 180. Pp. 519–530. DOI: 10.1016/j.conbuildmat.2018.06.011.

13. Zhao, Q., Cheng, P., Wang, J., Wei, Y. Damage prediction model for concrete pavements in seasonally frozen regions. Magazine of Civil Engineering. 2018. 84 (8). Pp. 57–66. DOI: 10.18720/MCE.84.6

14. Hezhev, T.A., Zhurtov, A.V., Tsipinov, A.S., Klyuev, S.V. Fire resistant fibre reinforced vermiculite concrete with volcanic application. Magazine of Civil Engineering. 2018. 80 (4). Pp. 181–194. DOI: 10.18720/MCE.80.16

15. Lee, T., Lee, J. Setting time and compressive strength prediction model of concrete by nondestructive ultrasonic pulse velocity testing at early age. Construction and Building Materials. 2020. 252. Pp. 119027. DOI: 10.1016/j.conbuildmat.2020.119027.

16. Fediuk, R.S., Lesovik, V.S., Mochalov, A.V., Otsokov, K.A., Lashina, I.V., Timokhin, R.A. Composite binders for concrete of protective structures. Magazine of Civil Engineering. 2018. 82 (6). Pp. 208–218. DOI: 10.18720/MCE.82.19

17. Malachanne, E., Sassine, R., Garcia-diaz, E., Dubois, F. Numerical model for mechanical behavior of lightweight concrete and for the prediction of local stress concentration. Construction and Building Materials. 2014. 59. Pp. 180–187. DOI: 10.1016/j.conbuildmat.2014.01.067

18. Boukli Hacene, S.M.A. Ghomari, F., Schoefs, F., Khelidj, A. Probabilistic Modelling of Compressive Strength of Concrete Using Response Surface Methodology and Neural Networks. Arabian Journal for Science and Engineering. 2014. 39 (6). Pp. 4451–4460. DOI: 10.1007/s13369-014-1139-y

19. Zhang, J., Ma, G., Huang, Y., Aslani, F., Nener, B. Modelling uniaxial compressive strength of lightweight self-compacting concrete using random forest regression. Construction and Building Materials. 2019. 210. Pp. 713–719. DOI: 10.1016/j.conbuildmat.2019.03.189.

20. Bingöl, A.F., Tortum, A., Gül, R. Neural networks analysis of compressive strength of lightweight concrete after high temperatures. Materials and Design. 2013. 52. Pp. 258–264. DOI: 10.1016/j.matdes.2013.05.022

21. Mehta, A., Siddique, R., Ozbakkaloglu, T., Uddin, F., Shaikh, A., Belarbi, R. Fly ash and ground granulated blast furnace slag-based alkali-activated concrete : Mechanical, transport and microstructural properties. Construction and Building Materials. 2020. 257. Pp. 119548. DOI: 10.1016/j.conbuildmat.2020.119548.

22. Hung, K., Alengaram, U.J., Visintin, P., Heng, S., Zamin, M. Influence of lightweight aggregate on the bond properties of concrete with various strength grades. Construction and Building Materials. 2015. 84. Pp. 377–386. DOI: 10.1016/j.conbuildmat.2015.03.040.

23. Cotto-ramos, A., Dávila, S., Torres-garcía, W., Cáceres-fernández, A. Experimental design of concrete mixtures using recycled plastic, fly ash, and silica nanoparticles. Construction and Building Materials. 2020. 254. Pp. 119207. DOI: 10.1016/j.conbuildmat.2020.119207.

24. Zhao, Q., Cheng, P., Wei, Y., Wang, J. Factors effecting the recovery process of self-repairing concrete. Magazine of Civil Engineering. 2019. 88 (4). Pp. 52–59. DOI: 10.18720/MCE.88.5

25. Chithra, S., Kumar, S.R.R.S., Chinnaraju, K., Ashmita, F.A. A comparative study on the compressive strength prediction models for High Performance Concrete containing nano silica and copper slag using regression analysis and Artificial Neural Networks. CONSTRUCTION & BUILDING MATERIALS. 2016. 114. Pp. 528–535. DOI: 10.1016/j.conbuildmat.2016.03.214.

26. Asteris, P.G. Concrete compressive strength using artificial neural networks. Neural Computing and Applications. 2019. 2. Pp. 1–20. DOI: 10.1007/s00521-019-04663-2.

27. Ambily, P.S., Umarani, C., Ravisankar, K., Ranjan, P., Bharatkumar, B.H., Iyer, N.R. Studies on ultra high performance concrete incorporating copper slag as fine aggregate. CONSTRUCTION & BUILDING MATERIALS. 2015. 77. Pp. 233–240. DOI: 10.1016/j.conbuildmat.2014.12.092.

28. Yoon, J.Y., Kim, H., Lee, Y., Sim, S. Prediction Model for Mechanical Properties of Lightweight Aggregate Concrete Using Artificial Neural Network. Materials. 2019. 12 (2678). Pp. 1–21.

29. Haile, B.F., Jin, D.W., Yang, B., Park, S., Lee, H.K. Multi-level homogenization for the prediction of the mechanical properties of ultra-high-performance concrete. Construction and Building Materials. 2019. 229. Pp. 116797. DOI: 10.1016/j.conbuildmat.2019.116797.

30. Anyaoha, U., Zaji, A., Liu, Z. Soft computing in estimating the compressive strength for high-performance concrete via concrete composition appraisal. Construction and Building Materials. 2020. 257. Pp. 119472. DOI: 10.1016/j.conbuildmat.2020.119472.

31. Shen, J., Xu, Q. Effect of elevated temperatures on compressive strength of concrete. Construction and Building Materials. 2019. 229. Pp. 116846. DOI: 10.1016/j.conbuildmat.2019.116846.

Information about authors:

Lina Zhang, *PhD*
ORCID: https://orcid.org/0000-0002-2024-3806
E-mail: 53860470@qq.com

Dongpo He,
ORCID: https://orcid.org/0000-0003-2427-1086
E-mail: hdp@nefu.edu.cn

Wenyuan Xu, *PhD*
ORCID: https://orcid.org/0000-0002-1397-9305
E-mail: xuwenyuan@nefu.edu.cn

Qianqian Zhao, *PhD*
ORCID: https://orcid.org/0000-0002-0209-4181
E-mail: 492954791@qq.com

Shubin Teng,
ORCID: https://orcid.org/0000-0002-2258-3708
E-mail: 53860470@qq.com

Magazine of Civil Engineering

journal homepage: http://engstroy.spbstu.ru/

Influence of the technological foam concrete manufacturing process on its pore structure

R.E. Lukpanov [ID] **, D.S. Dyussembinov** [ID] **, Zh.A. Shakhmov** ✉ [ID] **, D.O. Bazarbayev** [ID] **,
D.V. Tsygulyov** [ID] **, S.B. Yenkebayev** [ID]

L.N. Gumilyov Eurasian National University, Astana, Kazakhstan

✉ *zhanbolat8624@mail.ru*

Abstract. A two-stage foaming method of foam concrete production is proposed. The technical result of this method is aimed at improving the pore structure of the material. To assess the impact of the proposed production technology on the quality of the material, the construction properties of materials obtained by the classical method and the method of dry mineralization of foam were compared. The main assessment criterion of the quality of materials is the degree of homogeneity of foam concrete throughout the volume. Assessment of material porosity was carried out by analyzing the structure of dried specimens after soaking in water with and without colorant, as well as by pressing cylindrical specimens, segmented by height, while the assessment of material homogeneity was carried out through the analysis of discrete, particular measurements of the strength properties of the material at its height. The results of the porosity assessment gave a clear regularity of pore structure distribution of the materials of the methods compared. In general, the results of the comparison of water absorption and strength gave us an idea of the impact of technological production on the quality of foam concrete as a building product. The result of the research is the technology of foam concrete production by two-stage injection of foam: it is aimed at improving the pore structure of the material due to the uniform distribution of pores, as well as increasing the strength characteristics of the material by reducing the water-cement ratio and uniformly distributed structure of the supporting skeleton.

1. Introduction

The relevance of the study is due to the high demand for aerated concrete in the construction market. The reasons for the great interest in the material are the characteristics of aerated concrete, its density, thermal conductivity and features of a cellular structure.

Cellular concrete is divided into aerated concrete and foam concrete [1, 2]. The main distinctive feature of these materials is their porous structure. Aerated concrete is produced by the introduction of gas-forming components, which in the process of chemical reaction with a cement binder forms a gas emission, which facilitates the formation of intercommunicating pores [10]. Foam concrete is produced by the introduction of ready foam in the cement-sand mixture, which allows obtaining a closed pore system [3, 4].

The main competitor in the market of building materials for cellular concrete are lightweight aggregate concretes such as polystyrene concrete, expanded clay aggregate (ECA) concrete, slag-concrete, and others [5–9]. Each of these materials has its advantages and disadvantages. For example, polystyrene

concrete is produced using foamed polystyrene as an aggregate presented in the form of balls. The main disadvantage of polystyrene concrete is the low density of aggregates from 6 to 25 kg/m^3. Since polystyrene is much lighter than cement-sand mixture, as a result of its low density, it rushes to the surface of the mortar, resulting in uneven distribution of the aggregate in the structure of the mortar. The striving of polystyrene in the structure of concrete to the surface of the mixture creates the maximum concentration of polystyrene on the surface of the material, which leads to the formation of unstable and weak structure, easily deformed, and locally does not provide sufficient strength of the skeleton of the material as a building product. The latter also has a negative impact in the production of construction and installation works because the adhesion decreases when laying the material [10].

ECA and slag-concrete are alternative materials for cellular concrete, but the main disadvantage of these materials is the restricted density limit. The density limit of ECA concrete is from 800 to 1800 kg/m^3, which limits the use of this material. If it is necessary to reduce the density of the material to less than 800 kg/m^3, for example, to reduce the load on the supporting area of the structure, it is not possible with the ECA concrete. Therefore, the use of cellular concrete as wall structures in the construction of buildings and structures can reduce the structural load. It becomes especially relevant for high-rise construction when there is a need to reduce the load on the bases and foundations. Also, slag and ECA concrete are significantly inferior to cellular concrete in terms of thermal conductivity and soundproofing ability [11–14].

An additional advantage of using foam concrete is its technological ergonomics in the construction of building structures, and the resulting building structures of foam concrete have high thermal properties [15]. Thermophysical properties of cellular concrete open up possibilities of application of these materials in humid continental climatic conditions and in permafrost conditions [16–18]. The porous structure of the material allows to retain heat, and the use of thin-layer adhesive mortars for installation, due to the reduction of thermal bridges, allows reducing heat transfer to a minimum. No minor factor is the durability of cellular concrete in the basis of the composition of which is a cement binder and fine aggregate [19].

Despite the advantages among the analogues, one of the frequently encountered problems of foam concrete manufacturers is the instability of the structure of the foam concrete mortar, shrinkage, uneven density of the material and as a consequence, unstable strength and thermal conductivity of the product [20]. The reason for this shortcoming can be many factors, the main one of which is a high water cement ratio [21]. To solve this problem, plasticizing additives have been used. But since plasticizing additives are surface active substances (SAS), then, having received a decrease in the water-cement ratio of foam concrete manufacturers faced another problem: shrinkage of the material due to an increase in the setting time under the influence of the additive. To solve the problem with the quality of foam concrete material, many attempts were made with the use of additives accelerating curing in combination with a plasticizer. But a significant result ensuring the quality of foam concrete was not achieved [22, 23].

Despite the shortcomings of the practice of using foam concrete showed that this material deservedly takes a worthy place among the popular building materials and despite the existing technological and manufacturing shortcomings continues to develop actively.

The technology of geopolymer foam concrete production attracts a lot of research interest in construction. Its porous structure has such merits as lightweight, acoustic and thermal insulation [24]. Other technologies include fiber and special additives during technological process of foam concrete for increased compression, thermal and sound insulation [25]. But all of these technologies include some additives. the Introduction of foam concrete production technology by dry mineralization with foam was a breakthrough in the technological process of foam concrete production [26]. As a result of this technology, a number of issues concerning the quality of the pore structure and density have been solved, but the problem of shrinkage of the material in the process of setting has not been solved yet.

The unresolved problem of obtaining quality foam concrete has determined the purpose of this research work: to develop an affordable technology for the production of foam concrete, the technical result of which is aimed at improving the pore structure of the material due to the uniform distribution of pores, as well as increasing the strength characteristics of the material by reducing the water-cement ratio and uniformly distributed structure of the supporting skeleton.

The following tasks have been set to achieve this goal:

- study the theoretical features of the application of existing methods of foam concrete production;
- study the features of the formation of the structure of foam concrete in the application of various methods of its production;
- to make a comparative analysis of the methods under study.

The paper presents a comparison of methods of production of cellular concrete [27, 28], in particular, foam concrete, and the peculiarities of the technological process of preparing the material [29–32], without

comparing the composition of ingredients (additives) to improve the physical, mechanical and building properties of materials. Proposed method provides better distribution of pores which enhances durability, thermal and sound insulation of products.

For comparison with the proposed method, two main methods of foam concrete production with wide practical application have been adopted:

Method 1: Classical method (CM) [26];

Method 2: Dry mineralization method (DM) [26];

Method 3: The proposed method of two-stage foaming (TSF).

2. Materials and Methods

The research methodology includes the following stages:

- Preparation of foam concrete using comparable methods;
- Preparation of foam concrete by the proposed method of two-stage foaming;
- Laboratory testing of foam concrete specimens;
- Analysis of results.

Preparation of foam concrete by comparable methods was carried out in laboratory conditions in accordance with standard methods, specifications and the requirements of regulatory and technical documentation [1, 33]. An important condition was to maintain the same composition of components and ingredients (additives) of specimens for each method, as well as their dimensionality. For each of 3 methods (including the proposed one) 5 blocks were prepared.

Technological processes of specimens' preparation by CM, DM and TSF are presented in Fig. 1A, 1B, and 1C respectively.

A – technological process of foam concrete preparation by CM

B – technological process of foam concrete preparation by DM

C – technological process of foam concrete preparation by TSF
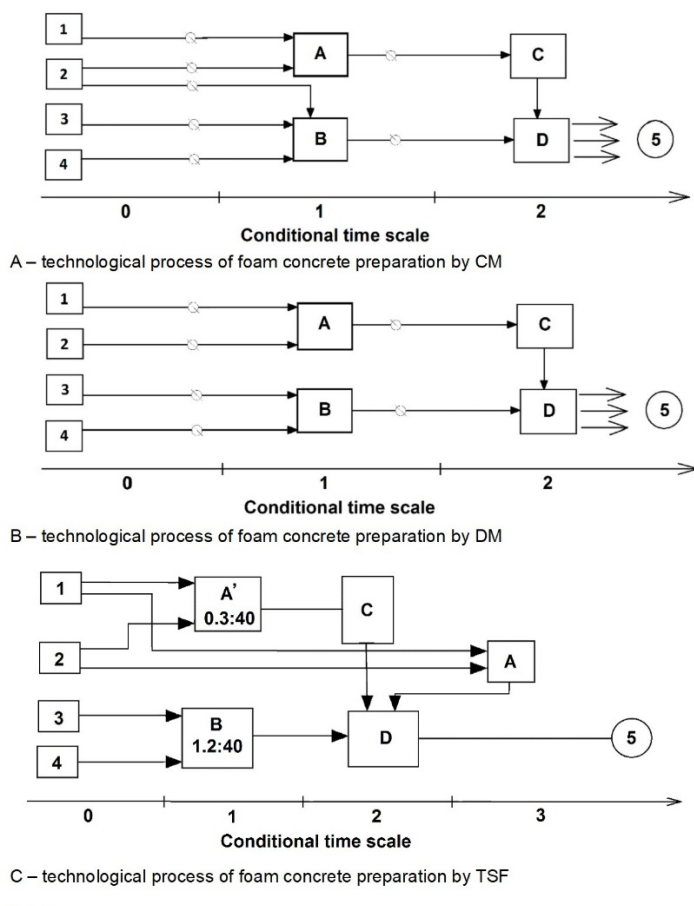
Notations:
- 1 – water, 2 – foam concentrate, 3 – cement, 4 – sand, 5 – final product;
- A' – tank for low-concentration mortar of plasticizing additive of foam concentrate in water 0,3:40 l,

A – tank for modified foam concentrate mortar in water 1.2:40 l, B – cement and sand mixer, C – foam generator, D – solvent mixer.

**Figure 1. Technology of foam concrete preparation
by the method of two-stage foaming [33, 34].**

The technological process of TSF consists of three stages. In the production process, it is necessary to follow a strict sequence of combination of components.

Stage 1: in a tank (A') foam concentrate (1) is thoroughly mixed with water (2), in a 0.3:40 l ratio to water; in parallel (independently) in a tank (A) foam concentrate (2) is thoroughly mixed with water (1), in a 1.2:40 l ratio; in parallel in a tank (B) cement (3) is mixed with sand (4), in a cement-to-sand ratio 1:3.

Stage 2: The mixture obtained in container (A') by means of foam generator (C) is transformed into foam and combined with a cement-sand mixture from container (D), in a mortar mixer (B).

Stage 3: The mixture obtained in container (A) is converted to foam by means of foam generator (C) and introduced into the solvent mixer (D).

After thorough mixing in a solvent mixer, the obtained mortar (5) is poured in the forms.

The main assessment criterion of the quality of the material prepared by different methods is the degree of its homogeneity, namely, even distribution of pores in the structure of foam concrete throughout the volume. This indicator is directly related to the technology of foam concrete production. The resulting factors of homogeneity of the material can be attributed to the homogeneity of construction properties of the material throughout the volume.

To study the homogeneity of the material, cylindrical specimens were used, which were 20 cm high, 6.4 mm in diameter, segmented by 2 cm in height (Fig. 2). Special attention is given to the height of foam concrete in terms of assessing its homogeneity because gravitational forces influence heavy ingredients (including excess water in the foam stratification) in the composition in the process of setting, which leads to uneven density of the material in volume.

Assessment of material porosity was carried out by analyzing the structure of the dried sample after soaking (up to a constant mass) in water with colorant, as well as pressing cylindrical specimens, segmented by height.

Assessment of material uniformity was carried out through the assessment of discrete, particular measurements of the strength properties of the height of the material of standard (factory) size: height of 20 cm, width of 30 cm, length of 60 cm.

Figure 2. Specimens for determining the construction properties of foam concrete.

Core cutting was carried out by means of a cylindrical crown with an electric drive with an inner diameter of 6.5 mm. To reduce the impact of mechanical action on the structure of the skeleton, the cutting was carried out with maximum rotation and minimum movement of the crown. In total, 6 specimens were taken from each compared foam block. Cutting of cylindrical and standard specimens was carried out by string cutting at maximum rotation, to reduce the risk of structural damage to the material. Prior to testing, each element of the specimen was labeled.

Laboratory testing and study of foam concrete specimens included:

- Determination of material water absorption by soaking samples with and without colorant (Fig. 3A);
- Determination of the porosity of the material by pressing it (Fig. 3B);
- Determination of the strength of solid and segmented cylindrical specimens by unconfined compression test (Fig. 3C).

A – Determination of water absorption of specimens

B – Determination of specimens porosity by pressing

C – Determination of the strength of segmented cylindrical specimens

Figure 3. Laboratory testing of foam concrete specimens.

Segmented cylindrical specimens were soaked to assess their water absorption. The soaking was carried out with holding out until the full absorption of water, to a constant mass (mass change did not exceed 0.1 % during 120 minutes of the observation). Specimens submerged in water at full soaking displace the volume of water commensurate with the volume of inert components, i.e., the skeleton volume of the specimen. At incomplete soaking, but maximum saturation with water, the filtration capacity of the material is revealed, which can be used to indirectly assess the structure and nature of pore distribution. This method of assessing the pore structure of foam concrete is considered acceptable because the material is made on a cement binder, the absorption of water by the material is absent.

Since water absorption implies the ability of the material to absorb (pass) water, its evaluation is reduced to comparing the values of water absorption of the material to its pore structure, expressed by the ratio of moisture at maximum water saturation of the specimen to moisture at full water saturation. Thus, the estimation of water permeability of segmented specimens is described by Eq. (1).

$$W_{\%} = \frac{m_s - m_d}{v_w \cdot \rho_w},\qquad(1)$$

where $W_{\%}$ is water absorption to pore volume ratio, %; m_s is wet specimen mass with total water absorption, g; m_d is dry specimen mass after drying to a constant mass, g; v_w is pore volume, cm³; ρ_w is water density, g/cm³.

When assessing the presence of communicating pores, green and red colorants were added to the water for greater contrast. After drying, samples were cut through the middle part to analyze the cross-sectional coloration of the material and to assess the capacity of the foam concrete. To ensure maximum access to the surface area for improved wetting and liquid penetration, the specimens were hanged. After achieving maximum soaking, the specimens were dried to a constant mass (mass change did not exceed 0.1 % during 30 minutes of observation). To assess the effect of the colorant on water penetration (after coloring), the results were corrected with respect to water permeability of specimens when soaked with water without colorant. The difference in masses of wetted specimens with the colorant and without one served as an assessment of the influence of the colorant on the water permeability, and the different nature

of their distribution by height testified for the different degree of homogeneity in the pore structure of the specimens of the compared methods.

Determination of water permeability of specimens of three methods is made by calculating the ratio of volumes of displaced water when soaked with colorless water to actual volumes of pores obtained by pressing (average density of specimens).

Material porosity was assessed by pressing the specimens. When pressing foam concrete, the pore structure of the material is destroyed, the inert aggregate of the material is compressed in volume, releasing the pores. The pressing was carried out on the equipment Press Automatic Pilot, with a total compressive load of 500 kN (50 tons). The lower strength limit of D600 foam concrete specimens is 4.2 MPa, and the upper one is 6.4 MPa. Since the specimens are subject to 25 times of maximum compressive strength of the specimen (160 MPa) with triple sequential pressing, the condition of pore release close to the maximum was accepted. Therefore, the difference in specimen volume before and after pressing will be equal to the pore volume.

Both monolithic and segmented specimens were tested. Monolithic specimens were tested using strain gauges to obtain accurate stress distribution results in the specimens compression. The results obtained were used to assess the test results of segmented specimens.

The segmented specimens were used to assess the less robust part of the specimen by height. Segments of one specimen were tested simultaneously. Since the specimens were mechanically subjected to cutting, the specimen surface had roughness that can lead to a point transfer of normal stress at the contact edge of the segments. Therefore, for better distribution of normal stress, supple gaskets made of nonwoven geotextile were used (Interstate standard GOST 8462-85, n.d.). The use of gaskets also simulated the tangential stresses at the contact edge of segments, which are inherent to a solid, monolithic specimen, when it is compressed.

Segmented specimens were tested until the specimens were completely broken, and strength measurements were made using two control readings:

A is registration of the load value, when breaking at least one segment, in order to identify the weakest area by the height of the specimen;

C is registration of the peak value of load to measure the maximum strength of the specimen as a product.

3.   Results and Discussion

3.1. Results and discussion of determining water absorption

The homogeneity analysis of the specimen structure according to three methods was performed by estimating the ratios of particular values of water absorption of segmented specimens by its height (Fig. 4). The greater is the difference of particular values of water absorption of segments, the greater is the heterogeneity of the material by specimen height [35].
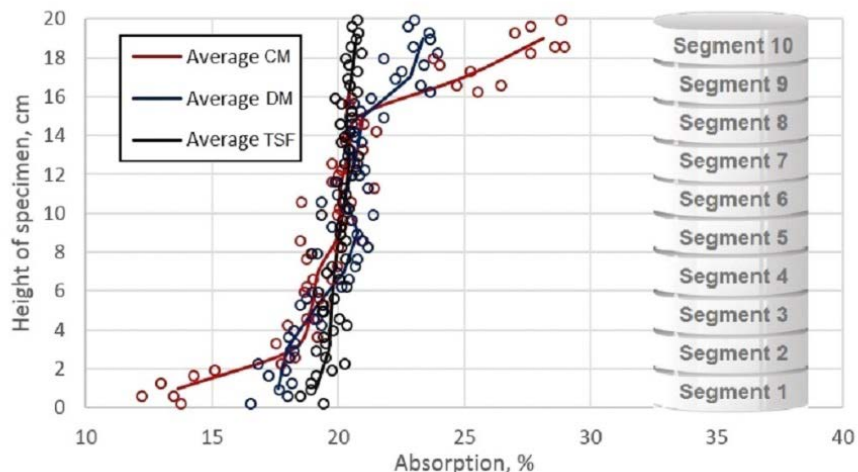

Figure 4. Change in water absorption across sample heights.

The largest difference was observed in CM specimens, the maximum values of water absorption were found in the upper segments, ranging from 56 to 69 %. Minimal water absorption was found in the

lower segments, ranging from 7.3 to 9.7 %. The average particular values of water absorption were 63.5 % in the upper segments and 8.68 % in the lower segments. The squared deviation of particular values was 4.89 for the upper specimens and 0.86 for the lower ones, and the average value of the squared deviation in height of the specimens was 15.31. The deviations of particular values did not exceed 7.7 % for the upper segments (in the upper horizontal plane of the block) and 9.9 % for the lower segments (in the lower horizontal plane of the block); the deviations of particular values by height (in the vertical plane of the block) was 62.1 %. Consequently, the homogeneity of CM specimens, which was assessed by the ability of the material to absorb water, has a better distribution in the horizontal direction than in the vertical one. Maximum values of water absorption for DM specimens ranged from 28 to 33 % in the upper segments, the minimum values ranged from 13 to 16 % in the lower segments. Deviations of particular values did not exceed 5.82 % for the upper segments and 6.61 % for the lower segments; deviations of particular values by height (in the vertical plane of the block) were 23.9 %. DM specimens had a better distribution in the horizontal direction than in the vertical one; however, in comparison with CM, they had a smaller spread in both directions. Water absorption of TSF specimens was ranging from 21 to 23 % for the upper segments and from 17 to 19 % for the lower segments. Deviations of the upper specimens did not exceed 2.23 %, the lower ones did not exceed 3.96 %, and deviations of particular values by height (in the vertical plane of the block) were 7.57 %. TSF specimens have lower dispersion of water absorption values in both directions in comparison with CM and DM specimens, therefore, better homogeneity in both horizontal and vertical planes.

The analysis of structure homogeneity was also performed by the ratio of specimen moisture at maximum water absorption to specimen moisture at full water absorption (100 % saturation of the pore structure with water), Fig. 5. The percentage ratio of the volume of water-filled pores to the volume of pores indirectly testified for the quality indicators of the pore structure of the material (different pore size, presence of communicating pores, etc.).
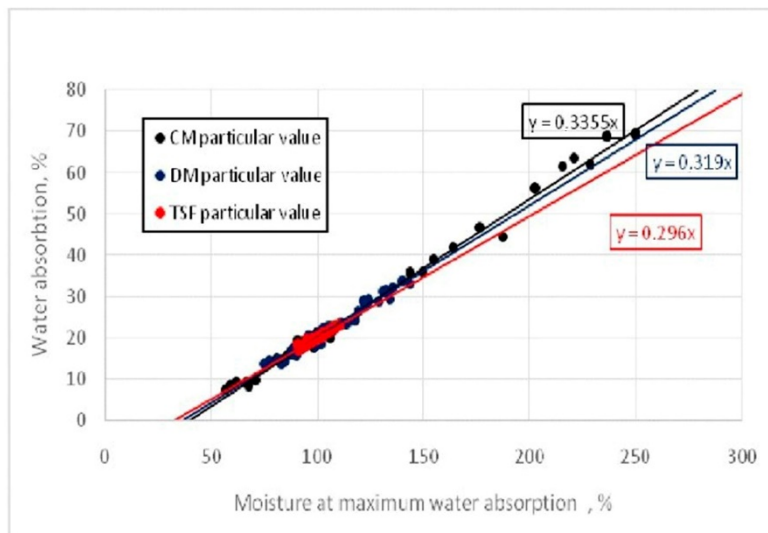

Figure 5. Assessment of absorption capacity.

According to the diagram, the maximum average absorption capacity was found in CM specimens (33.5 %), the lowest in TSF specimens (29.6 %). Comparing particular values, we obtained that CM specimens have a range of values from 12.24 % (lower segments) to 28.98 % (upper segments), which indicates a large difference in pore structure between the upper and lower segments. The range of values of DM specimens is in the range from 16.54 % to 23.97 %. The most homogeneous pore structure is in the TSF specimens, which values are in the range from 18.16 % to 20.94 %. It is possible to estimate the local heterogeneity of the pore structure within the segments of the same density located on one horizontal plane by comparing particular values of water absorbing capacity by material density. Thus, specimens of CM showed heterogeneity within 10 %, specimens of DM within 18 %, and specimens of TSF – 16 %. The CM specimens showed more stable results, however, more data are required for a complete statistical analysis of the local heterogeneity.

Fig. 6 shows the comparison of water absorption of the three methods, expressed by the ratio of particular values of TSF to CM and DM $\left(W_{TSE}/W_{CM} , \ W_{TSFF}/W_{DM} \right)$.
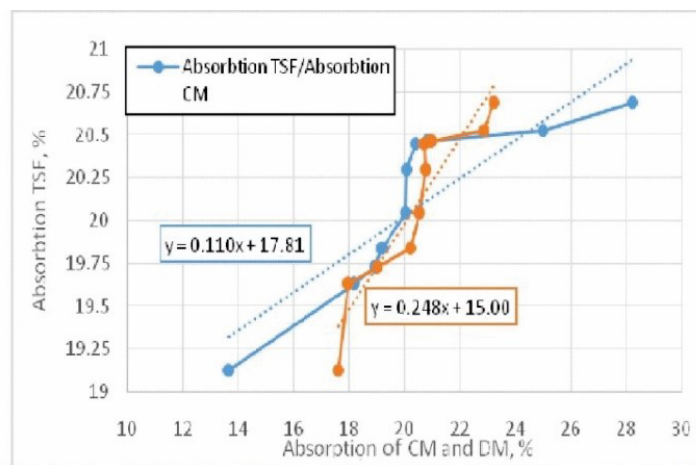
Figure 6. Comparison of particular values of water absorption of three methods.

According to the diagram, the difference in particular values of water absorption of TSF and CM specimens is from 0.73 (for the upper segments the difference in particular values is 73 %) to 1.40 (for the lower segments, the difference is 140 %). The difference between the values of TSF and DM specimens is from 0.89 (89 % for the upper segments) to 1.09 (109 % mainly for the lower segments). The results of comparisons showed that the greatest convergence of particular values of water absorption was for the TSF to DM ratio, in contrast to the comparison with CM, which confirmed the lowest homogeneity of CM specimens.

Fig. 7 shows the results of quality assessment of the pore structure of specimens made soaking them in water with colorant. Fig. 7a shows the sections of the most saturated specimens of the three methods after their drying to achieve maximum saturation. Fig. 7b shows the correction factors for the influence of the colorant on the absorbing capacity of specimens.


CM   DM   TSF

A - Colored specimens cross sections

B - Adjustment coefficients
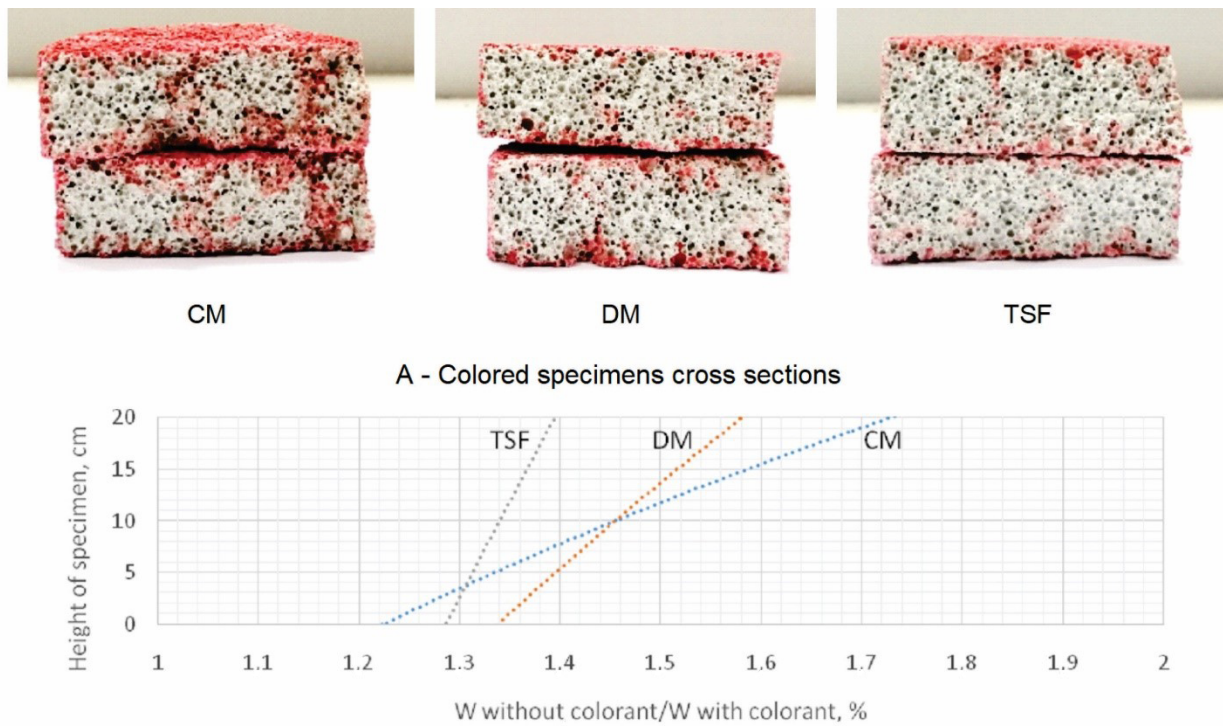
Figure 7. Comparison of specimens soaked in the colorant.

Visually, the greatest absorption is observed in CM samples, in the TSF and DM specimens, the absorption is within comparable ranges. After drying, all specimens have 100 % color of the contact zone (surface), which indicates a sufficiently reliable coloration of the material to assess the internal structure of the specimen. The internal structure of CM specimens had large local coloration areas in the cross-section (as compared to TSF and DM), which indirectly may indicate a greater number of communicating pores in CM specimens. In contrast, TSF and DM specimens demonstrated point-like coloration of the internal structure, which indicates a lower degree of the presence of communicating pores. Comparing the

dynamics of changes in height adjustment coefficients of the specimens, heterogeneity of the material can be deduced, because infiltration (except for the factor of communicating pores) is proportional to the pore size. In other words, if conditionally the quality of the communicating pores is identical, water absorption will be limited by the total volume of open surface pores.

3.2. Results of determining water absorption

Fig. 8 shows the results of density estimation of materials of three methods by height of specimens. The maximum density was observed in the lower segments of CM specimens, with an average density of 840 kg/m^3. The minimum density value was on average 365 kg/m^3, also observed in the specimens of CM, mainly in the upper segments. The density of DM specimens by height varied from 528 kg/m^3 (lower segments) to 630 kg/m^3 (upper segments), and in TSF specimens, from 608 kg/m^3 (lower segments) to 635 kg/m^3 (upper segments). As for the height, CM specimens were represented by grades of foam concrete from D350 to D800, DM specimens – from D500 to D600, and TSF specimens – D600.
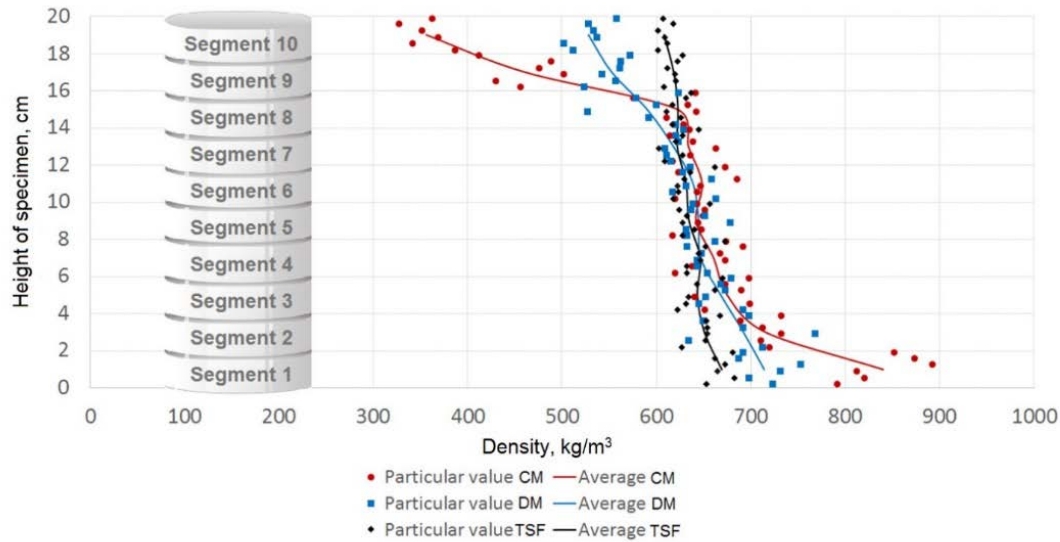

Figure 8. Comparison of specimen densities.

The degree of homogeneity in terms of material density by height of CM specimens was from 56.9 to 65.7 %, with a standard deviation of 125.8. For DM specimens the degree of homogeneity in height made up from 83.9 to 86.6 %, at a standard deviation of 55.6. The degree of homogeneity of TSF specimens was from 94.5 to 95.8 %, at the standard deviation of 17.2. Comparing particular values of density in the horizontal plane, we obtained: the degree of homogeneity of CM specimens was from 89.4 to 97.3 %, with the heterogeneity observed from a height of 16 mm, DM specimens from 89.2 to 97.8 %, with the maximum heterogeneity observed at a height of 14–16 mm, the degree of homogeneity of TSF was not less than 96.2 %. Thus, the compared methods had equally acceptable homogeneity in the horizontal direction in comparison with their homogeneity in height, where the worst is the specimen of CM [4].

3.3. Results and discussions of strength determination
of segmented cylindrical specimens by unconfined compression test

The results of strength tests of monolithic and segmented specimens are shown in Fig. 9. Maximum values of monolithic strength were shown by TSF and DM specimens, on average: strength of TSF exceeded strength of CM by 6.7 %, and strength of DM by 6.1 %. In general, individual values of monolithic strength of the three methods were closely related and lay within the following ranges: from 4.25 to 5.87 MPa for CM, from 4.56 to 5.76 MPa for DM, and from 4.65 to 5.72 MPa for TSF. Average values of monolithic strength were: 4.89 MPa for CM, 5.21 MPa for DM, and 5.25 MPa for TSF.
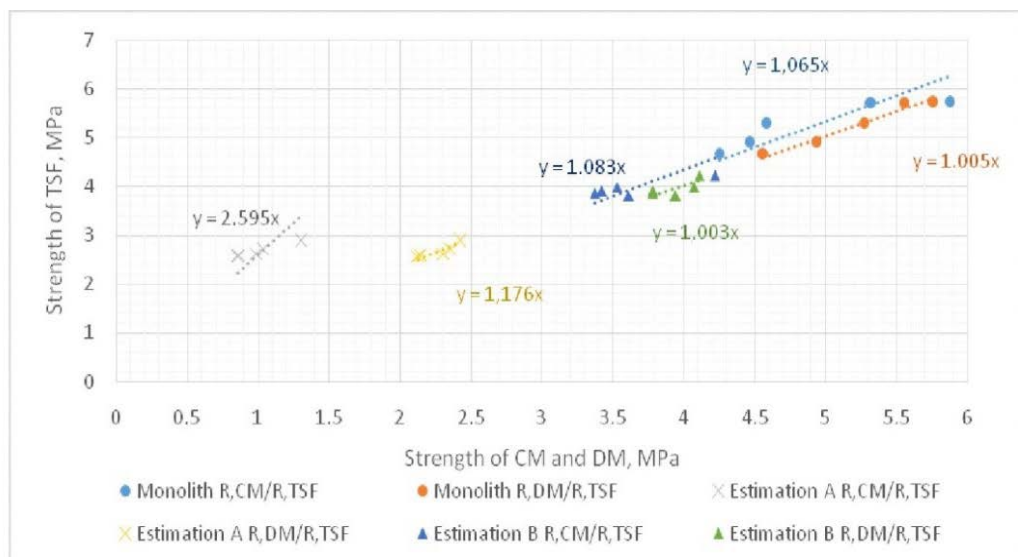
Figure 9. Strength test results.

In comparison of A, assessment values (identification of the weakest area by specimen height) also were expressed by the ratio of particular strength values of TSF specimens to CM and DM. According to the test results, the particular values of strength of the weakest segments of CM specimens varied from 0.85 to 1.31 MPa, which corresponds to the average value of foam concrete strength grade of D350. This means that all five CM specimens had weaker segments in height, the density of which did not exceed 350 kg/m^3. Particular values of strength of the weakest segments of DM specimens varied from 2.12 to 2.44 MPa, which corresponds to the average value of strength of foam concrete grade of D400. Strength of TSF segments varied from 2.57 to 2.87 MPa, which corresponds to the upper limit of strength of D400 grade foam concrete. Comparing the standard deviations of the obtained results on the strength of three methods (equal for CM specimens – 0.181, DM – 0.131, TSF – 0.122), it can be deduced that the greatest variation of the particular strength values was found in CM specimens. The smallest standard deviation was observed in the specimens of TSF, which indicates the maximum concentration of particular values of strength around the arithmetic mean of particular values. The ultimate deviations of particular values of were 17.8 % for CM specimens, 5.74 % for DM specimens and 4.57 % for TSF specimens, which indicates the heterogeneity of CM material in terms of strength in the horizontal plane (not only in the vertical plane).

In general, the assessment results showed that CM and DM specimens had a greater variation in height than TSF specimens. The weakest parts of the CM specimen were mainly the two upper segments 9 and 10 (Fig. 10A), with an average load of 2.8 kN, which corresponds to a strength of 1.01 MPa. The weakest parts of DM specimens were located in the upper part of the specimen, mainly in the three upper segments 8, 9 and 10 (Fig. 10B), with an average load value of 6.4 kN, which corresponds to a strength of 2.27 MPa. The lowest segment 4 (Fig. 10C) was not found in TSF specimens with an average load of 7.6 kN, which corresponds to a strength of 2.67 MPa.
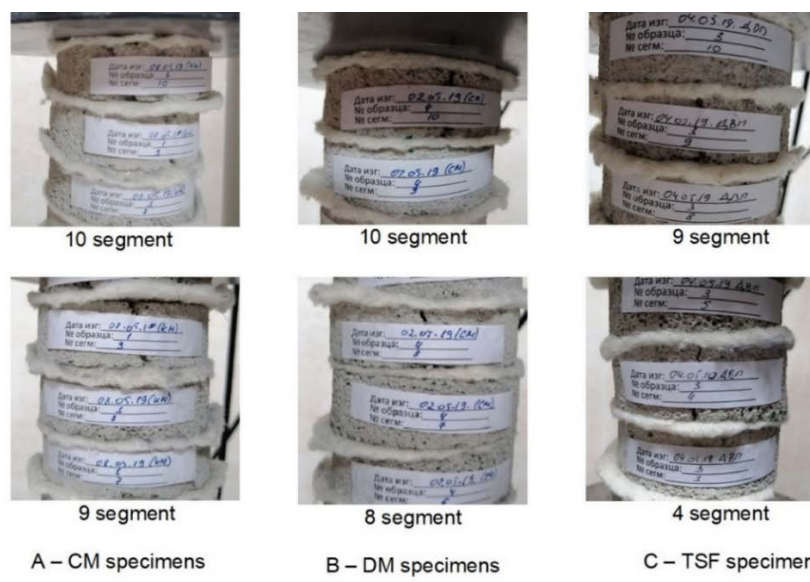

Figure 10. Weakest specimen segments.

In assessment B (maximum strength measurement) of CM and partially DM specimens, the tests were continued after removal of broken upper segments, otherwise, the peak load value would have been limited by the breakage of weak specimens due to the low value of their strength relative to other segments. In general, the values of maximum strength of the three methods are close to each other. The average value of maximum strength of CM specimens was 3.63 MPa, which corresponds to the average value of D500 grade foam concrete. DM and TSF specimens showed the strength of 3.93 and 3.95 MPa respectively, which corresponds to the upper limit of D500 grade.

Despite the fact that the selection of foam concrete composition and the ratio of foam concentrate to aggregate is calculated from the condition of obtaining the material density of D600 (600 kg/m^3), the obtained segmented specimens of the compared methods showed different results from the given values. The resultant factor of distortion of the results is the non-standard dimensionality of specimens and the fact that the specimens had no integral structure. But since all specimens were tested under the same conditions, the results may differ slightly from the actual values quantitatively but not qualitatively. And since the task was to compare the results relative to each other, the quantitative factor has no principal importance, since the results are expressed not by particular values, but by their ratio. Moreover, the obtained regularity of the ratio of strength parameters of the compared methods corresponds to the results of tests of monolithic specimens, therefore, tests of segmented specimens are suitable for qualitative evaluation of the strength distribution of the compared methods [20]. The results of strength showed high values compared with other technologies with and without additives, where the results were within 0.96–1.44 MPa [36, 37].

4. Conclusions

1. The resulting factor in the quality of foam concrete, with the same quality of components and ingredients, is the technological process of its production, as evidenced by the results of comparison of three methods of production: the classical method, the method of dry mineralization and the proposed method of two-stage foaming.

2. Evaluation of the homogeneity of the material was reduced to an analysis of its pore structure in volume, so the basis was taken as a discrete study of its local areas. Thus, the results of ratios of particular values of water absorption of segmented specimens by their height showed the degree of homogeneity of the compared methods: the maximum values of water absorption were found in CM samples (variation was from 7.3 to 69 %), the average values were in DM specimens (from 13 to 33 %), and the minimum values were in TSF (from 17 to 23 %). Consequently, TSF specimens have the maximum degree of homogeneity in height, because the greater the difference in particular values of water absorption of segments in height, the greater the difference in pore structure of individual segments.

3. Visual assessment of coloration of the internal structure of the specimens during soaking showed that the internal structure of CM specimens had large local areas of coloration in the cross-section (compared with TSF and DM), which may indirectly indicate a greater number of communicating pores in CM specimens. In contrast, TSF and DM specimens demonstrated point-like coloration of the internal structure, which indicates a smaller number of communicating pores.

4. The direct method of homogeneity was estimated by comparison of the obtained density values. In general, the density analysis showed that all the specimens of compared methods have the same acceptable homogeneity in the horizontal direction in comparison with their homogeneity in height, where the CM specimen performed the worst: with respect to height, CM specimens were represented by D350 to D800 grades of foam concrete (density from 350 to 800 kg/m^3), DM specimens – from D500 to D600 (from 500 to 600 kg/m^3), TSF specimens – from D600 to D600 (from 500 to 600 kg/m^3).

5. Comparisons of strength of monolithic specimens showed close results: 4.89 MPa, 5.21 MPa and 5.25 MPa for CM, DM and TSF specimens, respectively. The reason, albeit minor, for the difference is the dispersion of strength parameters by height and, as a consequence, the presence of weaker segments. The strength of the weakest segments: 0.85MPa for CM, 2.27 MPa for DM, and 2.67 MPa for TSF.

6. In general, the findings of the study confirmed the impact of the technological process of foam concrete production on its quality. The proposed production technology allows improving the pore structure of the skeleton due to the uniform distribution of pores, and as a consequence, increase the strength, physical and mechanical characteristics of the material as a product.

References

1. Kurweti, A., Chandrakar, R. Specification and Quality Control of Light Weight Foam Concrete. 2017. 5. 7.
2. Russian State Standard Gost|Official Regulatory Library – GOST 25485-2019 Available online: https://www.russiangost.com/p-375403-gost-25485-2019.aspx
3. Mohammed, J.H.; Hamad, A.J. Materials, Properties and Application Review of Lightweight Concrete. 2014, 37, 6.

4. Nguyen, T.T., Bui, H.H., Ngo, T.D., Nguyen, G.D., Kreher, M.U., Darve, F. A Micromechanical Investigation for the Effects of Pore Size and Its Distribution on Geopolymer Foam Concrete under Uniaxial Compression. Engineering Fracture Mechanics. 2019. 209. Pp. 228–244. DOI: 10.1016/j.engfracmech.2019.01.033

5. Babu, D.S., Ganesh Babu, K., Tiong-Huan, W. Effect of Polystyrene Aggregate Size on Strength and Moisture Migration Characteristics of Lightweight Concrete. Cement and Concrete Composites. 2006. 28. Pp. 520–527. DOI: 10.1016/j.cemconcomp.2006.02.018

6. Berndt, M.L. Properties of Sustainable Concrete Containing Fly Ash, Slag and Recycled Concrete Aggregate. Construction and Building Materials. 2009. 23. Pp. 2606–2613. DOI: 10.1016/j.conbuildmat.2009.02.011

7. Pioro, L.S., Pioro, I.L. Production of Expanded-Clay Aggregate for Lightweight Concrete from Non-Selfbloating Clays. Cement and Concrete Composites. 2004. 26. Pp. 639–643. DOI: 10.1016/S0958-9465(03)00103-3

8. Yang, K.-H., Song, J.-K., Lee, J.-S. Properties of Alkali-Activated Mortar and Concrete Using Lightweight Aggregates. Materials and Structures. 2010. 43. Pp. 403–416. DOI: 10.1617/s11527-009-9499-6

9. Arellano Aguilar, R., Burciaga Díaz, O., Escalante García, J.I. Lightweight Concretes of Activated Metakaolin-Fly Ash Binders, with Blast Furnace Slag Aggregates. Construction and Building Materials. 2010. 24. Pp. 1166–1175. DOI: 10.1016/j.conbuildmat.2009.12.024

10. Cadere, C.A.; Barbuta, M.; Rosca, B.; Serbanoiu, A.A.; Burlacu, A.; Oancea, I. Engineering Properties of Concrete with Polystyrene Granules. Procedia Manufacturing. 2018. 22. Pp. 288–293. DOI: 10.1016/j.promfg.2018.03.044

11. Bogas, J.A., de Brito, J., Figueiredo, J.M. Mechanical Characterization of Concrete Produced with Recycled Lightweight Expanded Clay Aggregate Concrete. Journal of Cleaner Production. 2015. 89. Pp. 187–195. DOI: 10.1016/j.jclepro.2014.11.015

12. Shafigh, P., Ghafari, H., Mahmud, H. Bin, Jumaat, M.Z. A Comparison Study of the Mechanical Properties and Drying Shrinkage of Oil Palm Shell and Expanded Clay Lightweight Aggregate Concretes. Materials & Designю 2014. 60. Pp. 320–327. DOI: 10.1016/j.matdes.2014.04.001

13. Committee, C. Specification for Slag Cement for Use in Concrete and Mortars; ASTM International;

14. Jiang, Y., Ling, T.-C., Shi, C., Pan, S.-Y. Characteristics of Steel Slags and Their Use in Cement and Concrete – A Review. Resources, Conservation and Recycling. 2018. 136. Pp. 187–197. DOI: 10.1016/j.resconrec.2018.04.023

15. Mikulica, K., Hájková, I. Testing of Technological Properties of Foam Concrete. Materials Science Forum. 2016. 865. Pp. 229–233. DOI: 10.4028/www.scientific.net/MSF.865.229

16. Stolz, J., Boluk, Y., Bindiganavile, V. Mechanical, Thermal and Acoustic Properties of Cellular Alkali Activated Fly Ash Concrete. Cement and Concrete Composites. 2018. 94. Pp. 24–32. DOI: 10.1016/j.cemconcomp.2018.08.004

17. Awwad, T., Shakhmov, Zh.A., Lukpanov, R.E., Yenkebayev, S.B. Experimental Study on the Behavior of Pile and Soil at the Frost Condition. Sustainability Issues for the Deep Foundations. GeoMEast 2018. Sustainable Civil Infrastructures. Springer, Cham. DOI: 10.1007/978-3-030-01902-0_7

18. Wu, H.; Liu, J.; Zhang, X. Feasibility Study on Use of Cellular Concrete for Air Convection Embankment on Permafrost Foundations in Fairbanks, Alaska. Transportation Geotechnics. 2020. 22. 100317. DOI: 10.1016/j.trgeo.2020.100317

19. Shakhmov, Z.A., Zhussupbekov, A.Z. Frost Susceptibility of Soil and In-Situ Monitoring of Frost Depth in Construction. Proceedings of the 15th Asian Regional Conference on Soil Mechanics and Geotechnical Engineering, ARC 2015: New Innovations and Sustainability; 2015.

20. Grinfeld, G.I., Gorshkov, A.S., Vatin, N.I. Tests Results Strength and Thermophysical Properties of Aerated Concrete Block Wall Samples with the Use of Polyurethane Adhesive. Advanced Materials Research. 2014. 941–944. Pp. 786–799. DOI: 10.4028/www.scientific.net/AMR.941-944.786

21. Hilal, A.A., Thom, N.H., Dawson, A.R. Failure Mechanism of Foamed Concrete Made with/without Additives and Lightweight Aggregate. Journal of Advanced Concrete Technology. 2016. 14. Pp. 511–520. DOI: 10.3151/jact.14.511

22. Nambiar, E.K.K., Ramamurthy, K. Shrinkage Behavior of Foam Concrete. Journal of Materials in Civil Engineering. 2009. 21. Pp. 631–636. DOI: 10.1061/(ASCE)0899-1561(2009)21:11(631)

23. Sun, C., Zhu, Y., Guo, J., Zhang, Y., Sun, G. Effects of Foaming Agent Type on the Workability, Drying Shrinkage, Frost Resistance and Pore Distribution of Foamed Concrete. Construction and Building Materials. 2018. 186. Pp. 833–839. DOI: 10.1016/j.conbuildmat.2018.08.019

24. Dhasindrakrishna, K., Pasupathy, K., Ramakrishnan, S., Sanjayan, J. Progress, Current Thinking and Challenges in Geopolymer Foam Concrete Technology. Cement and Concrete Composites. 2021. 116. 103886. DOI: 10.1016/j.cem-concomp.2020.103886

25. Liew, A.C.M. New Innovative Lightweight Foam Concrete Technology. In Use of Foamed Concrete in Construction. Conference Proceedings; Thomas Telford Publishing, 2005. Pp. 45–50. ISBN: 978-0-7277-4031-1.

26. Technological Parameters Influence on the Non-Autoclaved Foam Concrete Characteristics: AIP Conference Proceedings: Vol. 1800. No. 1 Available online: https://aip.scitation.org/doi/abs/10.1063/1.4973028

27. Chica, L., Alzate, A. Cellular Concrete Review: New Trends for Application in Construction. Construction and Building Materials. 2019. 200. Pp. 637–647.

28. Vardhan, R., Chandel, S., Sakale, R. Study of Cellular Light Weight Concrete. International Journal for Scientific Research and Development. 2016. Vol. 4. No. 07.

29. Amran, Y.H.M., Farzadnia, N., Abang Ali, A.A. Properties and Applications of Foamed Concrete; a Review. Construction and Building Materials. 2015. 101. Pp. 990–1005. DOI: 10.1016/j.conbuildmat.2015.10.112

30. Vine-Lott, K. Apparatus and Method for Producing Foamed Materials 1992.

31. Dunton, H.R., Rez, D.H. Apparatus and Method to Produce Foam, and Foamed Concrete 1988.

32. Ramamurthy, K., Kunhanandan Nambiar, E.K, Indu Siva Ranjani, G. A Classification of Studies on Properties of Foam Concrete. Cement and Concrete Composites. 2009. 31. Pp. 388–396. DOI: 10.1016/j.cemconcomp.2009.04.006

33. Interstate Standard, G. 21520-89. Small-Sized Wall Blocks of Cellular Concrete.

34. Lukpanov, R.E., Dyussembinov, D.S., Utepov, Ye.B., Bazarbayev, D.O., Tsygulyov, D.V., Yenkebayev, S.B., Shakhmov, Zh.A. Homogeneous pore distribution in foam concrete by two-stage foaming. Magazine of Civil Engineering. 2021. 103(3). Article No. 10313. DOI: 10.34910/MCE.103.13

35. Raj, A., Sathyan, D., Mini, K.M. Physical and Functional Characteristics of Foam Concrete: A Review. Construction and Building Materials. 2019. 221. Pp. 787–799. DOI: 10.1016/J.CONBUILDMAT.2019.06.052

36. Hilal, A.A., Thom, N.H., Dawson, A.R. On Entrained Pore Size Distribution of Foamed Concrete. Construction and Building Materials. 2015. 75. Pp. 227–233. DOI: 10.1016/j.conbuildmat.2014.09.117

37. Steshenko, A.B., Kudyakov, A.I., Ryabtseva, N.E. Cement Based Foam Concrete with Hardening Accelerators. IOP Conf. Ser.: Mater. Sci. Eng. 2020. 911. 012003. DOI: 10.1088/1757-899X/911/1/012003

Information about authors:

Rauan Lukpanov, *PhD*
ORCID: https://orcid.org/0000-0003-0085-9934
E-mail: Rauan_82@mail.ru

Duman Dyussembinov, *PhD in Technical Science*
ORCID: https://orcid.org/0000-0001-6118-5238
E-mail: dusembinov@mail.ru

Zhanbolat Shakhmov, *PhD*
ORCID: https://orcid.org/0000-0003-1680-5287
E-mail: zhanbolat8624@mail.ru

Daniyar Bazarbayev, *PhD*
ORCID: https://orcid.org/0000-0001-8547-5440
E-mail: phdd84@mail.ru

Denis Tsygulyov, *PhD in Technical Science*
ORCID: https://orcid.org/0000-0002-7061-699X
E-mail: denis_riza_72@mail.ru

Serik Yenkebayev, *PhD*
ORCID: https://orcid.org/0000-0002-5984-9346
E-mail: yenkebayev-serik@mail.ru

Influence of NaOH-concentration and blast-furnace-slag on the properties of geopolymer mortars

T.V. Lam[1] ✉ iD **, K.D. Vu[2]** iD

[1] *Hanoi University of Mining and Geology, Bac Tu Liem, Ha Noi, Vietnam*

[2] *Moscow State University of Civil Engineering (National Research University), Moscow, Russia*

✉ *lamvantang@gmail.com*

Abstract. The paper focused of the production of geopolymer materials using solid wastes, including fly ash, bottom ash (BA), granulated blast furnace slag (GBFS) in thermal power plants, and granulated blast furnace slag. Using the BA and GBFS as source material for geopolymer mortar is cost-effective, it allows safe disposal of the postproduction industrial wastes and improves properties of mortar for green buildings approach and development. In the present investigation, BA and GBFS were used as alumino-silicate materials for making alkali-activated bottom ash mortar (GPM). The effects of NaOH content in the sodium hydroxide solution with the concentration of 10–16 M and the presence of granulated blast furnace slag content (0–60 %) on the workability and the compressive strength development of alkali-activated bottom ash mortar were studied. The absolute volume method combined with the experimental results was used to determine the compositions of GPM specimens. Furthermore, the compressive strength of the mortar samples was performed following ASTM C109 and Vietnamese Standard TCVN 6016:2011. The results revealed that both NaOH concentration and granulated blast furnace slag content greatly affected the workability of mixtures and compressive strength development of the tested samples. Moreover, the relationship between the 28-day compressive strength and a water-to-geopolymer solid ratio of GPM specimens is also determined in this work.

1. Introduction

Ordinary Portland cement (OPC) clinker is made by heating a mixture of raw materials, including limestone and clay, to a calcining temperature exceeding 600 °C and then a fusion temperature of about 1450–1600 °C to sinter the materials into clinker, according to the following formula:

$$12CaCO_3 + 2SiO_2 + 2Al_2O_3 + Fe_2O_3 \rightarrow 3CaO.SiO_2\left(C_3S\right) + 2CaO.SiO_2\left(C_2S\right) +$$
$$+ 3CaO.Al_2O_3\left(C_3A\right) + 4CaO.Al_2O_3.Fe_2O_3\left(C_4AF\right) + 12CO_2.$$
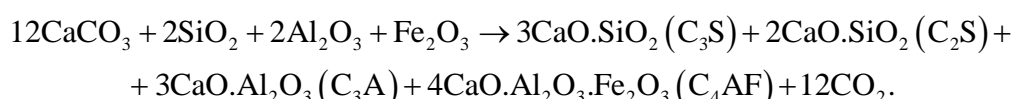
Ordinary Portland/pozzolanic cement manufacturing is an energy-intensive process and releases significant quantities of toxic fumes and carbon dioxide into the atmosphere [1–3].

In recent years, many investigations have been focusing on the potential of utilizing natural materials, like fly ash, bottom ash, slag, granulated blast furnace slag. Such materials can be considered an alternative for PC to reduce the cement content in the concrete mixture and improve the development of modern cementitious materials in construction materials manufacturing. In 1978, Davidovits [4, 5] proposed that a new binder could be produced by a polymerization process involving a reaction between alkali-liquid solutions and compounds containing aluminum and silicon. These binders were termed "geopolymers." The geopolymer, including alumino-silicate material with alkaline liquids, is currently one of the most promising materials of environmentally-friendly binders for green concrete in the construction industry [6, 7].

Material types containing silicon (Si) and aluminum (Al) atoms in amorphous form, which come from natural mineral additions or by-product materials, and industrial wastes, could be used as source materials for alkali-activated bottom ash mortar (GPM) and geopolymer concrete. On the other hand, some pozzolanic materials are by-products such as metakaolin, fly ash, bottom ash (BA), granulated blast furnace slag (GBFS), and palm oil fuel ash, etc. [8–12]. For the manufacture of geopolymer products, the choice of raw materials depends mainly on their availability and cost, the type of application, and the specific demand of the producers [13–15].

In the synthesis of geopolymer materials, the granulated blast furnace slag and bottom ash provide excellent geopolymer mortar and concrete properties in both the fresh and hardened state. These made them suitable materials for structural applications in green buildings and replacing cement [16–18].

For the geopolymer concrete and mortar, the type of alkali liquid played an important role in the polymerization process as a concrete binder. The alkali-activator solutions (AAS) of NaOH and Na_2SiO_3 or KOH and K_2SiO_3 with different concentrations are the most common alkali-liquid solutions used in geopolymerisation [19–21]. The published studies [22–25] showed that the engineering properties of concrete/mortar increases when water glass (Na_2SiO_3) is added to the sodium hydroxide, compared with using only NaOH. Further, the addition of waterglass increases the ratios of Si/Al and Na/Al, resulting in increased formation of sodium aluminosilicate gel (Na_2O-Al_2O_3-SiO_2-H_2O) which indicates higher strength behavior tested samples.

The bottom ash and granulated blast furnace slag are major by-products of thermal and steel plants. These materials often cause disposal challenges and environmental pollution. Industrial waste materials, in particular BA obtained from the combustion process in thermal power plants (TPP), were used widely as a mineral additive for concrete/mortar due to their pozzolanic properties. At present, over a million tons of BA TPP are generated each year globally [26–28]. The class-F BA TPP, containing highly amorphous SiO_2 and Al_2O_3, was used as a raw material to produce geopolymer concrete and mortar.

Moreover, granulated blast furnace slag-GBFS is one of the by-products generated during the extraction of iron from iron ore that contains a high silica content in the form of non-crystalline or amorphous silica – SiO_2. To make such a by-product be used more sustainably, in-depth knowledge of the engineering and environmental properties of GBFS is required. This material is considered reactive with the alkali-activator solution to produce the aluminosilicate gel that binds the aggregate types and provides the mechanical properties of GPM [18, 29, 30].

In Vietnam in recent years, granulated blast furnace slag (GBFS), a solid waste, is a by-product of pig iron production in blast furnaces of Hoa Phat Group in Hai Duong Iron and Steel Complex.

Because both Vietnamese GBFS and BA TPP "Vung Ang" contain high levels of Si and Al, these alumino-silicate materials are effective for producing GPM and geopolymer concrete. Furthermore, the AAS plays an important role in the dissolving process of Si-Al from amorphous silica-alumina to form gel geopolymer precursors and alumino-silicate materials. In addition, NaOH concentration significantly affects the workability of mixtures and the compressive strength of the tested GPM specimens. Therefore, the main aim of the current research is to investigate the effect of the influence of NaOH concentration and granulated blast furnace slag content on workability and compressive strength development of BA alkali-activated mortar.

2. Materials and Methods

2.1. Material properties

The characteristics of the raw materials used in this study were determined in the laboratory according to the guidelines of the related standards, with the results as follows:

a) No coarse aggregates were used in geopolymer mortars preparation. The fine aggregates used for geopolymer mortar mixtures were Red River quartz sands (QS) (Vietnam), which conformed to the

Vietnamese Standard TCVN 7570:2006. The fineness modulus of QS was M_k = 3.0, and its specific gravity was 2.65 g/cm^3.

b) Alumino-silicate materials (ASM) used in the study included granulated blast furnace slag "Hòa Phat" (GBFS) and bottom ash (BA) from TPP "Vung Ang" class-F.

The experimental results of chemical compositions and physical properties of GBFS and BA TPP "Vung Ang", determined by X-ray fluorescence analysis of raw materials, are given in Table 1. The BA TPP "Vung Ang" was composed mainly of SiO_2 (54.62 %) and Al_2O_3 (25.17 %) and that the main constituent of GBFS was SiO_2 (36.3 %) and CaO (40.1 %).

Table 1. Physical properties and chemical compositions of BA TPP "Vung Ang" and GBFS "Hoa Phat".

Materials		BA	GBFS
Physical properties	Specific gravity (g/cm^3)	2.35	2.92
	The volume of natural porous state (kg/m^3)	765	1650
	Specific surface area (m^2/g)	0.755	0.960
	Mean particle size (mm)	17.6	10.5
	Water requirement (%)	100.7	124.1
Average chemical composition (%)	SiO_2	54.2	36.3
	Al_2O_3	23.3	12.6
	Fe_2O_3	9.8	3.4
	SO_3	2.5	5.7
	K_2O	1.4	0.4
	Na_2O	1.1	0.3
	MgO	0.6	–
	CaO	1.2	40.1
	P_2O_5	1.4	–
	Loss on ignition	4.5	1.2

Particle size distributions of BA and GBFS, determined by XRD analysis, are given in Fig. 1 and Fig. 2, respectively. Moreover, these results showed that the particles of GBFS were significantly smaller than the particles of BA.
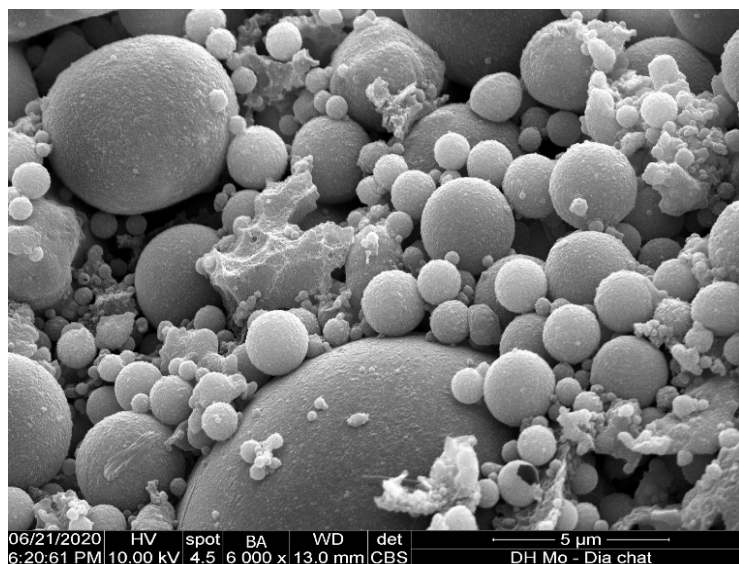

**Figure 1. Particle size distribution of BA TPP "Vung Ang".**
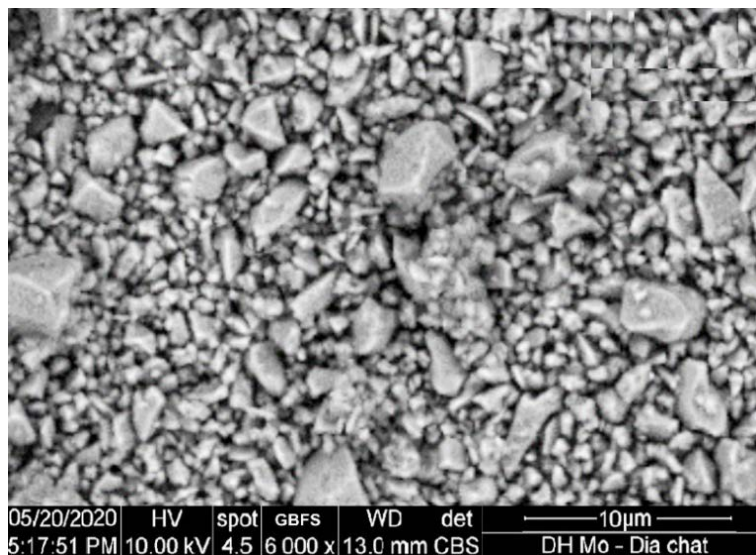
Figure 2. Particle size distribution of GBFS "Hoa Phat".

c). Activator: In the current experimental research, a combination of Na_2SiO_3 and NaOH solutions was used as the alkali-activator solution.

(i). The sodium hydroxide solids (NaOH) with 98–99 % purity was supplied by Viet-Nhat Co., Ltd. The sodium hydroxide solution was obtained by dissolving the NaOH flakes in the water to the required molarity. In this particular case, the molarity of sodium hydroxide (NaOH) solution was in the range of 10 M to 16 M. The specific gravity of the solution is 1.45 g/cm^3.

NaOH solution was prepared by simply dissolving the flakes in water. The mass of NaOH solids in a solution varied depending on the concentration of the solution expressed in terms of the molar – M. Note that the mass of NaOH solids was only a fraction of the mass of the NaOH solution where water was the major component [31, 32]. The composition of sodium hydroxide solution depending on its concentration is shown in Table 2.

Table 2. Composition of sodium hydroxide solution.

The concentration of the NaOH solution	Sodium hydroxide solution	
	NaOH solids (%)	Water (%)
10M	31.4	68.8
12M	36.1	63.9
14M	40.4	59.6
16M	44.4	55.6

(ii). Sodium silicate, also known as water-glass or liquid glass, is available in liquid (gel) form. In the present study, the Na_2SiO_3 liquid was supplied by Viet-Nhat Co., Ltd., with a $SiO_2/Na_2O = 2.5$, containing 29.5 % SiO_2, 11.8 % Na_2O, 58.7 % H_2O, and specific gravity of 1.55 g/cm^3. The chemical and physical properties of the silicates given by the manufacturer are shown in Table 3.

Table 3. Physical and chemical properties of Sodium Silicate.

1	Chemical Formula	Na_2OxSiO_2-xH_2O
2	Na_2O	11.8 %
3	SiO_2	29.5 %
4	H_2O	58.7 %
5	Appearance	Liquid (Gel)
6	Colour	Light Yellow Liquid
7	Boiling Point	102 °C for 40 % aqueous solution
8	Molecular Weight	184.04 g
9	Specific Gravity	1.55 g/cm^3

d) In the present study, the super-plasticizer admixture SR-5000F "SilkRoad" (SP) was procured from Hanoi-Korea Co., Ltd., with a specific gravity of 1.12 g/cm^3, which conformed to the Vietnamese

Standard TCVN 8826:2011. This admixture was used to increase the mortar mixtures' workability and reduce the water-cement ratios while increasing the strength of tested specimens.

e) Clean tap water (W) was used to prepare the sodium hydroxide solution and the curing of tested BA alkali-activated mortar specimens. All the tests met the requirements stated in Vietnamese Standard TCVN 4506:2012.

2.2. Experimental Methods

There have been very limited studies on the mixture design of geopolymer mortar and concrete raw materials to date. The influence of NaOH content and alumino-silicate raw materials on the geopolymer mortar properties was barely considered in the literature. First studies [29, 31, 32] proposing a composition of fly ash-based geopolymer concrete and bottom ash alkali-activated mortar were published in 2006 and 2008. This studied, however, did not discuss how to deal with the effects of a super-plasticizer content or the air content in the mixture. Recently, Ferdous et al. [33] have proposed a detailed mix design procedure for fly ash-based geopolymer concrete. In this study, the calculation method of the compositions of BA alkali-activated mortar mixture was applied following Ferdous et al. [33] and the absolute volume method, combined with the experimental results from the local raw materials in Vietnam.

- − The workability of the BA alkali-activated mortar mixture is determined by the standard slump cone with dimensions of 80×70×40 mm, available in Vietnamese Standard TCVN 3121:2003.
- − The compressive strength GPM tests were conducted to evaluate the BA alkali-activated mortar strength development for different periods. This experiment was performed in a standard mortar mould of 40×40×160 mm, at 3, 7, 14, 28, 56, and 90 days of curing time using 500T computer-controlled compression test. The "Controls Advantest 9" rig with a constant loading rate of 3000 N/s allowed maintaining the loading rate to a minimum. The compressive strength of the mortar samples was performed following ASTM C109 and Vietnamese Standard TCVN 6016:2011.

2.3. Mixture proportion

In the present research, the geopolymer mortars are prepared on the following basis:

(i) − Ratios of liquid-to-alumino-silicate materials $\left(\dfrac{L}{ASM}\right)$ ratio of 0.40 by mass, while sodium silicate solution-to-sodium hydroxide solution ratio of 2.5 [34, 35]. This ratio was fixed at 2.5 by mass in all the tested mixtures as the cost of sodium silicate solution is considerably cheaper than the sodium hydroxide solution.

(ii) − The sodium hydroxide solution was initially prepared by dissolving the NaOH flakes in water. The molarity of sodium hydroxide (NaOH) solution was considered in 10 M to 16 M [32]. These solutions were then mixed with the sodium silicate and were allowed to cool down to room temperature.

(iii) − In addition, GBFS was used to replace 0 %, 20 %, 40 %, and 60 % of BA TPP "Vung Ang" mass in the geopolymer mixtures [30]. Besides, the relative volume of entrapped air was 3.0 % in 1 m³ of tested concrete [29, 31, 32].

(iv) − Furthermore, a quartz sand-to-alumino-silicate materials ratio of 1.30 was maintained for all bottom ash alkali-activated mortar mixtures [26, 27].

(v) − The super-plasticizer "SR-5000F SilkRoad" was equal to 1.0 % by mass of ASM (ASM = BA + + GBFS) [28].

All compositions of GPM mixture used in this investigation are calculated and presented in Table 4.

Therefore, the water content, and water-to-geopolymer solid ratio $\left(\dfrac{W}{GS}\right)$ of mortar mixtures, are also shown in Table 4.

Table 4. Mixture proportions for the preparation of bottom ash alkali-activated mortar.

Sample code	$\frac{GBFS}{FA}$	NaOH molarities	Mix proportions of ingredients (kg/m³)								W	$\frac{W}{GS}$
							Solutions		Solid content			
			BA	GBFS	QS	SP	NaOH	Na₂SiO₃	NaOH	Na₂SiO₃		
GPM-01	0/100	10	816	0	1061	8.2	93	233	29	96	201	0.213
GPM-02	0/100	12	816	0	1061	8.2	93	233	34	96	197	0.208
GPM-03	0/100	14	816	0	1061	8.2	93	233	38	96	193	0.203
GPM-04	0/100	16	816	0	1061	8.2	93	233	41	96	189	0.198
GPM-05	20/80	10	662	166	1076	8.3	95	237	30	98	204	0.213
GPM-06	20/80	12	662	166	1076	8.3	95	237	34	98	199	0.208
GPM-07	20/80	14	662	166	1076	8.3	95	237	38	98	195	0.203
GPM-08	20/80	16	662	166	1076	8.3	95	237	42	98	192	0.198
GPM-09	40/60	10	504	336	1092	8.4	96	240	30	99	207	0.213
GPM-10	40/60	12	504	336	1092	8.4	96	240	35	99	202	0.208
GPM-11	40/60	14	504	336	1092	8.4	96	240	39	99	198	0.203
GPM-12	40/60	16	504	336	1092	8.4	96	240	43	99	194	0.198
GPM-13	60/40	10	341	511	1108	8.5	97	243	31	101	210	0.213
GPM-14	60/40	12	341	511	1108	8.5	97	243	35	101	205	0.208
GPM-15	60/40	14	341	511	1108	8.5	97	243	39	101	201	0.203
GPM-16	60/40	16	341	511	1108	8.5	97	243	43	101	197	0.198

2.4. Curing specimens

In the present study, all the tested BA alkali-activated mortar series patterns were de-molded 24 h after casting. Next, the specimens were heat cured at 80 °C for up to 30 minutes in a laboratory oven and then left in ambient conditions (25 ± 2) °C until the required testing time.

3. Results and Discussion

3.1. Workability of alkali-activated bottom ash mortar mixtures

The slump of the cone rates the workability of alkali-activated bottom ash mortar mixtures with dimensions of 80×70×40 mm. Table 5 and Fig. 3 shows the value of a slump cone of BA alkali-activated mortar mixture with different both NaOH concentration and granulated blast furnace slag contents. The average value of the slump cone of these mixtures was measured after 0, 30, and 60 minutes after the completion of mixing.

The standard slump cone determines the workability of the geopolymer mortar mixture with dimensions of 80×70×40 mm recommended by Vietnamese Standard TCVN 3121:2003.

Table 5. The average value of slump cone of alkali-activated bottom ash mortar mixtures.

Sample code	$\frac{GBFS}{FA}$	NaOH concentration	$\frac{W}{GS}$	The slump of alkali-activated bottom ash mortar mixtures (cm)		
				Immediately after the completion of mixing	30 minutes after the completion of mixing	60 minutes after the completion of mixing
GPM-01	0/100	10	0.213	21.0	17.2	14.0
GPM-02	0/100	12	0.208	19.0	16.5	13.1
GPM-03	0/100	14	0.203	18.2	15.5	11.5
GPM-04	0/100	16	0.198	18.0	14.4	10.8
GPM-05	20/80	10	0.213	20.5	16.6	14.0
GPM-06	20/80	12	0.208	18.8	16.6	13.0
GPM-07	20/80	14	0.203	17.6	14.2	11.2
GPM-08	20/80	16	0.198	16.0	13.5	10.2
GPM-09	40/60	10	0.213	19.3	15.6	13.5
GPM-10	40/60	12	0.208	18.5	14.8	12.8
GPM-11	40/60	14	0.203	17.0	14.0	10.6
GPM-12	40/60	16	0.198	16.0	13.0	10.0
GPM-13	60/40	10	0.213	18.2	14.6	12.3
GPM-14	60/40	12	0.208	15.8	12.6	10.5
GPM-15	60/40	14	0.203	14.5	11.5	10.0
GPM-16	60/40	16	0.198	13.9	11.0	10.0

Furthermore, data in Table 5 was shown that the addition of GBFS with different levels only slightly decreased the workability of alkali-activated bottom ash mortar mixtures. At the same time, the molarity of the NaOH solution in the range of 10 M to 16 M greatly influences the workability of these mixtures.
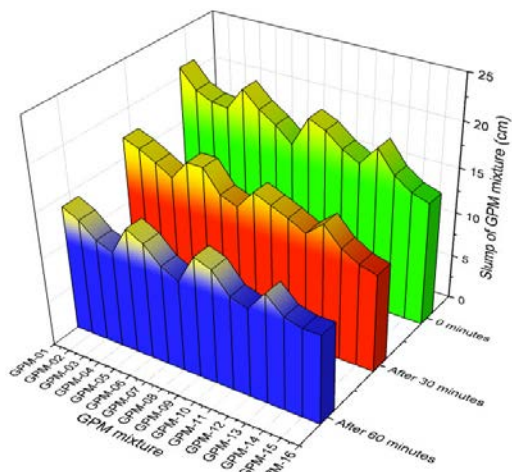

**Figure 3. The average value of slump cone of GPM mixtures
at times of 0, 30, and 60 minutes after the mixing.**

Immediately after mixing raw materials, their slump was in the range of 13.9 cm to 21.0 cm. This could be explained by (1) – the specific surface area of GBFS was larger, (2) – the GBFS particles were significantly smaller than the BA TPP "Vung Ang" particles, which have tended to increase water requirement in the mixing for these mortar mixtures, and (3) – the fact that the water requirement of GBFS (124.1 %) and BA (100.7 %) was greater than that of OPC (about of 29 %). Such observation would be in agreement with the basic principles of OPC concrete mixtures. In this case, the superplasticizer SR 5000F reduces the water-to-geopolymer solid ratio, thereby increasing the density in the structure of the BA alkali-activated mortar mixture.

As shown from Fig. 3, the average value of slump cone of mortar mixtures, measured after 30, and 60 minutes after completion of mixing, decreased in the range of 15 % to 20 % and 30 % to 40 %, respectively. The presented results are similar to those found in previous studies [30, 36, 37].

3.2. Compressive strength of BA alkali-activated mortar samples

Table 6 shows the compressive strength development of tested geopolymer samples prepared with different NaOH concentrations and different levels of granulated blast furnace slag contents.

Table 6. The average value of compressive strength of BA alkali-activated mortar samples at different hydration times.

Sample code	$\dfrac{GBFS}{FA}$	NaOH concentration	$\dfrac{W}{GS}$	Compressive strength – f_{cs} at different curing ages (MPa)					
				3-day	7-day	14-day	28-day	56-day	90-day
GPM-01	0/100	10	0.213	18.5	24.2	45.9	50.1	58.5	63.5
GPM-02	0/100	12	0.208	19.6	25.6	48.0	53.0	62.2	65.4
GPM-03	0/100	14	0.203	21.1	27.1	51.1	55.7	65.4	69.7
GPM-04	0/100	16	0.198	19.7	26.2	48.8	52.4	62.5	65.1
GPM-05	20/80	10	0.213	22.0	28.0	53.3	58.8	70.1	73.8
GPM-06	20/80	12	0.208	22.2	29.1	54.7	60.0	71.5	75.1
GPM-07	20/80	14	0.203	24.1	29.8	57.1	62.0	74.0	77.1
GPM-08	20/80	16	0.198	23.0	29.0	55.8	60.9	73.1	76.2
GPM-09	40/60	10	0.213	22.5	29.2	56.1	60.8	72.5	75.1
GPM-10	40/60	12	0.208	24.4	30.5	58.3	62.4	75.1	77.8
GPM-11	40/60	14	0.203	25.0	31.4	59.1	63.9	76.2	80.0
GPM-12	40/60	16	0.198	23.1	29.5	57.0	61.6	73.5	76.8
GPM-13	60/40	10	0.213	19.5	25.1	48.0	52.8	61.5	64.9
GPM-14	60/40	12	0.208	21.8	28.0	51.8	56.8	67.6	72.2
GPM-15	60/40	14	0.203	23.1	29.5	55.6	60.6	71.9	74.9
GPM-16	60/40	16	0.198	21.0	27.8	52.0	57.1	68.7	70.5

Data in Table 6 shows that the compressive strength values at 3, 7, 14, 28, 56, and 90-days of curing time were in the range of 18.5 ÷ 25.0 MPa, 24.2 ÷ 31.4 MPa, 45.9 ÷ 59.1 MPa, 50.1 ÷ 63.9 MPa, 58.5 ÷ ÷ 76.2 MPa, and 63.5 ÷ 80.0 MPa, respectively. The experimental results also prove the compressive strength development of the mortar specimens depends not only on the concentration of sodium hydroxide solutions but also on GBFS content.

3.2.1. Effect of granulated blast furnace slag content on the compressive strength development of BA alkali-activated mortars at different hydration times
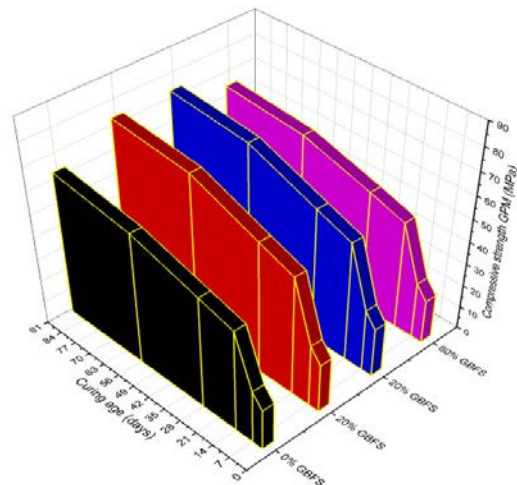
**Figure 4. The development of geopolymer mortar compressive strength at NaOH molarities of 10 M.**
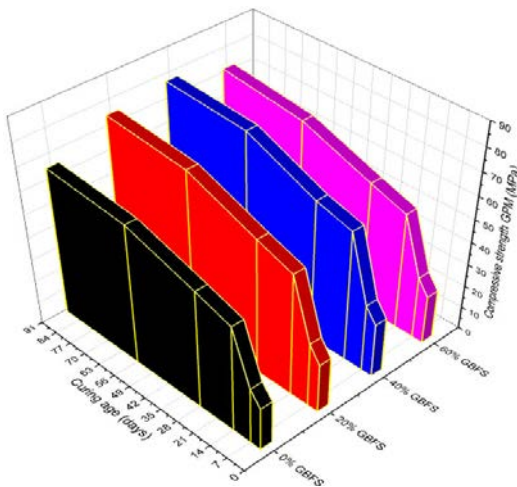
Figure 5. The development of geopolymer mortar compressive strength at NaOH molarities of 12 M.

The results also indicate that GPM compressive strengths have increased with curing periods (from 3 days to 90 days) and with the increase of Vietnamese granulated blast furnace slag content for all of the tested patterns. According to the study given by Kumar et al. and Venu et al. [18, 30], it has been reported that silica atoms increase with the increase in levels of GBFS content [23, 35, 38]. The strength of the alumino-silicate network in GPM structures should increase significantly with the increase in the amount of granulated blast furnace slag. Based on the outcomes of the present study, it is evident that the GPM compressive strength increased with the GBFS content from 0 % to 40 % and then started dropping back. The average value of the compressive strength at the 28-day curing time of BA alkali-activated mortar specimens that contained 0 %, 20 %, 40 %, and 60 % of GBFS felt in the range of 50.1÷55.7 MPa; 58.8÷62.0 MPa; 60.8÷63.9 MPa; and 52.8÷60.6 MPa, respectively.
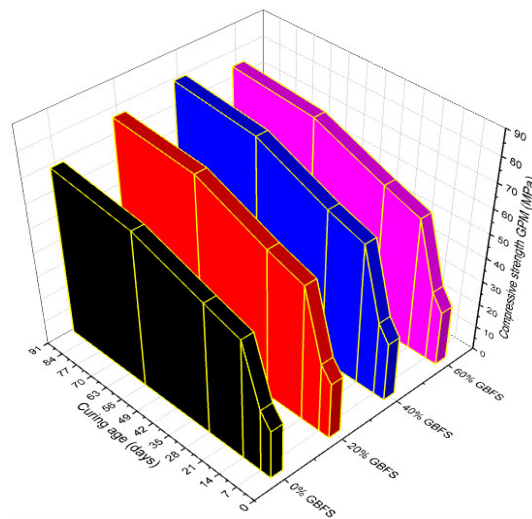
**Figure 6. The development of geopolymer mortar compressive strength
at NaOH molarities of 14 M.**
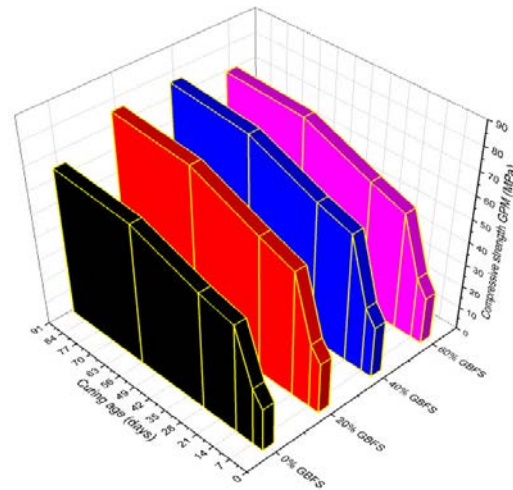
**Figure 7. The development of geopolymer mortar compressive strength
at NaOH molarities of 16 M.**

Moreover, Fig. 4, Fig. 5, Fig. 6, and Fig. 7 showed that the addition of Vietnamese GBFS in the mortar mixes modifies properties of BA alkali-activated mortar significantly, especially with the GBFS contents of 20 % and 40 %. These are caused by – the increased levels of reactive silica (Si in SiO_2) from the Vietnamese GBFS resulted in a higher density of bonds, leading to the higher compressive strength of the GPM-samples – with higher levels of granulated blast furnace slag content of a high specific surface area is responsible for modifying and improving the compressive strength of tested specimens. Furthermore, in the alkali activation of GBFS mortar, the main reaction product is a hydrated calcium-silicate (C-S-H) gel with low CaO/SiO_2 [18, 30]. The C-S-H gel improves the strength characteristic of geopolymer, similar to the results presented in previous studies [10, 35, 38].

Contrary to these principles, while the current work found that the strength behavior increased as Vietnamese granulated blast furnace slag increased to 40 %, that strength levels started declining after the content of GBFS content was 60 % by mass bottom ash (Table 6 and Fig. 4, 5, 6, 7). The effect of other parameters could explain this in the geopolymerization process on the engineering properties of tested geopolymer mortar samples [10, 36, 39]. The factors possibly responsible for these phenomena include (1) relatively larger Vietnamese granulated blast furnace slag solid particles negatively affecting the rate and extent of the geopolymerization process. Especially when the granulated blast furnace slag comprises a higher content of the mortar mixture leading to weaker GPM samples [35, 40]; and (2) a higher concentration of soluble silica, but lower soluble alumina, which hinders the reorganization of Si and Al atoms in the material structures and weakens tested geopolymer mortar samples [32, 34, 35, 39]. According to the experimental results of the strength behavior, the current research found a level of about 40 % of granulated blast furnace slag, delivering the highest compressive strength value for the BA alkali-activated mortar.

The results in Table 6 have shown that the compressive strength of BA alkali-activated mortar gradually increases with GBFS contents.

Moreover, Fig. 4, Fig. 5, Fig. 6, and Fig. 7 prove the development of the compressive strength of BA alkali-activated mortars at the different levels of GBFS contents, at the NaOH molarities of 10 M, 12 M, 14 M, and 16 M, respectively.

3.2.2. Effect of NaOH concentration on the 28-day compressive strength of BA alkali-activated mortars at different hydration times

The present work investigated the 28-day compressive strength of BA alkali-activated mortars at different NaOH molarities of 10, 12, 14, and 16 M. It was found that the compressive strength was proportional to the concentration of NaOH solution and reached the maximum value of 63.9 MPa at 28 days, with NaOH concentration of 14 M (in Table 6) and GBFS content of 40 %, by BA mass.
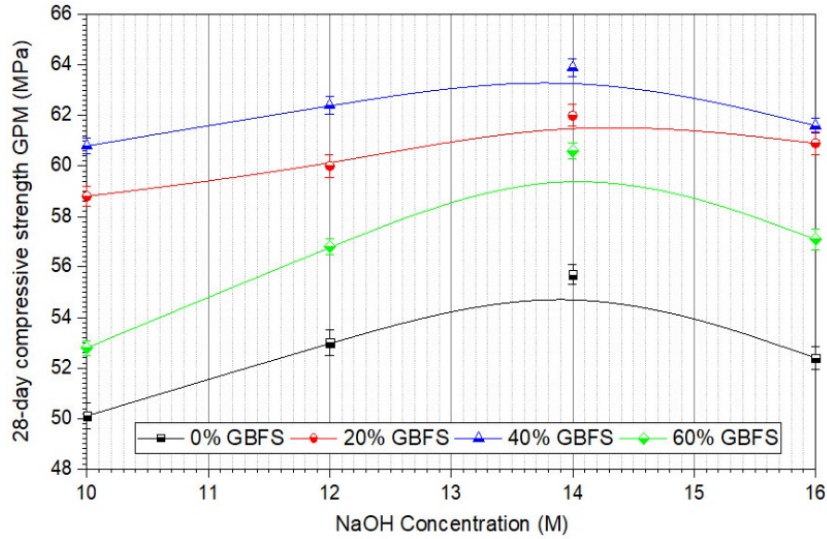

Figure 8. Effect of NaOH molarities on the 28-day compressive strength of BA alkali-activated mortars at 80 °C for 30 minutes.

In addition, Fig. 8 shows the influence of different NaOH contents on the 28-day compressive strength of BA alkali-activated mortars. Without GBSF addition and NaOH concentration of 10 M, this GPM sample contained only the bottom ash. The 28-day compressive strength was low, with only 50.1 MPa. This is due to the low pH value (only 10 M) of the liquid sodium silicate (Table 6) to form an effective excitation environment in this GPM sample, which is the main reason for its low compressive strength [19, 22, 41].

The alkalinity of the alkali-activator solution was significantly increased via the increase in NaOH concentration from 10 M to 14 M.

The pH value of NaOH solution has increased to the content of Na^+, which is very important to increase the polymerization degree and promote the formation of union alkali [2, 6, 40, 41]. Therefore, the 28-day compressive strength of these samples with NaOH concentrations of 12 M, 14 M was significantly higher when compared to that of the GPM sample with a NaOH concentration of 10 M.

In previous studies [23, 24, 34], it was proved that the increase in the concentration of sodium hydroxide solution leads to the following reaction processes: (1) the liberation of Si and Al ions species from aluminosilicate raw materials; (2) the formation of stronger ion pairs; and (3) the acceleration of polycondensation rates. These processes all contribute to the development of geopolymer strength.

3.2.3. Relationship between the water-to-geopolymer solids ratio and the 28-day compressive strength of BA alkali-activated mortars

Fig. 9 shows a relationship between the water-to-geopolymer solids ratio and the 28-day compressive strength of BA alkali-activated mortars.
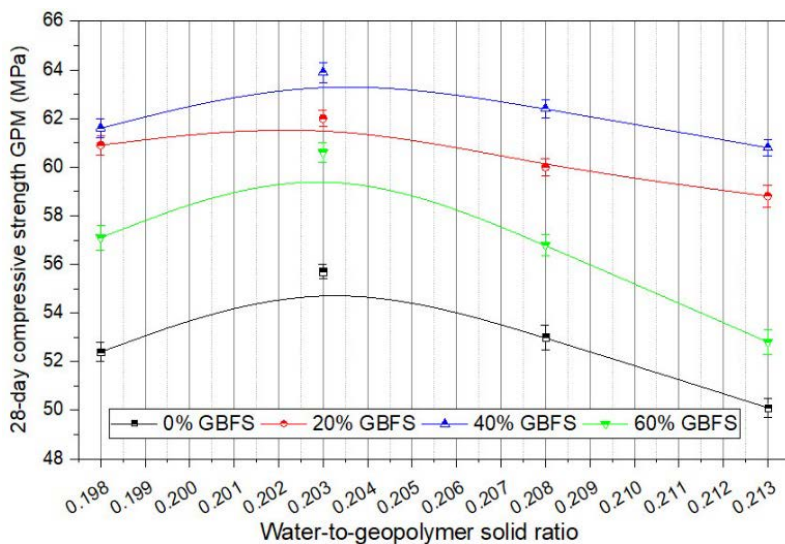
**Figure 9. Correlation between the water-to-geopolymer solids ratio
and the 28-day compressive strength of BA alkali-activated mortars.**

Data from Fig. 9 shows the relationship between the water-to-geopolymer solids ratio and the 28-day compressive strength of BA alkali-activated mortars. Similar findings were reported by Ferdous et al. [33]. The data required to plot relationships for BA alkali-activated mortars were obtained from laboratory conditions where samples were heated up to 80 °C for 30 minutes in the oven. The association was used at the initial composition calculation of the different geopolymer mortar types when the liquid-to-alumino-silicate material ratio was fixed at 0.4 and NaOH molarities in the range of 10 M to 16 M.

4. Conclusions

Based on the experimental results, the following conclusions are drawn on tested alkali-activated bottom ash mortar containing different levels of both NaOH concentrations and granulated blast furnace slag contents used in this investigation:

- For the bottom ash-based geopolymer mortar, the liquid-to-alumino-silicate material ratio and the quartz sand-to-alumino-silicate materials ratio are fixed at 0.4 and 1.30, respectively. Both the sodium hydroxide solution concentration (10–16 M) and Vietnamese granulated blast furnace slag content (0–60 %) greatly affected the workability mixtures and strength behavior of geopolymer mortars. The slump fell in the range of 13.9 ÷ 21.0 cm, while the compressive strength values at the 28-days curing time reached 50.1 MPa to 63.9 MPa.

- The average value of the slump cone of BA alkali-activated mortars, measured after 30 and 60 minutes after completion of mixing, decreased to 15 %, 20 %, and 30 % to 40 %, respectively, compared with the mixture slump immediately after the completion of raw materials mixing.

- The average compressive strength value of all tested BA alkali-activated mortar specimens increased with curing times test, from 3 days to 90 days. The results supported using different hydration times to develop the compressive strength of tested mortar specimens, reflecting Portland Cement behavior principles.

- Concerning the BA alkali-activated mortar samples, the optimum NaOH solution concentration and granulated blast furnace slag content were consistently associated with a higher average value of characteristic strength. The compressive strength of tested specimens peaked at the optimum value and then decreased gradually as NaOH concentration and Vietnamese granulated blast furnace slag content increased. Based on the results, the geopolymer mortar samples prepared with NaOH molalities of 14 M and a GBFS content of 40 % by BA mass exhibited high strength behaviors. Moreover, they were comparable with or even much higher than the GPM specimens with different levels of NaOH concentration and GBFS content.

- The development of compressive strength in the GPM-specimens was triggered not only by the hydration time but also by the NaOH molarities (10–16 M) and GBFS content (0–60 %) by bottom ash mass.

- In the present study, the experimental results showed that the compressive strength of mortar specimens decreased with an increase in the ratio of the water-to-geopolymer solid. Such observation agrees with the basic principles of OPC concrete, which used a binder from ordinary

Portland cement and mineral additive, the strength of which decreases with an increase in the water-binder ratio.

References

1. Efficiency, E., 2007. Tracking Industrial Energy Efficiency and CO2 Emissions. International Energy Agency, Paris, France.

2. Hardjito, D., Cheak, C.C., Ing, C.H.L. Strength and setting times of low calcium fly ash-based geopolymer mortar. Modern applied science. 2008. 2(4). Pp. 3–11.

3. Worrell, E., Price, L., Martin, N., Hendriks, C., Meida, L.O. Carbon dioxide emissions from the global cement industry. Annual Review of Energy and the Environment. 2001. 26. Pp. 303–329.

4. Davidovits, J. Chemistry of geopolymeric systems, terminology. 99 Geopolymer International Conference Proceeding, France, 1999.

5. Rangan, B.V., Hardjito, D., Wallah, S.E., Sumajouw, D.M.J. Studies on fly ash-based geopolymer concrete. Geopolymer, Green Chemistry and Sustainable Development Solutions. 2005. Pp. 133–138.

6. Lloyd, N.A., Rangan, B.V. Geopolymer concrete with fly ash. Second International Conference on Sustainable Construction Materials and Technologies, Italy. 2010. Vol. 3.

7. Palomo, A., Grutzeck, M.W., Blanco, M.T. Alkali-activated fly ashes-A cement for the future. Cement and Concrete Research. 1999. 29. Pp. 1323–1329.

8. Abdullah, M.H., Abuelgasim, R., Rashid, A.S.A., Mohdyunus, N.Z. Engineering properties of tanjung bin bottom ash. MATEC Web of Conferences. 2018. Vol. 250. p. 01006. EDP Sciences.

9. Bernal, S.A., de Gutierrez, R.M., Provis, J.L., Rose, V. Effect of silicate modulus and metakaolin incorporation on the carbonation of alkali silicate-activated slags. Cement and Concrete Research. 2010. 40(6). Pp. 898–907.

10. Chen, Z., Liu, Y., Zhu, W., & Yang, E.H. Incinerator bottom ash (IBA) aerated geopolymer. Construction and Building Materials. 2016. 112. Pp. 1025–1031.

11. García-Lodeiro, I., Palomo, A., Fernández-Jiménez, A. Alkali-aggregate reaction in activated fly ash systems. Cement and Concrete Research. 2007. 37. Pp. 175–183.

12. Provis, J.L., Palomo, A., Shi, C. Advances in understanding alkali-activated materials. Cement and Concrete Research, 2015. 78. Pp. 110–125.

13. Abbil, A., Kassim, A., Rashid, A.S.A., Hainin, M.R., Ullah, A., Matusin, S., Giwangkara, G.G. Effect of Alkali-Activator to Bottom Ash Ratio on the Undrained Shear Strength of Bottom Ash based Geopolymer. IOP Conference Series: Earth and Environmental Science. 2020. Vol. 498. No. 1. p. 012041.

14. Argiz, C., Moragues, A., Menéndez, E. Use of ground coal bottom ash as cement constituent in concretes exposed to chloride environments. Journal of Cleaner Production. 2018. 170. Pp. 25–33.

15. Ng, C., Alengaram, U.J., Wong, L.S., Mo, K.H., Jumaat, M.Z., Ramesh, S. A review on microstructural study and compressive strength of geopolymer mortar, paste and concrete. Construction and Building Materialsю 2018. 186. Pp. 550–576.

16. Marshdi, Q.S.R., Al-Sallami, Z.H.A., Zaichenko, N.M. Effect of multicomponent modifier on the properties of cement pastes formulated from self-compacting concrete. Magazine of Civil Engineering. 2020. 98(6). Article No. 9805 DOI: 10.18720/MCE.98.5

17. Chindaprasirt, P., Jaturapitakkul, C., Chalee, W., Rattanasak, U. Comparative study on the characteristics of fly ash and bottom ash geopolymers. Waste management. 2009. 29(2). Pp. 539–543.

18. Vu, K.D., Bazhenova, S.I. Modeling the influence of input factors on foam concrete properties. Magazine of Civil Engineering. 2021. 103(3). Article No. 10311. DOI: 10.34910/MCE.103.11

19. Zerfu, K., Ekaputri, J.J. Bond strength in PVA fibre reinforced fly ash-based geopolymer concrete. Magazine of Civil Engineering. 2021. 101(1). Article No. 10105. DOI: 10.34910/MCE.101.5

20. Ryu, G.S., Lee, Y.B., Koh, K.T., Chung, Y.S. The mechanical properties of fly ash-based geopolymer concrete with alkaline activators. Construction and Building Materials. 2013. 47. Pp. 409–418.

21. Huang, G., Ji, Y., Li, J., Zhang, L., Liu, X., Liu, B. Effect of activated silica on polymerization mechanism and strength development of MSWI bottom ash alkali-activated mortars. Construction and Building Materials. 2019. 201. Pp. 90–99.

22. Hanjitsuwan, S., Hunpratub, S., Thongbai, P., Maensiri, S., Sata, V., Chindaprasirt, P. Effects of NaOH concentrations on physical and electrical properties of high calcium fly ash geopolymer paste. Cement and Concrete Composites. 2014. 45. Pp. 9–14.

23. Huang, G., Yang, K., Sun, Y., Lu, Z., Zhang, X., Zuo, L., Xu, Z. Influence of NaOH content on the alkali conversion mechanism in MSWI bottom ash alkali-activated mortars. Construction and Building Materials. 2020. 248. 118582.

24. Tuyan, M., Andiç-Çakir, Ö., Ramyar, K. Effect of alkali activator concentration and curing condition on strength and microstructure of waste clay brick powder-based geopolymer. Composites Part B: Engineering. 2018. 135. Pp. 242–252.

25. Fernández-Jiménez, A.M., Palomo, A., López-Hombrados, C. Engineering Properties of Alkali- Activated Fly Ash Concrete. ACI Materials Journal. 2006. Title no. 103-M12. Technical paper.

26. Tang, V.L., Bulgakov, B., Aleksandrova, O., Larsen, O., Anh, P. N. Effect of rice husk ash and fly ash on the compressive strength of high-performance concrete. E3S Web of Conferences. 2018. Vol. 33. 02030. EDP Sciences. DOI: 10.1051/e3sconf/20183302030

27. Tang, V.L., Nguyen, T.C., Hung, N.X., Van Phi, D., Bulgakov, B., Bazhenova, S. Effect of natural pozzolan on strength and temperature distribution of heavyweight concrete at early ages. MATEC web of conferences. 2018. Vol. 193. 03024. EDP Sciences. DOI: 10.1051/matecconf/201819303024

28. Steshenko, A.B., Kudyakov, A.I. Cement based foam concrete with aluminosilicate microspheres for monolithic construction. Magazine of Civil Engineering. 2018. 84(8). Pp. 86–96. doi: 10.18720/MCE.84.9.

29. Rangan, B.V., 2008a. Low-calcium, fly-ash-based geopolymer concrete. Concrete construction engineering handbook, Chapter 26, Taylor & Francis.

30. Kumar, S., Kumar, R., Mehrotra, S. P. Influence of granulated blast furnace slag on the reaction, structure and properties of fly ash based geopolymer. Journal of materials science. 2010. 45(3). Pp. 607–615.

31. Rangan, B.V. Design and manufacture of flyash-based geopolymer concrete. Concrete in Australia. 2008. 34(2). Pp. 37–43.

32. Wallah, S., Rangan, B.V. Low-calcium fly ash-based geopolymer concrete: long-term properties. Research Report GC 2, Faculty of Engineering, Curtin University of Technology, Perth, Australia .2006.

33. Ferdous, M.W., Kayali, O., Khennane, A. A detailed procedure of mix design for fly ash based geopolymer concrete. Proceedings of the Fourth Asia-Pacific Conference on FRP in Structures (APFIS 2013), Melbourne, Australia, 2013.

34. Rattanasak, U., Chindaprasirt, P. Influence of NaOH solution on the synthesis of fly ash geopolymer. Minerals Engineering. 2009. 22(12). Pp. 1073–1078.

35. Hwang, C.L., Huynh, T.P. Effect of alkali-activator and rice husk ash content on strength development of fly ash and residual rice husk ash-based geopolymers. Construction and Building Materials. 2015. 101. Pp. 1–9.

36. Chou, J.D., Wey, M.Y., Liang, H.H., Chang, S.H. Biotoxicity evaluation of fly ash and bottom ash from different municipal solid waste incinerators. Journal of hazardous materials. 2009. 168(1). Pp. 197–202.

37. Hardjito, D, Rangan, B.V. Development and properties of low-calcium fly ash-based geopolymer concrete. Curtin University of Technology, Perth, Australia. 2005.

38. Xie, T., Ozbakkaloglu, T., Behavior of low-calcium fly and bottom ash-based geopolymer concrete cured at ambient temperature. Ceramics International. 2015. 41(4). Pp. 5945–5958.

39. Patra, R.K., Mukharjee, B.B., Influence of granulated blast furnace slag as fine aggregate on properties of cement mortar. Advances in Concrete Construction. 2018. 6(6). 611.

40. El-Habaak, G., Askalany, M., Abdel-Hakeem, M. Building up and characterization of calcined marl-based geopolymeric cement. Infrastructures. 2018. 3(3). 22.

41. Xu, H., Van Deventer, J.S.J. The geopolymerisation of alumino-silicate minerals. International Journal of Mineral Processing. 2000. 59 (3). Pp. 247–266.

Information about authors:

Tang Van Lam, PhD
ORCID: https://orcid.org/0000-0002-4857-835X
E-mail: lamvantang@gmail.com

Kim Dien Vu,
ORCID: https://orcid.org/0000-0002-3367-9043
E-mail: kimdienxdtb@gmail.com